PROBING THE WATER CONTENT OF THE EARTH'S MANTLE: AN EXPERIMENTAL STUDY OF HYDROGEN MOBILITY UNDER EXTREME CONDITIONS

Jennifer Brooke

Thesis submitted for the degree of Doctor of Philosophy

School of Geosciences

The University of Edinburgh

2016

Abstract

Previous research has established that the majority of nominally anhydrous minerals (NAMs) in Earth's mantle can incorporate water in the form of structurally bound hydrogen and, correspondingly, the mantle is thought to contain a substantial volume of water. Water has been shown to play a key role in the geodynamics of the Earth's interior and quantifying the amount, and distribution, of water in the mantle is an important step in understanding many deep-Earth processes. One of the parameters highly sensitive to the incorporation of water in the mantle is electrical conductivity, as hydrogen is highly mobile and acts as the dominant charge-carrying species. In theory, this relationship can be used in conjunction with geophysical techniques that measure mantle-scale electrical conductivity to 'map-out' the deep Earth's water content – but accurate interpretation of such data requires full understanding of hydrogen mobility in NAMs under extreme conditions, which remains poorly constrained.

The aim of this project is to contribute to the reconciliation of geophysical observations with laboratory measurements of electrical conductivity, by considering hydrogen-deuterium exchange in single crystals. In a novel experimental design, hydrogen in crystals synthesised under mantle conditions (such that the hydrogen defects present correspond to the conditions being studied) exchanges with deuterium from a liquid source under controlled (mantle) pressure and temperature conditions for a specified time period. This results in hydrogen-deuterium exchange profiles that can be characterised by SIMS and subsequently fitted to Fick's law to calculate hydrogen diffusion coefficients – which in turn can be related to electrical conductivity through the Nernst-Einstein equation.

Analysis of the experimental results underlines the complexity of the influence of hydrogen on electrical conductivity in NAMs, and emphasises the need for careful consideration when interpreting and applying the results of diffusion studies. Ultimately, the data obtained in this study provides a useful contribution to understanding hydrogen diffusion in mantle minerals, but the non-trivial nature of both the experimental and analytical aspects mean that the method cannot easily be applied to other mantle phases.

Lay summary

Unlike the implication in Jules Verne's 'Journey to the Centre of the Earth', the interior of our planet is not an easily accessible area of study. What few samples are available come mainly from xenoliths – fragments of the Earth's inner layers that are brought up from depth during, for example, volcanic eruptions – but these are not always truly representative and may be altered during their transport to the surface. Instead, the study of the deep Earth makes use of a range of indirect techniques in order to gather information and provide clues as to the internal structure and composition of the planet. In particular, laboratory studies that simulate the high pressure and temperature conditions found inside the Earth are useful to give an indication of the minerals present and the way that they behave.

The aim of this project is to use laboratory experiments to investigate the amount of water that may be stored in the mantle layer of the Earth. The definition of water in this sense is not as expected, but instead refers to the chemical ingredients for water, O and H, included in the minerals that make up the mantle. Based on their chemical formulae, these minerals are not expected to contain water, but it has been shown that H can sit in imperfections in the crystal structure next to O atoms, creating OH groups ('potential water'). The presence of water in the mantle is important because it influences key properties, including melting, strength and flow. Understanding water in the Earth's mantle will therefore lead to a greater understanding of the way the planet works.

In order to study water in the mantle, this project uses samples of mantle minerals specifically created in the laboratory to contain hydrogen. The minerals are subjected to high temperature and pressure conditions in the presence of deuterium, so that the hydrogen present begins to switch places with the deuterium. The exchange of hydrogen for deuterium can be measured, and the movement of hydrogen can therefore be tracked for different temperatures by repeating the experiment. Since hydrogen is a positive ion (H^+) and acts as a carrier of electrical charge, its movement can be related to the electrical conductivity of the mineral. By knowing the influence of hydrogen content on electrical conductivity, it is possible to infer the water content of the mantle by measuring conductivity and comparing results for 'wet' vs. 'dry' minerals. Thus, the relationship between hydrogen incorporation and mineral conductivity can be used to 'map-out' the water content of the Earth's mantle.

Author's Declaration

I declare that this thesis has been composed solely by myself and that it has not been submitted, either in whole or in part, in any previous application for a degree. Except where otherwise acknowledged, the work presented is entirely my own.

Jennifer Brooke

May 2017

Acknowledgments

First and foremost I would like to thank the UK Natural Environment Research Council, who supported this research through PhD studentship NE/K500835/1.

It goes without saying that there are numerous people without whom this project and my undertaking of it would not have been possible. I am incredibly fortunate to have had the support of amazing friends and family - to those named below and those I may have forgotten I am indebted. I also owe thanks to my current employer, GeoBus, and my colleagues Kathryn Roper and Sean Docherty for the flexibility and support afforded me over the past couple of months as I have finished writing up.

My thanks go to my supervisors Geoff Bromiley and Kathy Whaler for guidance, support and general advice throughout the entire project, as well as for reading and commenting on drafts of the final text. Particular thanks must go to Geoff for his continued patience and assistance with lab work, and discussions regarding the interpretation of results.

The experimental and analytical work would not have been possible without multiple members of staff within the department at Edinburgh, and my thanks go particularly to; Ian Butler for assistance with lab equipment and materials; Mike Hall for advice and assistance with sample preparation; Nic Odling for XRF analysis; Nicola Cayzer and Joaquin Cortes for assistance with SEM work; John Craven, Richard Hinton and Cees-Jan de Hoog for assistance with SIMS work (to Cees-Jan also for being my project advisor, and to John for particularly useful advice and support following initial experimental and analytical set-backs); and Vasileios Koutsos (Engineering) for assistance with WLI measurements. In addition to work in Edinburgh, I was fortunate enough to work with other experimental/analytical facilities over the course of the project - my thanks go to Simon Kohn for his help in carrying out FTIR analysis at Bristol, Fabrizo Nestola for orienting crystals of Cr-Fo at his lab in Italy, and especially to Sumit Chakraborty (along with others in the Thin Film laboratory at Ruhr-University, Bochum) for helpful discussions and for carrying out thin-film deposition of deuterium on my samples.

Completing a PhD is at times a tempestuous process, requiring significant emotional as well as academic support and my grateful thanks go to all my friends who have encouraged and believed in me. To all of the other PhD students past and present

who have shared the highs and lows: to Holly Spice and Catherine Gallagher who have always had time to listen and given advice (and for the welcome distraction of outdoor adventures), even when overcome by their own projects; to Tom Stokes and Maddy Berg for days and weeks of solidarity in the lab, to James Scott for enjoyable afternoons demonstrating Earth Dynamics and days out in the Scottish hills; and to Alex Iveson for his unique style of support from across the Atlantic. I am also grateful to those who regularly attended 'Igneous Coffee' over the years, for fruitful discussions and for generally showing an interest. In particular my gratitude goes to John Stevenson for encouragement and advice that helped me bounce back from experimental failures.

I count myself extremely lucky to have a supportive and understanding family, without whom I would never have embarked upon this academic journey - unquantifiable thanks are due to all of them; to my parents, Sarah and Charlie for putting up with me and my struggles with the project and for reading and commenting on various sections (to dad in particular; your general advice and comments the text were invaluable), and to Polly and Susie for providing me with a temporary home in Edinburgh.

Last but by no means least, my eternal thanks go to my wonderful husband, Nick - your support, encouragement and love (along with a strong desire on my part not to be outdone!) kept me going through the hardest times and I genuinely could not have made it without you.

Contents

References

A Olivine - fitting script

B Olivine - FTIR spectra

C Olivine - fitting plots

D Spinel - paper draft

E Spinel - fitting script

List of Figures

List of Tables

List of equations

CHAPTER 1

Introduction

The majority of the mineral phases that comprise the Earth's mantle are anhydrous; that is, their chemical formulae indicates that no water is present. Despite this, it was discovered several decades ago that, with the exception of spinel, most are in fact capable of containing water (Bell, 1992) - not molecular water (as H_2O), but instead as hydrogen incorporated at interstitial defects associated with oxygen atoms to form hydroxyl (OH) groups. These so termed 'nominally anhydrous minerals' or NAMs (notably the dominant upper mantle phases olivine, pyroxene and garnet, and the transition zone minerals ringwoodite and wadsleyite - see figure 1.1) are now known to be able to store substantial volumes of water in this manner (from 100's ppm to several weight percent), but no widely agreed constraint for the actual volume of water contained within NAMs under mantle conditions has yet been determined, despite multiple studies across a range of disciplines. Consequently, estimates of the water content of the mantle range from essentially dry to an amount equivalent to that stored in the surface oceans (Du Frane and Tyburczy, 2012), although the recent discovery by Pearson et al. (2014) of a natural sample of ringwoodite[1] containing around 1.5wt.% water lends substantial support to the idea that, at a minimum, the transition zone is locally hydrous.

---

[1] Contained within a host diamond and therefore preserved without reverting to olivine (its low pressure polymorph) at shallow depths.

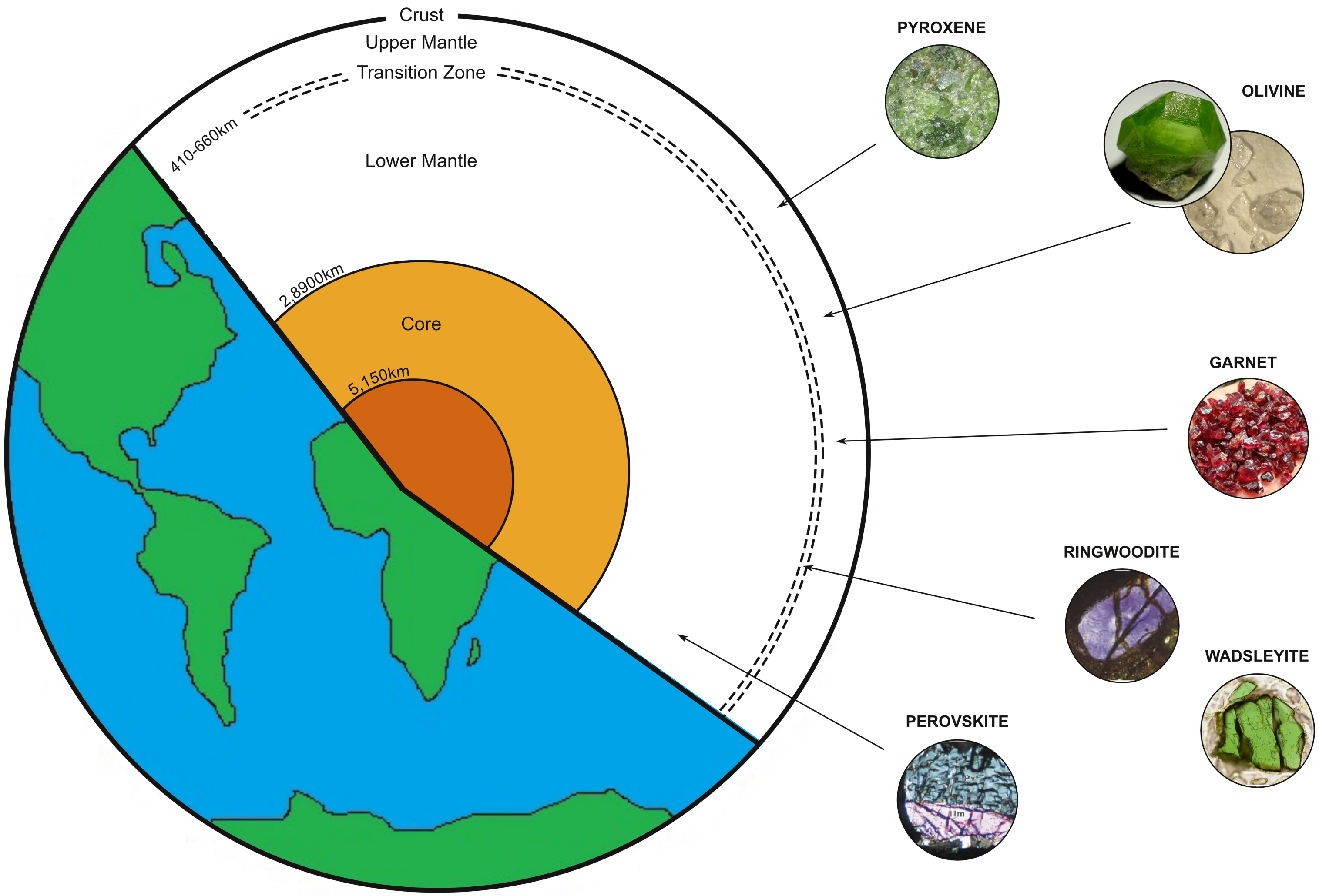

Figure 1.1: *Schematic section through the Earth's interior showing the occurrence of the major phases discussed in text.*

Constraining this estimate is key to developing an understanding of the deep Earth, as water plays an influential role in many critical processes. For example, the presence of water has been shown to: weaken Si-O bonds; affect elastic properties, rheology and phase equilibrium; alter transport properties (such as diffusion, deformation and electrical conduction) and melting behaviour; and may influence our understanding of both the depths at which phase changes occur and the properties of seismic discontinuities[2] (Bolfan-Casanova et al., 2000, among others; Bolfan-Casanova, 2005; Du Frane and Tyburczy, 2012; Khan and Shankland, 2012). Water may also affect planetary tectonics - models by Regenauer-Lieb and Kohl (2003) indicate that the unique system of plate tectonics that exists on Earth might only be possible above a threshold mantle water content, and suggest that this may explain the difference in tectonics between our planet and what is observed elsewhere in the solar system. In addition to the above, one proposal for the origin of water on Earth's surface is early degassing from depth and, as a result, continued investigation of water in the mantle could lead to a better appreciation of the link between processes in Earth's interior and the evolution of water on the surface (Bell, 1992).

---

[2] The presence of water in the Earth's mantle may thus also have important implications for petrological models since the seismic signature of the transition zone discontinuity is the only direct observation of the chemical/physical state of that region - broader than normal discontinuities observed may be associated with the presence of water.

1.1 Investigating water in the mantle

The deep Earth is clearly not an easily accessible area of study and, as as result, models of the interior structure of the planet are primarily based on geochemical and geophysical considerations, as well as analysis of the few samples that are available. Estimates of mantle water content have been calculated from samples of mid ocean ridge basalt (MORB), ocean island basalt (OIB) and mantle xenoliths, and are constrained by cosmochemical and geochemical arguments (based on the expected elemental abundances and distribution across Earth's reservoirs (Khan and Shankland, 2012)). The amount of water in the upper mantle can be estimated by relating the water content of primitive basaltic glass to both the degree of partial melting required to produce the glass and the extent to which water partitions between the melt and mantle residue (Berry et al., 2005). Initially it was thought that the source of this water would be hydrous minerals in cold parts of the mantle and liquid phases in hotter regions where these minerals are no longer stable (Martin and Donnay, 1972) - the identification of water in defect sites in NAMs significantly changed concepts of water storage, and has become the focus of more recent research.

Calculations on MORB and OIB imply an upper mantle source region containing between 0.0005-0.02 and 0.03-0.1wt.% water respectively, while bulk silicate Earth is geochemically constrained (using model-based mass balance calculations) to contain between 0.05 and 0.19wt.% (Bolfan-Casanova, 2005; Khan and Shankland, 2012). However, petrologically determined water contents may not be representative of that in deeper rocks - firstly as samples typically derive from shallow regions and secondly as geochemical estimates are highly model dependent and are weakened by the possibility of hydrogen sequestration in the core.[3]

Despite these constraints, xenoliths are a useful source of information on mantle mineralogy and processes as they can bring material from deeper regions to the surface. In some cases, lack of water in olivine fluid inclusions from such samples has been cited as evidence of dry conditions in the mantle, but it is generally thought that estimates are unlikely to be representative of the source region due to some modification of the original water content. Mackwell and Kohlstedt (1990) address the difficulty of extrapolating the water content of the mantle by analysing mantle

---

[3] In her 2005 *Mineralogical Magazine* paper 'Water in the Earth's mantle', Bolfan-Casanova gives a thorough review of how these figures are calculated and the considerations and assumptions involved.

minerals brought to the surface in xenoliths and conclude that, due to the rapid rate of hydrogen diffusion, loss during ascent is likely to be significant. This loss could explain the observation of inclusions in olivine containing nearly pure carbon dioxide, with little or no water (despite the instability of mantle olivine in fluids as oxidising as carbon dioxide). Thus the absence of water in fluid inclusions does not necessarily imply anhydrous conditions in the source region and xenolith data is likely to provide only a minimum estimate of mantle water content.

1.1.1 Defect sites and water incorporation in NAMs

Quantifying the amount of water that can be stored as hydrogen in mantle minerals and investigating its influence on chemical and physical properties is widely recognised as key to further understanding the Earth's interior. Fundamental background to this has been ascertaining the mechanisms of hydrogen incorporation relevant to mantle conditions and, accordingly, studies have focused on identifying these mechanisms, as well as determining the relative effects of temperature, pressure, oxygen fugacity (fO_2), and metal-content on hydrogen incorporation.

The incorporation of hydrogen in mantle minerals was first discovered by spectroscopy (as interstitial hydrogen bonds to oxygen atoms in the host, giving rise to spectographically active OH bonds - see further discussion in the following section and in section 4.5) and many subsequent studies have used similar methods to try to constrain the amount of water present. Typically, the basis of quantitative measurements of water content using this method is the Beer-Lambert law, which relates infra-red absorbance to the concentration of hydroxyl groups (c) and the thickness of the sample (t) via a molar absorption coefficient ε (equation 1.1).

$$Absorbance = \varepsilon \times c \times t \tag{1.1}$$

Infrared spectra for NAMs contain absorption peaks that can be attributed to O-H stretching modes in the mineral structure but quantitative data relies on independent calibration of ε which is not straightforward (Bolfan-Casanova, 2005) and, additionally, imprecise values can be obtained due to water contained in inclusions or bound to mineral surfaces. Accordingly, it has been widely used to estimate water contents but does not necessarily provide an unequivocal value for the quantity stored in chemically complex systems under mantle conditions.

As discussed by Ferot and Bolfan-Casanova (2012), although there is substantial experimental data on the solubility of water in upper mantle minerals, the temperatures and pressures observed are generally too low to be accurately extrapolated to true mantle conditions. In particular, the group have shown (using an experimental set-up at pressures up to 14GPa) that while the effect of Fe and Al on the solubility of water in olivine is pressure and temperature dependent, at high pressure their contribution is minor compared with the dependence on water activity. Thus the question of how much water is actually stored in NAMs under mantle conditions remains.

Once the potential for water incorporation in NAMs had been established, experimental work on the mechanisms responsible quickly indicated that hydrogen diffuses into the crystal lattice and is associated with point defects in the mineral structure. It is thought that, rather than occupying the normal cation position, when hydrogen enters the structure of NAMs the proton attaches to structural oxygen (Smyth et al., 2006). The creation of this protonated oxygen requires a charge balancing substitution or vacancy. In olivine, Smyth et al. (2006) suggest that the dominant substitution mechanism (at relevant temperature/pressure conditions) is $2H^+$ for Mg^{2+}, during which the proton (H^+) does not actually reside at the Mg position but protonates an oxygen on the edge of the vacant Mg octahedron. Alternatively, some molecular dynamics simulations have suggested that Si vacancies can charge balance the protonation, and other authors (for example Poe et al., 2010) suggest that the substitution is balanced by small polarons (electron holes). Additionally, experiments by Berry et al. (2005) (carried out on natural olivine crystals) indicate that in the absence of oxidation, the only available defect to accommodate water is associated with Ti.

Significant variation between samples has been observed in spectroscopy studies identifying OH-associated bands, indicating that the olivine crystal structure is able to incorporate water at a number of different defect sites (Berry et al., 2005) and therefore indicating that all of the incorporation mechanisms suggested above are viable (and indeed likely to exist in conjunction with one-another). In the majority of natural samples analysed, including olivines from basalt xenoliths, two distinct bands contain most of the intensity of the hydroxyl region but this observation is not reproduced in synthetic olivines. Instead, other bands are observed, indicative of different modes of water incorporation at different defect sites (this will be discussed in greater detail in section 4.5). As the spectra, and thus the hydrated defect sites, in synthetic and natural samples are different the implication is that either the mechanism of olivine water incorporation is not yet well understood or experiments fail to accurately stimulate the conditions under which water substitutes in natural samples. Alternatively, it may be an indication that hydrogen defects in xenoliths do not represent those stable under mantle conditions and experiments are more likely to be representative of defect stability in the mantle. The potential for water-content modification during ascent/exhumation of natural samples is likely to contribute to this discord. Additionally, Berry et al. (2005) caution that there is no reason to expect that the substitution of water at one type of olivine defect will have the same effect on the physical or chemical properties of olivine as water at another type of defect site and thus ensuring that studies investigate water in relevant defects is highly important (both for quantifying the amount of water present and for determining its effects).

Despite its inaccessibility, it is well agreed that the transition zone, between approximately 410km and 660km deep, is composed primarily of the high pressure phases of olivine; wadsleyite and ringwoodite (see figure 1.2). At high-pressures, wadsleyite and ringwoodite have a considerably higher water solubility than upper mantle minerals (both minerals are able to accommodate up to several percent (by weight) of water) (Medin et al., 2007; Huang et al., 2005; Bolfan-Casanova et al., 2000) and thus the mantle transition zone (TZ) has been identified and highlighted as a potentially important reservoir for water storage in the mantle (although it is thought that the water content of the transition zone is likely to vary regionally Huang et al. (2005)). In wadsleyite in particular, one of the oxygen atoms is highly underbonded, providing an ideal site for hydrogen incorporation and the formation of a spectroscopic O-H group (Chakraborty, 2010); experimental studies have shown that wadsleyite can incorporate up to 33,000ppmw water (Hae et al., 2006). Theoretical studies have also suggested that the effect of water in the transition zone is to stabilise wadsleyite over a large depth range, since water is preferentially incorporated into wadsleyite rather then olivine. For example, **VanderMeijde2003** cite evidence of a 20-35km thick discontinuity near 410km depth (usually reported to be sharp, at 4-10km thick) that they believe is most likely to be explained by as much as 700ppmw water.

While natural spinel, as found in the upper mantle, is known to be truly anhydrous and does not incorporate any water, non-stoichiometric (defect) spinel has been shown to accommodate a few 100ppm water (Bromiley et al., 2010). The mechanisms

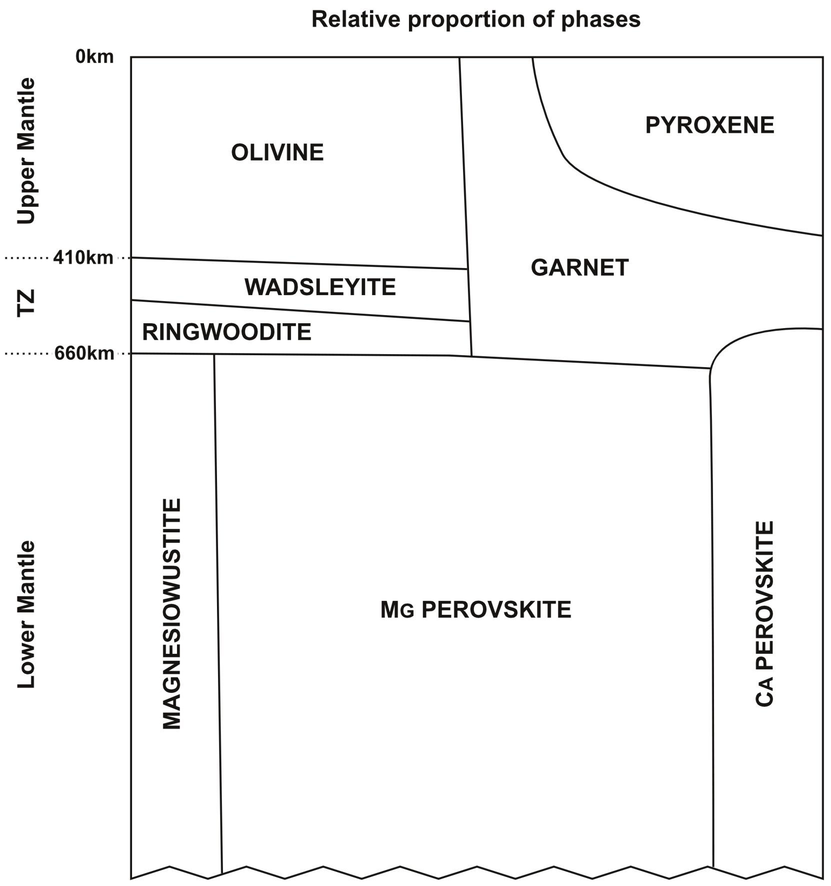

Figure 1.2: *The relative proportions of the major mineral phases across the upper mantle, transition zone (TZ) and lower mantle.*

of water incorporation in defect spinel have been shown to be similar to those in ringwoodite and as this similarity is also coupled with similarly high water solubility, it has been suggested that defect spinel may be a potentially useful low-pressure analogue for ringwoodite (Hertweck and Ingrin, 2005; Bromiley et al., 2010).

1.1.2 Geophysics

As the effect of water incorporation in NAMs on physical properties can be large, some geophysical measurements can be used to detect water in the mantle (Huang et al., 2005, and multiple others, e.g. Farver, 2010; Selway et al., 2014). Consequently, and in particular because the water content in the Earth's interior is likely to vary both laterally and radially, the ability to 'map out' the mantle water content from geophysical observations will contribute significantly to the understanding of geological processes. However, various other factors (such as temperature) are also likely to modify physical properties, and an important issue is therefore how to distinguish the effects of water from the effects of other variables.

Magnetotellurics (commonly, MT) is a geophysical technique that uses frequency dependent ratios of naturally occurring electric and magnetic fields at the surface of the Earth to determine the Earth's electrical conductivity from the measured response to interactions between solar winds and the ionosphere over long time periods. Conductivity is determined as a function of depth and increasing depths of sensitivity are obtained by recording lower frequency fields. Electrical resistivity in the mantle can be inferred from modelling the response measured from the Earth's surface to highlight anomalous regions but in order to interpret MT soundings, laboratory data constraining the electrical properties of mantle minerals are needed to interpret the modelled inversion of MT field data from the field (Farla et al., 2009). Laboratory data (such as those from Schock et al., 1989) and related models describing olivine conductivity are currently too resistive to arrive at conductivities expected from models of MT data corresponding to the upper mantle - recent models (such as the SEO3 model of Constable (2006)) for dry olivine conduction improve the agreement between dry olivine conductivity and the upper mantle (particularly at temperatures greater than 1300°C) but there is clearly still a discrepancy to be addressed.

As laboratory studies demonstrate that hydrogen is incorporated in minerals as a charged species and should theoretically increase the electrical conductivity, many authors (including Schock et al., 1989; Bolfan-Casanova, 2005) have suggested that the migration of hydrogen ions might be responsible for anomalously high conductivity in the mantle and that the presence of water in the mantle will reconcile the remaining differences between laboratory and geophysical measurements (Khan and Shankland, 2012; Poe et al., 2010; Bolfan-Casanova, 2005).

One of the supporting lines of evidence for this discrepancy being due to water in NAMs is anisotropy observed in electrical conductivity measurements of the mantle, which may reflect anisotropy in the movement of hydrogen through minerals (due to differences in diffusion as a result of crystallographic structure). Concurrent with anisotropy observed in mineral studies, Du Frane and Tyburczy (2012) suggest electrical anisotropies in the Earth's mantle could be significant in establishing the abundance and distribution of water in the mantle, as the effect of water in enhancing the deformation of olivine is anisotropic.[4] However, this is by no means conclusive evidence of enhanced conductivity being due to water - one alternative explanation is oriented melt pockets.[5]

MT observations also support the theory that the transition zone minerals (high pressure olivine phases) are able to incorporate greater amounts of hydrogen - commonly imaging features beneath the continents consistent with seismic low-velocity zones that are most easily explained by the presence of a small amount of water, or melt (Eaton et al., 2009). Measuring the effect of water on the conductivity of these phases is limited by the same problems as discussed above for the lower pressure phases, with the additional difficulty that samples are restricted in abundance and size due to their limited stability under surface conditions.

Geophysical techniques are thus a useful tool for investigating the interior of the planet, but modelling relies on the interpretation of data obtained that, in turn, is influenced by results from laboratory studies of mantle phases - highlighting a clear need for further relevant, well-constrained data on the influence of hydrogen on mineral conductivity, as well as further in-depth investigation of the relationship to mantle-scale electrical conductivity.

1.1.3 Conductivity

Mantle electrical conductivity is coupled to surface conductivity, allowing it to be measured by geophysical techniques which, in theory, can be used assess water/hydrogen content. Therefore, in addition to resolving the discrepancy between geophysical observations and lab experiments, if the influence of hydrogen in mantle minerals can be quantified, conductivity studies are potentially a useful method for determining the water content in the mantle through geophysical measurements.

Obtaining mineral electrical conductivity data relevant to mantle conditions has traditionally been problematic due to difficulties inherent in measuring conductivity

---

[4] Du Frane and Tyburczy (2012) found diffusion to be anisotropic in olivine, with [100] diffusion faster by approximately 1 log unit. The conductivity values obtained in their study are slightly lower than those from the study by Yoshino, Matsuzaki, Yamashita, et al. (2006) and 2-3 orders of magnitude lower than obtained by Wang et al. (2006).

[5] Although initially thought that this could only explain high conductivity in the asthenosphere, work by authors such as (Bercovici and Karato, 2003) has suggested melts may also be present deeper in the mantle (following upwelling of material).

in 'wet' samples[6] - highlighted by two papers published consecutively in *Nature* by Yoshino, Matsuzaki, Yamashita, et al. (2006) and Wang et al. (2006). While the comparison of laboratory results obtained by Wang et al. (2006) with geophysical observations suggests that the typical continental upper mantle contains 10^{-3}wt.% water, Yoshino, Matsuzaki, Yamashita, et al. (2006) obtained conductivity values several orders of magnitude lower and reach the conflicting conclusion that observations of highly anisotropic asthenospheric conductivity cannot be attributed to hydrogen in olivine. In a subsequent paper, Yoshino, Matsuzaki, Shatskiy, et al. (2009) postulates that conductivity measurements of hydrated minerals at high temperatures may lead to incorrect results because (at sufficiently high temperatures), small polaron (hopping) conduction contributes to the bulk conductivity and also because dehydration is unavoidable due to fast hydrogen diffusion. Additionally, he suggests that in the upper asthenosphere, temperatures are too low even for olivine containing water up to the solubility limit to be an adequate conductor (their different approaches to directly measuring electrical conductivity are discussed in more detail in section 2.2). This has led to recent modelling of mantle conductivity profiles by Khan and Shankland (2012) being based on two separate databases of conductivity data that respond differently to changes in water content. What Khan and Shankland (2012) label the 'YK' database (including results by Yoshino, Matsuzaki, Yamashita, et al., 2006) is generally insensitive to changes in either the upper mantle or transition zone, as well as being overall less conductive for a given set of conditions. This emphasises the importance of the continued refinement of lab-based mineral conductivity studies and indicates that the currently available methods may not produce relevant data.

Aside from direct measurements of electrical conductivity in minerals, as in the studies mentioned above, an alternative approach is to indirectly determine the influence of hydrogen on electrical conductivity through investigating hydrogen mobility under mantle conditions. This can be done using the Nernst-Einstein relation, which relates the contribution of charged mobile species (in this case, hydrogen) to the electrical conductivity of a solid;

$$\sigma = \frac{fDcq^2}{kT} \tag{1.2}$$

---

[6] Hydrogen is rapidly lost at high temperatures due to fast diffusion so experiments are often carried out at low temperatures and extrapolated, or durations are extremely short.

where σ is the electrical conductivity (S.m^{-1}), f is a unitless numerical correlation factor approximately equal to 1 (Du Frane and Tyburczy, 2012), D is the diffusivity of the charge-carrying species (m^{2}.s^{-1}), c is the concentration (m^{-3}), q is the electrical charge of the charged species (C), k is the Boltzmann constant (J.K^{-1}) and T is the temperature (K). There are several simplifying assumptions in using this approach - there is no correction for the pressure-dependence of hydrogen diffusivity,[7] the solubility of hydrogen may depend on oxygen partial pressure, and values at temperatures higher than 800°C are extrapolated assuming the same activation energy - but it allows conductivity to be calculated from experimental data determining hydrogen diffusion. Additional considerations and more complex versions of the calculation are required to determine the overall electrical conductivity of a mineral in which more than one species contributes, and one important consideration is that the diffusion measured should be equivalent to the movement of hydrogen during electrical conductivity - that is, independent of any counter-flux of species.

---

[7] Although this is often assumed to be relatively minor.

1.2 Relevance of this project

Although there is still considerable discrepancy in estimates of water in the mantle, large scale electrical conductivity studies may offer a complementary method for determining mantle water content, provided the influence of hydrogen can be adequately determined under the relevant conditions. Because olivine is the most abundant mineral phase in models of the upper mantle (see figure 1.2), the effect of water on olivine conductivity has been a major focus of research. However, difficulties in directly measuring conductivity in hydrogen-bearing samples (as discussed) mean that this currently remains poorly constrained (with different groups of researchers in different laboratories obtaining results that differ by as much as several orders of magnitude (Wang et al., 2006; Yoshino, Matsuzaki, Yamashita, et al., 2006)). As such, difficulties in directly measuring the effects of hydrogen on mantle electrical conductivity in the lab mean that accurately constraining mantle water contents from MT data remain problematic. In contrast, the Nernst-Einstein equation provides an alternative approach because, during diffusion experiments, hydrogen mobility can be directly and accurately constrained.

During MT measurements, the flow of current in the mantle is not coupled to any charge-balancing counter flux, and electrical conductivity observed is independent of any external force. Standard hydrogen diffusion experiments used to extrapolate electrical conductivity involve a counter flux of oppositely charged particles, meaning that the activation energy is not solely due to hydrogen mobility and correspondingly influencing the determined temperature dependence of hydrogen mobility. In contrast, the self-diffusion of hydrogen involves no chemical potential gradient (Zhang, 2010) and is, therefore, more equivalent to the movement of hydrogen in mantle minerals during geophysical measurements (such as MT). Data from experiments to determine hydrogen self-diffusion can, therefore, be used in conjunction with the Nernst-Einstein equation (2.6) to provide better measurements of mineral electrical conductivity under mantle conditions - provided data can be obtained at temperatures, pressures, and on (water) defects relevant to the conditions being studied.

In order to measure the self-diffusion of hydrogen, hydrogen-deuterium exchange experiments have been used, whereby the random movement of particles causes the exchange of hydrogen (in the mineral) for deuterium (from a source). Hydrogen-deuterium exchange experiments for olivine under mantle temperature and pressure conditions have only been carried out in one study to date - by Du Frane and Tyburczy (2012) on single crystals of San Carlos olivine at 750-900°C, 2GPa. This study aims to expand on their work by using samples of synthetic olivine that have been grown, containing water, under the conditions to be studied - in comparison to the samples used by Du Frane and Tyburczy who used a dry starting material and first ran a 'wet' anneal.

The incorporation of hydrogen, even in a relatively simple material such as olivine, is highly complex, and in order to best assess the mobility of hydrogen at mantle pressure/temperatures, it is essential to use samples that contain only the relevant defects that are stable under mantle conditions (whatever form they may take - vacancies, interstitials). The defect sites at which water is incorporated in natural samples are not easily re-equilibrated to mantle conditions (given that the samples are now at the surface, and are therefore highly likely to have undergone shallow-equilibrium over geological timescales prior to being collected and selected for study). Due to the slow diffusivity of metal vacancies, oxygen vacancies and substituting cations, the time taken to anneal crystals at high pressure/temperature in order to fully change the defect structure is significant (especially in mm-sized samples) and thus using synthetic samples grown under the pressure/temperature conditions to be studied (and hence already containing a stable population of relevant defects) offers a substantial advantage. In addition to olivine, synthetic samples of wadsleyite and defect spinel ($Mg_{0.4}Al_{2.4}SiO_4$) were also investigated, with the aim of developing a novel technique for obtaining hydrogen mobility data on a range of mantle minerals that can be used in conjunction with existing geophysical data in order to 'map out' the water content across the mantle.

CHAPTER 2

Project background and previous research

Since the discovery that NAMs can incorporate water in the form of structurally-incorporated hydrogen, numerous studies have tried to quantify the influence of hydrogen on the electrical conductivity of mantle minerals in order to 'map out' the water content of the mantle by linking mineral electrical conductivity to geophysical studies. The two primary approaches are experimental studies investigating the diffusion of hydrogen in olivine, and studies directly measuring conductivity, but there is currently no clear consensus between (or indeed within) them.[1] This chapter will introduce the different approaches and discuss the relevant theory in order to provide a contextual framework for the subsequent discussion of results from this study (alongside results from previous research).

---

[1] While there are those who still prefer the model of a dry mantle, the general discussion is not whether or not water is present, but focuses on where, and how much, water is incorporated.

2.1 Diffusion

Diffusion, be it in a solid, liquid or gas phase, occurs as a result of the atomic scale random motion of particles which results in net migration of a species across a non-uniform concentration (see figure 2.1). It is a widely measured parameter for a range of geological materials as it is the only mechanism by which elements in mineral lattices can move from one location to another (Zhang, 2010), and as it plays a key role in the supply of elements during crystal formation from melts, as well as in melt formation during partial melting. It also controls much of the interaction between Earth's reservoirs, due to its importance in the transfer of elements from crust to mantle to core. This project aims to use results from diffusion experiments to quantify the influence of hydrogen on the electrical conductivity of mantle minerals and must, therefore, measure diffusion relating to the movement of hydrogen atoms independent of any external force - essentially the mobility of hydrogen equivalent to its mobility as a charge-carrier during conduction. This specific type of diffusion is termed 'self-diffusion', and is defined by Zhang (2010) as occurring when there is no chemical potential gradient in the system with regard to elemental composition, but only a difference in isotopic ratios (it is also sometimes termed 'isotopic' or 'tracer' diffusion). The changing isotopic fractions can be monitored to give an indication of the diffusivity and, as there is no chemical gradient, the diffusivity is assumed to be constant (there may be minor differences in the diffusivity of isotopes, but such differences are generally considered negligible in determining self-diffusion).[2]

Although the physics of diffusion is complex, the mathematics are similar to that of heat conduction, and the relationship between concentration over time and diffusivity can be described by Fick's law;

$$J = -D \frac{\delta C}{\delta x} \tag{2.1}$$

where J is the diffusive mass flux (in units of amount of substance per unit area per unit time), D is the diffusion coefficient (diffusivity, in units of length^2/time), C is the concentration of the species (in units of mass per unit volume), x is distance,

---

[2] Note that, according to Zhang (2010), there are a few authors that consider true self-diffusion to be diffusion of the exact same species only - but such diffusion cannot be quantified.

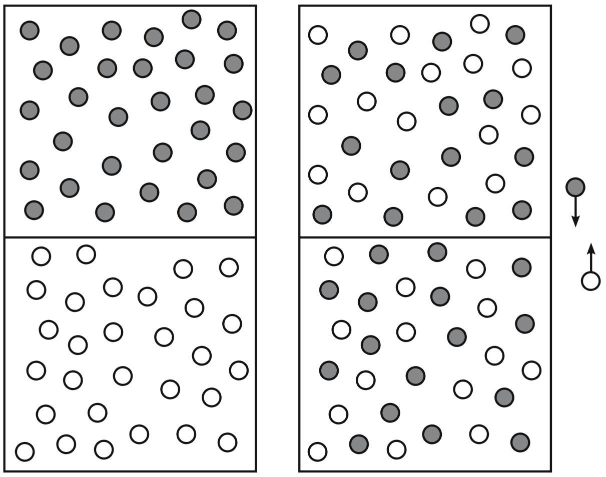

Figure 2.1: *During coupled diffusion the random motion of particles in two distinct reservoirs of different isotopic composition (left) results in complete mixing (right) after a period of time, controlled by the diffusivity of the species (adapted from Zhang (2010)).*

and $\frac{\delta C}{\delta x}$ is the concentration gradient, with the negative indicating that the direction of diffusion is opposite to the direction of the concentration gradient. As a result, when the concentration gradient is large (profile is steep) so is the diffusivity.[3]

In studies to investigate diffusivity, it is common to use coupled diffusion experiments that involve a *source*, from which the species will diffuse, and a *sink* into which it will move. Depending on the experimental conditions and the species of interest, the source may be a fine-grained powder, a thin film deposited on the surface of a mineral, or a surrounding solution or gas phase. In all cases the source will have a direct interface with the sink phase, and during the experiments the species will move from the source to the sink. For the one-dimensional case, this non steady-state diffusion with time is described by Fick's second law;

$$\frac{C - C_i}{C_0 - C_i} = 1 - erfc \frac{x}{2\sqrt{Dt}} \tag{2.2}$$

where C is the concentration of the species of interest in the sink, at a distance of x from the sink-source boundary, after time t, D is the diffusion co-efficient (as in

---

[3] For further details, a full description of the mathematical solutions for many diffusion problems are given in *The Mathematics of Diffusion* by Crank (1975), and analytical solutions to heat conduction that can be applied to diffusion are given by Carslaw and Jaeger (1959).

equation 2.1), C_0 is the (constant) concentration of the species at the sink-source boundary (equivalent to the initial concentration in the source), and C_i is the initial concentration of the species in the sink phase. For this relationship to hold true, the concentration of the diffusing species in the source must be sufficient to ensure that there is a constant supply to the sink - i.e. the source can be considered infinite. In such cases, the concentration (of the diffusing species) at the boundary between the source and sink phases will remain constant for the duration of the experiment. In order to fit *x*-*y* (concentration - distance) data obtained from experiments, this relationship can be simplified to;

$$C = C_0 - (C_0 - C_i)\, erfc\, \frac{x}{2\sqrt{Dt}} \tag{2.3}$$

and in cases where $C_i = 0$ (i.e. in D-H exchange experiments where the forsterite crystal initially contains no deuterium), this is further simplified to;

$$C = C_0\, (1 - erfc\, \frac{x}{2\sqrt{Dt}}) \tag{2.4}$$

For this project, experiments were designed to ensure an infinite source of the diffusing species (either hydrogen or deuterium). They were also designed to yield short, near surface profiles measured in a single direction (perpendicular to the source-sink boundary), ensuring that treatment of the data as one-dimensional is legitimate (Watson and Dohmen, 2010). As a result of these considerations, the above equations represent valid solutions for the diffusion profiles produced (depending on the initial concentration of the diffusing species in the sink phase).

2.1.1 Differences between hydrogen and deuterium diffusion

Considering the differences between hydrogen and deuterium in atomic size and mass,[4] a difference in diffusivity through the crystal lattice might be expected. However, as noted by Zhang (2010), the diffusivity variability between isotopes is considered negligible and, with specific reference to hydrogen isotopes, Du Frane

---

[4] Mass of H = 1.007825amu, D = 2.014102amu

and Tyburczy (2012) claim that their use of deuterium in exchange experiments on blocks of San Carlos olivine (similar to those carried out for this project) leads to an under-estimation of the true hydrogen diffusion coefficient that is less than 0.15 log units. In studies modelling D/H fractionation (for example, Bucholz et al. (2013)), the assumption is made that deuteron diffusivity is related to proton diffusivity following Graham's law of diffusion for gases, which states that the diffusivity is inversely proportional to the masses of the diffusing species. The equation relating the diffusivities of hydrogen and deuterium to their relative mass is therefore;

$$\frac{D_D}{D_H} = \left(\frac{m_H}{m_D}\right)^{\beta} \tag{2.5}$$

where D_D is the diffusivity of deuterium, D_H is the diffusivity of hydrogen, m_D is the atomic mass of deuterium, m_H is the atomic mass of hydrogen and β is a correlation value. For an ideal gas, $\beta = 0.5$ but in model curves for diffusive H_2O loss,[5] Bucholz et al. (2013) find that their experimental data fits best to a value of $\beta = 0.3$.[6] Calculated diffusivities using these values suggest that D_D is less than 10% slower than D_H in olivine. The assumption that D_D is equivalent to D_H in the modelling of data from exchange experiments is therefore valid, and has little influence on the results (the effect on values is within experimental error), but will nonetheless be considered during the modelling, analysis and discussion of results from diffusion profiles in this study.

---

[5] From olivine-hosted melt inclusions.

[6] Du Frane and Tyburczy (2012) use a value of 0.5, their justification for considering D_D to represent D_H without significant underestimation is $D_H = D_D\sqrt{2}$ therefore $D_{D-H} \approx D_H \approx D_D$.

2.2 Electrical Conductivity

The Nernst-Einstein equation links the diffusion coefficient of a charge-carrying species with its contribution to electrical conductivity;

$$\sigma_H = \frac{f\, D_H\, C_H\, q^2}{k\, T} \tag{2.6}$$

where σ (S/m) is the contribution of a species (in this case, H) to electrical conductivity, f is a unit-less numerical correlation factor (approximately equal to 1), D_H (m^2/s) is the diffusion coefficient, C_H (m^{-3}) is the concentration of the species of interest (for example the concentration in ions/m^3 of H in the mantle), q (C) is the charge, k (J/K) is the Boltzmann constant, and T (K) is the temperature (specific to the value of D_H).

Using the Nernst-Einstein equation to determine the contribution of a species to electrical conductivity assumes that the movement of the species for which the diffusion coefficient is determined is equivalent to the movement during electrical conductivity. As has been previously noted, the D-H exchange experiments in this study have been designed to yield hydrogen diffusion values directly relevant to electrical conductivity under mantle conditions, and thus the values can in theory be applied to equation 2.6 in order to calculate the contribution of hydrogen-associated conduction.

2.3 Research and approaches

Much of the work investigating the mechanisms of hydrogen incorporation in NAMs has been done using spectroscopic techniques such as FTIR (Beran and Libowitzky, 2006; Demouchy and Mackwell, 2003) and this approach has also been expanded to provide measurements of hydrogen uptake and/or diffusion. Experiments are generally performed on single crystals (either natural or synthetic) that have undergone annealing for varying lengths of time. FTIR analysis across resulting diffusion profiles can be used to determine hydrogen concentration and bonding environments, as quantified by integration of the area under the relevant OH absorption peaks. Although these studies have the advantage of being able to link diffusion to the different incorporation sites, the quantitative data obtained relies on a detailed calibration (based on the Beer-Lambert law - equation 1.1 - and mineral-specific absorption constants, as discussed in section 1.1.1). Recently, a whole-block FTIR method specifically for measuring hydrogen diffusion in NAMs has been developed by Ferriss et al. (2015), which allows a time-series of diffusion experiments to be carried out on the same sample.

Alternatively, diffusion is measured using microanalysis techniques (for hydrogen, this is commonly SIMS due to detection capability). Again annealing experiments are generally carried out and diffusion profiles are obtained by measuring concentration of hydrogen relative to distance from the crystal edge. The extent to which diffusion has progressed through the sample can then be modelled. Due to the detection accuracy of microanalysis techniques, this method yields reliable concentration data, but lacks structural information on hydrogen incorporation. Recently, authors such as Padrón-Navarta et al. (2014) have argued the importance for hydrogen diffusion of integrating both concentration data from SIMS studies and structural data from FTIR studies.[7]

Experiments to directly measure the electrical conductivity of hydrogen-bearing minerals (such as carried out by Constable (2006), Wang et al. (2006), and Yoshino, Matsuzaki, Yamashita, et al. (2006)) are based on complex impedence measurements of samples (response to an applied voltage is recorded as a function of frequency). However, due to the ease with which hydrogen escapes from silicate minerals at high temperatures, measurements must either be short in duration (to minimise hydrogen

---

[7] This was specifically addressed by a CIDER working group in Washington in August 2016, with the aim of publishing a re-evaluated dataset.

loss), or carried out at low temperatures and then extrapolated. This has led to significant differences in the results obtained by different labs choosing to solve the problem differently (at least an order of magnitude), and fundamentally different conclusions about Earth processes.[8] Indirect methods of determining the influence of hydrogen on electrical conductivity are therefore desirable.

2.3.1 Previous studies

The following studies have investigated the diffusion of hydrogen or its influence on mineral conductivity (or both) in mantle phases. A brief discussion on each is given to provide context to the data, which are compared to the results from this study in later chapters.

Previous studies focusing on hydrogen diffusion

Mackwell and Kohlstedt (1990) determined the OH concentration in San Carlos olivine after hydrothermal annealing at 0.2GPa confining pressure using IR spectra, and calculated diffusivities by comparing the concentration with depth in the sample. They identified fast rates of diffusion, and hypothesised that the mobile defects were protons (H^+ ions) moving by interstitial mechanisms, charge compensated by a (faster) counter flux of polarons (i.e. flux of electons, e^-). Their results also suggested that the concentration of OH defects stable in olivine is strongly dependent on the local thermodynamic state, such that different OH concentrations are found in crystals equilibrated under reducing compared to oxidising conditions. In later work, based again on measurements of OH distribution in single crystals of olivine, Kohlstedt and Mackwell (1998) showed that hydrogen concentration evolves towards an equilibrium. They discussed the nature of *extrinsic* - charged proton (H^+) interstitials - and *intrinsic* - metal vacancies, electrons - defects and suggested a two-process mechanism for hydrogen movement. The first is a rapid (10^{-10}m^2/s at 1,000°C) exchange process with polarons, resulting in a metastable equilibrium concentration of hydrogen, and the second is a slower (10^{-12}m^2/s at 1,000°C) process involving intrinsic defects.

---

[8] As as summarised by Jones et al. (2012): "Yoshino, Matsuzaki, Yamashita, et al. (2006) asserts that hydrogen in olivine cannot account for the conductivity at the top of the asthenosphere, but this is contradicted by an alternative study in the same issue of *Nature* by Wang et al. (2006) ... the conclusion of Huang et al. (2005) that the transition zone is wet is similarly contradicted by Yoshino, Matsuzaki, Shatskiy, et al. (2009) who instead concluded it is dry ... and this in turn is robustly challenged by Karato (2011) ..."

With reference to this work, Yoshino, Matsuzaki, Yamashita, et al. (2006) consider the difference in activation energy between these two mechanisms and indicate that the intrinsic conductivity of olivine is masked by the extrinsic conductivity.

Demouchy and Mackwell (2003) carried out experiments on single crystals of synthetic forsterite at both low (0.2GPa) and higher (1GPa) pressure and a range of temperatures (900-1,100°C) lasting 3-20hours. They found that chemical diffusion rates in forsterite are marginally slower than in natural olivine (for the same diffusion process) and show as a result that the transport of hydrogen-related species in olivine is not strongly coupled to iron concentration (in contrast to measurements of hydrogen solubility, which do increase with increasing iron content). In addition, they found both anisotropy in diffusion and activation energies to be similar in forsterite and Fe-bearing olivine. They suggested that for low temperature, short duration experiments a diffusion mechanism involving the redox exchange of protons and polarons dominates, but that at higher temperature and/or longer durations, a second process involving defects associated with protons and point/intrinsic defects becomes more important. Only the second process occurs in forsterite due to the lack of iron, leading to slower diffusion rates (10^{-12}m^2/s at 1,000°C). In an expansion of this work using natural samples of San Carlos olivine (Demouchy and Mackwell, 2006), they showed that only a modest amount of hydrogen can diffuse by the redox-exchange process and, consequently, the proton-vacancy process is the dominant (and therefore limiting) mechanism of hydrogen transport in olivine under mantle conditions. Demouchy (2010) further investigated the influence of grain-boundary diffusion and Thoraval and Demouchy (2014) use data from all of the studies noted so far to numerically model 1D and 3D ionic diffusion (specifically with reference to dehydration of natural samples), showing that dehydration is strongly anisotropic.

Recently, Padrón-Navarta et al. (2014) carried out a study with the aim of determining hydrogen diffusion as a function of the type of point defect by which OH is incorporated. Building on work by previous authors (e.g. Berry et al. (2005), Kovacs et al. (2010), and Lemaire et al. (2004)) they assigned IR stretching bands to different substitution mechanisms (Ti-associated, Si-vacancies, Mg-vacancies, trivalent-cation-associated point defects - see further discussion in section 4.5.7) in doped and undoped forsterite crystals synthesised to contain hydrogen (deliberately avoiding the fast redox-exchange mechanism by using Fe-free samples). They report a bulk diffusion coefficient for hydrogen associated with Si vacancies that is significantly slower than in previous studies, and show that hydrogen diffusion depends strongly on the defect chemistry of the crystals (which, in their study, is artificially set by the thermodynamic conditions of synthesis), both because specific defects have different diffusivities and also as a result of the kinetic interactions between them. In particular, this study emphasised the complexity of hydrogen diffusion even in Fe-free samples, and underlined a need for better knowledge of the intrinsic diffusivities of different hydrous defects (including the relationships between them, and the relative proportions in each sample).

Previous D-H exchange studies

Although isotope exchange with deuterium has been used to calculate hydrogen diffusivity in a range of mantle minerals (see Ingrin and Blanchard (2006) for a review), at the time of writing only two previous groups have published D-H exchange experiments similar to those carried out for this project.[9] Du Frane and Tyburczy (2012) carried out D-H exchange experiments to investigate hydrogen self-diffusion in oriented single crystals of San Carlos olivine. Their experimental design first sets a defect population in the samples using a ‘dry’ anneal, then saturates the defects with hydrogen during a ‘wet’ anneal before finally allowing the exchange of deuterium for hydrogen at 2GPa over a range of temperatures (750-900°C). Results show that the self-diffusion of hydrogen is approximately 1 log unit lower than the redox-exchange process (which they also show to be dependent on the self-diffusion term). Additionally, Du Frane and Tyburczy use their results in conjunction with the Nernst-Einstein equation (equation 2.6) and measurements of electrical conductivity in dry olivine (from Du Frane, Roberts, et al., 2005), to estimate the contribution of hydrogen to the electrical conductivity of olivine (σ_{tot}). More recently, Sun et al. (2015) used a similar method to investigate hydrogen self-diffusion in ringwoodite. They used SIMS to measure the interdiffusion of hydrogen and deuterium in a pair of coupled, synthetic, Fe-bearing crystals (one initially D-rich, on initially H-rich) - finding hydrogen self-diffusion to be faster than in olivine - and also used results in conjunction with the Nernst-Einstein equation to estimate electrical conduction.

---

[9] Although Ingrin and Blanchard (2006) include an unpublished dataset for D-H exchange in forsterite in their review paper.

Previous studies focussing on electrical conductivity [related to H^+]

It is worth noting that most studies of H^+ assisted electrical conductivity in olivine are based on the dry electrical conductivity model of Constable (2006), which is based on a study of point defect behaviour. Although this work (compared to preceding work on dry olivine) improves the reconciliation with geophysical measurements, the need to invoke enhanced conductivity as a result of water in the mantle is only lessened (not removed).

Karato (1990) first predicted electrical conductivity in wet olivine using an estimated value of D_H based on chemical diffusion coefficients determined by Mackwell and Kohlstedt (1990), and noted in further work (2006) that different diffusing species could have potentially different mobilities (dependent on defect sites). However, the first experiments to address this hypothesis were the classically quoted olivine electrical conductivity experiments by Wang et al. (2006) and Yoshino, Matsuzaki, Yamashita, et al. (2006 and additionally 2009), with both groups attempting to directly measure electrical conductivity in hydrous olivine, using slightly different approaches. Wang et al. concluded that even 80 ppmw H_2O in olivine increases electrical conductivity by a factor of 10 (at 1400°C) - accounting for high values observed for oceanic lithosphere. Contrastingly, Yoshino, Matsuzaki, Yamashita, et al. showed, by extrapolation of their experimental data to high temperatures, that increased electrical conductivity in olivine is not sufficient to explain values observed in the upper mantle. As a result of the difficulties in directly measuring electrical conductivity highlighted by these studies, and in conjunction with the suggestion by Karato (2006) that D_H relates to σ_H, this project (and that of Du Frane and Tyburczy, 2012) was designed to indirectly determine σ_H by investigating hydrogen diffusion in mantle minerals.

However, more recently, Karato (2013) and Dai and Karato (2014) have suggested that, in fact, the direct comparison of electrical conductivity from isotope diffusion coefficients and actual electrical conductivity may not be justified - claiming that isotope diffusion does not represent self-diffusion of any atomic species but instead corresponds to an average mobility. In particular, these authors claim that if all hydrogen-related species diffuse equally (or only one hydrogen-related species is present), the difference in activation energy between isotope diffusion and electrical conductivity cannot be explained. They suggest that electrical conductivity in olivine (and wadsleyite) is indeed enhanced by a fast moving H^+ species, but that the kinetics of isotopic exchange are instead controlled by the slowest diffusing species. If this holds true, hydrogen-enhanced conductivity in olivine ought to be higher than has been calculated from D-H exchange data. Dai and Karato (2014) assert that this enhancement, relative to calculated values, explains geophysical observations - and there is consequently no need for alternative hypothesises to explain the observed electrical conductivity in the mantle.

Gardés et al. (2014) also suggest that it is not possible to interpret electrical conductivity in hydrous minerals using available data for the mobility of hydrogen defects, and additionally caution that the nature of H^+ conduction is also still poorly understood. They suggest that the differences in methodology between Wang et al. and Yoshino, Matsuzaki, Yamashita, et al. ought only to produce an uncertainty of 10-20%, and instead propose that the discrepancy results primarily from the concentration of water present. Jones et al. (2012) have also made an attempt to reconcile laboratory conductivity studies, agreeing that a significant proportion of the discrepancy stems from the range of water contents studied - such that both approaches appear to be applicable (but result in different conclusions). In recent work, Jones (2016) re-asserts that diffusion is heavily dependent on the defects present (and mobile), but suggests that diffusion associated with none of the defects studies is fast enough to explain observed proton conductivities. He notes that considering bulk diffusion, combining lattice and grain boundary diffusion, resolves some of this discrepancy - but is still unable to explain geophysical models for the mantle (given grain size considerations).

Spinel specific studies

Fewer previous studies have investigated the incorporation of hydrogen in spinel, and the majority have been carried out only at ambient pressure, rather than the high pressure and temperature conditions under which defect spinel has been shown to incorporate comparable amounts of water to other mantle phases (and under which experiments for this study are carried out). The hydrogen incorporation mechanism is thought to be via the protonation of both octahedral and tetrahedral edges, charge balanced by octahedral vacancies.

Gonzalez et al. (1987) first identified the diffusion characteristics of deuterium and hydrogen in non-stoichiometric $MgAl_2O_4$ spinel using IR measurements on polycrystalline material at 1600K, observing an increase in OD bands as the intensity of OH bands decreased. They consider the mobility of hydrogen and deuterium to be equivalent, and specifically focus on deuterium as the diffusing species as it can more easily be distinguished (compared to hydrogen which may be inherently present in the sample).

Hertweck and Ingrin (2005) investigated Mg_2GeO_4 spinel, proposing it as a low pressure analogue for the incorporation of water in ringwoodite in the transition zone. Again using IR measurements, they identified similar OH contributions resulting from D-H exchange at low temperature (700°C) and ambient pressure, confirming the protonation of tetrahedral edges as the likely mechanism. They also calculated hydrogen diffusivity, but did not repeat the experiments at alternative temperatures in order to determine temperature-dependence. Bromiley et al. (2010) suggested an alternate defect spinel (synthetic, non-stoichiometric $Mg_{0.4}Al_{2.4}O_4$) as analogous to ringwoodite, showing similarities in the incorporation mechanisms and amounts during annealing experiments. However, problems with the recrystallisation of spinel samples at high temperatures (above 1000°C) prevented them from extracting hydrogen diffusion data.

Two sets of studies from same research group - Fukatsu et al. (2002) and Okuyama et al. (2009) - have also investigated hydrogen mobility in defect spinel, in attempts to determine its suitability for use in high temperature proton conductors. Both studies use IR analysis to determine hydrogen self-diffusion across a range of spinel compositions ($Mg_{1-x}Al_2O_{4-x}$ with x in the range 0-0.3 (Fukatsu et al., 2002), and 06-0.34 (Okuyama et al., 2009)). Values from both studies agree well, and are similar to those of Gonzalez et al. (1987). Okuyama et al. (2009) additionally show that the diffusion of hydrogen is independent of composition, for the range studied, and claim that the self-diffusion of hydrogen is equivalent to hydrogen diffusion as a result of being coupled to Mg. They further suggest that the mobile Mg^{2+} ion is actually the dominant charge-carrier.

2.3.2 Anisotropy of diffusion

Olivine has an orthorhombic crystal structure, with three distinct, non-equivalent, crystallographic directions. This results in diffusion anisotropy (Du Frane and Tyburczy (2012) and Mackwell and Kohlstedt (1990)), which is a function of both the mineral structure, and the diffusion mechanism (Farver, 2010). In synthetic, Fe-free forsterite, Demouchy and Mackwell (2003) found that the measured chemical diffusion of hydrogen was fastest along the [001] axis, and slowest along [100] - similar to observations in Fe-bearing olivine by Mackwell and Kohlstedt (1990). Demouchy and Mackwell show that this effective diffusion anisotropy results from the anisotropy of the proton-metal vacancy diffusion mechanism, suggesting that rapid hydrogen diffusion via the proton-polaron (redox-exchange) process - which is fastest parallel to [100] - does not occur in Fe-free forsterite. This difference in anisotropy between the two incorporation/diffusion mechanisms is also noted by Kohlstedt and Mackwell (1998), and the fact that measurements on both forsterite and Fe-bearing olivine yield $D_{[001]} > D_{[010]} > D_{[100]}$, suggests that the iron content does not affect the anisotropy of diffusion (Demouchy and Mackwell, 2003). In their D-H exchange experiments, Du Frane and Tyburczy (2012) found the anisotropy of hydrogen self-diffusion to be fastest parallel to [100], and approximately similar in the other two directions.

Anisotropy of diffusion is demonstrably a complicated parameter, depending on the hydrogen-associated defect species and mechanisms involved. Knowledge of the crystallographic orientation of samples is therefore useful for interpretation of results from diffusion experiments. In previous studies (such as by Du Frane and Tyburczy (2012)), experiments have been carried out on cuboids cut from an oriented crystal, such that each axis of the cuboid represents a crystallographic direction (with each a different length so that they can be easily identified). However, due to the small nature of the synthesised crystals used in this study, this was not a viable method.[10] Instead, the original aim was to identify the crystallographic direction of each grain post-SIMS analysis using Electron Backscatter Diffraction (EBSD) - with the expectation that from an extensive selection, several of each orientation would be identified. In actuality, due to the development of the experimental and analytical method during the project (as will be discussed in the following chapters), EBSD analysis on a large number of samples was not possible. As a result there is no precise orientation data available for the samples used in this study, but an estimation of the principle axis along which diffusion was measured was made by identifying the relative x, y and z contributions to the (strongly orientation dependent) silica overtone peaks in FTIR spectra, following the method used by Lemaire et al. (2004). This is further discussed in section 4.5.2.

---

[10] Cuboids would be $<100\mu$m along the largest axis!

2.4 Research aims and objectives

The investigation of Earth's interior water content has been undertaken using a range of different approaches, but, as demonstrated, there is little consensus between different studies. The relevance and applicability of individual datasets is unclear, and many large scale assumptions or further models (e.g. of mantle electrical conductivity) are based on poorly constrained estimates (or, often, on a range).

This project was therefore designed in order to address the following main aims;

1. The development of a method to directly investigate the mobility of hydrogen in mantle phases, under relevant conditions (including both experimental and analytical considerations).
2. A comparison of resulting data with existing literature, and a reconciliation of previous approaches based on a consideration of the relevance of each data set, within specific parameters.
3. The collection of experimental data on hydrogen mobility for a range of mantle phases (contributing to the investigation of mantle electrical conductivity.

As a result of the progression of the project, and the discovery of experimental and analytical constraints, these aims evolved to include the study of hydrogen mobility in non-stoichiometric spinel - both as a potential analogue for ringwoodite, and as a contribution to hydrogen diffusion literature.

CHAPTER 3

Apparatus, techniques and approaches

In order to simulate the high pressure and temperature conditions of the Earth's mantle for experimental runs, specialist equipment housed in the University of Edinburgh GeoSciences Solid Media Laboratory was utilised. Once the experiments had been carried out, it was also necessary to use specialist analytical equipment to measure the concentration of hydrogen and/or deuterium present in the samples. This was primarily carried out at the Edinburgh Materials and Micro-Analysis Centre (EMMAC), which is also housed within the School of GeoSciences, University of Edinburgh. A brief introduction to the experimental (section 3.1) and analytical (section 3.2) techniques used is given in the following chapter - the detailed use of each technique with specific regard to the experiments carried out for the project is discussed in the relevant sections of later chapters.

3.1 Experimental apparatus

3.1.1 Piston cylinder

To achieve mantle pressure and temperature conditions, the majority of the experimental work was carried out using a piston cylinder press. The piston cylinder is a piece of high pressure apparatus, designed to subject a small volume sample to the desired conditions through the simultaneous application of pressure and temperature. Pressures up to up to 4GPa and temperatures up to 1,800°C (dependent on the melting point of the capsule material used) are achievable, allowing conditions equivalent to approximately 120km depth in the Earth to be investigated. The application of pressure is achieved through the compression of a solid pressure medium (in comparison to lower pressure apparatus that use gas or fluid) and the piston cylinder stack (figures 3.1 and 3.2) comprises a series of components that act to apply load on a laterally confined sample. The sample capsule is contained within an assembly of deformable material (figures 3.3 and 3.4), containing a graphite cylinder that acts as a furnace when a current is applied. The sample assembly in turn sits inside a 0.5inch hole in a tungsten carbide ‘bomb’ that forms the central part of the piston cylinder stack (component E in figure 3.1) and comprises a series of rings decreasing in hardness from the centre out - the central ring of the bomb is tungsten carbide and this is surrounded by outer steel rings that act to minimise lateral expansion (that would otherwise shatter the carbide).

During experimental runs in the piston cylinder pressure is applied in two steps, both of which are manually controlled via a compressed air pump and a hand pump linked to two hydraulic lines. Figure 3.5 shows the control panel for the piston cylinder press used. The first step is to apply an end load pressure of 150tonnes, which acts to stabilise the stacked components.[1] Then, the sample pressure is increased through a small internal ram contained within the bridge. This ram acts on a carbide piston (component D in figure 3.1) that moves up into the hole in the bomb and directly pressurises the sample assembly. This application of sample pressure is done at a rate of approximately 50MPa/min[2] and can be ‘topped-up’ during heating of the sample (pressure tends to decrease slowly following the initial temperature ramp) as well as during the experimental run. The piston cylinder assembly components act to

---

[1] And additionally stops the small hydraulic ram from blowing apart.

[2] For certain runs, specifically those using larger samples, a more gradual application of pressure was required - this is noted and discussed further where relevant.

convert the applied differential pressure to a hydrostatic pressure, ensuring the required pressure condition is applied evenly across the sample. Pressure is determined from oil pressure and the ratio between the ram head and piston area, with a correction applied for pressure loss due to the internal friction within the assembly. This is calibrated against the quartz-coesite and kyanite-sillimanite transitions, as well as the diopside melting point. For the talc-pyrex-graphite assembly used, an 8% correction was applied to 0.5inch assemblies and a 20% correction was applied to tapered 0.75inch assemblies. Quoted pressure is accurate to within less than 5% of the stated value.

The sample temperature is controlled by a fused electrical system - a current is applied to the stack via copper electrodes, and is directed through the graphite furnace in the sample assembly. Temperature is monitored throughout using a type-R thermocouple ($Pt_{87}/Rh_{13} - Pt$) that sits in the top of the assembly; thus the junction of the thermocouple is within 1mm of the sample capsule (figure 3.3). Cooling water is circulated throughout the stack in order to ensure that the apparatus does not overheat. Power, voltage, current and temperature are monitored and noted periodically during experiments. Generally temperature is increased slowly, at a rate of approximately 50°C per minute, to allow time for the apparatus to adjust. Run temperatures over the experimental conditions are within 10°C of the quoted values - no correction is made for the effects of pressure on thermocouple EMF. At the highest temperature used in this study, temperature gradients within the assembly cells are less than 15°C, and are typically much lower at the final annealing temperatures used for H-D exchange and hydrogen diffusion experiments (Bromiley, unpublished data). In some specific runs, the application of pressure and/or temperature is more critical - details are noted where relevant in later sections.

Following experimental runs, the sample is quenched by switching off the power to the stack, which rapidly drops the temperature (to below 100°C within 30 seconds). The sample is recovered by slowly bleeding off the hydraulic fluid and then disassembling the stack. The capsule is then recovered from the surrounding assembly (which is typically soft and friable having been at high PT conditions) and the sample can subsequently be recovered from the capsule.

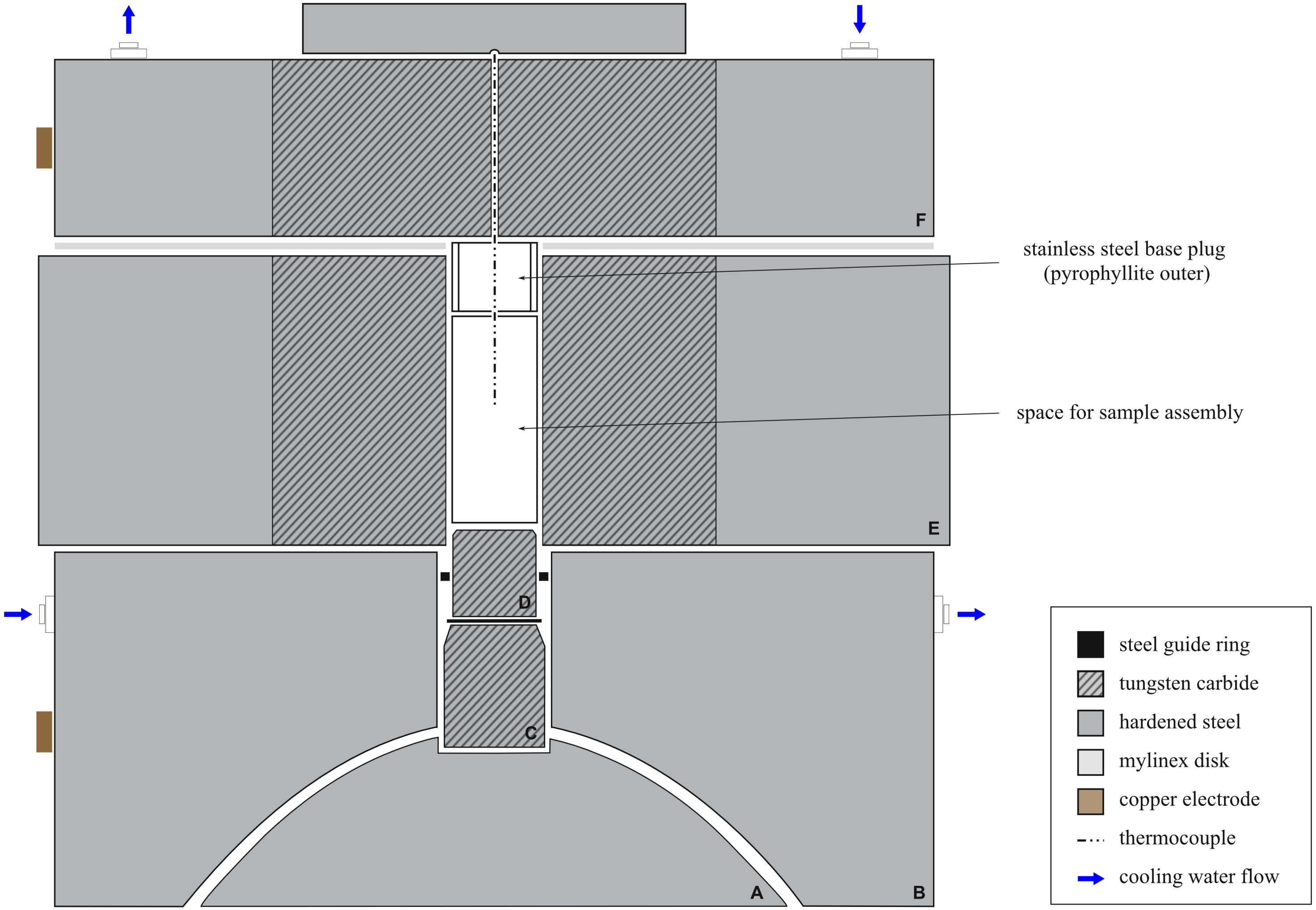

Figure 3.1: *Cross-section of PC stack. A - Ram head, B - Bridge, C & D - Pusher & piston, E - Bomb, F - Thermocouple plate. The central space for the sample assembly is 0.5inch in diameter, and the entire stack is cylindrical in 3D. Components are shown approximately to scale.*

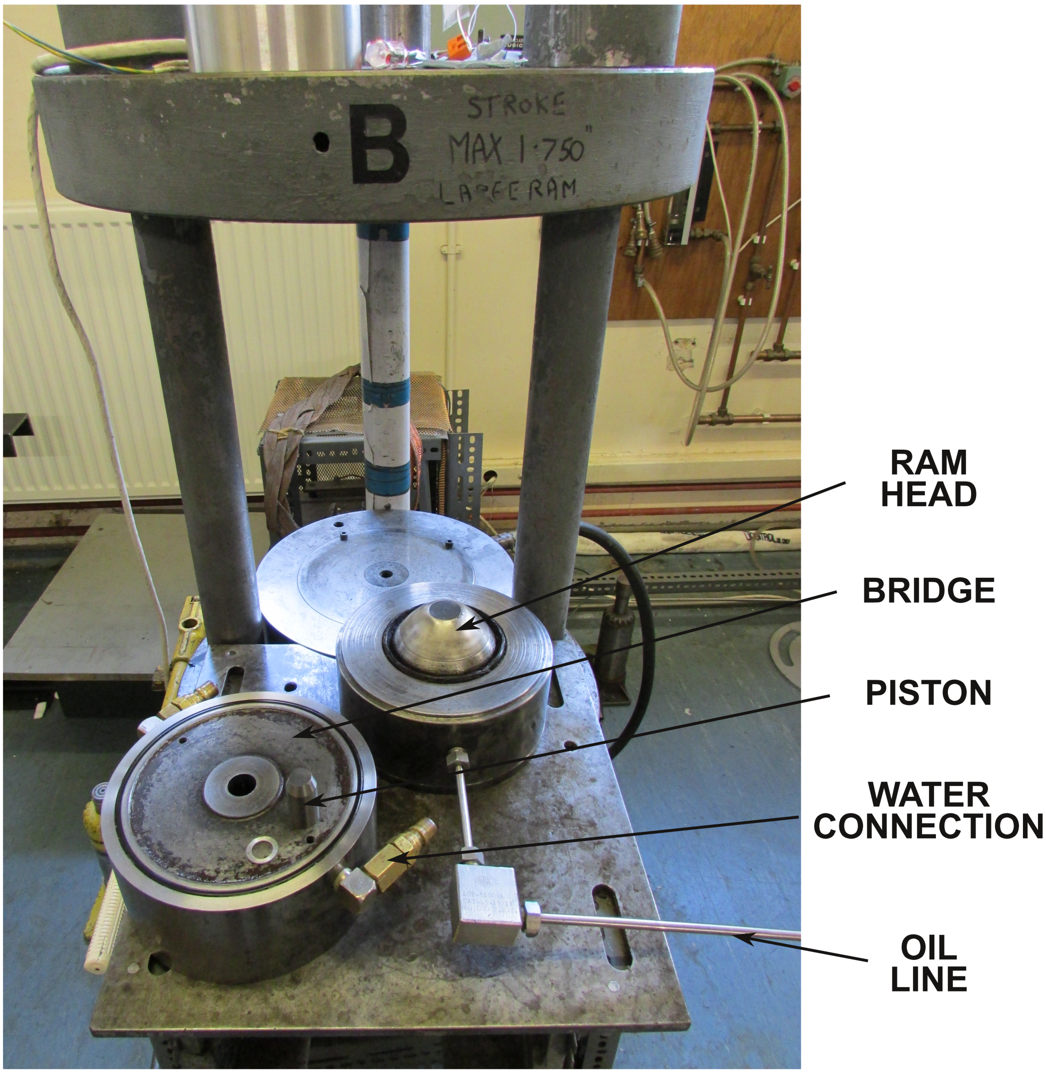

Figure 3.2: *Image showing the piston cylinder stack at The University of Edinburgh that was used for experiments. Components are assembled on the circular platform visible in the rear middle of the image, with a large aluminium spacer placed on top to fill the gap to the top. Copper electrode cables can be seen in the background, and the white cable to the left attaches to the thermocouple to read the temperature.*

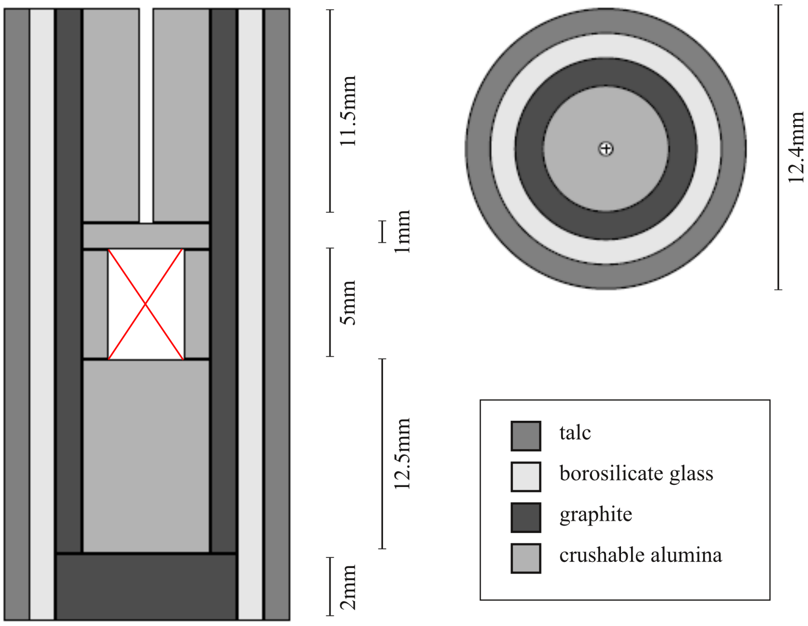

Figure 3.3: *Cross-section through a standard talc-pyrex sample assembly - vertical section (left), horizontal slice (top right). The sample sits in the 5mm tall central void, surrounded by a crushable alumina holder. The thermocouple sites in the narrow void in the upper crushable alumina plug.*

Figure 3.4: *Components of the sample assembly ready for construction. From left to right; talc pressure medium containing pyrex sleeve and graphite furnace that forms the main body of the assemblage (and into which the other components shown are placed), alumina spacer, alumina capsule sleeve, capsule (in this case, platinum), alumina disk, alumina spacer with hole for thermocouple. The steel base plug, which sits on top of the sample assembly, is shown to the rear. Prior to being loaded in to the central hole of the bomb for experimental runs, a thin sheet of lead (not shown) is wrapped round the outside of the assembly in order to provide lubrication. Size of components as given in figure 3.3.*

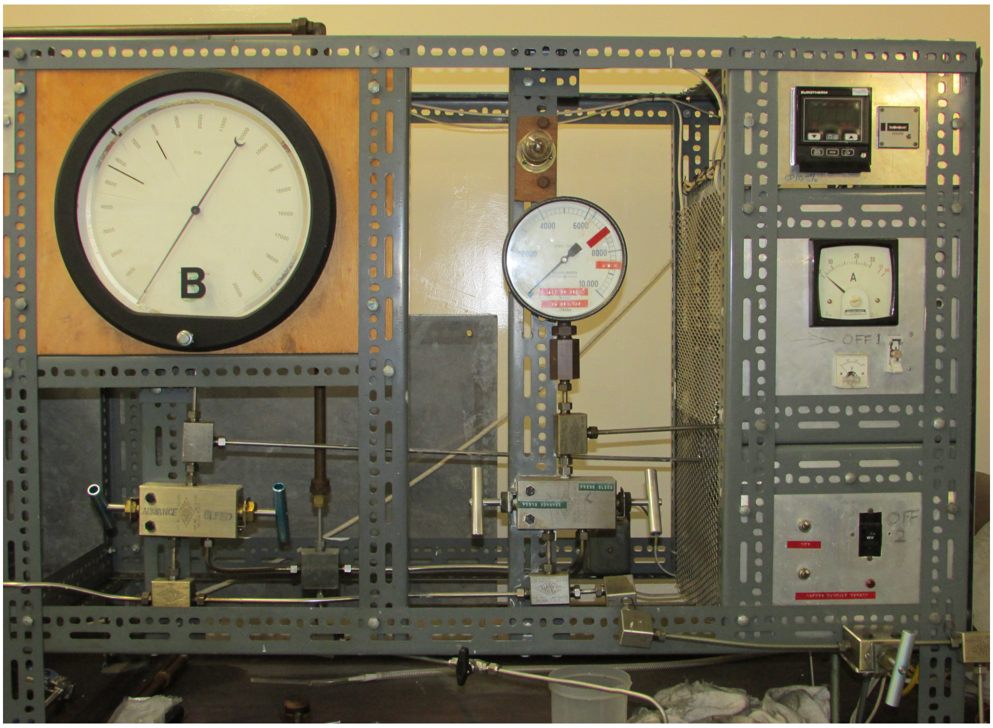

Figure 3.5: *Control panel for the piston cylinder press - end load and sample pressure are applied separately through the middle and left hand controls respectively. The temperature controls are shown to the right of the image.*

3.1.2 Atmospheric and controlled atmosphere furnace

In experimental runs requiring only high temperatures (without high pressures), or where the sample was more valuable and recovery needed to be more assured, a vertical tube gas mixing furnace was used. The gas mixing furnaces housed in the University of Edinburgh GeoSciences Solid Media Laboratory are able to reproduce a range of fugacity conditions through controlled gas flow, but all experimental runs for this project were carried out in air, with no imposed control of the internal gas mixture.

In a similar manner to the piston cylinder apparatus, application of temperature is controlled through the application of an external current, in this case across to a set of platinum heating elements. The internal temperature of the furnace is measured using a thermocouple that sits inside the heating tube and records the temperature at its centre (the furnace ‘hot-spot’). Once the desired temperature for an experimental run has been reached, the thermocouple is removed and the sample is inserted, hanging in a capsule on platinum wire attached to the bottom end of a ceramic rod (see figure 3.6). The ceramic rod is of the correct length to ensure that the sample capsule sits in the centre of the furnace (in the calibrated hot-spot), and is inserted in to the central tube of the furnace. The temperature gradient inside the furnace, coupled with the rate at which the sample is lowered, controls the rate at which the sample is heated - in most experimental runs the sample was brought to temperature as fast as possible (approximately 500°C per minute) in order to minimise hydrogen/deuterium diffusion at non-run temperatures. Following the specified run duration, the temperature of the sample can be rapidly decreased by removing the ceramic tube from the furnace and allowing the capsule to cool in air. The gas mixing furnaces in the Solid Media Lab have a drop quench facility (florentine flask, as shown in figure 3.6) but due to the nature of the experimental set-up this was not used. Any variation in the temperature of the furnace hot spot is identified by re-inserting the thermocouple after the sample has been removed.

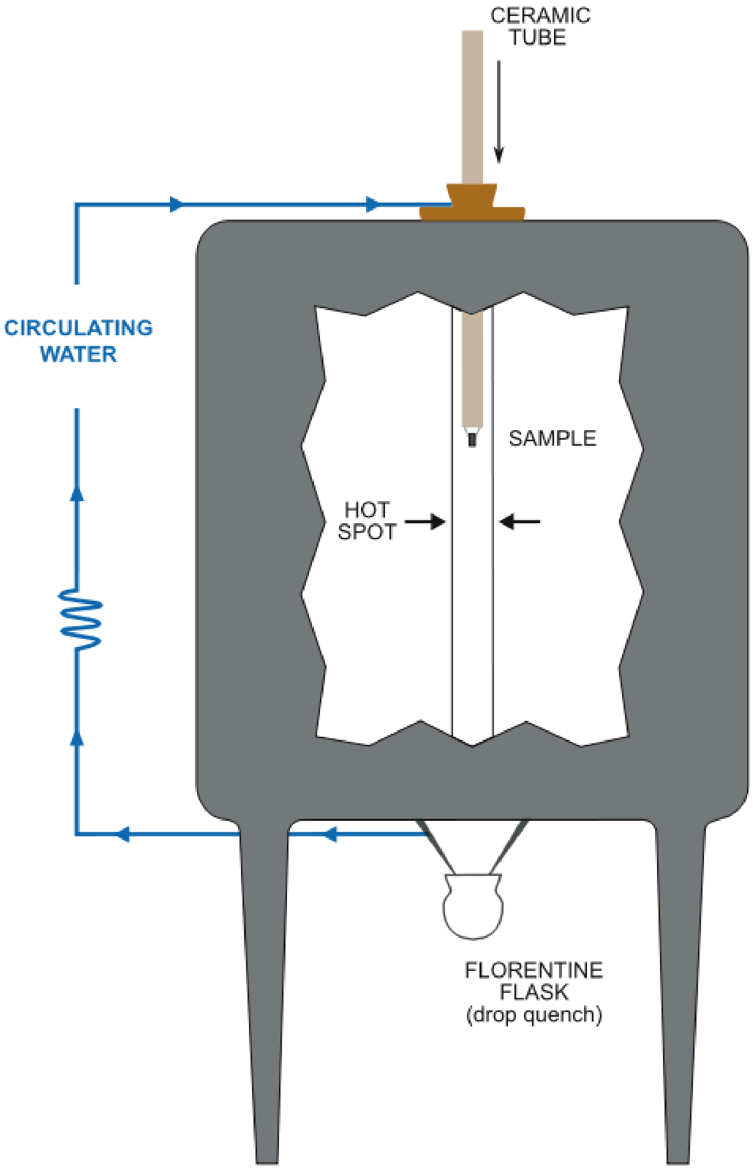

Figure 3.6: *Schematic showing the main components of the gas mixing furnace used for ambient pressure diffusion experiments. Cold water is circulated as shown in order to prevent over-heating. The ceramic tube can be raised and lowered to control the position of the sample within the furnace, and is approximately 2cm in diameter.*

3.2 Analytical techniques

Due to the small nature of the samples being analysed, coupled with the fact that hydrogen is one of the most difficult elements to accurately measure, the analysis of samples to obtain concentration (and hence diffusion) profiles involved careful use of several techniques. Secondary Ion Mass Spectrometry (SIMS) was used to measure the concentration of hydrogen/deuterium in the samples and this was then related to a length scale by measuring the depth of the sputtered pit in the sample surface using White Light Interferometry (WLI). Concentration-distance profiles were also measured as transects across cut and polished samples which had undergone longer duration runs. In addition to the SIMS work, the same samples were subsequently analysed using Infrared spectroscopy (IR) to provide structural information - namely details regarding the nature of the hydrogen incorporation.

3.2.1 Secondary ion mass spectrometry

Secondary Ion Mass Spectrometry (SIMS) is a high resolution, quantitative analysis technique that is able to measure concentrations of all naturally occurring elements over the elemental range H-U with detection limits of ppm-ppb (depending on the element). The analysis chamber is kept under ultra high vacuum ($4\text{x}10^{-10}$ Torr in the Cameca imf-4f instrument used) and a finely focussed beam of charged ions is generated and directed at the sample surface. The collision of incident ions from the primary beam with the sample surface results in the sputtering of secondary ions that are ejected and collected by a mass spectrometer. These secondary ions are deflected based on their energy and mass/charge ratio, and a set of detectors are set up to count the specific masses/charges of the species being analysed. There are several potential sources for the primary beam ions, which can be either positively or negatively charged depending on the instrument set-up and species of interest - typically the generation probability of secondary ions is increased by using oxygen primary ions if the species to be analysed is electropositive, and caesium primary ions if the species is elecronegative. For the analysis of hydrogen (and deuterium), a negative ($^{16}O^{-}$) primary beam generated from the duoplasmatron source is used, with a minimum spot size of approximately 20µm or smaller.

The process of sputtering of secondary ions, and therefore the ion yield, is variable

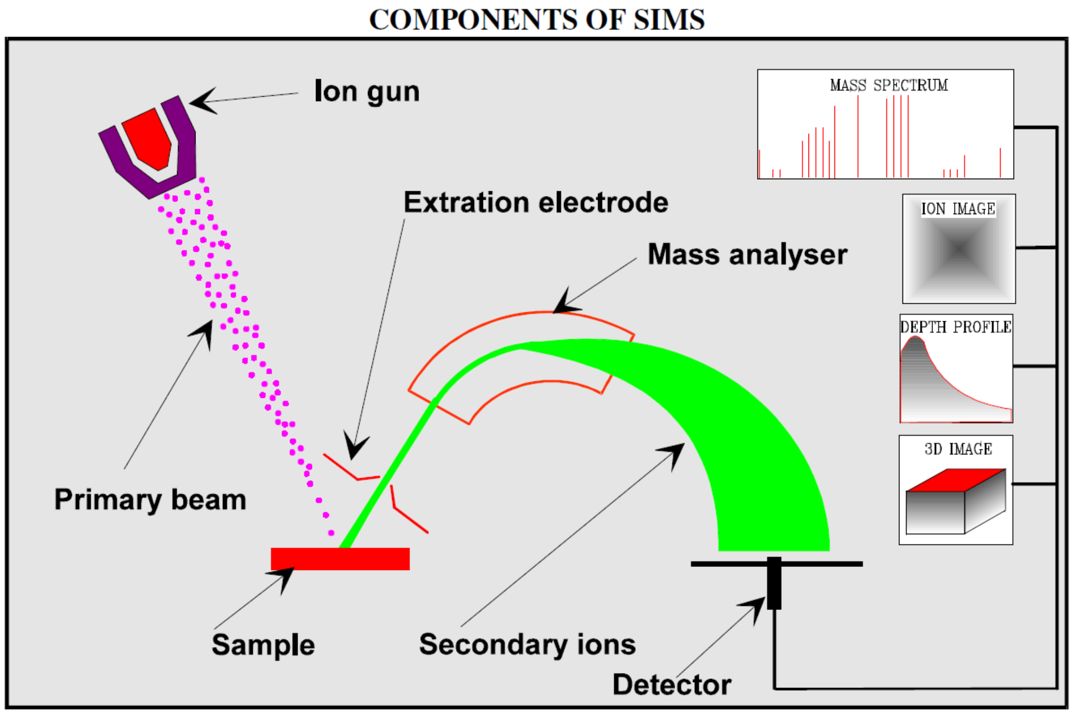

Figure 3.7: *Simplified depiction of the standard components of a SIMS instrument, taken from the Edinburgh Materials and Micro-Analysis Centre (EMMAC) 'Information for SIMS users' booklet. The generated primary ion beam is fired at the sample under high vaccum conditions and the collision causes secondary ions to be sputtered from the sample surface. The secondary ions are passed through an analyser and deflected based on mass so that the species of interest can be detected and counted.*

and not entirely understood - thus the use of known standards is particularly important in SIMS work. Count rates for the analysed species are compared to measurements in known samples to obtain quantitative data and convert to absolute values (e.g. ppm values). As sputtering rates are highly influenced by composition and structure of the phase being analysed, the nature of the standards (particularly the composition, which should be as close to that of the material being investigated as possible) is important. Sample preparation is also particularly critical to the quality of SIMS data obtained. Most importantly, samples must be mounted in a medium that is compatible with the ultra high vaccum and must be polished to a flat (1µm) finish. Any micro-topography on the sample surface can affect the sputtering process, and lead to inaccurate species concentrations being measured.[3] In addition, non-conductive samples must be gold coated (with a layer 10-30nm thick) prior to SIMS analysis, to prevent the build up of charge on the sample surface. Specific sample preparation and the use of standards is discussed in more detail where relevant in the following chapters.

Distance-concentration profiles

Typically, concentration (and diffusion) profiles are measured by SIMS as a series of analysis spots across a surface, with a specified (or subsequently measured) spacing in between. This requires the sample to have been cut and polished to expose a surface parallel to the direction of diffusion, which is not always possible with small samples and hence depth profiling is used as an alternative.

Depth profiling

During SIMS analysis, the sample surface is progressively destroyed as the incident primary beam causes the sputtering of secondary ions. As a result, during typical analysis the primary beam actively ‘drills down’ in to the sample and, over a prolonged period of time, creates an analysis pit of (relatively) substantial depth. As this occurs, the instrument effectively collects and measures ejected particles at increasing levels of depth in the sample (figure 3.8).

The progressive recording of data with depth in to the sample can theoretically be utilised in studies investigating processes such as diffusion, where concentration-depth profiles are a desirable outcome of the analysis. This technique, known as depth profiling, is useful when high spatial/depth resolution is important because data points are collected almost continuously as the beam drills through the sample. This allows for much higher spatial resolution than in studies where single spots are taken across the surface of interest (with a separation of 10-20µm) and is particularly useful for investigating short and near-surface diffusion profiles the detail of which might otherwise be missed (figure 3.9). Furthermore, the relatively small footprint of depth profiling provides advantage in cases where obtaining large samples is

---

[3] Through a process that is only poorly understood, any topography present on the sample is substantially exaggerated as the analysis pit is created (Hunter, 2009). Greater degrees of surface topography result in greater inaccuracies in the SIMS concentration data, as the beam is not collecting data from the same area of sample at each point - this is difficult to mitigate against and simply requires as good a polish on the sample surface as possible.

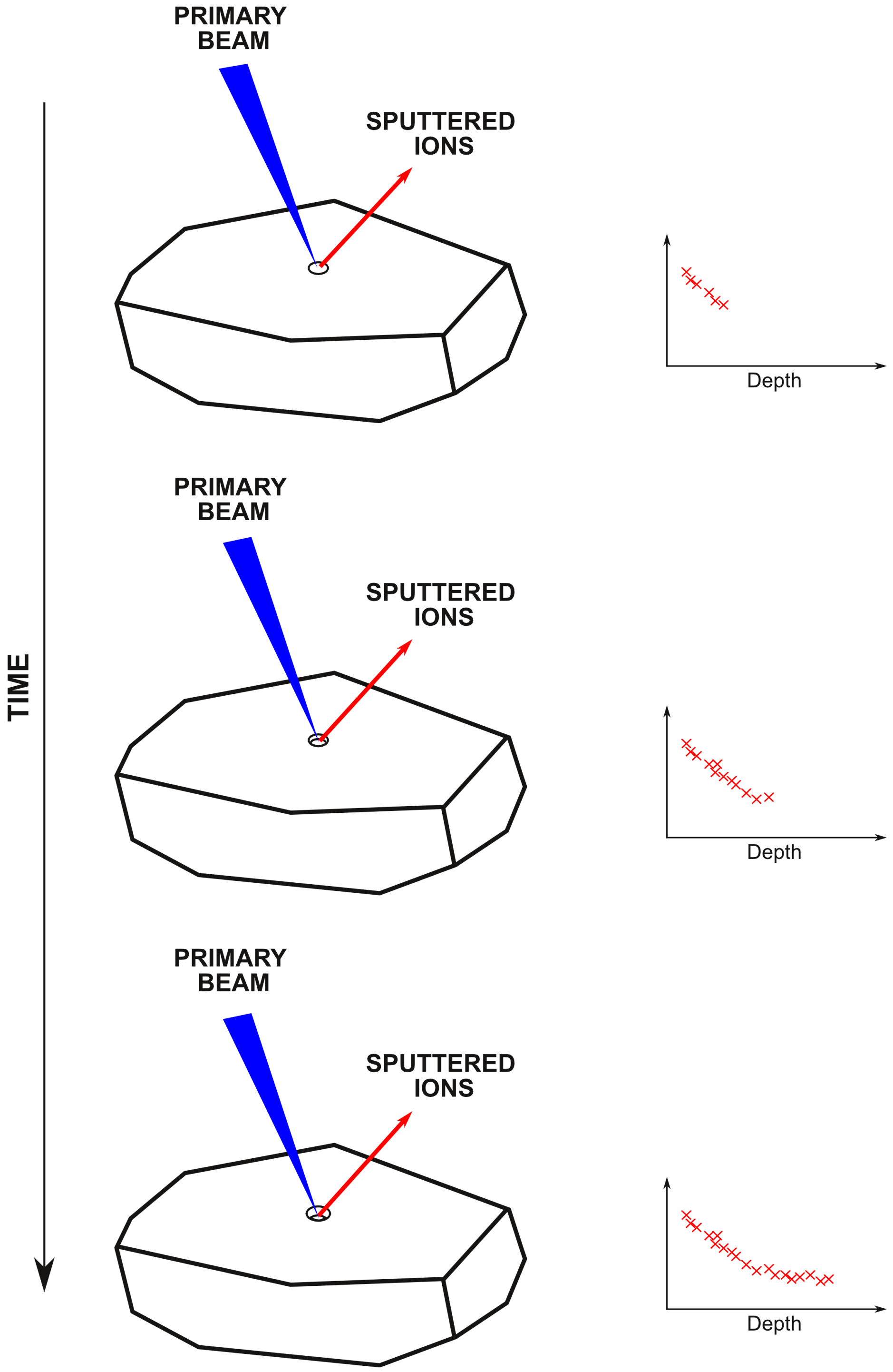

Figure 3.8: *Creation of an analysis pit in the crystal surface as the destructive SIMS beam 'drills down' in one place over time, resulting in the collection of sputtered ions from progressively deeper levels in the sample.*

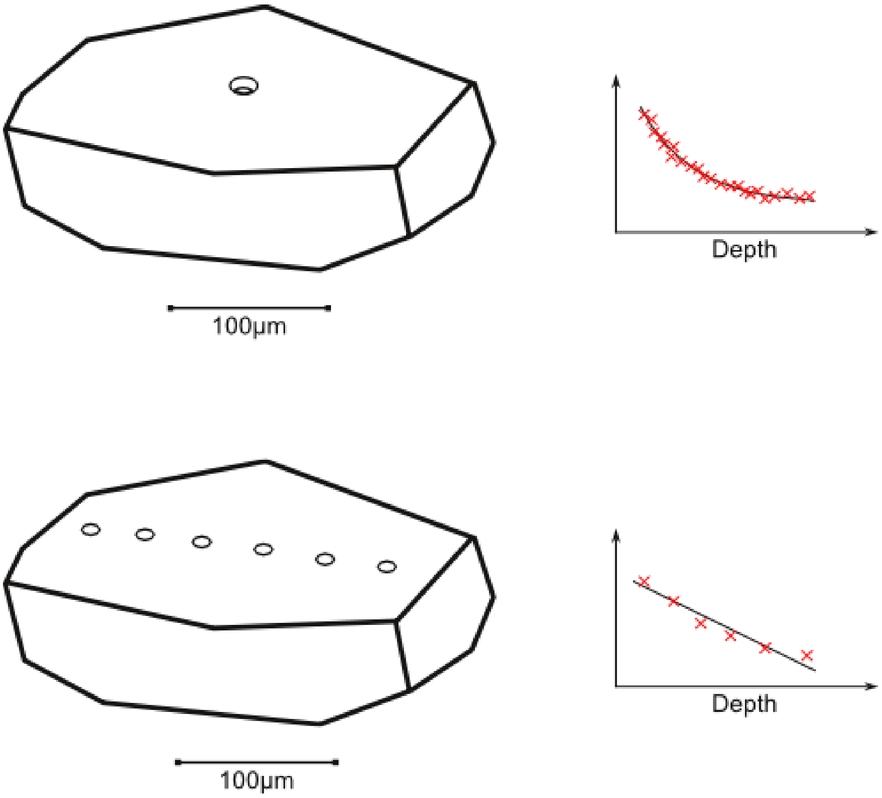

Figure 3.9: *Higher resolution is obtained from depth profiling (top) compared to taking measurements at several intervals across a sample surface (bottom). Particularly in diffusion profiles, lack of resolution may lead to an incorrect fitting and interpretation of the data - for example a straight line fitting to the data. Note that, in reality, the depth scale on the two profiles would be entirely different as the depth profile (top) only represents the area within a small distance of the sample surface (approximately 1-2µm).*

problematic, expensive or simply not possible. However, one of the problems with this method is that there is no well-defined correlation between the analysis conditions, sample material and sputtering process/rate. Therefore, in order to quantify depth-concentration data obtained using this SIMS method, the length of the profile (which is equivalent to the depth of the analysis pit in the sample) needs to be measured after analysis is complete. Additionally, the assumption is made that the sputtering process occurs consistently and that the data points (recorded in equal time steps) represent equal increases in depth.[4]

---

[4] Such that the measured depth of the pit can be validly split in to equal increments corresponding to the number of data points measured.

Despite these limitations, depth profiling is theoretically the ideal analysis method for investigating short (and near-surface) diffusion and when initially designing the D-H exchange experiments the intention was to use the technique to identify diffusion profiles in small (less than 200µm) synthetic samples. During analysis of samples for the project, several diffusion profiles were characterised in this manner. However, during the analysis, an additional limitation to using depth profiling as a technique became apparent. During sputtering, secondary ions are not exclusively ejected from the (progressively deeper) bottom of the analysis pit and, particularly problematically, material can be ‘dragged’ in from the edges of the crater created by the beam (see figure 3.10). This is partly evidenced by the laterally growing analysis pit which ends up larger than the expected beam footprint. The result is that rather than only measuring the concentration of the species of interest in progressively deeper ‘layers’, sputtered ions from shallower levels (or the sample surface) are mixed with those from deeper in the sample. There is no way to distinguish the contribution of ions captured from the pit edges from the true profile. Therefore, in reality, if the beam is simply allowed to drill straight down into the sample, an anomalous concentration profile will be obtained. For diffusion profiles measured using this technique, the result is an over estimation of the diffusion coefficient value (figure 3.10) since the anomalous concentration profile essentially represents a smearing out of the true profile.[5] Further discussion on the impact of this phenomenon in SIMS studies can be found in Hunter (2009) and examples/further discussion directly relevant to the data in this project can be found in section 4.3.2.

If depth profiling is to be used as a quantitative technique, a method is required to mitigate against this phenomena. Rather than drilling down in one spot, the SIMS instrument can be set up to measure a depth profile by rastering the beam over an area significantly larger than the width of the beam (generally a minimum of 3-4 times the width in each direction - see figure 3.11). It is then possible to apply an electronic gate to the instrument, ensuring that only material sputtered from the centre of the larger pit is collected and counted. As the analysis is done at a distance from the edges this reduces the effect of ions dragged in to negligible. However, rastering in this manner results in a substantially larger analysis pit and consequently requires sufficient sample surface area and sample size, placing additional constraints on the application of this method of analysis.

---

[5] Albeit in a more complex manner, and one that it is not possible to correct for.

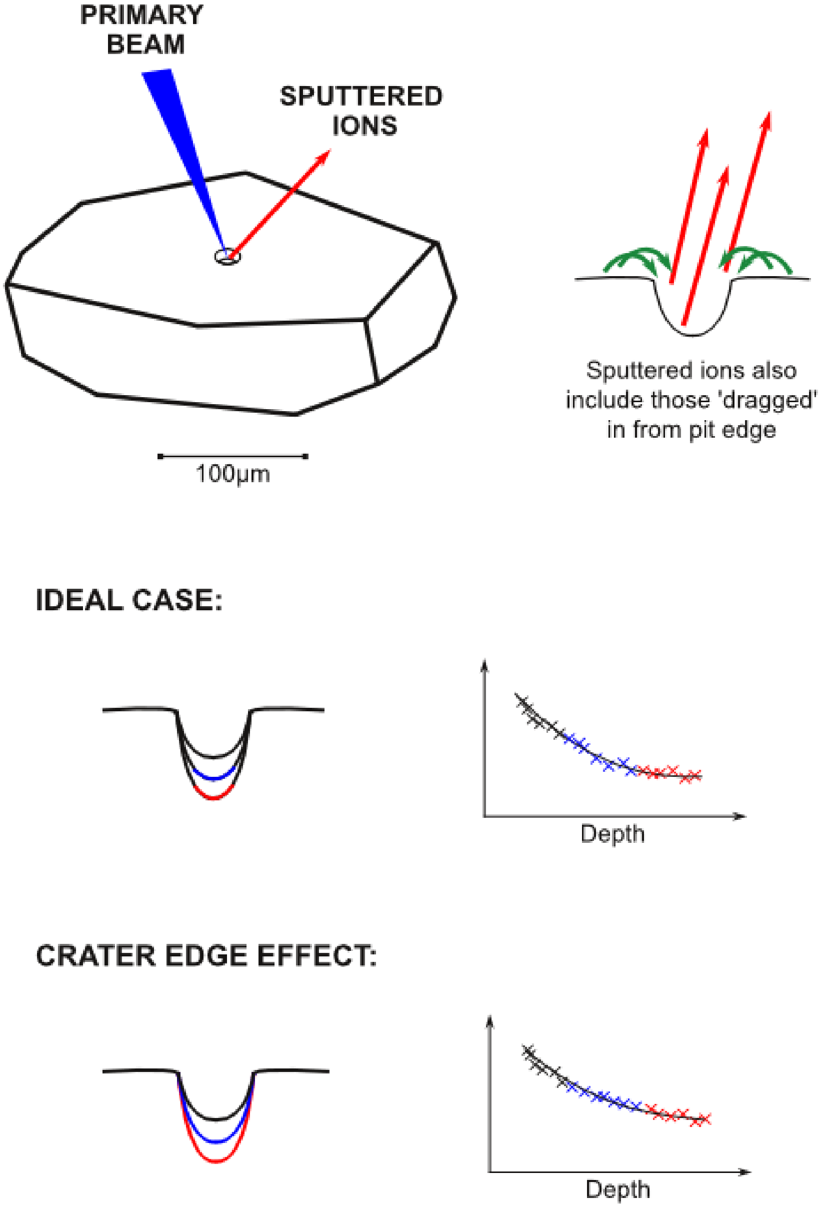

Figure 3.10: *During continued analysis at a single location, ions from the edge of the created crater/pit are dragged inwards and contribute to the secondary ions sputtered and counted (left) - therefore the resulting signal (right) is not simply a reflection of the species concentration at progressively greater depths within the sample. Although the two profiles only appear subtly different, fitting of the obtained profile (lower right) leads to an overestimation of the diffusion coefficient compared to the true profile (upper right).*

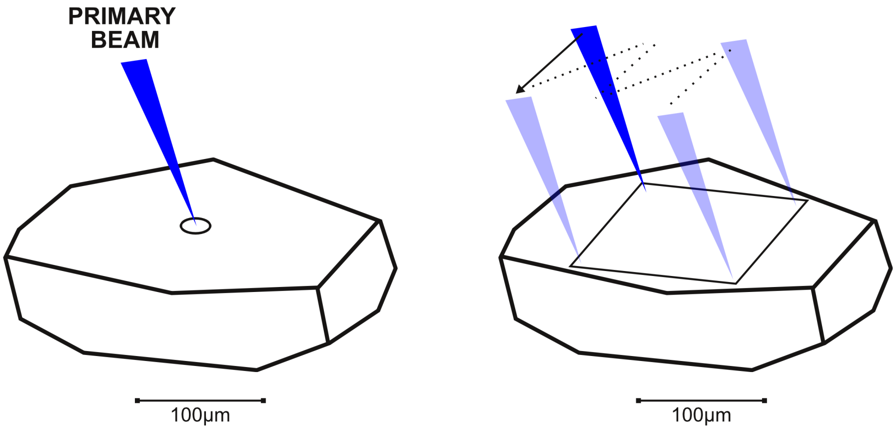

Figure 3.11: *When the SIMS beam 'drills down' at a single point on the sample surface (left), the data collected may not be a true representation of the change in a species with depth, due to the mixing-in of ions from higher levels (as discussed in text). In order to mitigate against this for accurate depth profiling analysis, the primary beam is allowed to scan over a larger area (right) and the instrument is electronically gated so that only ions sputtered from the centre of the pit are recorded.*

3.2.2 White light interferometry

White light interferometry (WLI) is a non-contact optical method that measures the roughness of a sample surface using the wave properties of light. The instrument splits light of known wavelength from a source into two fractions - one is directed at and reflected back from the sample surface (through the microscope objective) and the other is reflected from a reference mirror. The stage on which the sample sits is adjusted so that the distance between the beam splitter and the sample surface is the same as that from the beam splitter to the reference mirror. When the beams are recombined inside the instrument, constructive and destructive interference occurs where the lengths are different, creating light and dark bands known as interference fringes (see figure 3.12). Since the reference mirror is essentially perfectly flat, any differences in the distance travelled by the light beams must be due to variations in height on the sample surface. By calculating the exact height differences using the known wavelength of the original light, the WLI instrument can reconstruct the 3D surface of the sample to within less than 1nm. To work accurately, WLI requires that the same surface be both as reflective and as flat as possible. As samples analysed by SIMS have already been prepared with flat surfaces and have been gold coated (making the suitably reflective), WLI is the ideal technique to measure the depth of SIMS analysis pits - and hence quantify the length scale for diffusion profiles. Alternative methods include Stylus Profilometry, where an instrument drags a fine-tipped needle over the sample surface and records the depth to which the needle drops - this is useful for measuring large pits but is unable to resolve the detail of small SIMS pits (resolution is generally not less than 10nm).

Figure 3.12: *Example of light and dark interference fringes produced by the phase shift between the reference light signal and the reflectance from the sample surface.*

3.2.3 Infrared spectroscopy

Infrared spectroscopy (IR) is a non-destructive analytical technique that identifies the molecular structure of samples by measuring the extent to which they absorb different frequencies of radiation. During IR measurements, a spectrum is produced that graphs the absorbance peaks (i.e. absorption in the sample due to molecular vibration modes) against the frequency/wavelength of radiation. As absorption due to vibration modes of different molecular species is highly characteristic, and also dependent on local structural environment, the position of the peaks yields information on the species present in the sample, their structural arrangement, and the relative concentration.

Initial dispersive IR instruments (in which a prism or grating separated a light source into individual frequencies and a detector then measured the transmission/absorbance by the sample at each) were limited by a slow scanning process. To improve this the Fourier Transform Infrared (FTIR) method was developed, which allows the simultaneous measurement of all infrared frequencies. This is achieved through the use of an interferometer - an optical device that produces a signal with all of the relevant frequencies encoded within it - and the subsequent application of a Fourier Transformation in order to decode the resulting signal (resulting in the name FTIR). During FTIR measurements, a background spectrum is always measured to serve as a reference scale for absorption. This is usually a 'blank' measurement taken with no sample present and allows correction for any absorption within the instrument or the sample holder - ensuring that all of the spectural features present in the final data are truly from the sample.

There are four major sampling techniques available during FTIR measurements; Transmission, Attenuated Total Reflection (ATR), Specular Reflection and Diffuse Reflectance. Transmission is the most common and preferred method for quantitative analysis, and is the only FTIR sampling technique used in this project. During transmission measurements, the sample is placed directly in to the path of the IR beam, as shown in figure 3.13. Since higher quality IR spectra are obtained when the sample surface is flat, and the thickness of the sample must be known to correlate the absorbance with concentration, samples are often prepared as double polished wafers.

Details of the sample preparation and instrument set-up specific to this study can be found in section 4.5 and a thorough review of the application of IR techniques (specifically regarding measurements of the water content in nominally anhydrous minerals) is given by Rossman (2006) in the 'Water in Nominally Anhydrous Minerals' volume (62) of the *Reviews in Mineralogy & Geochemistry* series.

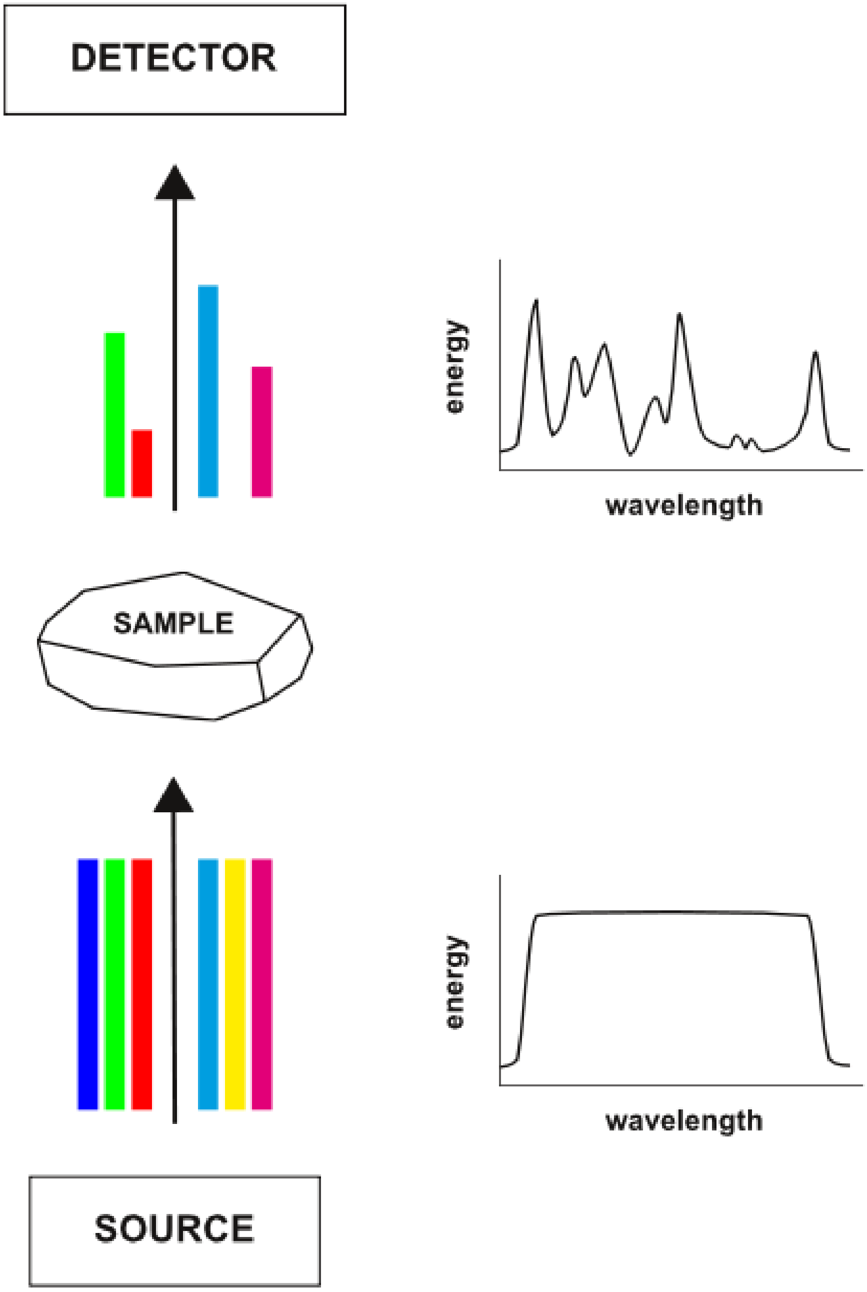

Figure 3.13: *FTIR measures the absorbance/transmission of radiation at different frequencies by the sample. The resulting spectrum of absorbance peaks is directly related to the molecular structure of the sample. Diagram adapted from 'Introduction to Fourier Transform Infrared Spectrometry' produced by Thermo Nicolet Corporation, 2001 (available for download from the ThermoFisher Scientific website).*

3.2.4 Scanning electron microscopy

Scanning electron microscopes (SEM) are commonly used to characterise the surface of solid materials by producing high resolution, high quality images. Using a thermal emission source, the SEM produces a beam of electrons which is focussed using electromagnetic lenses and scans over the surface of a sample. The collision of the beam with atoms at the sample surface (and near surface) results in the scattering of electrons ('interaction products') that are detected by the instrument. A value for the concentration of electrons detected per unit time is assigned to each pixel and represented by a greyscale level such that a black and white image is built up as the beam scans across the sample surface. As the electron beam is narrow (a few nanometres), the SEM has a large depth of field and produces characteristic images with a 3D appearance (see figure 3.14). Images to a nanometer scale resolution can be taken in two primary modes - backscatter electron imaging (BSE) or secondary electron imaging (SE). In BSE mode, the electrons ejected during high energy elastic interactions with the sample are detected. As the number or electrons backscattered is highly dependent on atomic number, this detection mode is well suited to identifying compositional variations in a sample. Contrastingly, in SE mode the SEM detects the scattering of low energy electrons, the number of which is more affected by the topography of the sample. SE is therefore more suited to investigating surface morphology, and is the primary method utilised in this study.

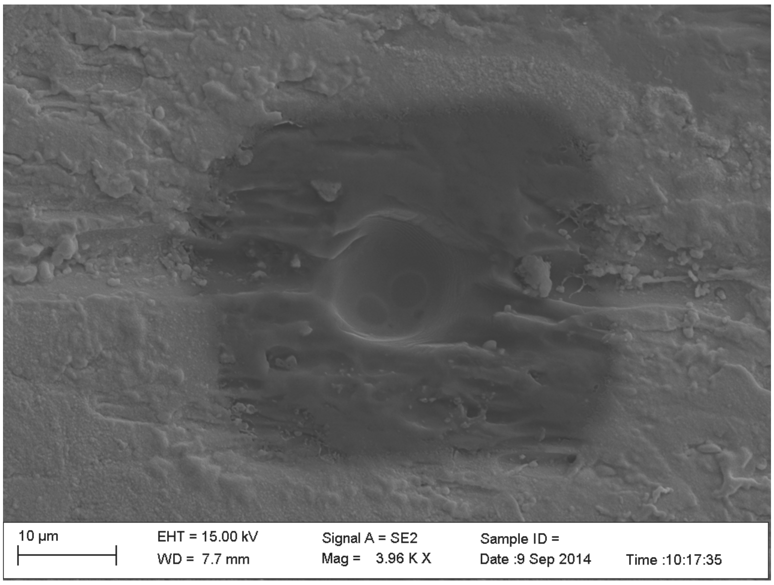

Figure 3.14: *Standard SEM image taken in SE, showing the surface texture of a SIMS analysis pit in a forsterite crystal.*

CHAPTER 4

Olivine

4.1 Introduction

As introduced, the primary aim of the project is the development of an experimental method to provide data on hydrogen self-mobility in mantle minerals under mantle conditions, applicable to a range of phases across the mantle. The movement of hydrogen defects in mantle minerals enhances mantle electrical conductivity. This means that the ability to collect relevant self-diffusion data, as opposed to simply measuring hydrogen diffusion, is important for linking laboratory studies to large scale geophysical measurements.

The method was initially developed and tested using olivine, because it is one of the dominant minerals in the upper mantle (conditions for which can be simulated fairly easily in the laboratory). In addition to being easily synthesised at high pressure/temperature, olivine has the advantage of having been extensively studied - both in terms of hydrogen incorporation mechanisms and hydrogen solubility as a function of temperature, pressure and composition. The pure magnesium olivine end member forsterite was used for the majority of the work as it lacks iron, making it simple to synthesise and study, as well as ensuring that hydrogen movement is not coupled to polaron diffusion related to the presence of Fe ions. Starting materials for the exchange experiments were synthesised under mantle pressure and temperature conditions, ensuring appropriate incorporation of water for the conditions being studied.[1] Synthesised samples were then subjected to exchange runs (again directly under mantle conditions), during which deuterium from an essentially infinite fluid source exchanged with hydrogen already present in the crystal structure under controlled conditions. The extent to which this exchange proceeds (at chosen temperatures and periods of time) can be quantified by measuring the concentration of the relevant species with depth in the sample. The resulting concentration-depth profiles can be fitted to Fick's law to determine the diffusion coefficients.

The exchange between hydrogen and deuterium can be considered to represent the self-diffusion of hydrogen. Thus, the fitted diffusion profiles will give values for the hydrogen self-diffusion coefficient and accurately constrain the temperature dependence of hydrogen mobility. The advantage of using deuterium is that during analysis (carried out by SIMS, see further review in section 4.3), it can be difficult to reduce hydrogen backgrounds to a level that eliminates signal noise. By comparison, deuterium background concentrations can be reduced effectively to zero. The experimental design was also set up to collect corresponding measurements of hydrogen diffusing out of the samples (as the deuterium signal falls with depth, the hydrogen signal ought to rise correspondingly).

---

[1] In comparison to natural samples that are likely to contain a defect population equilibrated under shallower conditions, as previously noted.

4.2 Experimental procedure

A substantial part of the work carried out involved the development and refinement of an experimental method first to synthesise mantle phases containing relevant ‘water’ defects and then to allow the exchange of hydrogen for deuterium under controlled conditions. One of the particular challenges was doing so while also ensuring the final sample was suitable for analysis. The background to the experimental apparatus has already been given in chapter 3 and the detail of the experimental procedures and the refinements made during the evolution of the project are discussed below.

4.2.1 Capsule preparation

For all experimental runs, samples were contained within a metal capsule. Capsules were prepared from a platinum, silver palladium or gold thin-walled tube (depending on experimental conditions, and availability) with either 3mm or 2mm outer diameter cut to approximately 6mm in length. The cut length was annealed in a blue bunsen flame to remove surface impurities and soften the metal for easier manipulation, and then one end was triple crimped and welded shut (see figure 4.1). After a second anneal, the welded end was flattened and the open ended capsule pressed through a pin press with an internal diameter of 3mm (or 2mm, correspondingly), in order to ensure the width of the capsule was correct to fit in the assembly. Each experimental capsule was filled with the relevant sample material and the open end was then crimped and welded in the same manner. During this second weld, the capsule was cooled, using either coolant spray or a damp paper ‘jacket’, to ensure that no liquid was lost due to boiling. The final step was to flatten the welded top end and the entire capsule was then passed back through the pin press several times to ensure the final result was a cylindrical capsule 5mm in length, with the relevant diameter.

During the preliminary analysis on the first set of exchange experiments, no deuterium was detected in any of the forsterite samples. Having eliminated the possibility that the deuterium source was not suitably pure,[2] it was considered likely that deuterium had escaped from the capsule/s during the experimental run/s. In all subsequent runs containing liquid H_2O or D_2O, the welded seal on the final capsule was checked by immersion of the capsule in a beaker of silicone oil at 120°C. The

---

[2] Samples of the liquid D_2O were accurately weighed and compared to (de-ionised) H_2O.

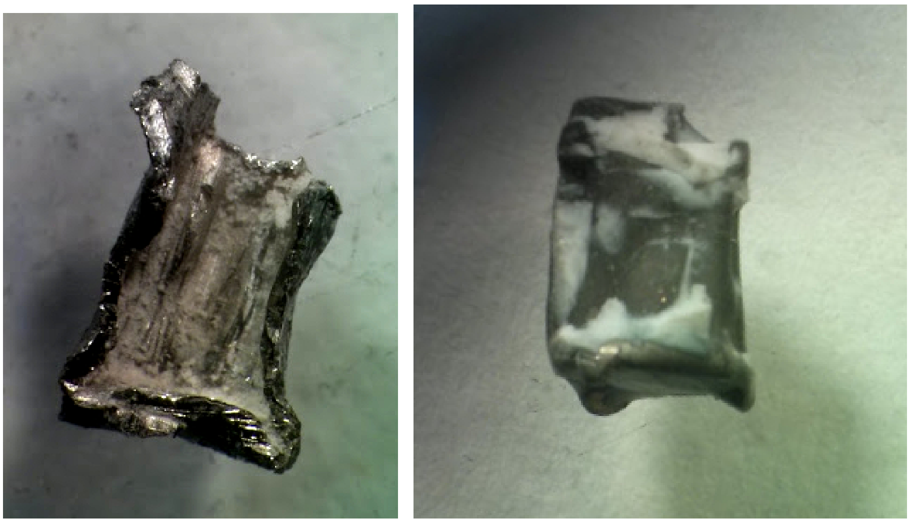

(a) *(b)*

Figure 4.1: *(a) 3mm diameter platinum capsule that has been cut open (and the sample retrieved), showing the flattened bottom weld; (b) Recovered synthesis capsule coated in alumina from the assembly.*

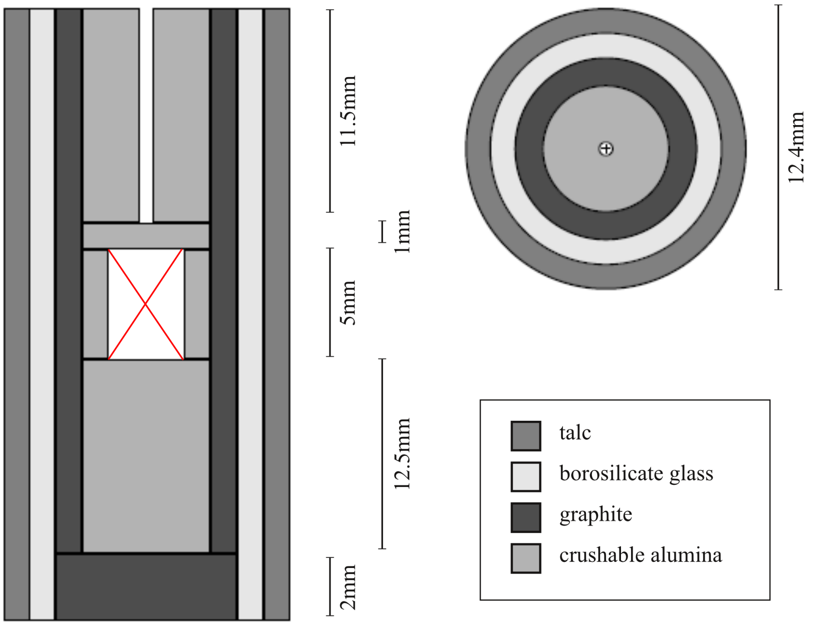

Figure 4.2: *Schematic cross-section (left) and top view (right) showing the standard 0.5" talc-pyrex piston cylinder assembly (containing an internal graphite furnace) used in synthesis and exchange runs. Approximately 3 times actual size.*

immersion causes the capsule to be rapidly heated and the small volume of air trapped inside to expand such that, if the capsule had a leak, bubbles would escape and rise up through the silicone oil. The problem of deuterium escape was confirmed when approximately two thirds of prepared capsules were found to leak at this stage. Only capsules with no evidence of any leak were used in subsequent experimental runs; those that produced bubbles were opened and the starting materials were retrieved to be reused. Individual capsules were also weighed before and after welding to identify any volatile loss as a result of heating during the weld. Capsules were also weighed before and after piston-cylinder runs where possible (often capsules removed from the piston cylinder assembly were too closely coated in Al and an accurate post-run weight could not be determined - see figure 4.1(b)) in order to identify any sample loss due to rupture of the capsule during the experimental run.

4.2.2 Synthetic olivine

H-forsterite

Pure Mg-olivine (Fo_{100}), containing water/OH defects relevant to the mantle conditions to be studied (henceforth ‘H-forsterite’), was synthesised from high purity oxide powders (99.9%) of SiO_2, MgO and $Mg(OH)_2$. The molar proportions required to produce a starting mix containing approximately 6wt.% water were calculated according to the reaction:

$$2SiO_2 + 3MgO + Mg(OH)_2 = 2Mg_2SiO_4 + H_2O \tag{4.1}$$

and the calculated mass of each oxide powder required to produce a total of 3g of powder was accurately weighed out (as shown in table 4.1).

The oxide powders were mixed and homogenised by gentle grinding under acetone for 5-10 minutes at room temperature using an agate mortar and pestle. The mixture was left undisturbed for at least an hour to allow the acetone to evaporate, before being transferred to a glass vial for storage. For each synthesis, a platinum capsule of 3mm diameter was filled with starting mix (compacted using a steel rod in order to minimise empty space) and sealed following the procedure outlined above. During piston cylinder runs, capsules sit in the middle of a talc-pyrex assembly - as shown in figure 4.2. This was assembled around the prepared capsule, then loaded into the piston cylinder (as shown in figure 3.1). The pressure was raised to 2GPa, then the temperature was raised to approximately 1600-1700°C and held for 1hour in order to melt and homogenise the mixture. The temperature was then slowly reduced to 1200°C and maintained for several days, with pressure maintained at 2GPa throughout. The exceptions were runs S1, S3 & S4, in which the temperature was simply maintained at 1200°C for the entire duration without first being raised. In general, larger crystals were produced when runs were first heated to higher temperatures, so this was done where possible (a summary of all run conditions is shown in table 4.2). At the end of the run, the sample was quenched by switching off the power, which rapidly dropped the temperature (to below 100°C within 30 seconds). The capsule was recovered from the stack and carefully sliced open to retrieve the sample. This synthesis method successfully produced colourless H-forsterite crystals that spilled out of the capsule easily - with occasional reluctant crystals encouraged out using a wooden cocktail stick to avoid damage (see figure 4.3). Crystals were colourless and clear - with no evidence of any inclusions - and were generally 100-300μm in size and relatively equant in shape.

Table 4.1: *Proportion of oxide powders in starting mixes for olivine synthesis runs.*

	Fo$_{100}$	**Fo**$_{100}$ *	**Fo**$_{90}$	**Fo**$_{90}$ *	**Fo**$_{50}$
MgO	1.21150g	1.71879g	0.65863g	0.49351g	0.17069g
$Mg(OH)_2$	0.58441g	-	0.38931g	-	0.38956g
FeO	-	-	0.18375g	0.09776g	0.78415g
SiO_2	1.20409g	1.28121g	0.76831g	0.40874g	0.65567g
Total	3.0g	3.0g	2.0g	1.0g	2.0g

* *Denotes 'dry' mixtures (liquid H_2O or D_2O subsequently added to capsule).*

Table 4.2: *Forsterite synthesis runs and conditions.*

Run #	Composition	T (°C) and duration	Notes
S1	H-Fo$_{100}$	1200, 70hr	produced well formed H-forsterite crystals 100-200μm in size
S2	H-Fo$_{100}$	1600, 1hr; 1200, 68hr	produced well formed H-forsterite crystals 100-200μm in size
S3	D-Fo$_{100}$	1200, 48hr	no crystals produced (water loss?)
S4†	D-Fo$_{100}$	1200, 68hr	small D-forsterite crystals (approx. 100μm)
S5	D-Fo$_{100}$	1700, 1hr; 1200, 47hr	no well formed crystals produced, capsule deformity implies water loss
S6	D-Fo$_{100}$	1650, 1hr; 1200, 60hr	produced well formed D-forsterite crystals
S7	H-Fo$_{100}$	1700, 2hr; 1200, 44hr	micro crystalline H-forsterite (run too short?)
S8	H-Fo$_{100}$	1700, 20min; 1200, 71hr	no well formed crystals, capsule deformity implies water loss
S9	H-Fo$_{100}$	1600, 1hr; 1200, 66hr	well formed H-forsterite crystals, approx. 200μm average size
S17†	H-Fo$_{100}$	1200, 1hr; 1700, 72hr	H-forsterite crystals 200-400μm in size

† *Denotes runs in which evidence for liquid was observed on piercing the capsule.*
All runs were carried out at 2GPa.
For Fo$_{100}$ + D synthesis runs, the capsule contained a 'dry' forsterite powder mix with 1μl liquid D$_2$O.
In the majority of runs, a high starting T was chosen to promote melting & homogenisation. After 1-2hours, T was decreased over a further 1-2hours then maintained for the duration of the run.
Details of starting mix compositions are given in table 4.1.

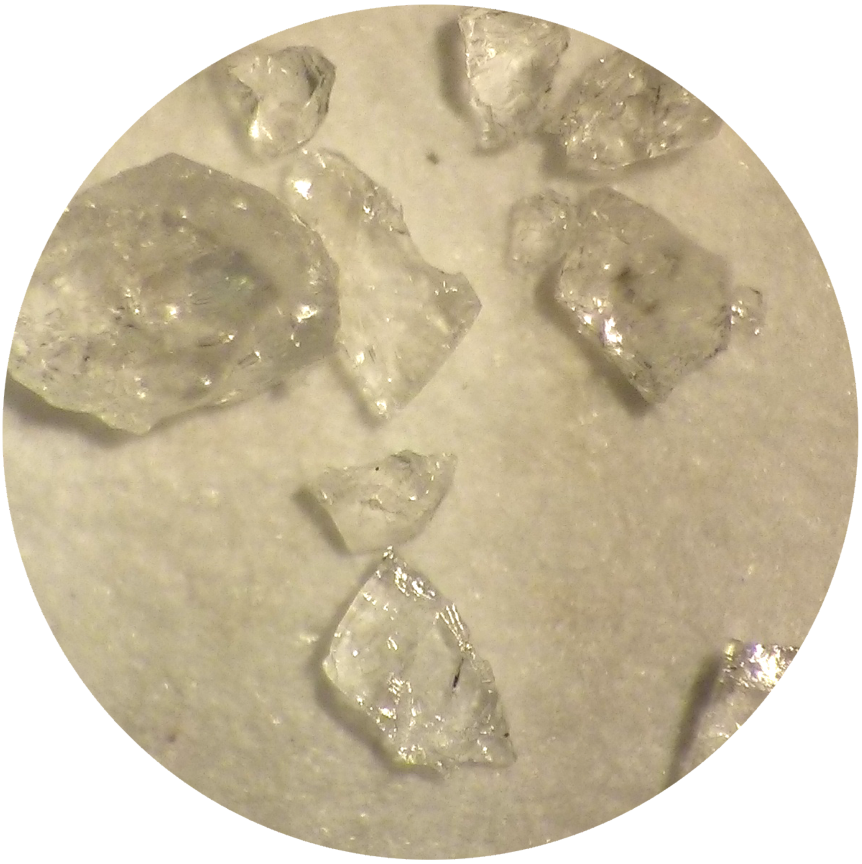

Figure 4.3: *Synthesised H-forsterite crystals from run S2, shown loose on filter paper. Field of view is approximately 500µm.*

D-forsterite

In addition to H-forsterite, four synthesis runs were carried out to produce forsterite containing deuterium in place of hydrogen so that reverse (H in, D out) exchange experiments could be carried out and analysed. As noted above, deuterium diffusion profiles are easier to identify/quantify during analysis and therefore the aim was to obtain a 'diffusion out' profile using these H-D exchange experiments (to compliment the standard 'diffusion in' profiles obtained from D-H exchange). High purity SiO_2 and MgO oxide powders were weighed out according to the reaction:

$$SiO_2 + 2MgO = Mg_2SiO_4 \tag{4.2}$$

and homogenised in the same manner as the H-forsterite mix. 1µl D_2O (0.0110g) was measured into the bottom of a capsule, and 0.1000g of the oxide powder mix was added so that approximately 10 wt.% D_2O was present. Each capsule was sealed, checked and loaded into the piston cylinder assembly as described above. The pressure and temperature conditions used for D-forsterite synthesis were the same as for H-forsterite (2GPa, 1700°C for 1hour then 1200°C for several days - see table 4.2). Recovered D-forsterite crystals were consistently smaller and of poorer quality than the H-forsterite crystals. This may be due to the increased viscosity of D_2O inhibiting crystal nucleation and growth, but is not thought to represent any reason not to consider D-H exchange equivalent to hydrogen self-diffusion.

Other H-olivine compositions

In order to investigate the influence of structural Fe on hydrogen incorporation and diffusion in olivine, the initial aim was to synthesise a variety of olivine compositions and repeat the exchange experiments. Starting mixes were made for the synthesis of Fo_{90} ($Fe_{0.2}Mg_{1.8}SiO_4$) and Fo_{50} ($FeMgSiO_4$) using the same method as outlined above (see table 4.1). Synthesis of H-Fo_{90} was attempted both with $Mg(OH)_2$ as the source of water, and using a 'dry' mix with liquid water but did not successfully produce crystals of the desired composition - see table 4.3 for details of the runs carried out. X-ray powder diffraction (XRD) analysis on the product of run S12 (a mixture of colourless and slate-grey/black micro-crystals) identified the presence of magnetite (see figure 4.4), indicating that the piston cylinder environment was potentially too oxidising to produce Fe-olivine. Several further attempts were made using alternative capsule materials and different temperature conditions, but ultimately a decision was taken to progress the project in an alternative direction in order to make best use of remaining time and resources.

Table 4.3: *Olivine (Fo_{90}) synthesis runs and conditions.*

Run #	**Composition**	**T (°C) and duration**	**Notes**
S10	H-Fo_{90}	1700, 1hr; 1200, 65hr	T/C failed & T unknown, capsule melted
S11	H-Fo_{90}	1650, 1hr; 1200, 66hr	crystals 50μm, heterogeneous (black/grey + colourless + yellowish)
S12[1]	H-Fo_{90}	1650, 1hr; 1200, 65hr	colourless & grey/black micro-crystals
S13	H-Fo_{90}	1150	PC FAILURE (unknown duration), greenish micro-crystals
S14[†]	H-Fo_{90}	1150, 66hr	grey/black micro-crystals/powder
S15[†]	H-Fo_{90}	1150, 65hr	grey/black micro-crystals/powder
S16[†] [2]	H-Fo_{90}	1150, 63hr	micro-crystals/powder

[†] *Denotes runs in which evidence for liquid was observed on piercing the capsule.*

[1] *Starting mix was ground for an additional 10mins before run, to eliminate potential source of heterogeneity in S11.*

[2] *In S16, a dry Fo_{90} mix was used with liquid H_2O added to the capsule.*

All runs were carried out at 2GPa.

S10 - S12 used Pt capsules, S13 - S16 used $Ag_{70}Pd_{30}$.

Details of starting mix compositions are given in table 4.1.

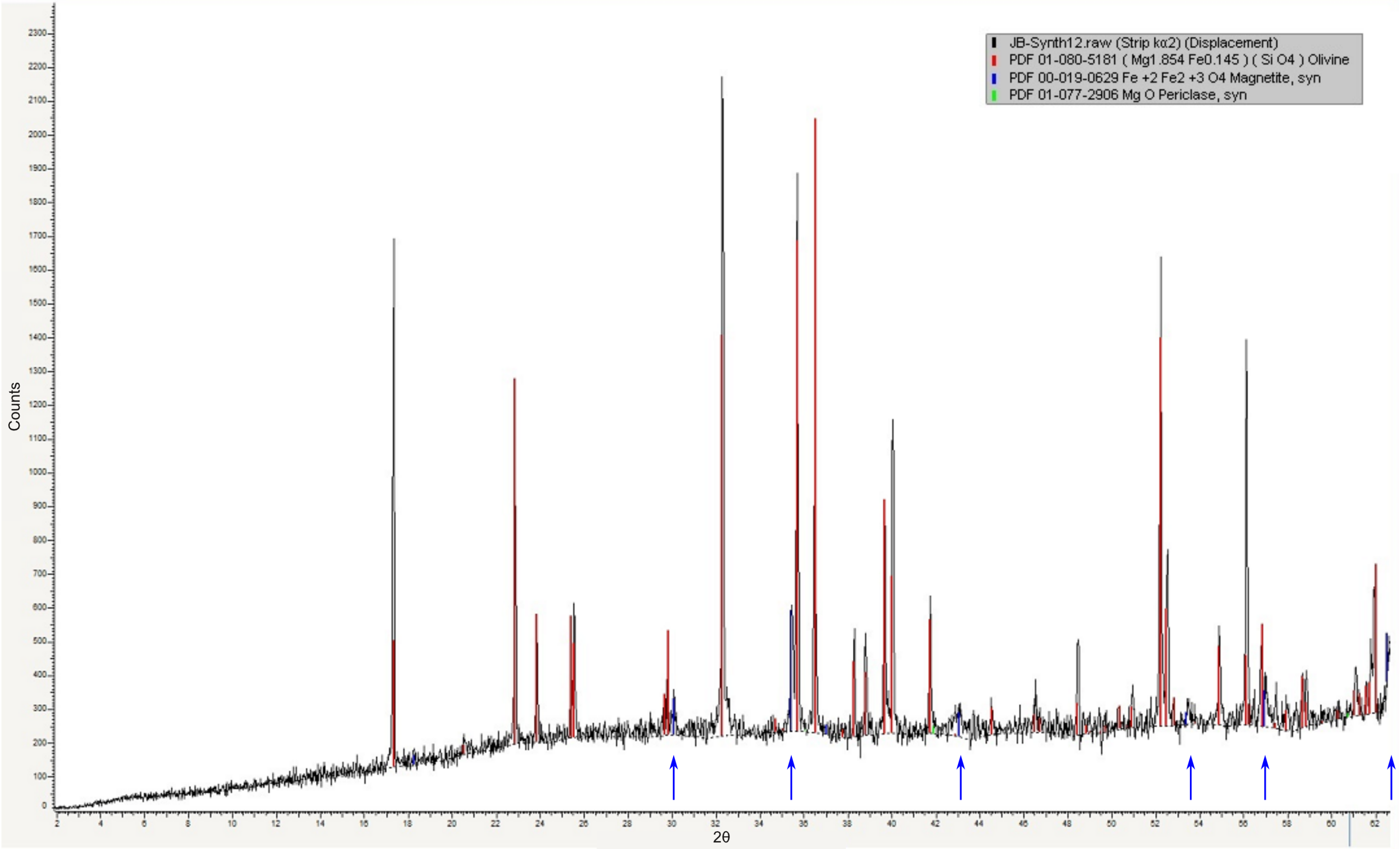

Figure 4.4: *XRD analysis of the crystals from synthesis run S12, indicating the presence of magnetite and confirming the desired olivine composition (H-Fo$_{90}$) has not been produced. Blue arrows indicate standard magnetite XRD positions and peaks can be seen in the sample data (black line) at these points, in addition to at the Mg-rich olivine positions (red bars).*

4.2.3 Polishing

In order to obtain good quality concentration profiles using SIMS, crystal faces are normally polished in order to provide a flat analysis surface. However, the experimental set-up deliberately produces shallow diffusion profiles (approximately 1μm total length) and therefore to polish the surface of the H-forsterite crystal after the D-H exchange run would remove the area of interest. As a result, during analysis of the first set of exchange experiment samples, a significant number of the grains were found to have uneven crystal faces and were therefore unsuitable for analysis. As the crystals were free-grown, it had initially been hoped that the crystal faces would be of sufficient quality without the need for polishing but, as this was shown not to be the case, H-forsterite crystals were polished prior to the D-H exchange step in all subsequent runs. This resulted in the majority of grains being suitably flat for analysis (although, because the grains undergo the exchange step post-polish, the polish was not preserved in all cases - not least because maintaining the orientation when retrieving and mounting is difficult with small, colourless samples) and was found to be a reasonable compromise between potentially removing the diffusion profile by polishing after exchange runs and reducing the quality (and quantity) of the data by not polishing at all.

Each individual H-forsterite grain was mounted in crystalbond[3] on a small cylindrical steel peg. This was achieved by heating the peg to 130°C on a hot plate and melting crystalbond directly on to it, then carefully placing a forsterite crystal in the molten crystalbond. Initially, attempts were made to polish multiple grains at one time by melting crystalbond into an epoxy mould with drilled holes, but an issue with the crystalbond softening during polishing was thought to stem from it not melting and solidifying properly. Additionally, the samples were so small that polishing several at once involved the substantial possibility of polishing straight through one grain while trying to achieve the desired result on another. Thus, the multiple mount method was abandoned.

Once set in the crystalbond, polishing of the H-forsterite crystals was carried out by fitting the peg inside a metal cylinder. To polish, the cylinder (rather than the peg) was rotated to ensure the only pressure directly on the sample was the weight of the peg, protecting the grains from being crushed. Instead of standard mechanical

---

[3] Crystalbond 509^{TM} - chosen as the mounting medium for polishing as it is easily dissolved in acetone so that the polished sample can be removed without damage (or loss).

polishing apparatus (for which the peg-mount was not suitable), a flat glass plate was covered in layers of aluminium foil and this was used as the polishing surface, with the ‘action’ carried out by hand. Grains were first polished on wet 1200 grit paper to remove any crystalbond that had enveloped the forsterite, and to expose the entire face at the same level. Oil based diamond polishing solutions of 6, 3, 1µm (as are standard for polishing SIMS mounts) were then used sequentially - 6µm for approximately 3-4mins, 3µm for approximately 5-6mins and 1µm for approximately 3-4mins - to achieve a suitable flat face for analysis. Mounts were viewed in reflected light to monitor polishing progress, and thoroughly cleaned at each stage to prevent any contamination with coarser material. Once a satisfactorily polish was obtained, the crystalbond was dissolved using acetone and recovered crystals were washed in de-ionised water to remove all traces of acetone and crystalbond, before being dried on filter paper and transferred to glass vials for storage.

4.2.4 Exchange experiments

Once synthesised and polished, H-forsterite grains were subject to an exchange run during which deuterium from a source was allowed to diffuse into the crystals, with hydrogen correspondingly diffusing out. Capsules were prepared following the same method outlined above, but were 2mm rather than 3mm in diameter to limit empty space within the sealed capsule, and platinum was generally not used as capsule material - its advantage (for the added expense) being a high melting point which was not necessary for the range of exchange experiments carried out. Each capsule contained 5µl D_2O and 10-15 polished synthetic crystals.[4] In some exchange runs (denoted with $^+$ in table 4.4), dry forsterite powder (created from high purity oxide powders) or small, unpolished, forsterite crystals from the same synthesis were used to fill space in order to prevent the capsule crumpling under pressure. Where unpolished crystals were used to fill space, the polished crystals (of interest) and D_2O were separated from the unpolished filler crystals by thin gold foil.

The approximate length of time of each exchange experiment was determined using published hydrogen diffusion coefficients from Du Frane and Tyburczy (2012) in order to allow the deuterium-hydrogen exchange to proceed just enough to give a measurable concentration change over a depth of approximately 2µm. For exchange

---

[4] A balance between how many crystals it was feasible to polish - each took approximately 1hour - and ensuring a sufficient number of grains for each temperature were available for analysis.

runs at 500°C - 700°C this duration is 600s. Experiments at temperatures in this range were run at high pressure conditions in the piston cylinder. Prepared capsules were loaded into the piston cylinder assembly (as described in section 3.1.1) and subject to a pressure of 2GPa for the duration of the run. For temperatures above 700°C, the run time required is less than 300 seconds. Due to the safety limitations of the piston cylinder, reaching such temperatures fast enough to prevent significant diffusion occurring before reaching the target temperature was not possible. Instead, these higher temperature experiments were run at ambient pressure in air in a gas furnace heated to the required temperature prior to inserting the capsule. Capsules for these experiments were prepared with long, flattened ends to allow for expansion of air trapped inside the capsule during heating (as the capsule is not under any pressure constraint). In both piston-cylinder and furnace runs, temperature was continually monitored and adjusted if necessary, and samples were quenched after the appropriate duration. Exchange run capsules were carefully opened to recover the forsterite crystals, and those in which the polished face was clearly identifiable were stored in glass vials until mounted for analysis.

In addition to the D-H exchange runs on H-forsterite grains, two H-D exchange runs were carried out on the synthesised D-forsterite grains (both in the furnace, at ambient pressure). One (EF3) was run for 1hour at 600°C in order to allow a full H-D exchange and one was run at for 300s at 800°C. Table 4.4 lists the D-H exchange runs that were carried out.

4.2.5 Wadsleyite

Wadsleyite is a high pressure polymorph of forsterite, found in the mantle transition zone (see figure 1.1). Six hydrous wadsleyite crystals 150µm-200µm in size that had been previously synthesised by G. Bromiley (using a 10,000tonne kawaii-type multi-anvil press at the Bayerisches Geoinstitut, Bayreuth, Germany) were used as the starting material for this study. To obtain data on hydrogen diffusion in wadsleyite, the aim was to perform D-H exchange experiments for several temperatures, following the same procedure as for forsterite. However, due to the limited number of samples, and the increased potential for loss during PC runs, it was decided to run these at ambient pressure in a gas mixing furnace (as for forsterite runs EF#). Of the six crystals supplied, five were successfully polished (same procedure as for forsterite - see section 4.2.3) and recovered. These were loaded into two $Ag_{70}Pd_{30}$ capsules (2mm diameter,

Table 4.4: *D-H and H-D exchange runs carried out using synthetic H-forsterite and H-wadsleyite.*
E(#) runs were carried out at pressure in a piston cylinder.
EF(#) runs were carried out in a gas mixing furnace (in air).

Run #	**Phase**	**Pressure**	**T (°C)**	**Duration**	**Notes**
E1	H-Fo_{100} (S1)	2GPa	600	600s	
E2	H-Fo_{100} (S1)				apparatus failed
E3	H-Fo_{100} (S1)	2GPa	500	600s	
E4	H-Fo_{100} (S1)	2GPa	500	600s	
E5	H-Fo_{100} (S2)	2GPa	600	600s	
E6	H-Fo_{100} (S9)	2GPa	600	600s	
E7	H-Fo_{100} (S2)	2GPa	700	600s	
$E8^+$	H-Fo_{100} (S9)	2GPa	700	600s	
$E9^+$	H-Fo_{100} (S9)	2GPa	500	600s	
EF1	H-Fo_{100} (S1)	0GPa	500	600s	
EF2	H-Fo_{100} (S1)	0GPa	700	300s	
EF3	D-Fo_{100} (S4)	0GPa	600	1hr	
EF4	D-Fo_{100} (S4)	0GPa	800	300s	
EF5	H-Fo_{100} (S2)	0GPa	500	600s	
EF6	H-Fo_{100} (S2)	0GPa	600	600s	
EF7	H-Fo_{100} (S9)	0GPa	700	600s	apparatus failed
EF8	H-Fo_{100} (S9)	0GPa	700	300s	apparatus failed
EF9	H-Fo_{100} (S9)	0GPa	700	300s	
EF10	H-Fo_{100} (S9)	0GPa	800	300s	apparatus failed
EF11	H-Fo_{100} (S2)	0GPa	800	300s	
EF12	H-Fo_{100} (S2)	0GPa	900	300s	
EF13	H-Fo_{100} (S9)	0GPa	1,000	300s	
EF14	H-Wad_{100}	0GPa	500	600s	
EF15	H-Wad_{100}	0GPa	700	300s	
EF16	H-Fo_{100} (S9)	0GPa	500	600s	

Runs E1-E4 and EF1-EF4 were prior to the polishing step being added.
$^+$ *Denotes runs in which either Fo_{100} powder or unpolished Fo_{100} grains were included in the capsule.*

flattened end design as for forsterite D-H exchange runs EF#), each with 0.5µl D_2O. One capsule was run at 500°C for 600s (EF14) and the other at 600°C for 300s (EF15). The low pressure reversion of wadsleyite to forsterite is reported between 800°C and 900°C (Inoue et al., 2004); therefore care was taken to stay at lower temperature. Of the five wadsleyite crystals polished and included in D-H exchange runs, three were successfully recovered from opened capsules and mounted for SIMS analysis.

4.2.6 D/H standard

In order to provide a reference point, and constrain the background deuterium during analysis, a basaltic glass containing quantified proportions of both deuterium and hydrogen was created for use as a standard. The glass was prepared from sintered powder of JB1, a Japanese basalt standard used in SIMS, provided by Cees-Jan de Hoog (Edinburgh Materials Micro Analysis Centre). 0.05802g of powdered JB1 was weighed in to a 3mm Pt capsule along with 1µl each of liquid D_2O and de-ionised H_2O - resulting in a basalt mixture containing 2.1wt.% D_2O and 1.7wt.% H_2O. Following the same procedure as described for exchange experiment capsules, the capsule was welded shut, checked for leaks, and loaded into a piston cylinder assembly. The sample was subjected to 1500° at 2GPa for 1 hour, then quenched to prevent any crystallisation. The recovered glass was broken into fragments and polished, then mounted alongside the samples. Calculated weight percentages of deuterium and hydrogen were compared to other known standards and the glass served both as a known deuterium rich sample for setting up the analysis, and as a standard for calibrating and quantifying deuterium in forsterite samples.

As noted by Du Frane and Tyburczy (2012), the SIMS hydrogen sensitivity is different in basaltic glass compared to olivine, and therefore a more ideal standard would be an independently characterised deuterated olivine. Attempts were made to synthesise D-forsterite crystals (table 4.2) for this purpose, but as discussed crystals produced were small (consistently less than 100µm) and were therefore not suitable. Measuring the absolute concentration of deuterium with a high degree of accuracy is not critical to this study (as the shape of the diffusion profile is independent of concentration), but for future studies a deuterated olivine SIMS standard is to be recommended.

4.3 Analytical procedure

4.3.1 Sample preparation

Sample preparation is particularly important due to the small grain sizes involved and the increased difficulties encountered when measuring a highly mobile element such as hydrogen. As previously noted, H-forsterite crystals were polished prior to D-H exchange (and not after) and, as a result, some samples were not of sufficient quality for SIMS analysis. Additionally, due to the small nature of the samples (100-200μm average size), mounting with the polished face in the appropriate orientation was challenging (some samples were lost and some, once mounted, did not have an identifiable polished face). Although care was taken to mount multiple samples from each experimental run, the return rate was variable, and it was therefore not possible to obtain reliable data at every temperature for the samples available.

Recovered crystals from exchange experiments were mounted in indium for analysis. Indium is an ideal mounting medium for analysis of small crystals, especially where measurements of hydrogen are required, as it is soft enough that samples can be gently pushed in without damage, and - unlike epoxy-based compounds - it does not de-gas hydrogen (that would significantly increase background signals).[5] To prepare the mount, indium pellets were melted in an aluminium holder with a central well on a hot plate at approximately 170°C (the melting point of indium is 156.6°C). The indium was allowed to cool and then pressed to ensure that it fills the entire well and has a flat top surface. Each sample is placed into the indium by hand (under a binocular microscope) with the polished face upwards and pressed in carefully using a small press and sheets of melinex to prevent sticking. Multiple grains from each experimental run were mounted, alongside standards (the DH glass described above, and a samples of dry olivine). High magnification reflected light images[6] of individual grains were taken to allow the position of analysis pits to be recorded and images were also taken of the whole mount to create 'maps' to aid navigation and identification of samples during analysis (see figure 4.5).

---

[5] Additionally, samples can be easily retrieved from the indium following analysis, if necessary.

[6] Taken using a Leica DMLP reflected/transmitted light polarizing microscope, within the School of Geosciences Optical Microscopy Facility.

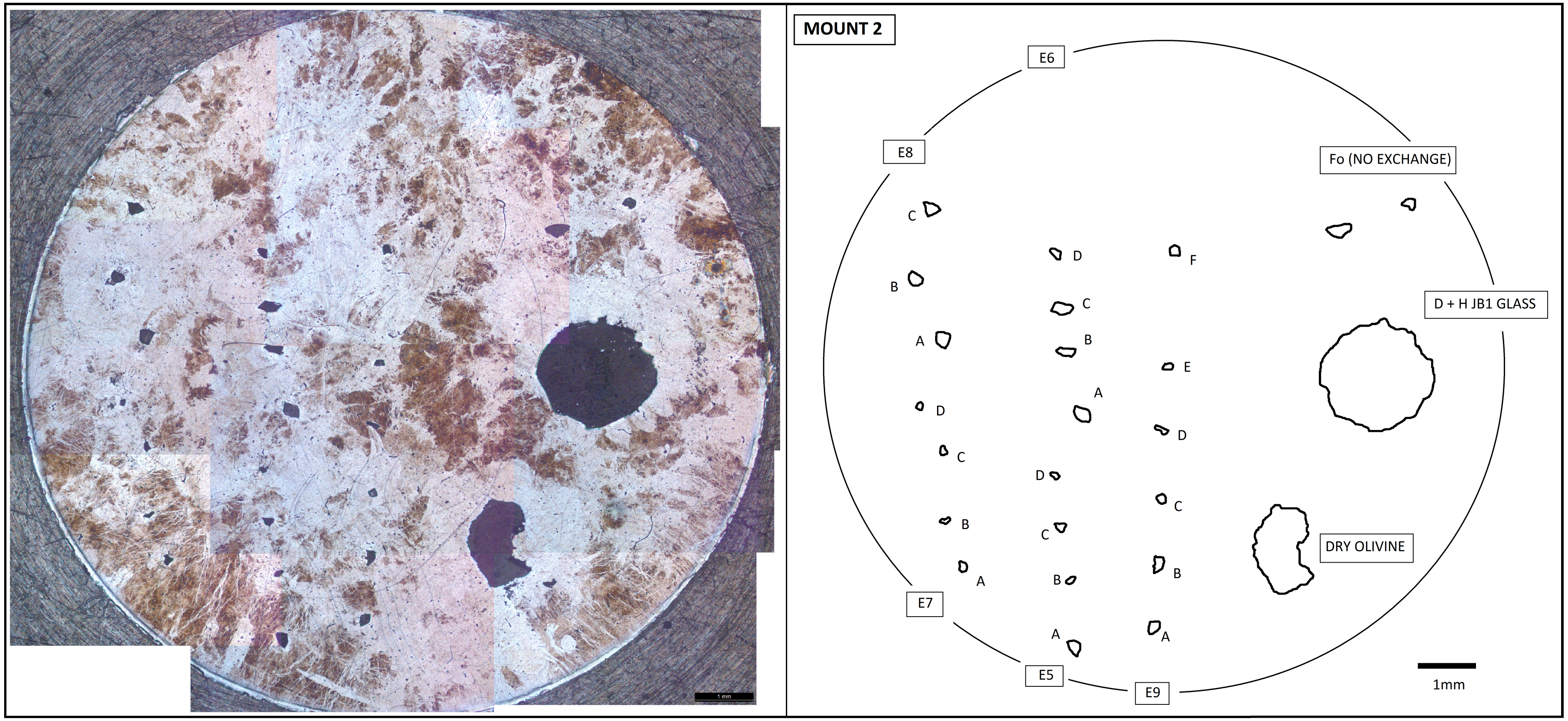

Figure 4.5: *Example of a reflected light image showing forsterite crystals mounted in indium for SIMS analysis (left) and and outline 'map' created of the same mount to aid navigation during analysis (right). Grains from the same exchange run (same temperature) are mounted in vertical rows in order to aid identification. Black bar is 1mm in both images, field of view approximately 1.5cm.*

4.3.2 SIMS Analysis

SIMS analysis of the mounted samples was carried out on the Cameca ims 4f Ion Probe at the Edinburgh Materials Micro Analysis Centre (EMMAC). Each mount was coated in a thin (approximately 30nm) layer of gold and loaded into an air lock chamber in the instrument (the air lock accommodates several mounted blocks, that can then be moved in and out of the analysis chamber while maintaining the instrument vacuum). In addition to being important for conversion to absolute values, the D-H basaltic glass standard was used to help identify and set up the detectors with the relevant species peaks for analysis - particular care was required to ‘find’ and set up the deuterium peak accurately as it is very close to the 2H peak (peaks are distinguished by subtle differences in mass). Figure 4.6 shows the resolution of the two peaks - these can only be well distinguished on a sample containing substantial amounts of both hydrogen and deuterium. Inaccurate resolution of the peaks leads to the deuterium count including both species, resulting in an inflated signal.

When the project was initially designed, the expectation was to carry out the analysis by allowing the ion probe beam to ‘drill down’ in one spot on the sample surface, collecting and counting sputtered atoms with depth through the sample. However, as discussed in section 3.2.1, material can be ‘dragged’ in to the analysis pit from the edges of the crater created by the beam, resulting in an anomalous concentration profile and leading to an over estimation of the diffusion coefficient. In order to prevent this the instrument must be set up to raster the beam, creating a large analysis pit from which data are only collected from the centre.

In suitable samples from this study, this technique of ‘true’ depth profiling was used. However, a combination of poor quality surfaces and small grain sizes meant that many grains were not suitable - single spot ‘drill down’ profiles were measured on these grains to provide a comparison (as discussed further in section 4.6) but the data from these single pits are not useful as quantitative analyses because the crater edge effect is difficult to quantify. None of the wadsleyite grains were suitable for the ‘true’ depth profiling technique due to their small size.

Following the analysis by SIMS the samples were imaged in detail using the Carl Zeiss SIGMA HD VP Field Emission Scanning Electron Microscope (SEM) that is also part of the EMMAC facility. High magnification images of the sample surfaces and analysis pits were taken (using SE mode, see section 3.2.4) to allow

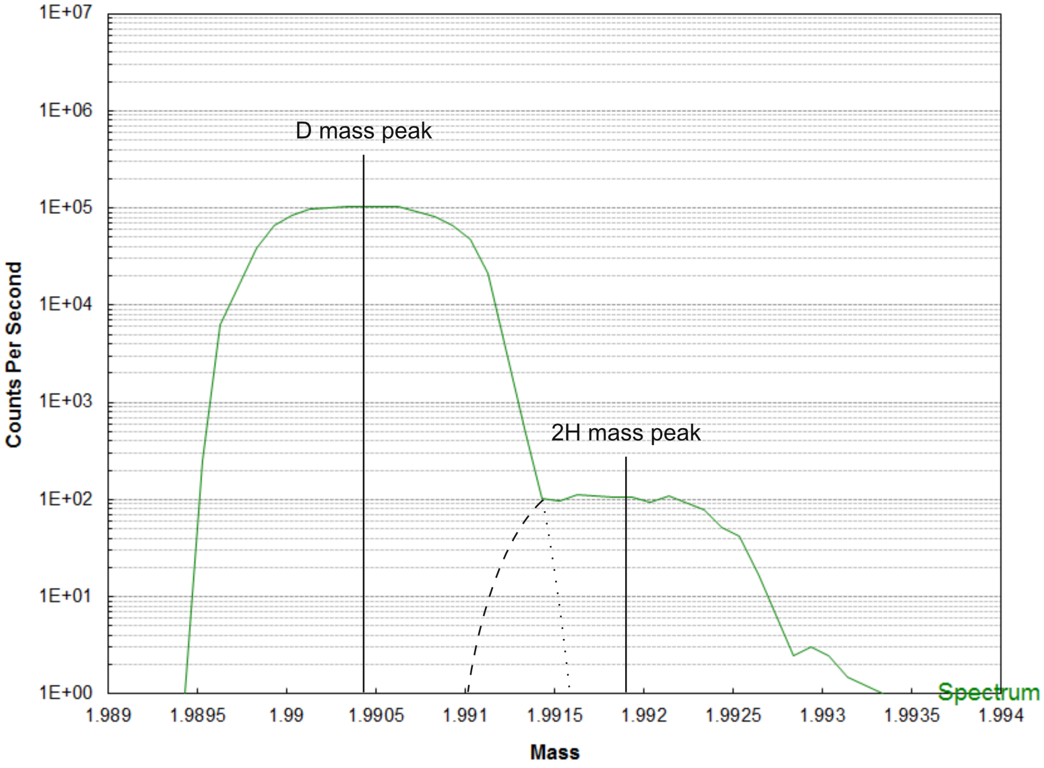

Figure 4.6: *SIMS spectrum showing the SIMS signal obtained in the mass range of 2H and D. The peaks overlap slightly, and care must therefore be taken to resolve the D peak before analysis is carried out in order to count only D, not 2H (the magnet is set up with the relevant mass value for the centre of the peak).*

characterisation of the depth profiling pits (see figure 4.7). In particular, samples were carefully checked for any evident cracks or inclusions that might have had an influence on the incorporation and diffusion of hydrogen and/or deuterium.

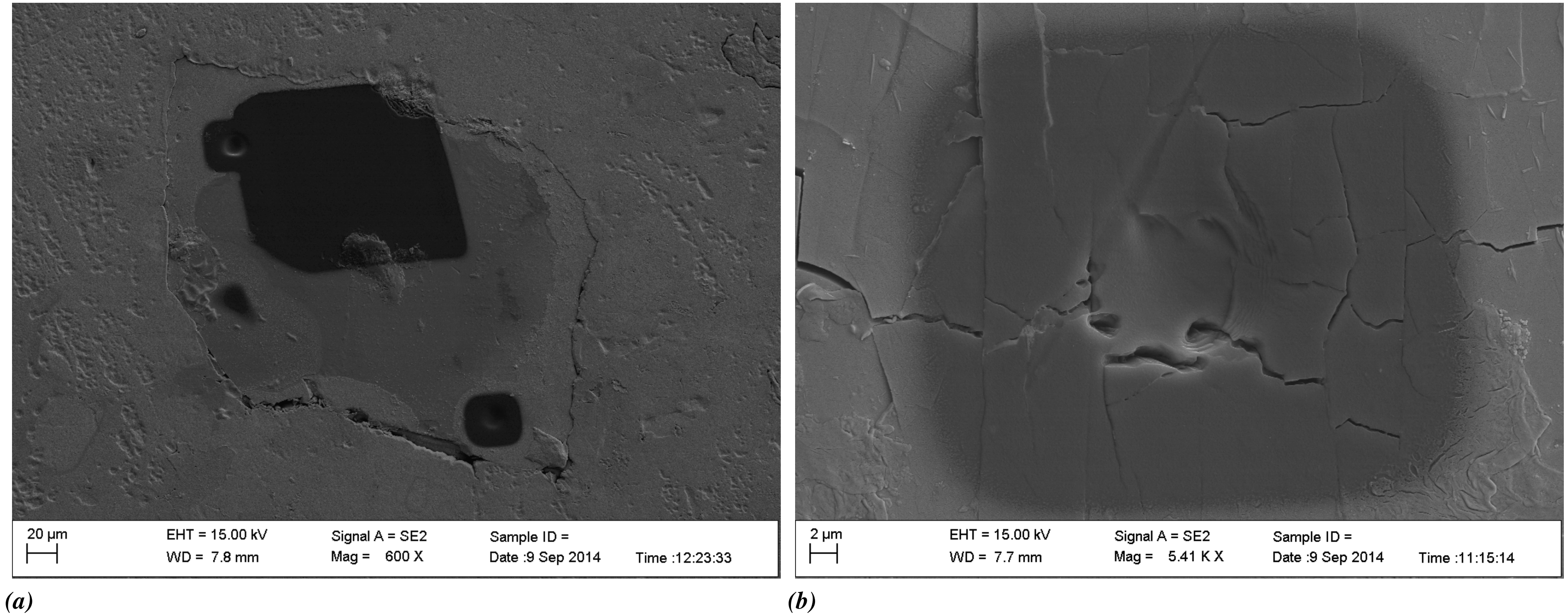

Figure 4.7: *(a) SEM image of H-forsterite grain E6_A showing the full depth profile pit (top left of the grain), as well as two small pits where the beam has just drilled down in one place (following an initial surface raster of approx. 20µm - represented by the darker square outline around the pits); (b) close up of a small pit on EF15_A (wadsleyite grain), showing cracks in the surface. Note the variation in surface quality. Text below images shows standard SEM set-up parameters for SE analysis.*

4.3.3 White light interferometry

Due to the destructive nature of the SIMS technique, with data continuously collected as the beam drills down through the sample, the depth of the resulting analysis pit is equivalent to the length of the concentration profile for the species being analysed. As a result, in order to quantify the depth-concentration (and hence diffusion) profiles, the morphology (specifically depth) of each pit must be measured. As the single pits (drill down spots) are small (<20µm), the most suitable method is to use white light interferometry (WLI) to obtain a 3D map of the sample surface.

For this study, depth measurements of the SIMS analysis pits was carried out using a Zygo white light interferometer housed in the School of Engineering, University of Edinburgh. The mounts used for SIMS analysis were given a second gold coat approximately 30nm thick (to ensure maximum possible surface reflectivity, but also to ensure the insides of the SIMS pits were coated, in as far as that was possible) and placed on the stage of the Zygo instrument. The light intensity and image focus were adjusted using *MetroPro* software in order to produce clearly visible interference fringes. Best results are obtained when a low number of fringes are visible, but this was not always possible to achieve due to sample surface topography. The instrument was set up to take a 10µm depth scan at either low or normal resolution (depending on the quality of the sample surface). Settings were adjusted for individual pits and often several scans were carried out in order to maximise the coverage and quality of data for each individual profile. With precise adjustment of the focus and reflective fringes, the large depth profile pits were relatively easily imaged, as were a reasonable number of the smaller pits.

The resulting surface topography data files were manipulated using the open source data analysis software *Gwyddion* to produce 3D images of the pits, as shown in figure 4.8 for one of the large pit depth profiles. Although the pit floor has some topography, the application of the electronic gate during collection means that the distance corresponding to the concentration profile is that from the centre of the pit to the crystal surface. In the narrow single pits, the pit floor topography is not substantial - although it is also more difficult to get reasonable data coverage for these as it is harder to detect reflected light from the bottom. This is illustrated in figure 4.9 which shows the topography shaded by height on grain EF11_A - the white areas are where there are no data available.

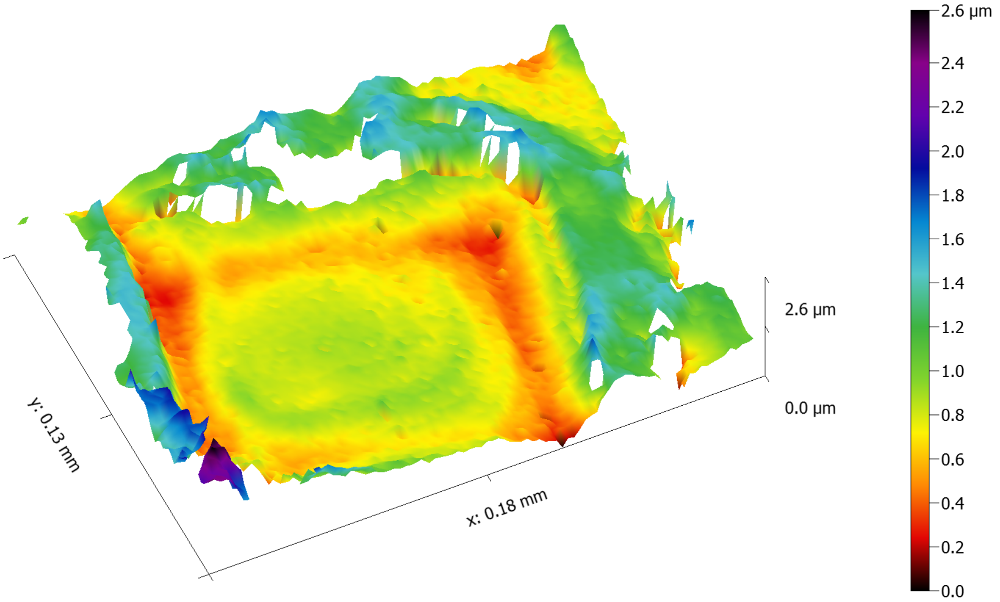

Figure 4.8: *False colour 3D image showing the full depth profile SIMS analysis pit on forsterite grain E6_A. The deeper sections to the sides of the pit are a result of the rastering beam changing direction - the beam remains at the edge slightly longer as this occurs and therefore sputters more material from these areas.*

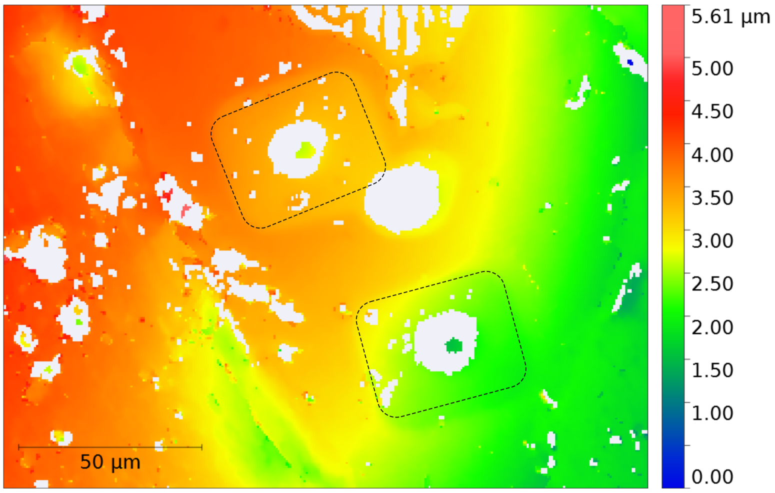

Figure 4.9: *Topography shaded by height for H-forsterite grain EF11_A (WLI data). Two single pit sites can be seen as approximately 30µm square marks (highlighted with black dashed outline) with circular areas in the centre. White areas indicate where no data is available - this is primarily due to a lack in reflectivity and is common in the small profile pits due to their morphology (narrow with relatively steep sides).*

For the large depth profile pits, 15-20 height profiles were taken across the pit, and the depth from the averaged pit edge height to the depth in the centre of the pit was measured (both using the in-built 'fit step height' function in *Gwyddion*, and by plotting profiles and manually measuring the depth). An average of the depth values was calculated, and this was used as the distance measurement for the relevant concentration profile. For both depth profile pits, the average depth was less than 0.5µm. Table 4.5 lists the average values for each DP pit, along with the miniumum and maximum depth values which were used to calculate the corresponding error on the resulting D_H values (see further discussion in section 4.6). For the small analysis pits that it was possible to measure, substantial variation in the depths was found, with no clear correlation between the number of cycles (essentially analysis time) and the resulting depth. This is likely due to inconsistencies in the SIMS beam and sputtering rates, in addition to variations in the sample surfaces.[7] The fitting of data from some of the spot profiles (also including those for which depths were not obtained by WLI) is therefore based on an approximation of depth.

Table 4.5

	Depth (µm)		
	Minimum	Average	Maximum
E6_A	0.298	0.491	0.684
E8_A	0.287	0.401	0.513

---

[7] It is not uncommon in diffusion studies to analyse only a small number of pit depths in order to calibrate sputtering rates - this finding suggests that, where possible, more care should be taken to identify individual pit depths more accurately.

4.4 Fitting data

Due to the shallow nature of the profiles in this study, the diffusion of hydrogen/deuterium through the structure of forsterite can be modelled using a one-dimensional solution to Fick's second law, assuming a species diffusing from an infinite source into a finite sink (Carslaw & Jaeger, 1959). This can be expressed as:

$$C = 1 - erf\frac{d}{2\sqrt{D_H t}}C_0 \tag{4.3}$$

where C (y data) is the concentration of the diffusing species at a given point in the crystal, d (x data) is the distance (m) of that point from the source (essentially distance from crystal edge), D_H is the diffusion coefficient (m^2/s), t is the duration of the D-H exchange experiment (s) and C_0 is the concentration of the diffusing species at the source-sink interface (crystal edge).

Using the data obtained from WLI measurements, depths for each pit were correlated with the concentration data obtained from the SIMS analysis, assuming a near constant sputter rate of material (such that if 100 points are collected over a 100nm distance, each point is 1nm apart). The resulting distance-concentration data for each sample was fitted to equation 4.3 using standard non-linear regression analysis, in order to determine C_0 and D_H values. This was done using both the commercially available curve-fitting software *DataFit*, and a *Python* script using the *curve_fit* fuction from the Scipy library.[8] *DataFit* was originally used to fit the data, but due to the number of profiles (and the expectation to develop the method and therefore carry out further analysis and fitting in the future) the *Python* script was written such that the data and parameters input can be manipulated for ease and legerity.

Fick's law is entered in the form:

$$y = (1 - erf(x/(2*((D*600)**0.5))))*C \tag{4.4}$$

---

[8] The *Python* script used is given in appendix A.

and initial estimates of both D_H and C_0 are specified (note that $**$ represents exponentiation in python notation). The x-y (C-d) data for a given profile is entered and the values of D_H and C_0 that yield the best solution are calculated. In most cases, a solution was found using the initial values $D_H = 1$ x 10^{-15} and $C_0 = 500$, although for a few of the single pit profiles, the values had to be varied (reduced) in order to find a solution. The solutions obtained were plotted alongside the original distance-concentration data for each profile, in order to visualise the quality of fit - in all profiles that were fit using both methods, the resulting value of D_H and C_0 were the same.

Due to the inherent assumptions in Fick's law, and the nature of the curve-fitting program/s, the fit always finds a best fit that drops to zero before flattening out/tailing off. Therefore, in order to obtain better visual fits, the data were artificially shifted to a zero baseline by subtracting the average of the last 10 analyses of the profile from each data point. This is a valid treatment of the data as ultimately it is the fit to the shape of the profile that is important in determining values of D_H. In addition, it was found that the typical baseline was 10-20ppm deuterium, which is within the error of the instrument sensitivity to deuterium, and/or may indicate background values or some instrument artefact. Figure 4.10 shows a 'fixed' data set (baseline adjusted to zero) and fit, along with an unaltered fit for the same profile. Note that the deuterium concentration values (ppm) are artificial as a result.

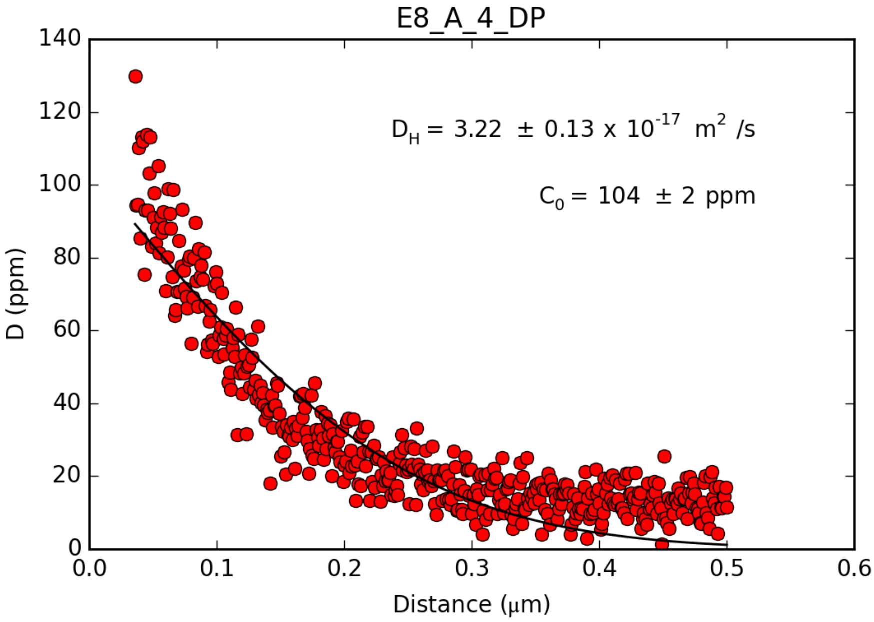

(a)

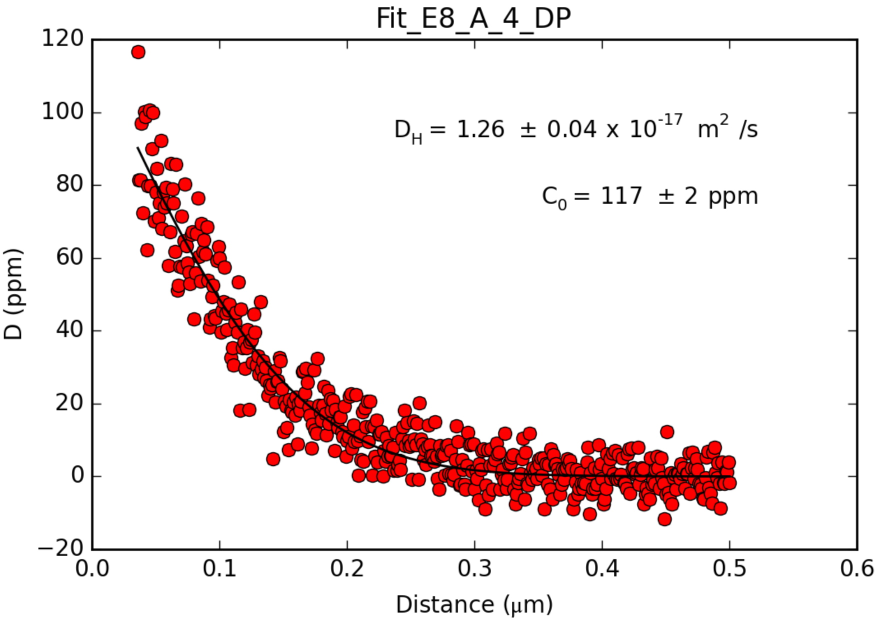

(b)

Figure 4.10: *Plotted data for full depth profile analysis on H-forsterite E8_A (a) without adjustment, (b) with the average of the last ten values removed from all values, so that the profile tails out at zero concentration. Red circles indicate data points, black line indicates plotted solution for Fick's law, as calculated by the Python script. Corresponding values for the fitted parameters* D_H *and* C_0 *are given.*

4.5 IR Spectroscopy

IR spectroscopy is a useful method of obtaining structural data in order to characterise specific water/hydrogen defects present in mantle minerals. As previously alluded to, the incorporation and diffusion of hydrogen is influenced by many factors, the mechanisms of which are still poorly understood. Recent work on untangling the discrepancies between different studies has highlighted the importance of the crystal defect structure, that is, the mechanisms of hydrogen incorporation in the crystal structure and its distribution between different incorporation sites. It has been suggested that the defect site at which hydrogen sits in a sample of olivine/forsterite, and the extent of coupling between interstitial hydrogen and other defects, has a significant influence on the measured hydrogen diffusivity in that sample (Karato, 2013; Padrón-Navarta et al., 2014) and that, as a result, for a diffusion coefficient to be meaningful it must explicitly correspond with a known defect chemistry. This added level of complexity when determining hydrogen diffusion in forsterite (let alone olivine) emphasises the need for a variety of approaches and techniques to be combined in order to approach an understanding of diffusion phenomena. As cautioned by Padrón-Navarta et al. (2014);

> *"water profiles in NAMs obtained exclusively by bulk techniques (such as SIMS) lack the structural information ... and are therefore not sufficient to unravel the complexity of water diffusion".*

A number of previous studies have investigated hydrogen incorporation in forsterite/olivine using structural techniques. Therefore, to compare more accurately the results obtained in this study, measurements were undertaken to characterise the defect structure and OH defects present in the synthetic H-forsterite (both pre- and post- D-H exchange runs). The concentration of OH defects stable within a crystal lattice is dependent on the local thermodynamic state (Mackwell and Kohlstedt, 1990) and the conditions of synthesis are thus of particular importance. Obtaining structural data for the samples also tests the hypothesis that the defect population produced in crystals synthesised to be H-bearing under mantle conditions (rather than a defect population subsequently imposed by experimental hydration) is more relevant to the study of hydrogen mobility under mantle conditions during in-situ electrical conduction.

To investigate hydrogen diffusion for this study, the region of the spectrum influenced by the presence of structurally incorporated hydrogen in olivine (generally accepted to be 3,400cm^{-1} - 3,200cm^{-1}, Lemaire et al., 2004) can be carefully examined, and the major absorption bands identified and related to previous results published for both natural and synthetic samples. IR measurements for this study were done by FTIR, with assistance from Simon Kohn, using a Nikolet iN10 FTIR spectrometer in the FTIR lab within the School of Earth Sciences at the University of Bristol.

4.5.1 Sample preparation and instrument set-up

Typically, samples for IR analysis are prepared as oriented double-polished wafers of known thickness so that polarised measurements can be taken to determine the absorption in different crystallographic orientations. However, the samples used in this study are not oriented and were not initially prepared to be suitable for IR measurements, having only a single polished face. Due to the small size of the grains and the potential for loss and/or breakage, subsequently polishing the samples to produce double-polished wafers was not feasible. Consequently, the data collected are not quantitative (because the thickness of the sample is variable over the analysis area, the absorption is variable and cannot be calibrated to concentration). However, spectra do provide useful qualitative information on the structure and OH-related defects present.

As IR spectroscopy works by transmitting light through the sample, the first step in preparing the forsterite grains for IR analysis was to remove the opaque gold coat applied for SIMS/WLI analysis. This was done prior to removing the grains from the SIMS mount, by gently buffing the surface with 1µm diamond polishing solution on aluminium foil and then wiping the surface with acetone and de-ionised water to clean. Individual grains were then carefully picked out of the indium under a binocular microscope,[9] and mounted on a glass slide (for transport to Bristol). The sample number of each grain was noted and a separate slide was used for each D-H run (E5-E9 & EF11) to aid identification. Once transported to the Bristol FTIR analysis laboratory, H-forsterite grains were removed from the superglue using acetone, and were rinsed with ethanol and water to remove all traces of both glue and acetone (which produce

---

[9] Indium is sufficiently soft at room temperature that this can be achieved using fine point tweezers and a cocktail stick, avoiding damage to the sample.

CH bands in the IR spectra at around 2,950cm^{-1}, potentially obscuring the peaks of interest). Although care was taken, the small and colourless nature of the grains made this difficult and there is evidence in some grains for absorption peaks resulting from the presence of CH bonds. Some grains were lost during the retrieval process, but all of those retained were individually identifiable and importantly included E6_A and E8_A (for which diffusion coefficients were calculated based on reliable SIMS depth profile data).

In addition to characterisation of the D-H exchange samples, grains of the synthetic H-forsterite (starting material) were also analysed. These were not prepared specifically for FTIR measurements, nor for any previous analysis, but loose crystals with no specific orientation or polished face were analysed to get an indication of the OH defects present (and any variation both between synthesis runs and between synthesis and D-H exchange).

Samples were placed, polished face down where applicable, and loose on to transparent CaF_2 disks and imaged in order to record the position of the individual grains. Disks, contained within a custom sample holder, were then transferred to the instrument chamber, which is continuously flushed with dry purified air. Unpolarised measurements were taken in transmitted light on all samples, using an aperture of 100µm by 100µm. Where possible, analysis points were chosen to avoid cracks and imperfections in the samples, and in a few cases the aperture size was reduced to allow for this. 128 scans at a resolution of 2cm^{-1} were collected during each analysis (one per sample), with a collection time of 22s. As well as unpolarised measurements, polarised spectra were also collected for H-forsterite grains E6_A and E8_A. For these, an aperture of 150µm by 150µm was used (encompassing the majority of the grain surface in both cases) and 256 scans were taken (again at a resolution of 2cm^{-1}). Spectra were collected at 20° intervals of rotation of the polariser (see figure 4.11).

4.5.2 Crystallographic orientation

From the polarised measurements on samples E6_A and E8_A, crystallographic orientations were determined by examining the strongly orientation dependent silica overtones in the region 1,200-2,200 cm^{-}1 (Lemaire et al., 2004). As seen in figure 4.12, the x,y and z directions each have specific associated peaks. As the samples from this study are uncut crystals with randomly oriented original faces (i.e. not oriented in a specific crystallographic orientation), no single pure x,y or z direction was observed. However, the most distinct directions were identified, and used to estimate the principal axis (Asimow et al., 2006; Lemaire et al., 2004). Both samples E6_A and E8_A contain strong z-axis contributions in the two most distinct orientations identified (at 90° to each other), indicating that both crystals are oriented with the z-axis closest to perpendicular to the identified face (see figure 4.13). This suggests that diffusion data collected from these two grains is most equivalent to diffusion along the z-axis, and additionally that the two profiles represent a similar crystallographic orientation.

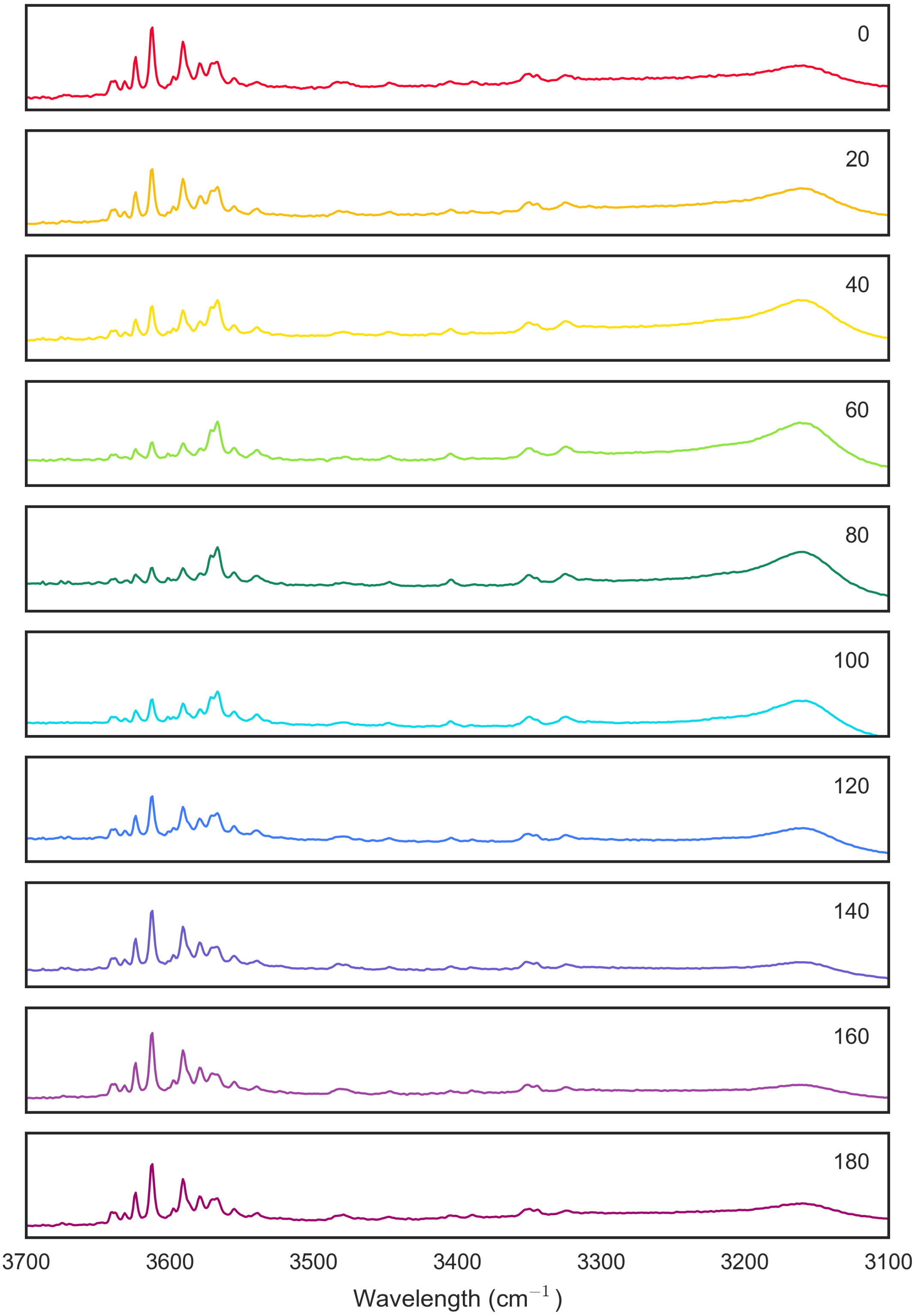

Figure 4.11: *Polarised FTIR spectrum (in selected wavelength range) for sample E6_A taken at 20° intervals of rotation of the polariser. The peak at 3,160cm^{-1} varies in intensity relative to the others depending on the orientation - see further discussion in section 4.5.6.*

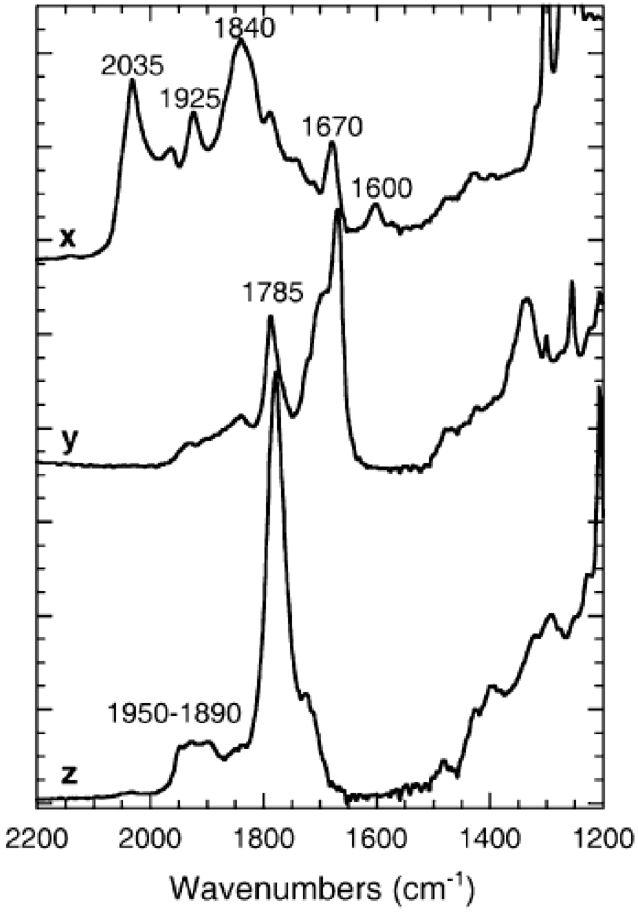

Figure 4.12: *Figure from Lemaire et al. (2004) showing silica overtone peaks in each of the three pure crystallographic orientations, in IR spectra taken on oriented forsterite samples.*

Figure 4.13: *Polarised FTIR spectra for the two most unique directions in (a) E6_A and (b) E8_A, showing orientation dependent silica overtones. By comparison with figure 4.12, a strong z signal (prominent peak at 1,785cm*$^{-}$1*) can be seen in both grains.*

(a)

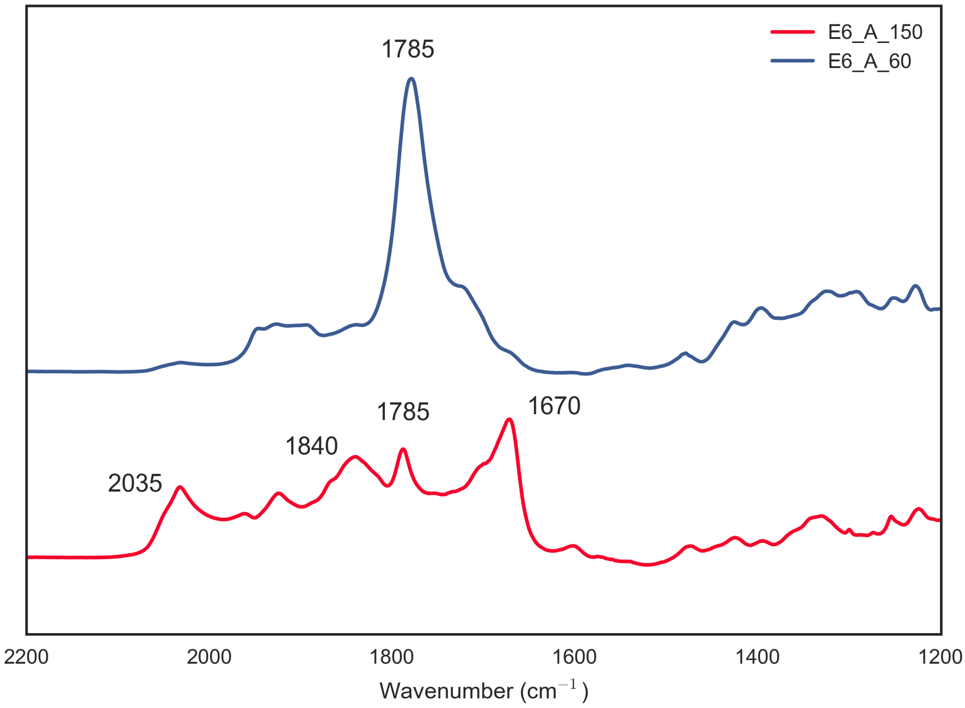

(b)

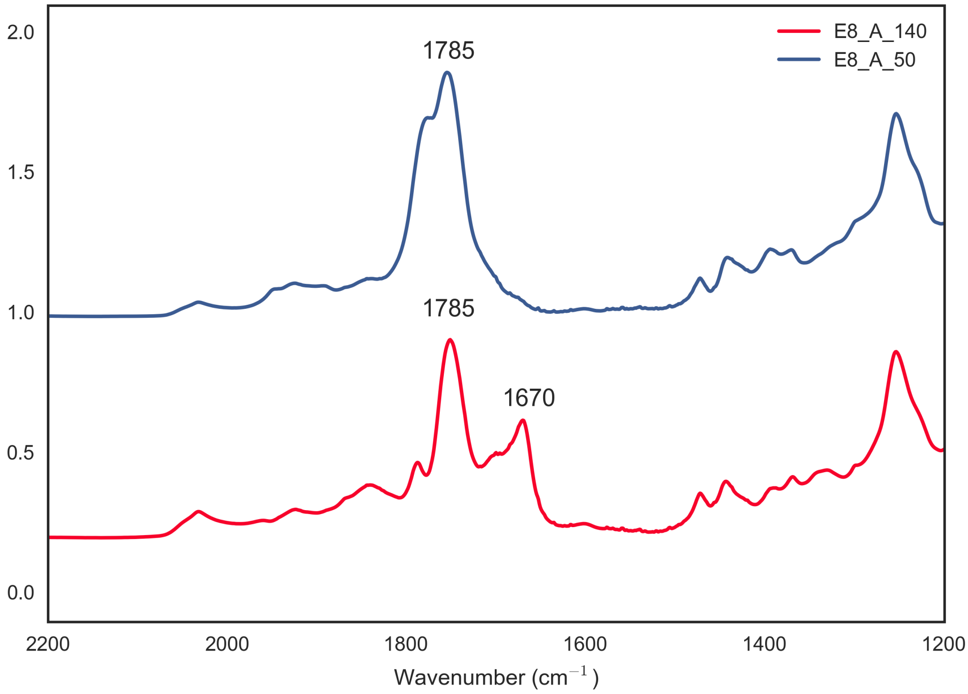

4.5.3 Hydrogen-associated peaks

Absorption peaks as a result of OH groups in forsterite are generally regarded as being in the range 3,700 - 3,100cm^{-1} (e.g. Lemaire et al. (2004)), but the exact positions of the major bands observed differ between various studies and have been attributed to the prevalence of different incorporations mechanisms. The most prominent OH-associated bands observed in samples from this study are between 3,700 - 3,500cm^{-1}, as indicated in figure 4.14.

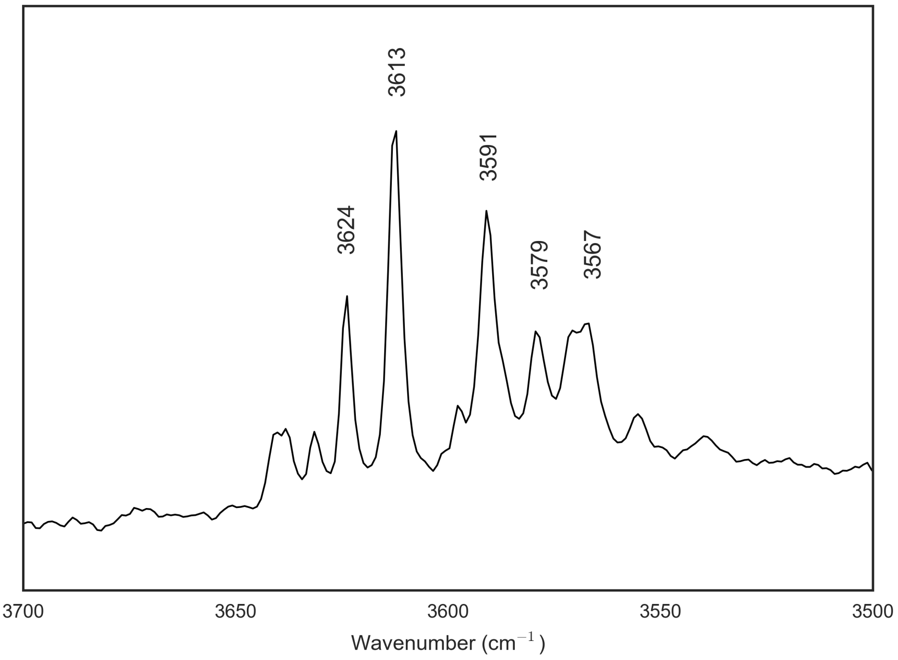

Figure 4.14: *FTIR spectrum for sample E6_A (unpolarised measurement) showing the main peaks in the OH stretching region, typically of the majority of samples from this study.*

4.5.4 Deuterium-associated peaks

While the region of the IR spectrum that is influenced by the incorporation of water/hydrogen in olivine is well studied, the region affected by the presence of deuterium is less so and there are few published studies that discuss deuterium content using spectroscopic methods. During the excitement of atoms in a sample for IR measurements, the frequency of vibration (ν), that gives the band position, is dependent on the contributing masses according to the relationship:

$$\nu = \frac{1}{2}\pi\sqrt{f/\mu} \tag{4.5}$$

where ν is frequency, f represents the forces between the atoms, and μ is the reduced mass (stronger force and smaller mass equate to higher frequency). Thus the deuterium peaks are expected to be represented by a shift (from the location of the hydrogen peaks) to lower frequency by a factor of $\sqrt{\frac{m_D}{m_H}}$ equal to approximately 1.41. In practice, due to the weaker anharmonicity of O-D vibrations compared to strong O-H vibrations, the bond shift is not ideal and instead varies around a value of approximately 1.35 (Libowitzky and Beran, 2004). Peaks resulting from the exchange of deuterium for hydrogen in samples from D-H exchange runs should therefore be visible in the region 2,740 - 2,290cm^{-1} (based on exchange for hydrogen in the region 3,700 - 3,100cm^{-1}) - see figure 4.15.

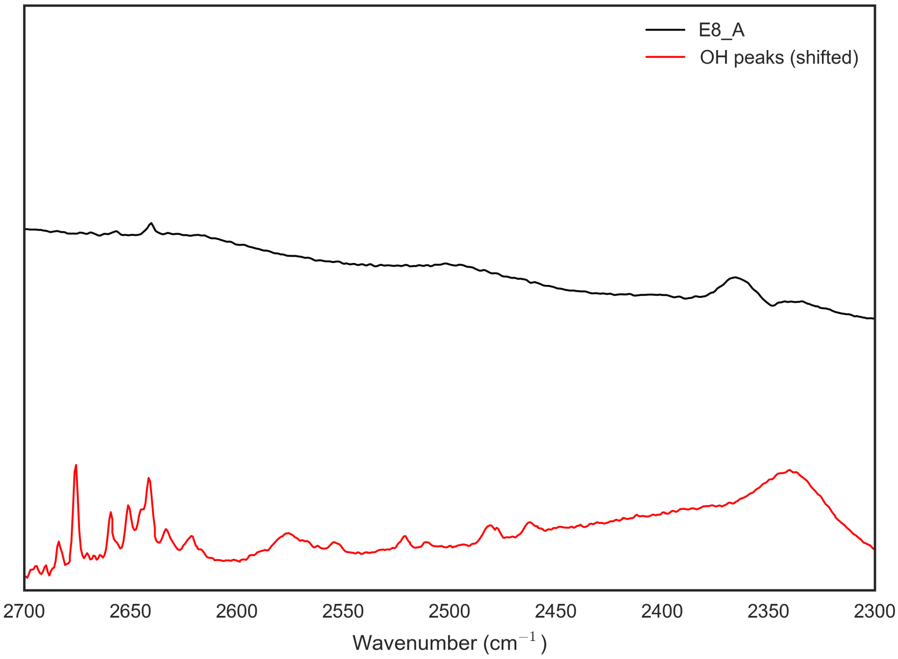

Figure 4.15: *FTIR spectrum for sample E8_A showing the OD stretching region (black line). Shown below (red line) is the resulting position of the peaks from the OH region if a shift factor of 1.35 is applied - the peaks in the OD stretching region are minor in comparison, but there does appear to be some correlation in the positions in this one sample (not seen in any others).*

4.5.5 Characterisation of starting material

Multiple grains from synthesis runs S2, S9, S17 and S18 (all of which produced H-forsterite grains that were subsequently used in D-H exchange experiments) were analysed, as loose, non-oriented, unpolished single crystals. None of the H-forsterite grains from synthesis run S1 were available for FTIR analysis, having all been used in either exchange experiments (or in work by M. Pankhust[10]) and runs S3-S8 & S10-S16 were all unsuccessful (see table 4.2).

Figure 4.16 shows a selection of the IR spectra obtained, and table 4.6 gives the prominent OH bands identified in each synthesis run. There is significant variation in the defects present in samples from different synthesis runs, despite runs being carried out following the same experimental procedure, under almost identical P-

---

[10] H-forsterite crystals synthesised for this project are also being used by M. Pankhurst (and others) at the Universities of Leeds and Manchester in current work to develop a material standard for quantified X-ray attenuation measurements.

T conditions[11] and using the same powder starting material. There appears to be consistency across multiple grains from the same synthesis run indicating relative homogeneity, but some heterogeneity within the capsule cannot be entirely ruled out. Of the synthesis runs, S9 contains the most prominent peaks in the OH stretching region (containing almost all of the peaks that appear in any of the other samples). In contrast, samples analysed from synthesis runs S17 and, in particular, S18 contain relatively few peaks in the main OH stretching region and generally lack any in the region above 3,400cm^{-1}. There are no major peaks that are consistent across all four synthesis runs, indicating that local, potentially minor, changes in the conditions within the synthesis capsule may play an important role in the defect structure of the forsterite crystals grown. This is likely to contribute to the range in deuterium concentration profiles measured in grains post D-H exchange, and while there appears to be some consistency across grains within an individual run (see figure 4.16), it is difficult to be certain there are not minor heterogeneities within each run. In addition, the lack of OH peaks in samples from S17 and S18 may indicate the loss of water from the capsule during these synthesis runs.

---

[11] S2 - 1600C for 1hr then 1200 for several days, S9 - 1700°C for 2hr then 1200°C for several days, S17 - 1700°C for 1hr then 1200°C for several days, S18 - 1700°C for 1hr then 1200°C for several days.

Figure 4.16: *FTIR spectra in the OH stretching region (3,700 - 3,100cm^{-1}) for synthesised H-forsterite grains (none of which have undergone D-H exchange), showing the variability in hydrogen defects present.* ***a*** *- S2,* ***b*** *- S9,* ***c*** *- S17 &* ***d*** *- S18. Note that the absorbance scale (y-axis) varies between plots.*

(a)

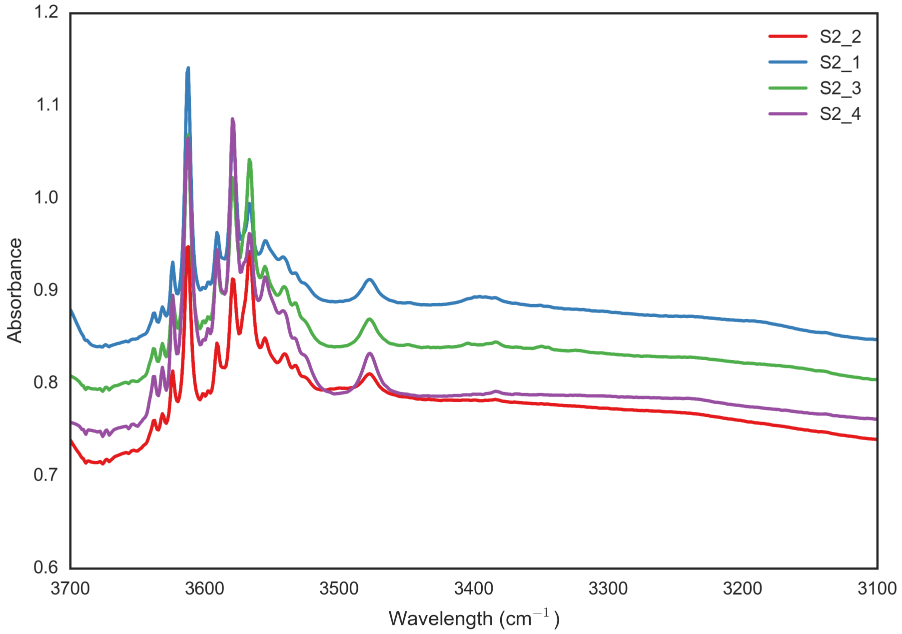

(b)

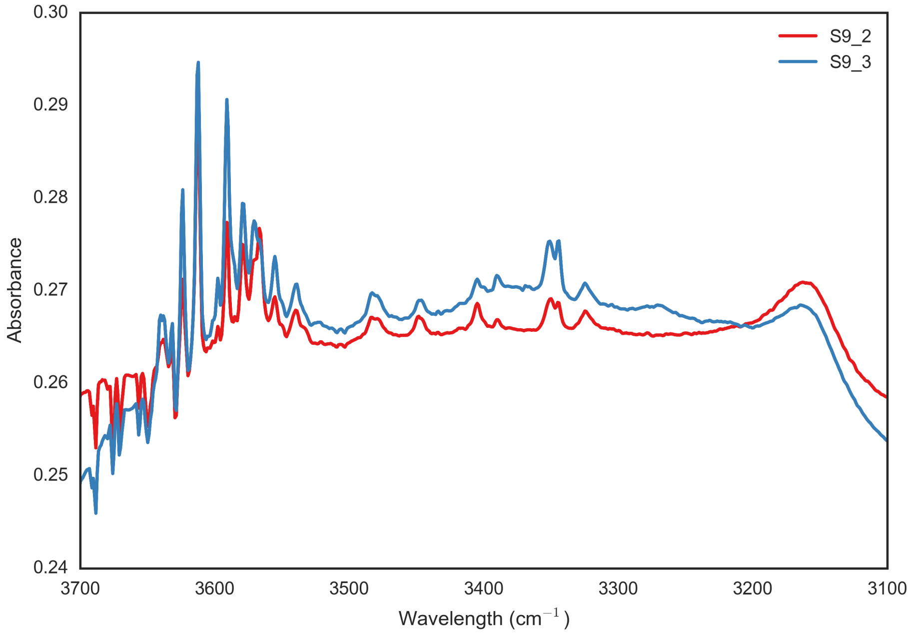

(c)

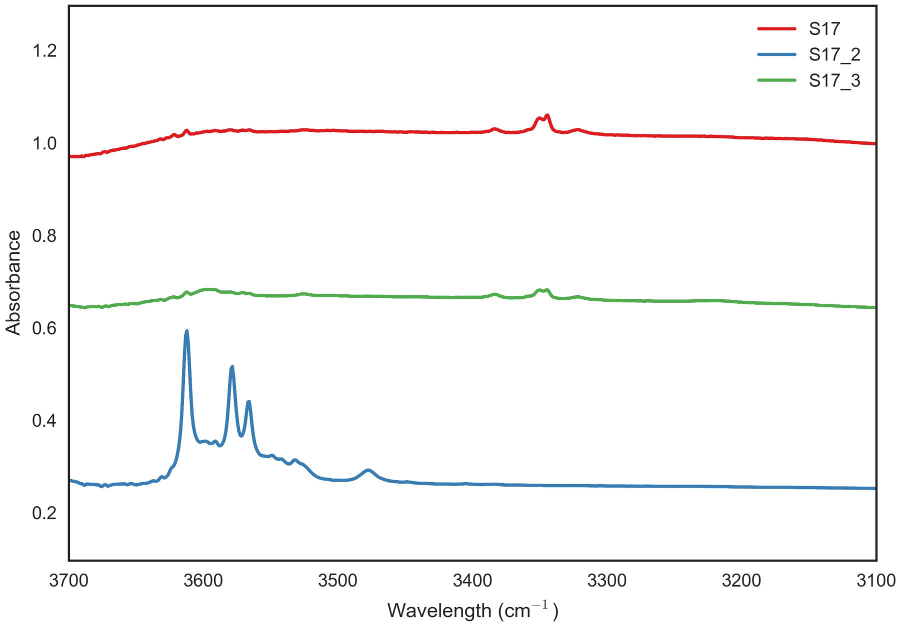
S17
S17_2
S17_3
1.2
1.0
0.8
0.6
0.4
0.2
Absorbance
3700
3600
3500
3400
3300
3200
3100
Wavelength (cm^{-1})

(d)

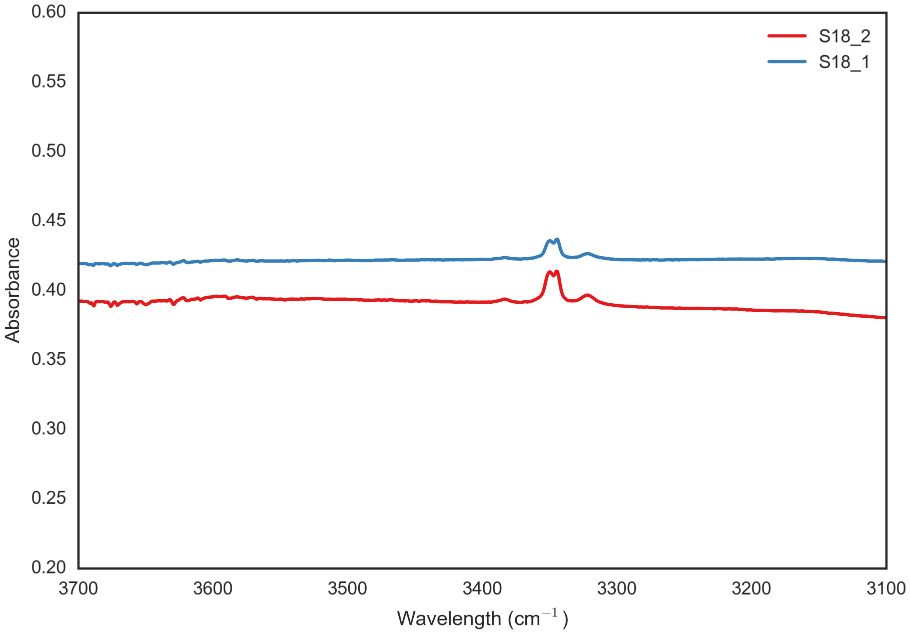
S18_2
S18_1
0.60
0.55
0.50
0.45
0.40
0.35
0.30
0.25
0.20
Absorbance
3700
3600
3500
3400
3300
3200
3100
Wavelength (cm^{-1})

Table 4.6: *FTIR absorption peaks (cm^{-1}) observed in the OH stretching region in H-Forsterite grains from specified synthesis runs.*

S2	**S9**	**S17**	**S18**
3701		3699	
3623	3623		
3612	3612	3612	
3591	3591		3591
3579	3579	3578	
3566	3566	3566	
3554	3555		
	3540		
		3531	
3477	3483	3477	
	3448		
	3404		
3391			
			3383
	3350		3349
	3344		3344
	3324		3321
	3160		
3071			
3051			

Bands at approximately the same location have been grouped together but there are evident differences in the defect populations between synthesis runs.

4.5.6 Characterisation of D-H exchange samples

H-forsterite grains from D-H exchange runs E5, E6, E7, E8, E9 & EF11, recovered from SIMS indium mounts, were also analysed by FTIR. As with the analysis of the H-forsterite starting material samples, all measurements were taken on loose, unoriented single crystals. Table 4.7 gives a summary of the primary OH peaks observed for each analysed sample, and figure 4.16 gives a selection of the spectra obtained with the main peaks highlighted and compared. Note again that, as the samples vary in thickness, no accurate quantification of the amount of H or D present at each site can be made from these measurements.

As shown in figure 4.17, very minor peaks at 2,640cm^{-1} and 2,500cm^{-1} in some samples may be attributed to incorporation of deuterium, although in general the samples that have undergone D-H exchange do not exhibit strong bands in this region. This apparent lack of deuterium in the post D-H exchange samples is most likely a consequence of the fact that, once the whole thickness of the sample is considered, the relative concentration of deuterium is extremely low (as to be negligible).[12] While deuterium is present at 100ppm levels at the crystal surface (as measured by SIMS, see for example figure 4.10), the exchange experiments were specifically designed to yield shallow diffusion profiles and the concentration of deuterium decreases rapidly to approximately 0ppm over diffusion profiles that are < 1µm in length. Considering the total thickness of the sample measured by IR is 50-100µm, it is not unexpected that even the relatively high concentrations of deuterium measured in shallow SIMS profiles are not evident on the majority of IR spectra (taken through the entire grain).[13]

---

[12] In some samples, the concentration of deuterium may also be below detection levels.

[13] Particularly since the SIMS depth profile covers a significant area of the relevant crystal face and removes material down to the depth at which D(ppm) = 0, by design.

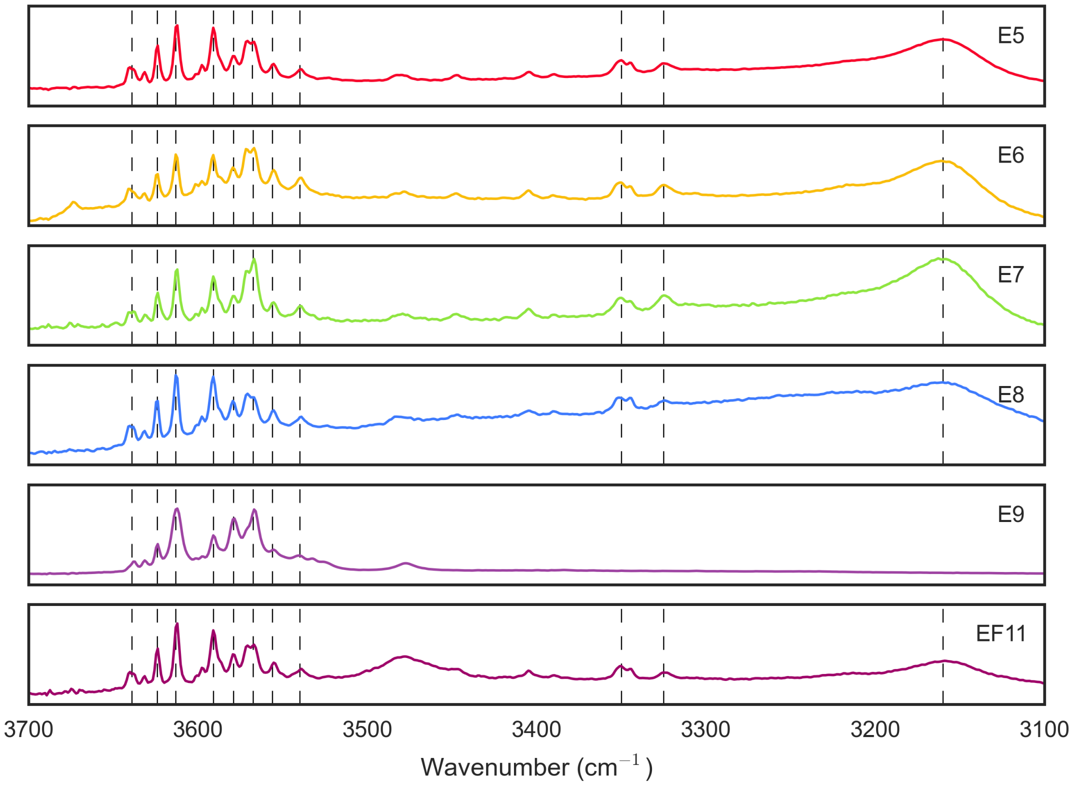

Figure 4.16: *FTIR spectra in the OH stretching region (3,700 - 3,100cm^{-1}) taken from H-forsterite samples following D-H exchange runs. Runs E5(600°C, 2GPa), E6(600°C, 2GPa), E7(700°C, 2GPa), E8(700°C, 2GPa), E9(500°C, 2GPa) & EF11(800°C, 0GPa). Dashed black lines indicate the major OH peaks observed, which are consistent between samples with the exception of E9, which lacks the peaks below approximately 3,500cm^{-1}. Note that the absorbance scale (y-axis) is not consistent and has been adjusted to show the peaks clearly for each example.*

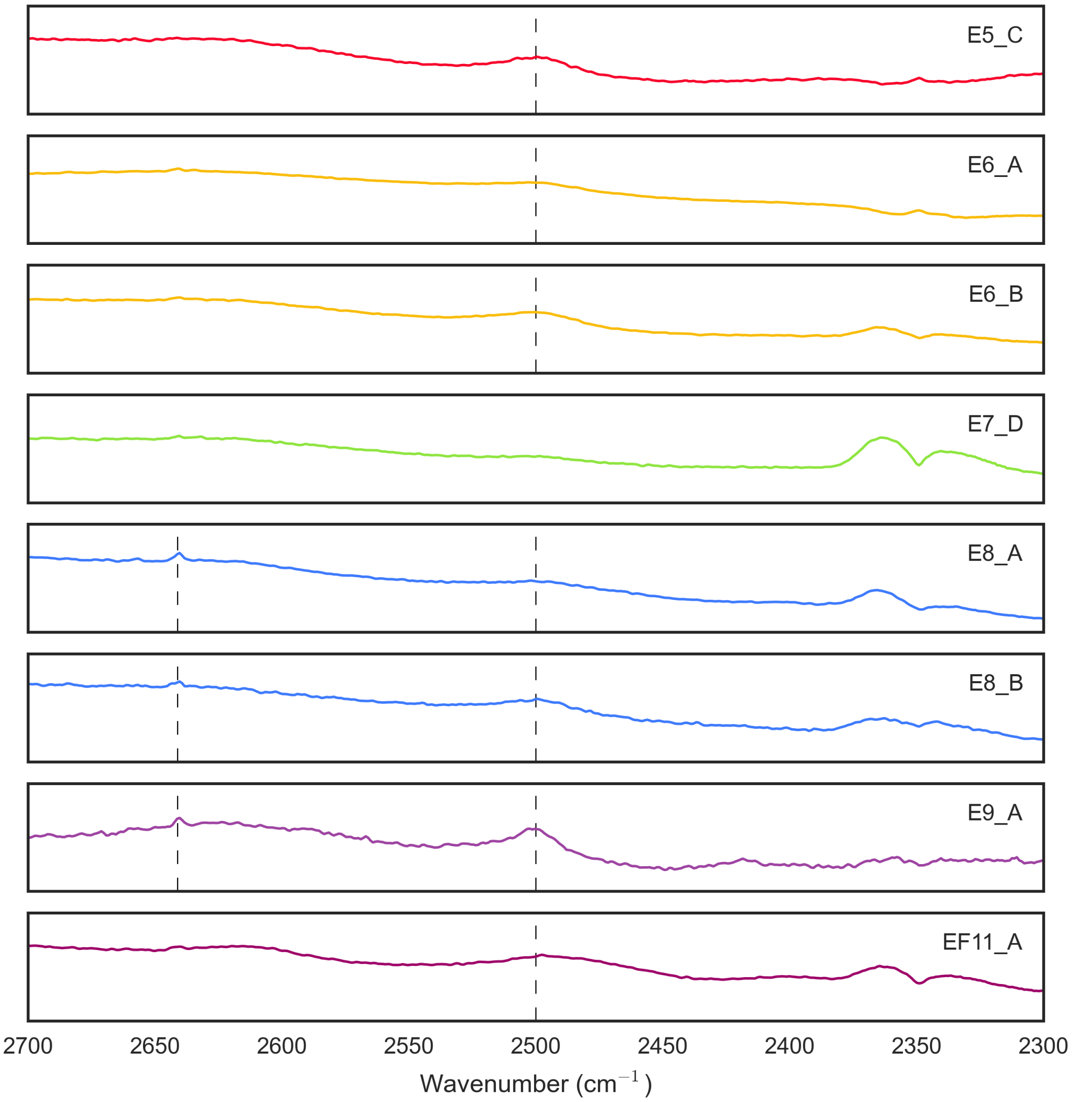

Figure 4.17: *FTIR spectra in the OD stretching region, following D-H exchange runs (as in figure 4.16. Dashed black lines indicate minor peaks, that may represent the incorporation of deuterium. The broad double peak around 2,350cm^{-1} in some samples is more likely to represent contamination of the sample with either the mounting material, or acetone (see further discussion in text). Note that the absorbance scale (y-axis) is not consistent and has been adjusted to show the peaks clearly for each example.*

Table 4.7: *FTIR absorption peaks (cm^{-1}) observed in the OH stretching region in H-Forsterite grains from specified D-H exchange runs.*

E5	E6	E7	E8	E9	EF11
		3671			
3639	3638	3638		3638	3640
3630	3631				
3624	3624	3624	3624	3623	3624
3613	3613	3612	3613	3613	3612
3591	3591	3591	3591	3591	3591
3579	3579	3579	3579	3579	3577
3567	3567	3567	3567	3567	3569
3555	3555	3555	3555		3554
3539	3540	3539	3541	3540	3539
3482	3479	3478	3479	3477	3478
3448	3448	3446	3447		
3404	3405	3404	3405		3406
3389		3389	3390		
3351	3350	3350	3350		3350
	3345		3344		
3324	3324	3324	3325		3323
3159	3161	3162	3157		3158

Bands at approximately the same location have been grouped together.

Comparison with starting material

The variation in OH peaks in H-forsterite grains from different synthesis runs is mirrored in the IR spectra of the post D-H exchange samples. As shown in figures 4.18 and 4.19, the same peaks are seen post-exchage as in the relevant starting material, with no significant change in relative concentration.[14] Comparison of multiple grains from each synthesis pre- and post- D-H exchange suggest that there is no major change in the incorporation sites during the exchange process although, as previously discussed with reference to the lack of deuterium peaks, the shallow nature of the exchange profiles coupled with the whole-grain nature of FTIR analysis means that the detail to confirm this unequivocally is lacking. The consistency in the defects present between pre- and post- exchange run samples indicates that the hydrogen mobility measured relates

---

[14] Although, as previously noted, the IR data from this study are not accurately quantitative due to the varying thickness of the samples.

to all of the OH-associated defects, rather than any subset of them. This confirms the need for detailed structural characterisation, and influences any discussion on the extent to which hydrogen at specific sites has moved and/or exchanged with deuterium - without having identified the defects present in individual grains both before and after, potential heterogeneities in the starting material could contribute to perceived changes during the exchange runs.

The variability in IR spectra between crystals, even from runs carried out under the same conditions additionally alludes to the difficulty in synthesising truly homogeneous samples - due to small fluctuations in chemical environment, conditions within the entire capsule can be inconsistent. This is true of all experimental studies (whether focusing on hydrogen diffusion, D-H exchange, or directly measuring electrical conductivity) and will result in measurements that are essentially an average of hydrogen mobility in grains with subtly different defect chemistries. The variability is likely to be more profound in samples studied under varying pressure/temperature conditions, strengthening the need for approaches, like the one used in this study, that investigate hydrogen mobility in crystals fully equilibrated under high pressure conditions identical to those used for exchange experiments.

Anisotropy

Previous work (e.g. Lemaire et al., 2004) has indicated that some of the hydrogen incorporation in forsterite is anisotropic, with evidence of pleochroism in the IR peaks. Although the samples analysed for this study were not oriented, polarised measurements were taken on E6_A and E8_A. No highly pleochroic absorption bands appear in these samples in the predominant OH stretching region (3,700 - 3,500cm^{-1} for samples in this study), but the peak observed at 3,160cm^{-1} does appear to vary in intensity with changes in the x,y,z contributions (figure 4.20), which may be indicative of some preferential orientation of OH groups. This pleochroism is also observed in H-forsterite grains from synthesis S9, but not other synthesis runs. The nature of the hydrogen incorporation in the synthesised starting material is evidently important for controlling the defects available for D-H exchange.

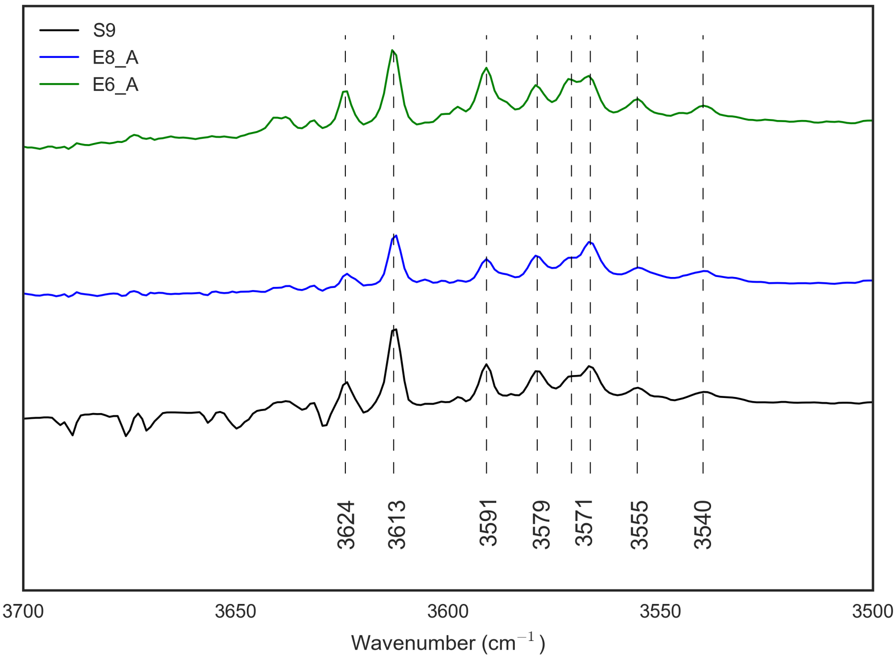

Figure 4.18: *The major OH stretching peaks in H-forsterite samples E6_A (green) and E8_A (red) - having undergone D-H exchange runs - are the same as those present in the pre-exchange starting material S9 (black), used for both runs. Note that although the relative size of the peaks is shown to scale, the actual absorption values are not shown as the spectra have been offset vertically for clarity.*

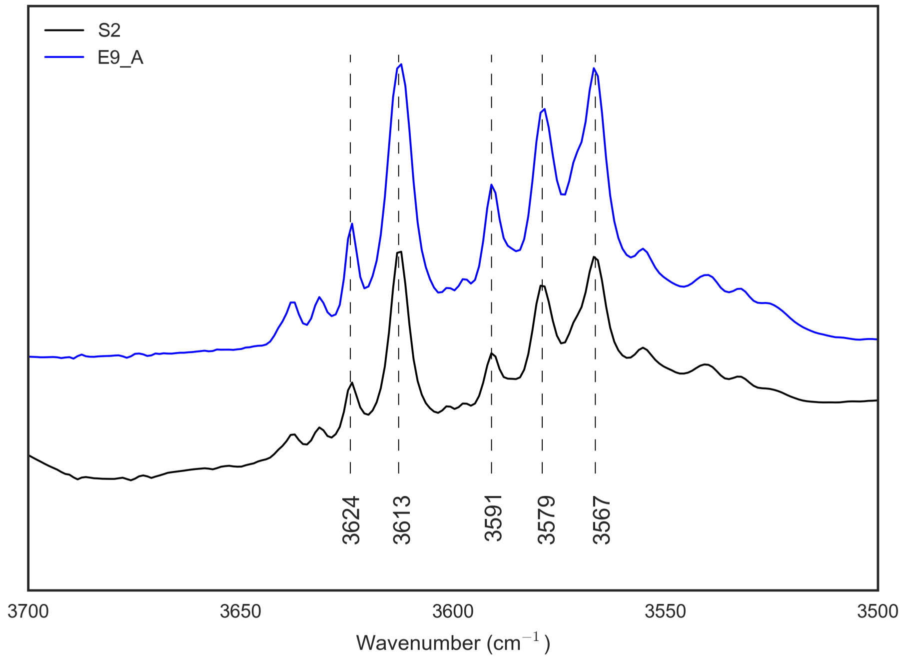

Figure 4.19: *The major OH stretching peaks in H-forsterite sample E9_A (blue) - having undergone D-H exchange - are the same as those present in S2 (black). As in figure 4.18, although the relative size of the peaks is shown to scale, the curves have been shifted to be displayed alongside each other and the actual absorption values are therefore not shown.*

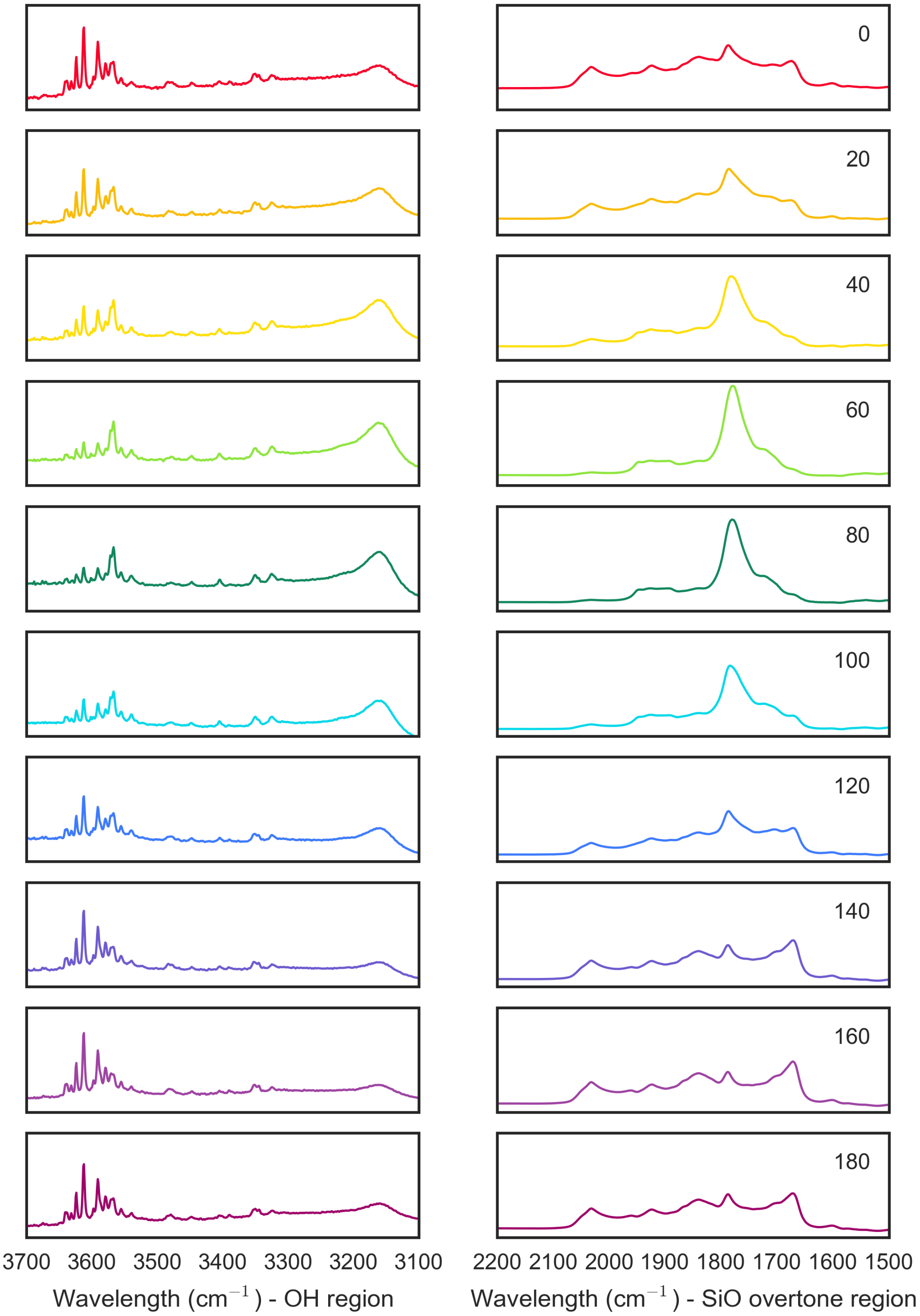

Figure 4.20: *FTIR spectra for H-forsterite E6_A taken at 20° intervals of rotation of the polariser (labelled 0-180). The relative intensity of the peak at around 3,160cm^{-1} (shown in left hand plots) varies with crystallographic orientation (as indicated by the changing SiO overtones in the right hand plot). The peak is largest when the contribution from the z direction (prominent peak at approximately 1,785cm^{-1}) is largest, at 60/80.*

4.5.7 Association of IR peaks with specific defects

Previous studies that have used IR techniques to investigate the incorporation of hydrogen in forsterite have attempted to assign peaks at specific positions to different incorporation mechanisms. Four distinct incorporation sites are generally identified - two associated with the protonation of Si vacancies and two associated with the protonation of Mg vacancies (Berry et al., 2005; Kovacs et al., 2010). Based on theoretical modelling of IR spectra, Balan et al. (2012) separate the incorporation mechanisms and associated peaks as follows;

i [Si] Narrow IR bands at relatively high frequencies (above 3,480cm^{-1}) are generally attributed to the replacement of an Si atom by 4 protons, and are predominant in forsterite samples synthesised under low silica activities (Lemaire et al., 2004).[15]

ii [Ti] The substitution of Ti^{4+} on the M1 site, charge-balanced by a Si vacancy containing 2 protons, is represented by bands at 3,572 and 3,525cm^{-1}.

iii [Mg] Broad IR bands at 3,160 and 3,220cm^{-1} correspond to the substitution of 2 protons on the M1 site.

iv [triv] The coupled substitution of a trivalent element plus a proton for two Mg results in bands between 3,400 - 3,300cm^{-1}.

Based on this correlation, [Si] appears to be the dominant hydrogen incorporation mechanism in both samples E6_A and E8_A (figure 4.21).[16] The bands present are similar to those observed by Lemaire et al. (2004) in samples synthesised under low silica activities, but also contain the 3,160cm^{-1} pleochroic band that they observe primarily in samples synthesised under the highest silica activity conditions (assigned to [Mg]).

---

[15] Note that, alternatively, Smyth et al. (2006) attributed these same peaks to Mg vacancies using x-ray diffraction studies.

[16] These two are the only grains from which data will be discussed in detail here as they are the only two for which reliable diffusion data was obtained - for IR spectra from other D-H exchange runs see appendix B.

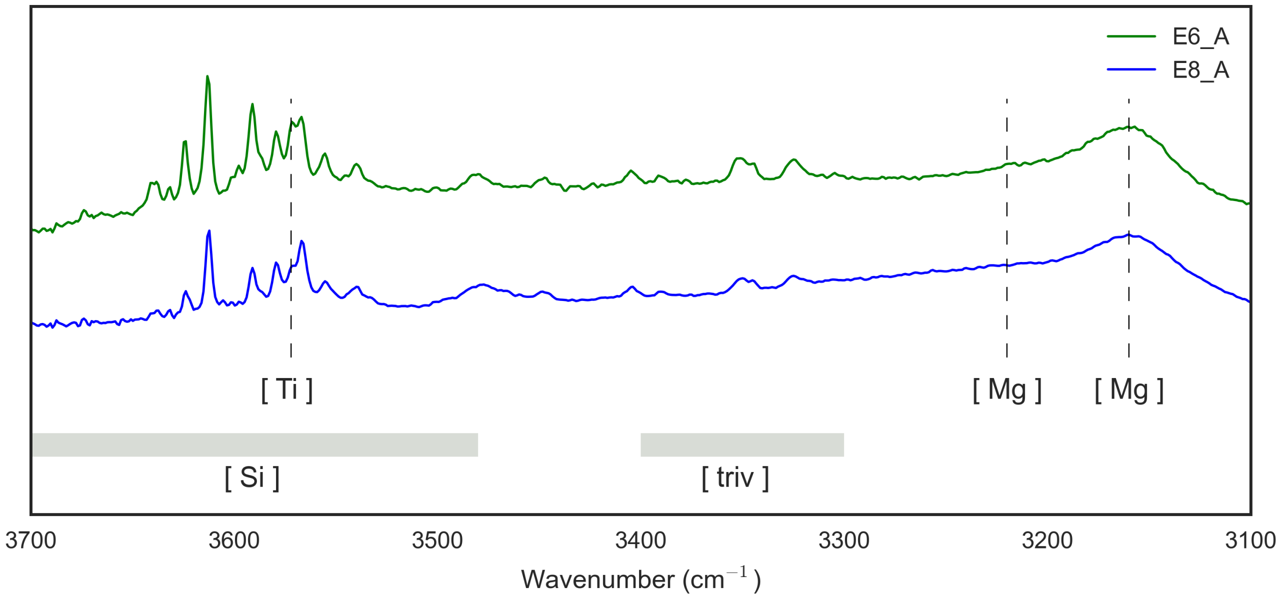

Figure 4.21: *FTIR spectra for H-forsterite grains E6_A (green line) and E8_A (blue line), unpolarised measurements, shown in comparison to the positions of the IR peaks associated with each of the incorporation/defect mechanisms [Si], [Ti], [Mg] and [triv] (grey and dashed lines) as discussed in text. Peaks are predominately in the region that is attributed to [Si] - straightforward protonation of and Si atom, generally associated with synthesis under low silica activity conditions (Lemaire et al., 2004).*

Contamination

Although the wavelength region of the IR spectra studied primarily contains peaks associated with the accepted incorporation of H (or D) in forsterite, there are several peaks that can appear in the same region that have been attributed to contamination of the samples - either resulting in traces non-relevant species, or contributing to alternative H (or D) incorporation mechanisms. For example, the group of peaks around 2,950cm^{-1}, seen particularly strongly in E8_A and EF11_A (see figure 4.22), are characteristic of CH group vibrations (Kohn, personal communication) indicating some contamination from either the mounting material (crystalbond) or acetone.

Additionally, several authors (Ingrin, Kovács, et al., 2014; Sykes et al., 1994) have identified specific OH bands in boron-rich synthetic forsterite that they suggest result from the coupled substitution of B = Si and OH = O (referred to as B(F,OH)$Si_{-1}O_{-1}$, Sykes et al. (1994)). The band observed by Sykes et al. (1994) at 3,672cm^{-1} is present in E6_A, and potentially also in E7_D (see figure 4.22) suggesting that there may be some boron contamination in the H-forsterite samples. Boron in the H-forsterite samples could potentially come from the piston cylinder sample assembly - part of the assembly is made of borosilicate glass (see figure 4.2) and at the temperatures and timescale for synthesis runs (1200°C for several days) boron may diffuse into the capsule. Evidence of boron diffusion in to samples during piston cylinder runs was also observed by Kohn, who used a similar sample assembly for hydrogen diffusion experiments in forsterite (personal communication) and has been detected at ppm level in melts analysed from runs using pyrex assemblies (Craven, personal communication). In theory, BO_3 stretching bands around 1,164 and 1,257cm^{-1} should be visible to confirm the presence of boron - as can be seen from figure 4.23, there is evidence of small peaks here in both E6_A and E7_D but the spectra are slightly too noisy at these low frequencies for this to be conclusive. Moreover, the bands at 3,704, 3,598 & 3,525cm^{-1} attributed by Ingrin, Kovács, et al. (2014) to the boron substitution mechanisms are not prominent in samples from this study, suggesting that perhaps the levels of boron contamination are not substantial enough to contribute significantly to OH incorporation.

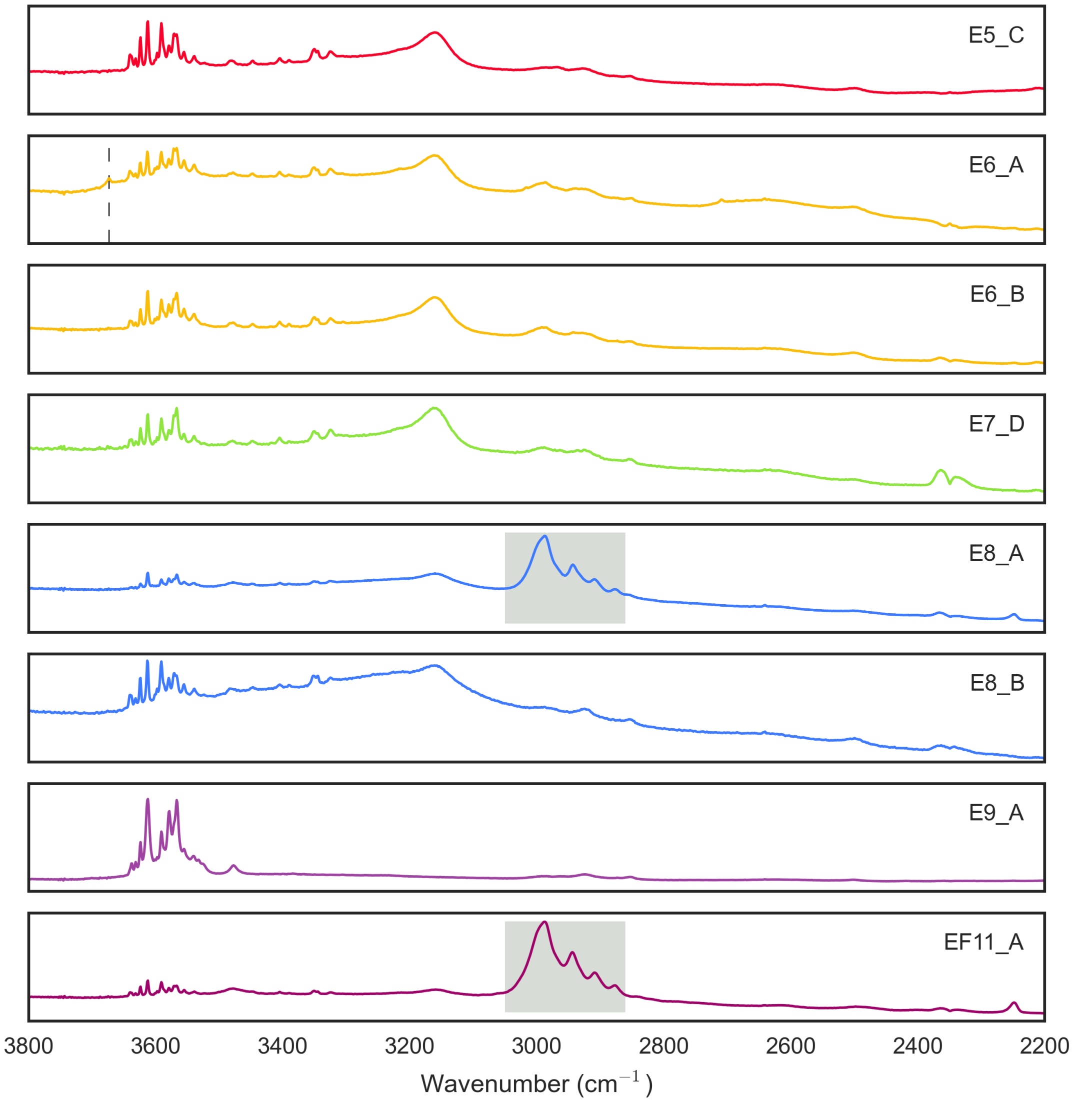

Figure 4.22: *FTIR spectra for post D-H exchange H-forsterite samples, highlighting peaks in the range of interest that are likely to be as a result of contamination. Grey shaded area in E8_A and EF11_A indicates CH vibrations (also weakly present in other samples). Black dashed line (E6_A) indicates possible Boron-related defect (see discussion and references in text), potentially also present in E7_D. Note again that the absorbance scale has been adjusted so the size of the peaks between samples is not relative.*

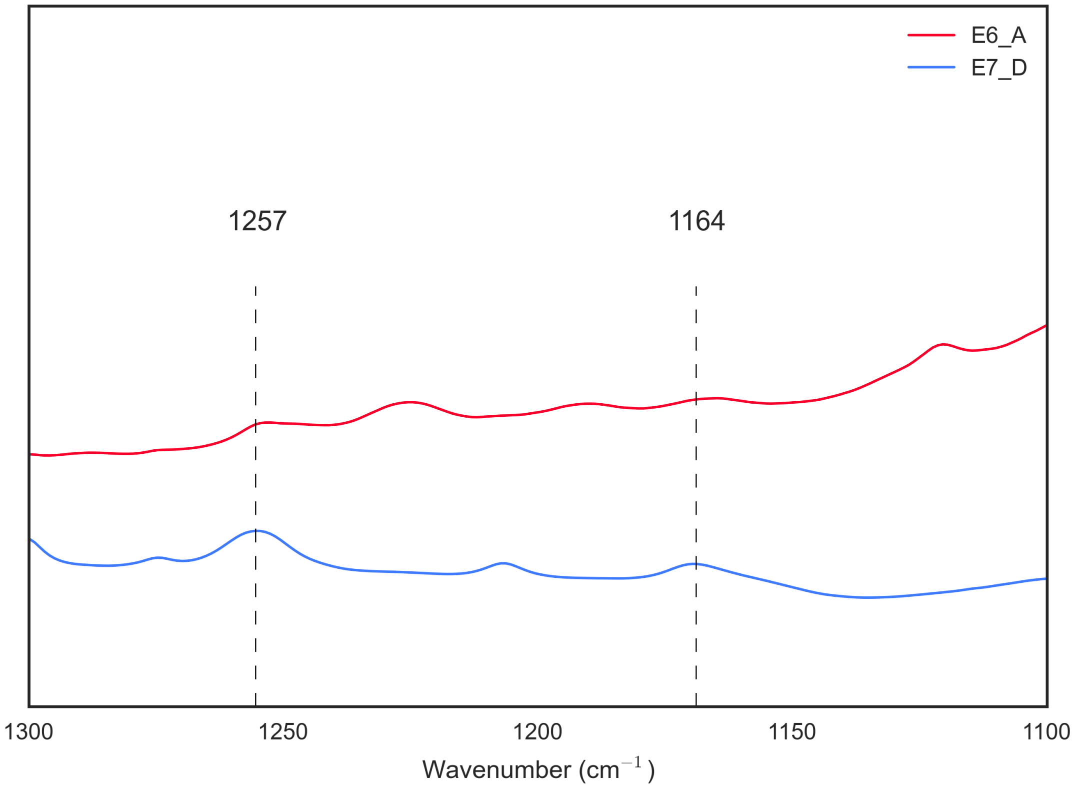

Figure 4.23: *FTIR spectra for E6_A and E7_D indicating the potential presence of peaks related to* BO_3 *at 1,164 and 1,257cm*$^{-1}$.

4.6 Results

Exchange runs E1-E4 and EF1-EF4 were analysed in April and September 2013 as part of a SIMS pilot study to aid development of the experimental method, but did not produce usable data. As discussed in sections 4.2.1 and 4.2.3, the first stage of preliminary analysis (April, samples from runs E1-E3 & EF1-EF2) showed samples did not contain any deuterium[17] and the second stage of preliminary analysis (September, samples from runs E4 & EF3-EF4) showed that the grain surfaces were not of sufficient quality for analysis.[18] Following this preliminary analysis, the bulk of the experimental work was carried out August 2013 - July 2014, with exchange runs E5-E9 and EF5-EF16 analysed in August 2014 (excluding failed runs - see table 4.4). All of the results that will be discussed in detail are from this main suite of experimental work, and subsequent SIMS analysis in August 2014.

A total of 56 concentration-depth profiles were measured across 29 H-forsterite grains. 21 of these profiles (across 16 different grains) were suitable for fitting to Fick's law - that is, contained a sufficient concentration of deuterium (above background/detection limits of 2-4ppm), showed concentration clearly decreasing with depth into the samples, and had a known pit depth (either measured by WLI or satisfactorily estimated by comparison with measured pits). Table 4.8 lists all of the successfully fitted profiles, along with the corresponding D_H and C_0 values. Values are given both for un-adjusted profiles, and for 'fit' profiles (where the data was shifted to flatten out at zero, as discussed in section 4.4). In all cases, the adjusted ('fit') profile gives a better fit to the data, particularly with regard to the profile shape.[19] Concentration-depth plots with fits to Fick's law for each of the 21 profiles are shown in appendix C. The single pit profiles are distinguished by either 'HD' or 'HSi' - this refers to the reference species used during SIMS analysis, and does not appear to have any significant bearing on the subsequently calculated diffusion coefficients (see figure 4.24).

---

[17] As a result of which a check for leaks in the welded capsule was introduced, and a D-H glass standard was created.

[18] As a result of which H-forsterite grains for subsequent runs were polished prior to exchange.

[19] As discussed in section 4.4, fitting the overall shape of the data is more important than the absolute concentration when considering diffusion.

Table 4.8: *D_H and C_0 values obtained from D-H exchange profiles fitted to Fick's law.*

Sample	**T (°C)**	**D_H (m^2/s)**	**D_H_fit (m^2/s)**	**C_0 (ppm)**	**C_0_fit (ppm)**
E6_A_5_DP	600	4.25 ± 0.18 x10^{-18}	2.73 ± 0.04 x10^{-18}	441 ± 11	487 ± 4
E8_A_4_DP	700	3.22 ± 0.13 x10^{-17}	1.26 ± 0.04 x10^{-17}	104 ± 2	117 ± 2
E9_A_1_HD_600	500	4.86 ± 9.96 x10^{-17}	3.20 ± 0.79 x10^{-17}	9 ± 1	10 ± 1
E5_A_1_HD_600	600	6.34 ± 1.26 x10^{-17}	4.68 ± 0.23 x10^{-17}	33 ± 1	35 ± 1
E6_A_HD_600	600	2.93 ± 9.70 x10^{-16}	1.76 ± 0.57 x10^{-17}	180 ± 2	224 ± 2
E7_D_2_HD_600	700	1.39 ± 0.85 x10^{-17}	8.01 ± 0.38 x10^{-18}	32 ± 19	34 ± 26
E8_A_HD_600	700	2.67 ± 0.23 x10^{-14}	2.03 ± 0.71 x10^{-16}	46 ± 2	96 ± 1
E8_B_1_HD_600	700	3.81 ± 0.56 x10^{-14}	2.47 ± 0.24 x10^{-15}	29 ± 3	33 ± 5
EF6_A_1_HD_600	600	1.20 ± 0.45 x10^{-17}	8.20 ± 0.22 x10^{-18}	5 ± 1	6 ± 2
EF6_A_2_HD_600	600	2.53 ± 1.02 x10^{-16}	1.02 ± 0.52 x10^{-16}	3 ± 1	3 ± 1
EF16_C_1_HD_600	500	1.42 ± 0.21 x10^{-16}	9.74 ± 0.94 x10^{-17}	91 ± 6	94 ± 4
EF16_C_2_HD_600	500	3.74 ± 0.65 x10^{-16}	2.03 ± 0.28 x10^{-16}	43 ± 3	46 ± 3
EF9_E_1_HD_300	700	9.72 ± 0.33 x10^{-14}	1.64 ± 1.48 x10^{-14}	19 ± 1	11 ± 1
EF9_A_1_HD_300	700	2.53 ± 0.58 x10^{-14}	1.73 ± 0.22 x10^{-14}	10 ± 1	9 ± 1
E9_D_1_HSi_600	500	5.76 ± 0.35 x10^{-16}	5.00 ± 1.36 x10^{-16}	38 ± 1	38 ± 2
E9_E_1_HSi_600	500	3.94 ± 0.53 x10^{-15}	1.19 ± 1.86 x10^{-15}	71 ± 2	76 ± 2
E5_C_1_HSi_600	600	3.15 ± 0.41 x10^{-16}	1.17 ± 1.18 x10^{-16}	22 ± 8	22 ± 11
E6_C_1_HSi_600	600	1.34 ± 1.40 x10^{-15}	5.05 ± 1.32 x10^{-17}	70 ± 1	107 ± 3
E7_D_1_HSi_600	700	2.50 ± 1.35 x10^{-15}	2.26 ± 0.80 x10^{-17}	6 ± 3	11 ± 4
E8_D_1_HSi_600	700	6.88 ± 0.89 x10^{-15}	4.12 ± 0.79 x10^{-16}	49 ± 2	52 ± 2
EF9_D_1_HSi_300	700	1.44 ± 0.41 x10^{-14}	5.11 ± 0.14 x10^{-16}	16 ± 4	19 ± 6

For 'fit' values, the SIMS depth-concentration data was shifted to flatten out at zero (by calculating the average of the last 20 data points and subtracting this value from each individual data point), giving a better fit to the shape of the profiles. E# runs were carried out at 2GPa, EF# runs at atmospheric pressure.

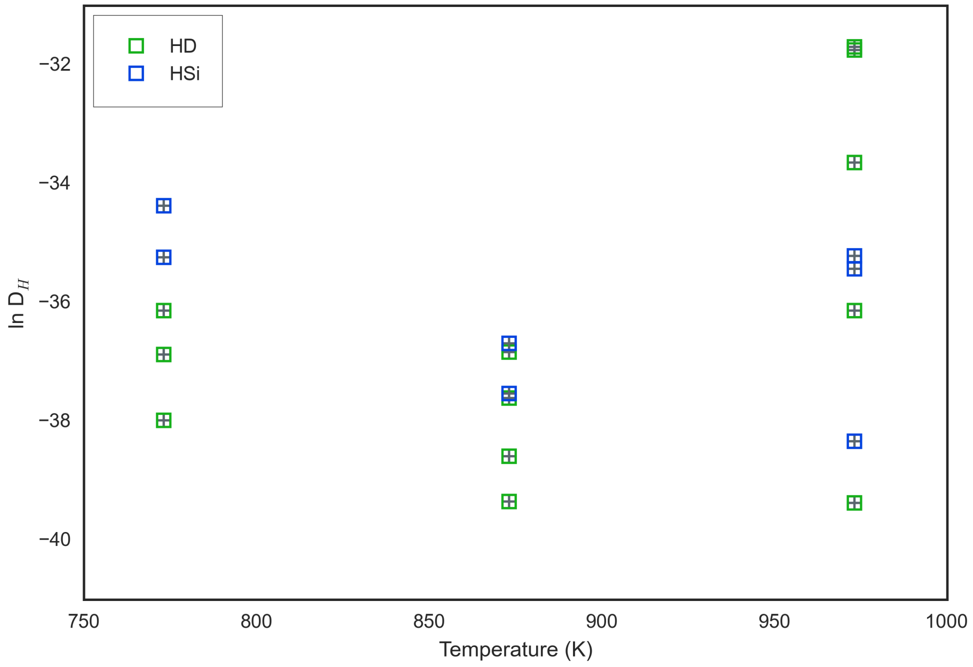

Figure 4.24: *Data from all fitted profiles plotted as lnD against T. Blue boxes highlight SIMS data collected with reference to Si (HSi), green boxes highlight data collected without reference to Si (HD). There is no convincing trend to suggest that the reference species used during SIMS analysis significantly influences the resulting diffusivity value.*

4.6.1 Deuterium vs. hydrogen diffusion

As introduced in section 2.1.1, the diffusion data obtained for H-forsterite grains is for the diffusion of deuterium (D_D) rather than hydrogen (D_H) as this was the species measured during SIMS analysis.[20] Due to the increased mass of deuterium relative to hydrogen, D_D is slower than D_H by a factor of around 0.8, depending on the value of β in equation 2.5 (which relates mass to diffusivity).

Table 4.9 shows a comparison of the values calculated for E6_A and E8_A (strictly speaking D_D) with values adjusted using β values of 0.3, 0.4 and 0.5.[21] Figure 4.25 shows this range in D_H values plotted as black bars on the depth profile data points, in comparison to the rest of the data points, illustrating the minimal effect of adjusting by any value of β. Once plotted on an Arrhenius plot (e.g. figure 4.29) at a standard scale (typical for published experimental data of this type - see later discussion), the difference resulting from converting D_D to D_H (using any reasonable β value) is smaller than the size of the data point marker, illustrating that the effect is negligible for the purposes of this study. Consequently, no conversion has been carried out and the values reported and discussed henceforth will simply be referred to as D_H results.

Table 4.9: *Variation in D_H values as a result of differing values of β in equation 2.5.*

	E6_A	**E8_A**
unadjusted	2.73 x 10^{-18}	1.26 x 10^{-17}
$\beta = 0.3$	3.36 x 10^{-18}	1.55 x 10^{-17}
$\beta = 0.4$	3.60 x 10^{-18}	1.66 x 10^{-17}
$\beta = 0.5$	3.86 x 10^{-18}	1.78 x 10^{-17}

---

[20] Again as previously noted, the initial intention had been to collect data for both by measuring the corresponding hydrogen profiles in the grains - due to analysis constraints, the hydrogen signal was not distinct enough to identify diffusion profiles.

[21] 0.3 is the value that best fits experimental data on D-H partitioning by Bucholz et al. (2013), 0.5 is the value used by Du Frane and Tyburczy (2012) for previous D-H exchange experiments.

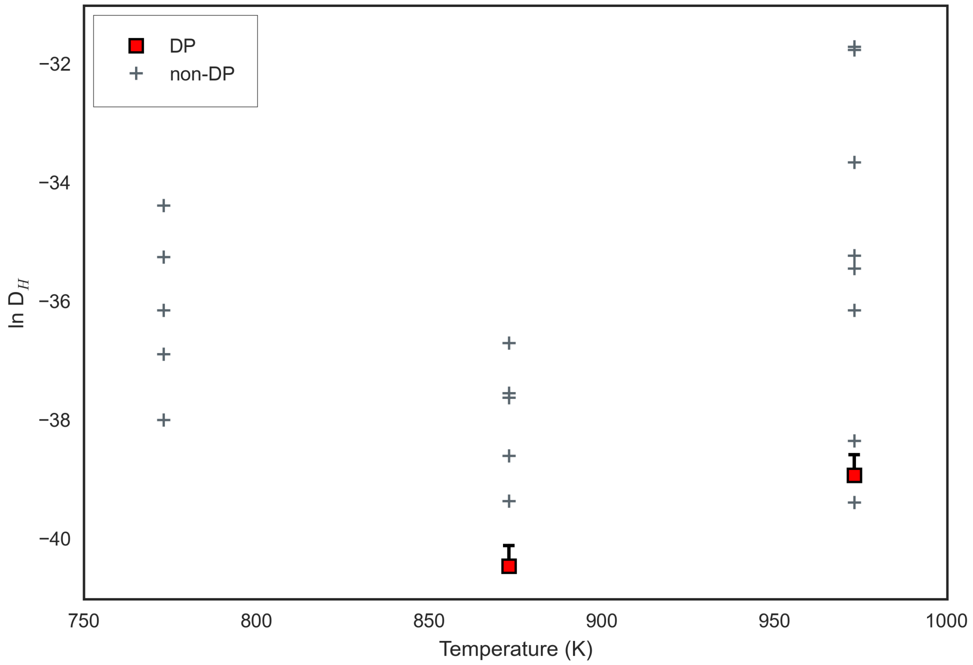

Figure 4.25: *Variation in D_H values as a result of adjusting for D_D measurements using differing values of β in equation 2.5 are shown as black bars on the depth profile data points (red squares). The effect on diffusion values is essentially negligible (i.e. D_H can be considered equivalent to D_D).*

4.6.2 Depth profiles vs. single pit profiles

As a result of the small surface area of the H-forsterite grains, two (of the 21 fitted) diffusion profiles represent data collected by full SIMS depth profiles. As discussed in section 3.2.1 a full, or 'true' SIMS depth profile involves rastering the beam over an area three times the beam size in each direction, in order to avoid crater edge effects that occur when data is collected from a single pit (where the beam 'drills down' in place). In the following discussion, these full depth profile analyses (taken only on H-forsterite grains E6_A and E8_A) will be referred to as depth profiles, and analyses taken with the SIMS beam stationary will be referred to as single pit, or non-depth, profiles.

As shown in figure 4.26, across data from all 21 fitted profiles, diffusion coefficients obtained by fitting single pit profiles are larger (implying faster diffusion) than those from depth profiles at the same temperature, with only a single exception. This is true even for single pit profiles on the same grain as the corresponding depth profile (highlighted with red boxes in figure 4.26, and confirms that the crater-edge and associated effects lead to an over-exaggeration of values caused by 'smeared out' diffusion profiles due to the unwanted contribution of material from shallower levels. This over-exaggeration of diffusion is also illustrated in figures 4.27 and 4.28 which show the drawn out nature of the single pit profiles compared to the depth profiles on grains E6_A and E8_A respectively.

The range in non-depth profile analysis values, even from grains subjected to the same conditions, is clearly substantial and is also highly variable. The variability appears to be unsystematic - the sputtering process is complicated by physical processes such as fluctuations in the diameter and positioning of the beam, and is essentially random. Modelling of the resulting over-estimation is, therefore, not possible. Consequently, only the two diffusion coefficients, obtained from the two depth profile analyses (E6_A and E8_A), are suitable for further comparison and consideration. This also limits the potential for future studies using the method described, as any grains to be analysed using SIMS depth profiling need to be large enough to accommodate a 150-200µm analysis pit - requiring a method that consistently synthesises larger H-forsterite grains than was achieved for this study. Additionally, larger crystals are harder to recover from high pressure experiments without cracking.

The difficulty in recovering whole crystals from piston-cylinder experiments has impeded previous diffusion studies (Demouchy and Mackwell, 2003), however a newly developed method by Jollands et al. (2016) appears to overcome this issue - reportedly with 100% complete recovery although at lower pressures of around 1.5GPa - and may allow for future investigations in this direction.

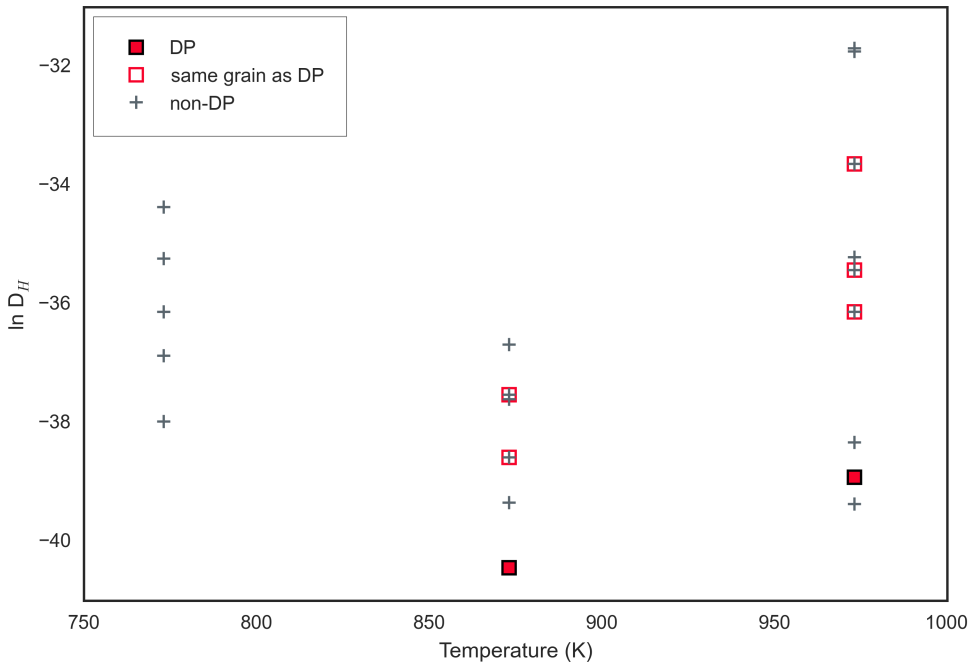

Figure 4.26: *Data from all fitted profiles plotted as lnD*$_H$ *against T. Depth profile values are shown as filled red squares, non depth profile values as grey crosses. Non depth profile values from analyses on the same grain as the corresponding depth profile are highlighted with red boxes. The non depth profile analyses yield (in some cases significantly) faster diffusion coefficients, and there is substantial variability in these values (variability in the depth profile values cannot strictly be constrained, due to the lack of data).*

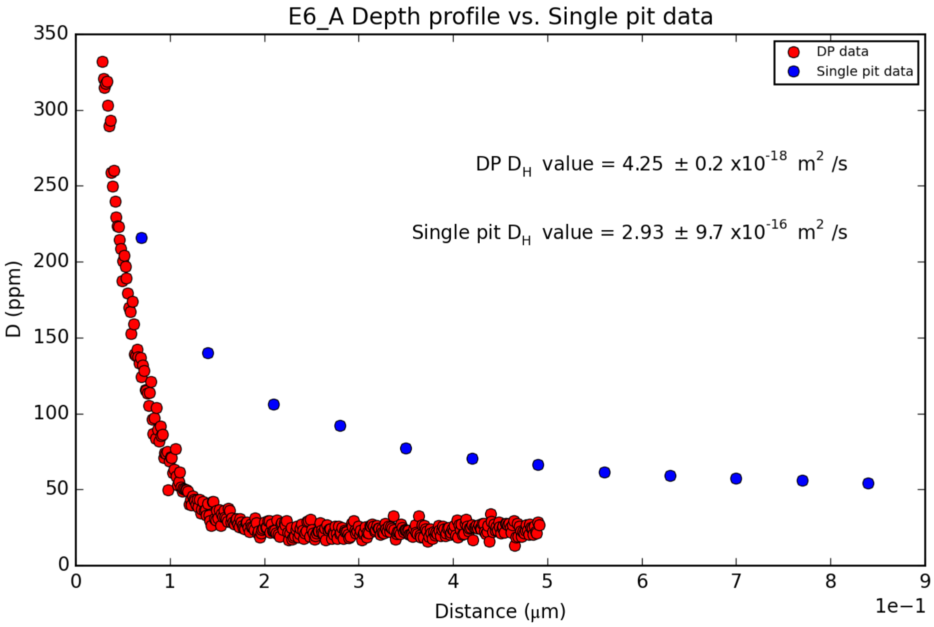

(a)

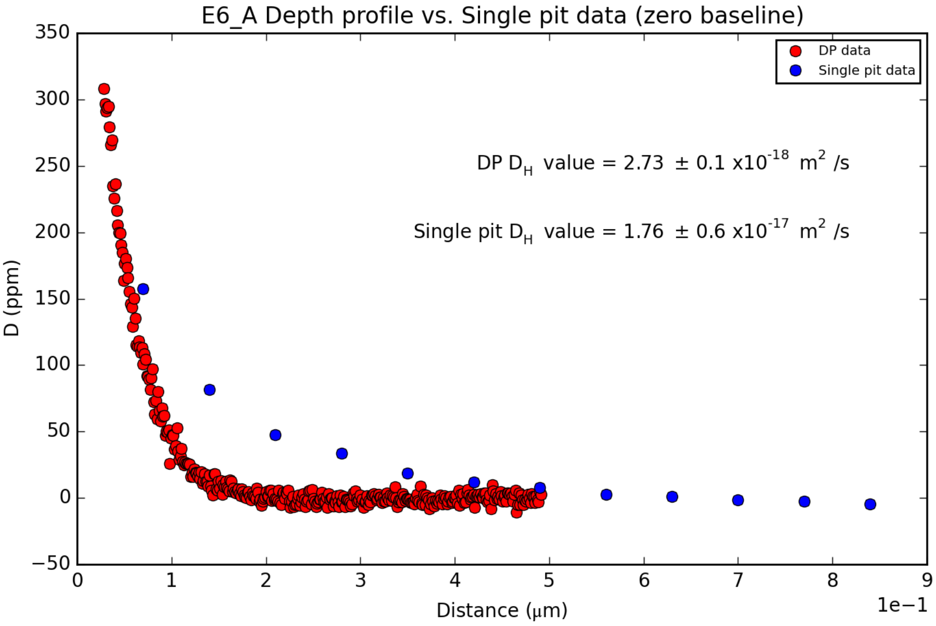

(b)

Figure 4.27: *(a) Depth-concentration plot for E6_A, obtained from both a full depth profile (red) and small single pit (blue) analyses. Compared to the depth profile, the single pit profile overestimates the concentration of deuterium for any given depth and therefore results in a faster diffusion coefficient. (b) This remains the case when both sets of data are adjusted to a 'zero baseline' in order to best fit the data.*

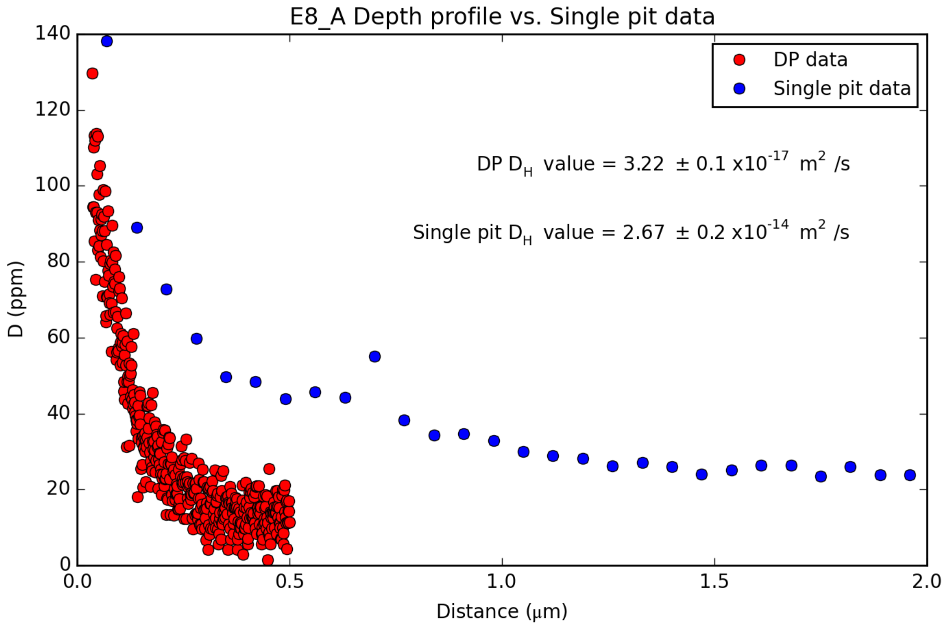

(a)

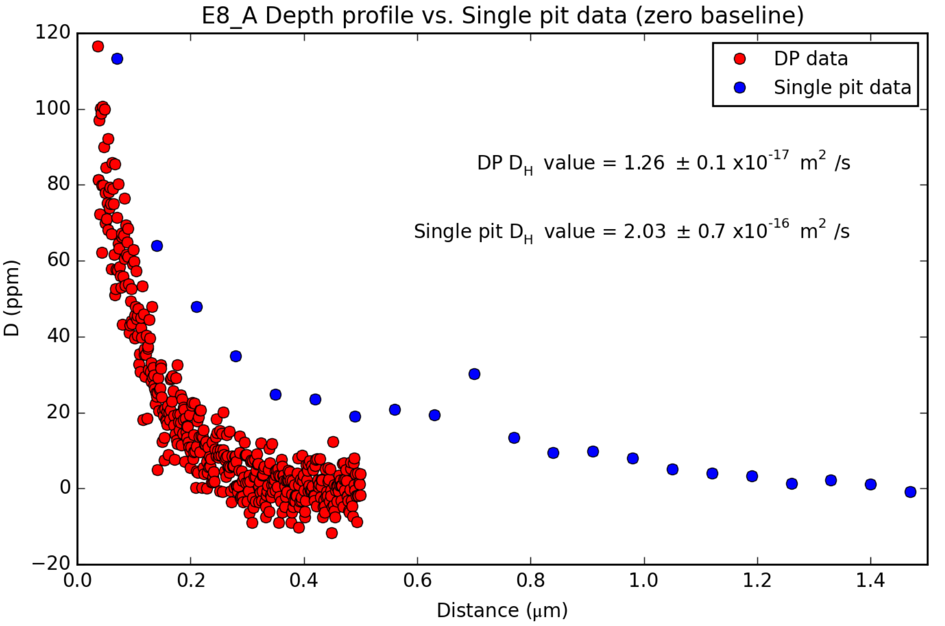

(b)

Figure 4.28: *(a) Depth-concentration plot for E8_A, obtained from both a full depth profile (red) and small single pit (blue) analyses. Compared to the depth profile, the single pit profile overestimates the concentration of deuterium for any given depth and therefore results in a faster diffusion coefficient. (b) This remains the case when both sets of data are adjusted to a 'zero baseline' in order to best fit the data.*

4.6.3 Temperature dependence of diffusion

The temperature dependence of diffusion is well known (Zhang, 2010), and is described by the Arrhenius equation:

$$D_i = D_i^0 \, e^{\,[-Q/RT]} \tag{4.6}$$

where D_i is the diffusivity of the species i, D_i^0 is a pre-exponential factor, Q is the activation energy (J/mol), R is the gas constant (J/(mol.K)) and T is the temperature (K). This relationship indicates the rapid increase in diffusivity with temperature, and results in a straight line fit with a negative slope when data are plotted as $\ln D_i$ (or $\log D_i$) against inverse T (typically $10^4/T$).

Figure 4.29 shows the temperature dependence of D_H from this study, on a standard Arrhenius plot. The error bars shown represent the range of D_H values calculated from the minimum and maximum pit depths measured by WLI. As previously noted the difference in values resulting from the conversion between D_D and D_H is significantly less than this error, as is the fitting error.[22] There are likely to be additional errors associated with measurements of concentration by SIMS, but without multiple data points at each temperature to indicate the spread of the data these are difficult to quantify. A best fit straight line to the data (including errors) is shown as a black dashed line. As there are only two data points available from this study, and as the crystallographic orientation of the crystals is unknown, the trendline lacks any substantial constraints, but nonetheless gives an estimation of the temperature dependence. Furthermore, although the exact orientation of the samples is not known, it is estimated (from silica overtones in FTIR spectra) that the two data points represent approximately the same orientation - see previous discussion.

Determining the best fit of the data points for E6_A and E8_A to equation 4.6 yields values of Q = 105 ± 7 kJ/mol and D_i^0 = 5 ± 4 10^{-12}, giving the diffusivity-temperature relationship for hydrogen self-diffusion in forsterite:

---

[22] In fact, variation is less than the height of the marker point.

$$D_H = 5 \pm 4 \times 10^{-12}\, e^{\,[-105\pm 7kJ.mol^{-1}/RT]}\, m^2/s \tag{4.7}$$

This determined value for activation energy (Q) compares well with the value of 110kJ/mol calculated by Demouchy and Mackwell (2003) for the self-diffusion of H^+ ions in forsterite,[23] and is within error of the values calculated by Du Frane and Tyburczy (2012) for olivine (140 ± 30kJ/mol forthe [100] direciton, 170kJ/mol for [010] and 100kJ/mol for [001]). The value is also similar to the activation energy determined by Sun et al. (2015) for the self-diffusion of hydrogen in Fe-bearing ringwoodite (101 ± 10 kJ/mol).

Experiments for this study were carried out at lower temperatures than the majority of previous work, but when compared to the spread of literature values for the diffusivity of hydrogen in forsterite (shown as grey circles in figure 4.29), values appears to fit within the general scatter in the existing data. For comparison, figure 4.30 shows previously published hydrogen diffusion values for forsterite and olivine. As noted by Demouchy and Mackwell (2003), the diffusion of hydrogen is slower in forsterite than in olivine for the same process. Plots 4.31 (for forsterite only) and 4.32 (for forsterite + olivine) show these data with individual datasets picked out by study and crystallographic orientation (or vacancy association), including straight line fits to each data set. Results from this study suggest slightly slower diffusion than those previously published - with the exception of values determined by Padrón-Navarta et al. (2014) for diffusion associated with Si vacancies (PN_14_Si).

---

[23] Based on a mathematical relationship between D_H (self-diffusion) and D_{eff} (the chemical diffusion measured in their experiments).

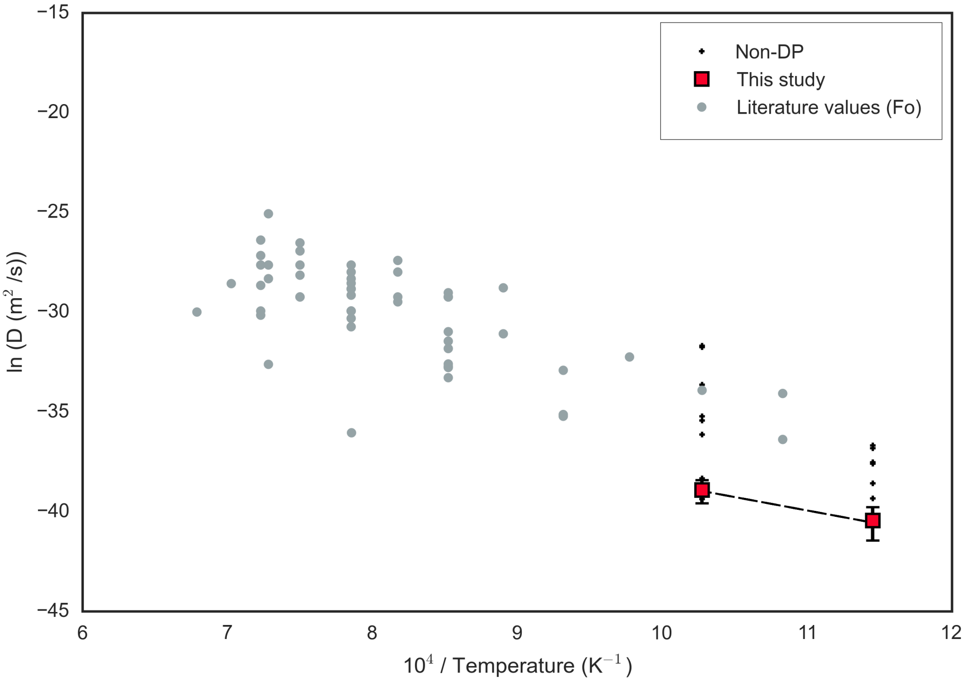

Figure 4.29: *Temperature dependence of hydrogen diffusion in forsterite. Values from this study (red squares, with black dashed line showing best fit) are shown in comparison to published data for forsterite (grey circles). Data points for the non depth profile analysis pits (black crosses) are shown for comparison only - as discussed these represent exaggerated diffusivities.*

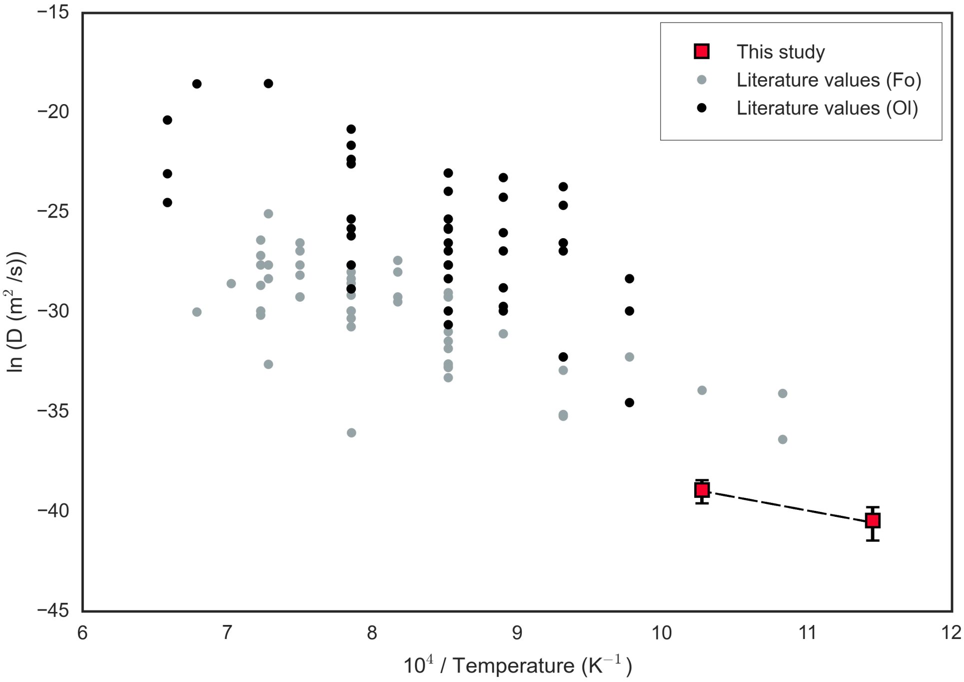

Figure 4.30: *Temperature dependence of hydrogen diffusion in forsterite and olivine. Values from this study (red squares) are shown in comparison to previously published data for both forsterite (grey circles), and olivine (black circles).*

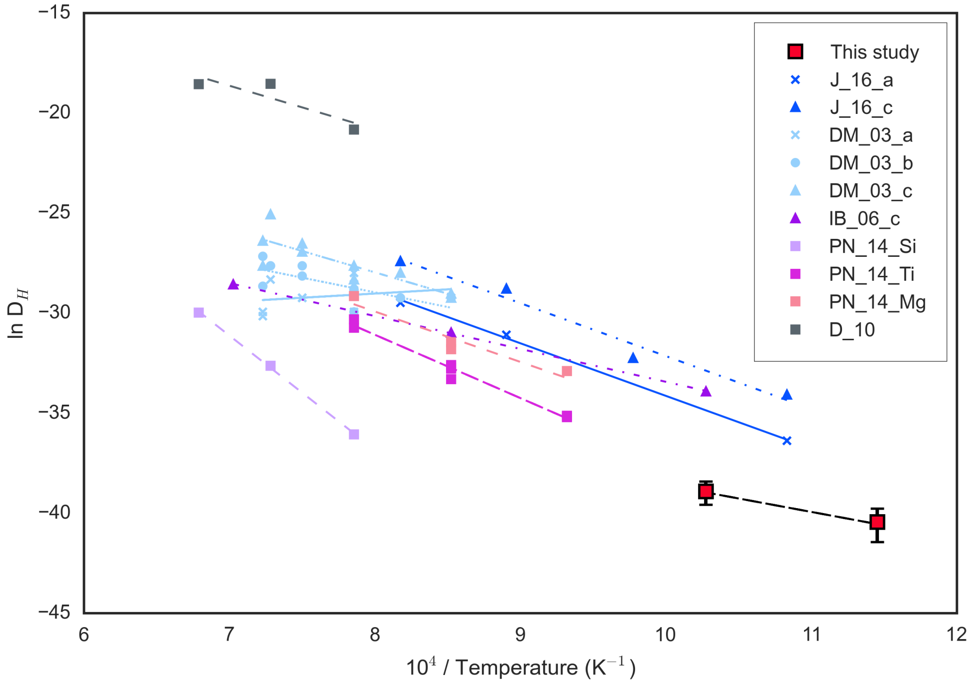

Figure 4.31: *Temperature dependence of hydrogen diffusion in forsterite, by study. Values from this study (red squares) are shown in comparison to published data, separated by study and by crystallographic orientation (where relevant - data from PN_14 are instead separated by the defect to which they associate values). Un-oriented data are plotted as squares, with dashed lines, _a indicates [100] direction (solid lines), _b = [010] (dotted lines), _c = [001] (dot-dash lines). References: J_16 - Jollands et al. (2016), DM_03 - Demouchy and Mackwell (2003), IB_06 - Ingrin and Blanchard (2006), PN_14 - Padrón-Navarta et al. (2014), D_10 - Demouchy (2010).*

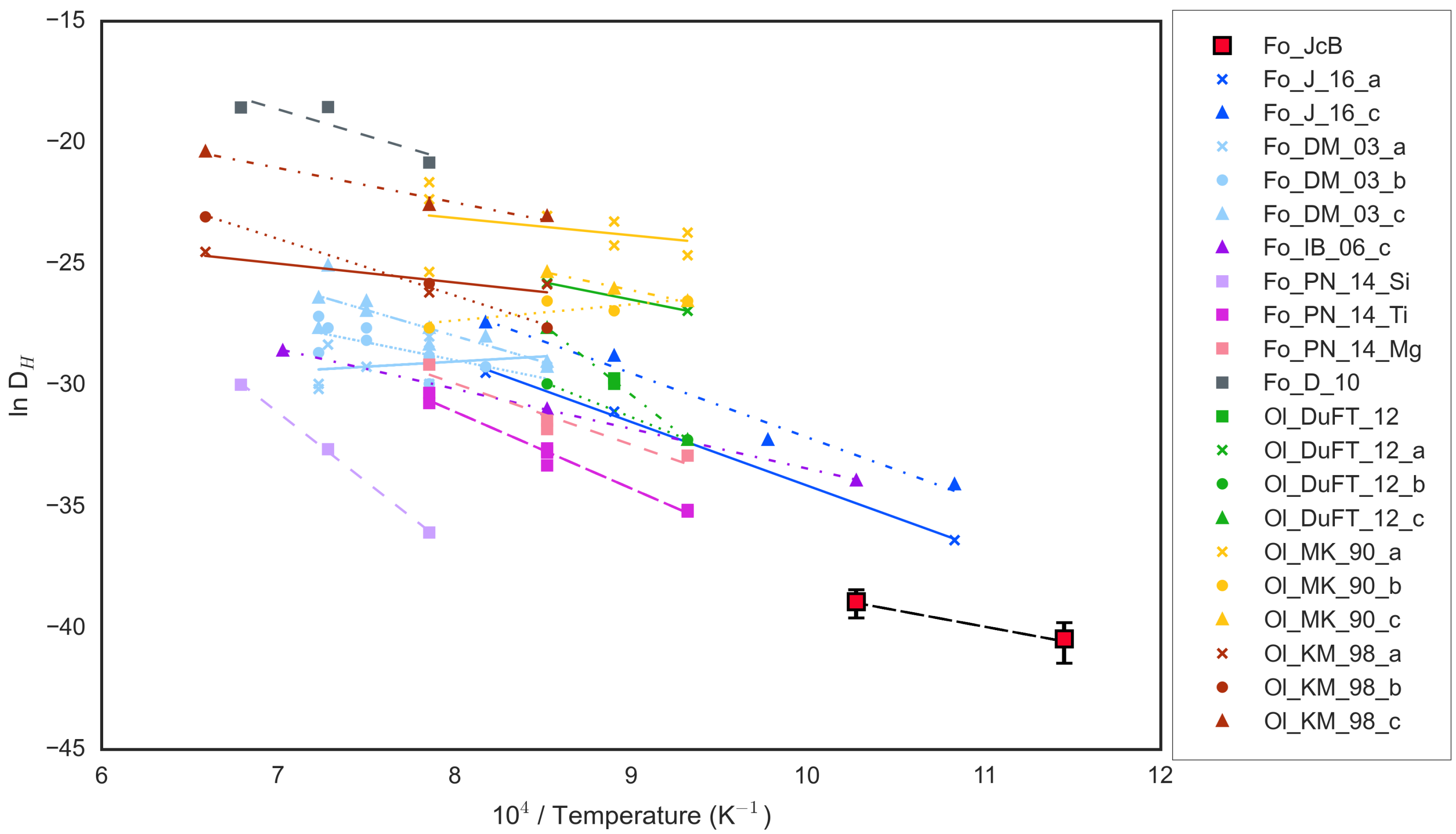

Figure 4.32: *Temperature dependence of hydrogen diffusion in forsterite (Fo_) and olivine (Ol_), by study. Un-oriented data is plotted as squares, with dashed lines, _a indicates [100] direction (solid lines), _b = [010] (dotted lines), _c = [001] (dot-dash lines). References: JcB - this study, J_16 - Jollands et al. (2016), DM_03 - Demouchy and Mackwell (2003), IB_06 - Ingrin and Blanchard (2006), PN_14 - Padrón-Navarta et al. (2014), D_10 - Demouchy (2010), DuFT_12 - Du Frane and Tyburczy (2012), MK_90 - Mackwell and Kohlstedt (1990), KM_98 - Kohlstedt and Mackwell (1998), DM_06 - Demouchy and Mackwell (2006).*

It is reasonable to assume that the scatter in the data is partly a result of the different mechanisms by which hydrogen can diffuse through the olivine structure. Data from Demouchy and Mackwell (2003; 2006) and Jollands et al. (2016) - plotted as [Fo_DM_03], [Ol_DM_06] and [Fo_J_16] respectively - are for coupled hydrogen-M site vacancy diffusion; data from Mackwell and Kohlstedt (1990) and Kohlstedt and Mackwell (1998) - [Ol_MK_90] and [Ol_KM_98] - are for proton-polaron exchange (redox-exchange); data from Demouchy (2010) - [Fo_D_10] - are for grain boundary diffusion; data from Padrón-Navarta et al. (2014) are for the diffusion out of hydrous defects related to Mg-vacancies [Fo_PN_14_Mg], Si vacancies in Ti-doped forsterite [Fo_PN_14_Ti] and Si vacancies in undoped forsterite [Fo_PN_14_Si]; and data from Ingrin and Blanchard (2006), Du Frane and Tyburczy (2012) and this study - [Fo_IB_06], [Ol_DuFT_12] and [Fo_JcB] - are for D-H exchange, theoretically representing hydrogen self-diffusion.

4.6.4 Hydrogen self-diffusion

The diffusion of hydrogen is clearly variable depending on the associated defects. Consequently, values from this study are only strictly comparable to other values for the same mechanism, the self-diffusion of hydrogen. In addition to values for D-H exchange studies from Ingrin and Blanchard (2006) and Du Frane and Tyburczy (2012), self-diffusion values calculated from bulk chemical diffusivity are also available from the work of Demouchy and Mackwell (2006) and Mackwell and Kohlstedt (1990). A comparison with these self-diffusion values (truly also D_H values) is shown in figure 4.33. Again, values from this study suggest slower rates of diffusion than has previously been identified from other studies. To some extent, this may represent a difference in diffusion between Fe-bearing olivine and forsterite - as the studies of Mackwell and Kohlstedt, Demouchy and Mackwell and Du Frane and Tyburczy were all carried out on natural olivine compositions (all approximately Fo_{90}) and the study of Ingrin and Blanchard was carried out on 'near-pure forsterite' rather than Fo_{100}. As the D-H exchange data quoted in Ingrin and Blanchard (2006) are unpublished (the values only are quoted in the paper, which is a review of the literature for hydrogen diffusion in minerals), further details of their study are not available. It is also possible that the difference reflects a difference in crystallographic orientation. The data from Ingrin and Blanchard are for the [001] orientation, whereas the orientation of samples from this study are only estimated to be approximately in the

[001] direction (and the two data points could reflect different orientations). However, the fast direction for hydrogen self-diffusion in olivine (as determined by Du Frane and Tyburczy) is [100] - with [010] and [001] being fairly similar - suggesting one would not expect the data for [001] from Ingrin and Blanchard to be significantly faster than this study, regardless of orientation. As previously noted, the activation energy calculated for this study compared well with other values for hydrogen self-diffusion (this study: 105kJ/mol, Demouchy and Mackwell: 110kJ/mol, Du Frane and Tyburczy: 100-170kJ/mol).

It is interesting to note that the D-H exchange values sit at the slower edge of the range of olivine and forsterite values (as relevant). This may support the assertion by Karato (2013) that during D-H exchange, the rate-controlling species is the slowest diffusing species (which he suggests is two protons at an M-site vacancy).

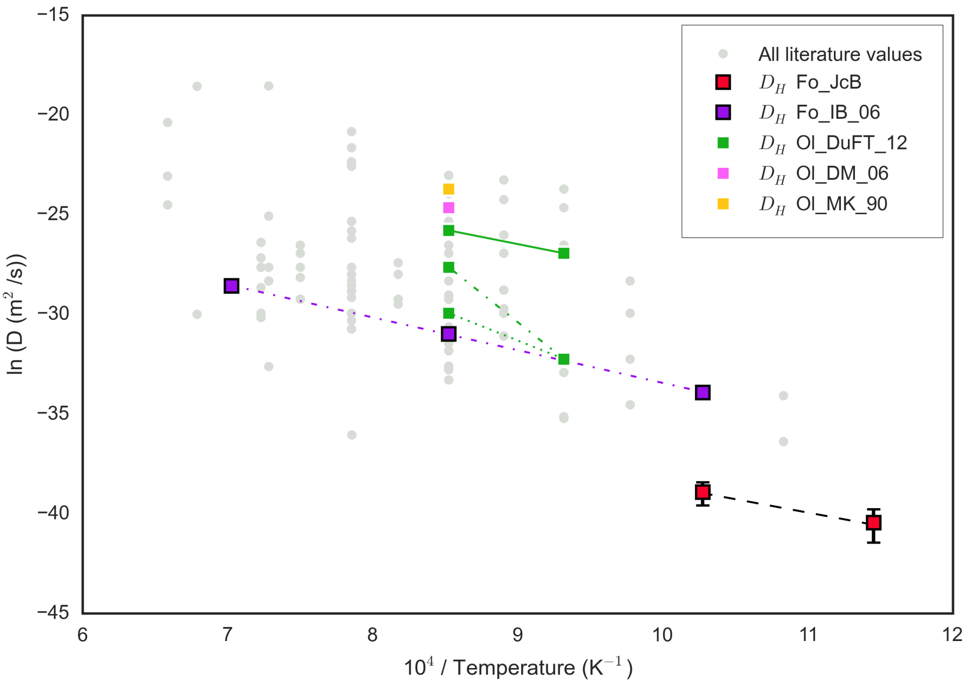

Figure 4.33: *Temperature dependence of D_H - hydrogen self-diffusion by study (all literature hydrogen diffusion values are shown for reference. As in previous figures, a dashed trendline indicates non-oriented samples, solid line = [100], dotted line = [010] and dot-dash = [001]. References: JcB - this study, IB_06 - Ingrin and Blanchard (2006), DuFT_12 - Du Frane and Tyburczy (2012), DM_06 - Demouchy and Mackwell (2006), MK_90 - Mackwell and Kohlstedt (1990).*

4.6.5 Influence of type of hydrogen species present

As previously discussed, FTIR spectra for the H-forsterite samples synthesised for use in this study appear to be dominated by peaks that have been allocated to the [Si] incorporation mechanism - generally the replacement of Si with 4 protons. Samples share similar peaks to the undoped, MgO-buffered forsterite crystals investigated by Padrón-Navarta et al. (2014) - also synthesised to contain H in the starting material - and one might therefore expect to see a correlation between data from this study and [Fo_PN_14_Si]. However, as seen from figures 4.32, 4.33, this is not the case as the data from Padrón-Navarta et al. predict slower [Si] diffusion, with a high activation energy. As this study measures D-H exchange, rather than hydrogen diffusion coupled to any other (slower) diffusing defect, the data are likely to represent the faster D-H exchange process for the same hydrogen species (i.e. coupled to Si defects) - but it is then surprising that the D-H exchange data are relatively slow. When extrapolated to the same temperatures, diffusivity data from this study in fact compares best with values from Padrón-Navarta et al. for [Mg] and [Ti] (substitution of 2 protons for Mg or Ti respectively at the M1 site) in Ti^{4+}-doped samples. Figure 4.34 shows the fit of hydrogen diffusion values from Padrón-Navarta et al. (2014) to depth-concentration profiles from this study - at 700°C the [Ti] mechanism fits the SIMS data within error, but otherwise there is no strong correlation.

Although samples from this study do not contain Ti, it is possible that trace amounts of Al (from the piston-cylinder sample assembly, similar to B contamination detected by FTIR, discussed in section 4.5.7) were incorporated into H-forsterite grains during the synthesis, and could be having a similar influence on hydrogen diffusion as Ti. However, FTIR spectra for E6_A and E8_A do not appear to contain the absorption peaks that Padrón-Navarta et al. (2014) associate with either the [Mg] or [Ti] mechanism. The absence of these peaks associated with the substitution of two protons at the M1-site is notable, as Karato (2013) suggests that this species, which is the slowest diffusing, controls the rate of hydrogen diffusion during D-H exchange (and further suggests that kinetic data from D-H exchange experiments cannot therefore be used to determine electrical conductivity contributions, as this is differently controlled). Contrastingly, the fact that there are no obvious changes in the IR spectra in the annealed samples may suggest that the diffusion data represent the mobility of all defects present, rather than a small group of them, and consequently support the assertion by Karato that bulk hydrogen is mobilised during diffusivity studies (in contrast to electrical conductivity studies that potentially measure only a small subset of interstitial hydrogen). This is difficult to affirm, however, as changes may occur that are simply not be visible in the IR spectra - in the same way that the deuterium peaks are not well represented. Additionally, it has been suggested that different diffusion mechanisms in hydrogen proceed over different timescales (Jollands, personal communication), and it may be that not all of the defects were mobilised during the relatively short D-H exchange runs.

4.6.6 Treatment of errors

Due to the nature of the SIMS data collection technique (depth profiling, whether as single pits or full depth profiles), the error associated with the depth parameter in the D-H exchange data sets (e.g. figure 4.10) is not specific to each point but is an error in the WLI measurement of the total depth of the SIMS analysis pit.[24] As a result, error bars in the x direction (depth/distance) are not included on SIMS data plots. The magnitude of the overall depth error resulting from is shown in figure 4.29 (and discussed in section 4.6.3).

The error on D_H and C_0 values calculated from the fitted data (i.e. in table 4.8) is given as one standard deviation from the least squares fitting solutions[25] and the error in the resulting temperature dependence (Arrhenius relationship) is similarly given accordingly.

---

[24] The SIMS points are assumed to be collected at regular intervals over this depth such that the spacing of data points is calculated as total depth $\div$ number of data points.

[25] Using pcov values from scipy optimize curve_fit where the error on each parameter is calculated using np.sqrt(np.diag(pcov)).

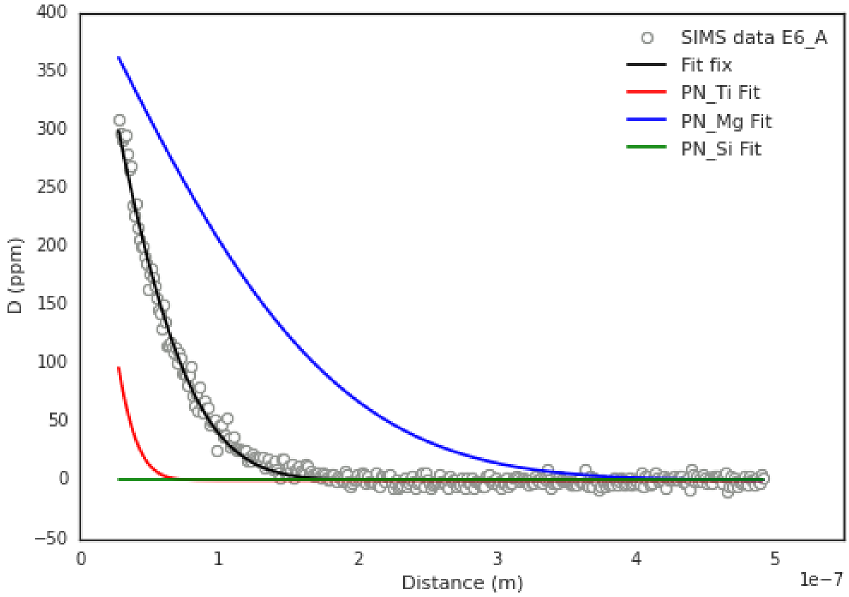

(a)

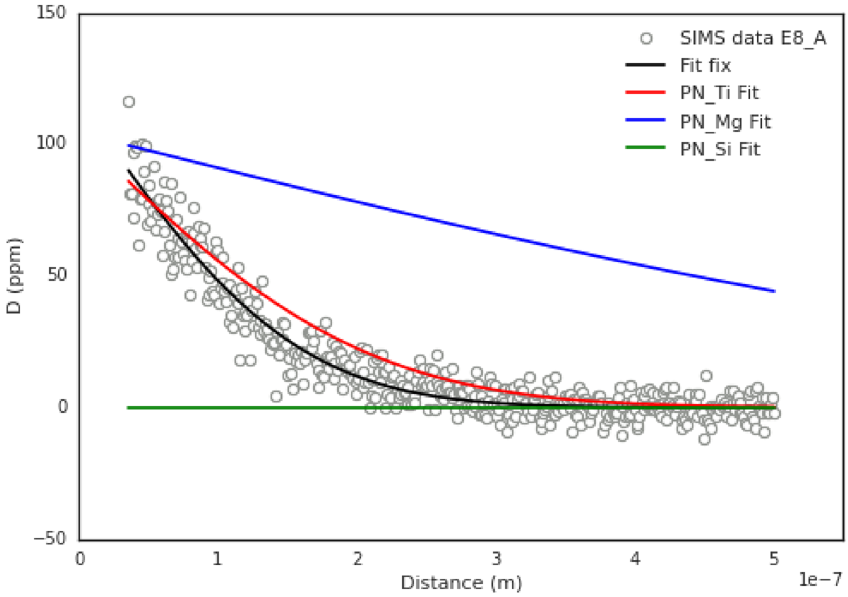

(b)

Figure 4.34: *Fit of hydrogen diffusion values from Padrón-Navarta et al. (2014) to depth-concentration profiles from this study (a) - E6_A, (b) - E8_A. Assuming the same initial concentration at the sink-source interface, and the same t, T run conditions, diffusion co-efficients for each mechanism identified by Padrón-Navarta et al. were used to calculate best fit distance-concentration lines, and compared to the distance-concentration data measured by SIMS for the two grains. At 700°C ((b) - E8_A), the data for the [Ti] mechanism (red line) appear to fit the data reasonably well, but for 600°C ((a) - E6_A) the SIMS data falls between the [Ti] (red) and [Mg] (blue) curves. It is apparent that the diffusivity of [Si] (green line) does not fit the SIMS data, and represents much slower diffusion than is measured in this study.*

4.7 Alternative investigations

In order to run longer diffusion profiles and compare data obtained using a non-depth profiling collection technique (spots across a surface), a large crystal of dry synthetic forsterite was purchased and oriented by F. Nestola (Department of Geosciences, University of Padova, Italy) before being cut into 3mm x 2mm x 1mm cuboids - see figure 4.35. The aim was to follow the procedure outlined by Du Frane and Tyburczy (2012) for San Carlos olivine to compare the data obtained to that from the developed technique - specifically to quantify the effect of using crystals synthesised to contain hydrogen (in comparison to starting with dry samples and using a hydration experiment).

A polished cuboid of forsterite was loaded into a 4mm Pt capsule, along with 4μl liquid H_2O (deionised). The capsule was placed into a standard piston cylinder assembly and stack, as has been previously described, and pressure was increased to 2GPa over 8hours. The temperature was increased to 1000°C and maintained for 16hours, then the run was quenched. Pressure was reduced over a further 8hours and the retrieved capsule was opened. This was repeated with two cuboids of forsterite but intact crystals were not recovered (both were essentially powdered on retrieval), and once again a decision was taken to progress the project in an alternative direction in an attempt to maximise remaining time and resources.

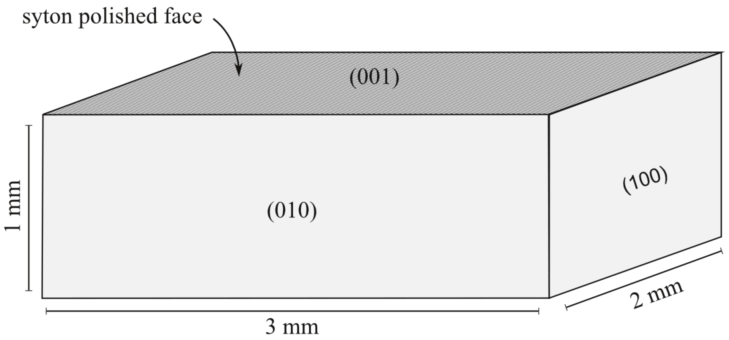

Figure 4.35: *A cut sections of a large forsterite crystal was oriented by F. Nestola and cut into cuboids as shown with different edge lengths for each crystallographic direction.*

4.7.1 Thin films

Note that the work described below represents preliminary developmental work of an alternative experimental procedure. The aim was to compare experiments carried out with a) deuterium thin films and SYTON polished crystals and b) liquid D_2O and SYTON polished crystals in order to investigate the extent to which surface defects influence diffusion, but delays due to equipment failure and unforeseen complications have unfortunately not allowed for further progression in this direction within the timescale of this project.

Reliable SIMS analysis requires good quality (namely, flat) sample surfaces. One of the significant hurdles to obtaining robust hydrogen self-diffusion data using the D-H exchange experimental method outlined is ensuring that this is the case, whilst being unable to polish samples post-exchange.[26] This difficulty is compounded by the presence of D_2O as a fluid phase during experimental runs as there is evidence that in some cases surface reaction and/or partial dissolution occurs leading to micro-topography on crystal faces. This micro-topography may inhibit the diffusion of deuterium in to the sample - deuterium may instead diffuse along grain boundary pathways, or remain on the sample surface (deuterium spikes at the sample surface were evident in some SIMS analysis of H-forsterite grains). Furthermore, D_2O as a fluid under experimental conditions may allow deuterium to be more readily lost from the capsule by diffusion out through the capsule walls, leading to problems maintaining a high a_{D_2O} during runs (Brooker, personal communication, March 2016).

Using liquid D_2O as a source of deuterium may, therefore, influence the diffusion profiles, and experiments could potentially yield diffusion coefficients that are slower than the real values as a result.[27] In order to better describe and quantify the influence of these factors, a method of collecting data under the same experimental conditions and parameters, but utilising a solid deuterium source, was investigated.

The most suitable method available was the ‘thin film’ method (Dohmen et al., 2002; Watson and Dohmen, 2010) in which a discrete layer containing a high concentration of the species of interest is deposited on the sample surface to act as a source. During the experimental run, as diffusion proceeds, the sharp interface between the film and the sample becomes more diffuse, and the concentration profile

---

[26] As discussed previously, polishing would remove the shallow diffusion profiles.

[27] Particularly due to the shallow and therefore near-surface nature of the diffusion profiles being investigated.

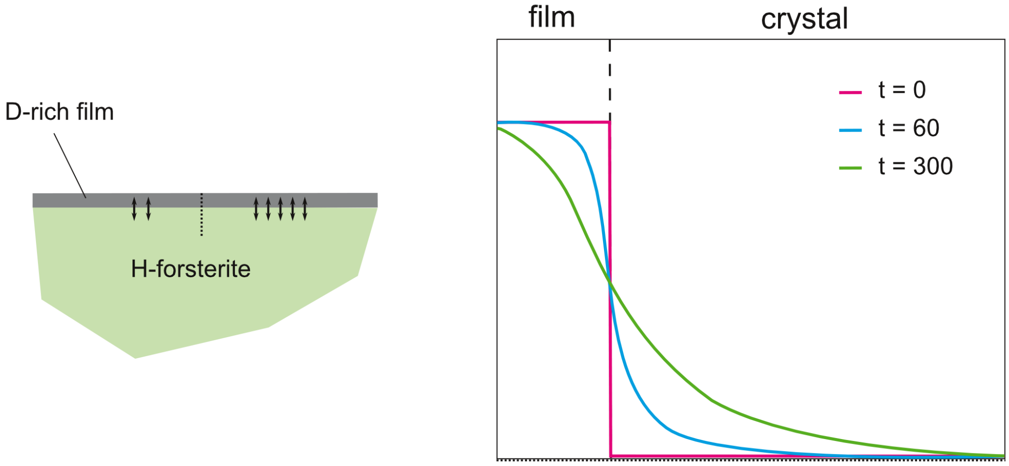

Figure 4.36: *Representation of thin D-bearing film on H-forsterite grain (left): arrows show D-H exchange. At increasing (arbitrary) time intervals, a diffusion profile (right) extracted along the dotted line shown becomes more diffuse. After figure 2, Watson and Dohmen, 2010*

(as measured by SIMS) can be identified and fit in order to determine the diffusion coefficient (see figure 4.36).

Thin films of hydrogen have previously been used in diffusion studies (Chakraborty, 2010), but the deposition of deuterium thin films for use in D-H exchange studies has not been previously attempted. In conjunction with Prof. Sumit Chakraborty and colleagues at the Thin Film laboratory housed within the Institute of Geology, Mineralogy and Geophysics at Ruhr-University (Bochum, Germany), the aim was to deposit 200-300nm thick deuterium-rich films on individual H-forsterite grains, and subsequently run D-H experiments over a similar temperature range as those carried out previously using liquid D_2O. As there is some suggestion that crystal damage introduced by the grit-based (mechanical) polishing of samples may influence diffusion (Chakraborty, personal communication, September 2015), it was additionally decided that samples for thin film deposition should be polished using colloidal silica (i.e. finished with a chemical rather than mechanical polish to avoid a damaged final surface). The plan was to carry out further D-H experiments using (i) thin film samples and (ii) samples polished using colloidal silica but a liquid D_2O source under the same conditions and compare these to previous results in order to determine both the the influence of mechanical polishing and the influence of a solid compared with a liquid source of deuterium.

Preparation of samples for thin film deposition

H-forsterite grains from synthesis S17 and S18 were sorted by hand into large (greater than 200µm) and small (less than 200µm) fractions[28] and epoxy mounts were prepared by carefully placing the grains on sticky tape, placing a standard ring mould around them and then pouring in the epoxy mixture. The epoxy was left to cure under pressure and the mounts were removed from the ring moulds once completely set. Each mount was polished using 6µm, 3µm and 1µm diamond polishing solutions successively, then polished using colloidal silica (SYTON polish method of Flynn and Powell (1979)) - this chemical polishing method avoids the surface damage that can be caused by mechanical polishing. The polished grains were recovered by heating the epoxy blocks on a hot plate until slightly softened, and then gently prizing out each individual crystal using tweezers and a cocktail stick. Retrieved H-forsterite grains were placed polished side up on a sticky-carbon disk (as used to adhere mounts to metal stubs for SEM analysis) in a small plastic sample box in order to easily transport them to the thin-film deposition lab in Germany.

The deposition of a thin film on the sample surface is achieved by pulsed laser deposition (PLD, Dohmen et al. (2002)) - requiring a solid 'target' material on which the laser is focussed to produce a plasma that can be directed at the polished sample surface ('substrate') and deposited in a specified thickness (between 10-500nm). Figure 4.37 shows the thin film deposition set-up as at the Thin Film laboratory in Bochum. A target that is at least 2-3mm square in size and that has a well polished face is desirable to aid with focussing of the laser, making sure that no background material is incorporated into the production of the plasma. In addition, the target should be of a composition that is in equilibrium with the samples on which it will be deposited (Chakraborty, personal communication, April 2016) - ideally of the same composition. A deuterium-bearing solid of forsterite composition was therefore created to serve as a target. A 4mm Pt capsule (the largest that can be used in the 0.5inch piston cylinder assembly) was filled with 6µm D_2O (liquid) and 0.0224g $Fo_{100}*$ starting mix (dry forsterite), welded shut, checked for leaks and placed into a graphite-furance piston cylinder assembly (following the same procedures as outlined in section 4.2). A sample pressure of 2GPa was applied, and temperature was increased to 1700°C at a rate of approximately 50°C/min. After 1hour, the run was quenched and the retrieved

---

[28] Too large a variation in grain sizes can lead to grains being lost during polishing, as to obtain a flat surface on larger grains, the surface has to be polished to a level that is greater than the thickness of the smaller grains.

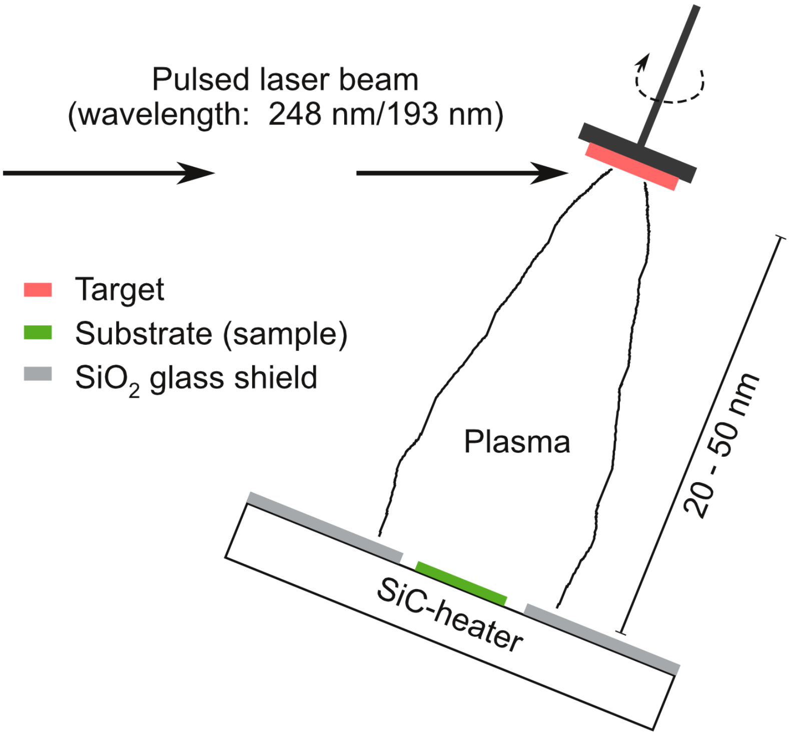

Figure 4.37: *Set up for thin film deposition using Pulsed Laser Deposition (PLD), as used in the Thin Film laboratory in Bochum. After figure 2, Dohmen et al. (2002).*

capsule was cut open along a vertical axis using a diamond wire saw, in order to maximise the surface area. Although the conditions were not sufficient to produce a D-Forsterite glass, the resulting microcrystalline mass was adequately coherent to allow the exposed face to be polished to 1μm diamond solution, as shown in figure 4.38(a) (again, following the procedure outlined for H-forsterite crystals - see section 4.2.3).

The polished H-forsterite samples and target material were sent to Prof. Sumit Chakraborty at the Thin Film laboratory. Several oriented 1mm x 2mm x 3mm cuboids of Cr-forsterite (polished on the largest face) were also sent - firstly so that deuterium diffusion in to the crystals[29] in specific crystallographic directions could be investigated, but also to act as a substantially larger sample on which to test the deposition of deuterium thin films. In an initial trial run, a film approximately 200nm thick was successfully deposited on one of the larger Cr-Fo samples, but SIMS analysis

---

[29] Not D-H exchange, as these do not contain H.

showed that the film contained only negligible amounts of deuterium.[30] Several reasons could explain the lack of deuterium in the film;

i Target material contained none, or very little deuterium

ii Target was too small and the deuterium content in the film produced was diluted

iii Deuterium was lost during PLD process (thin films of deuterium have not previously been produced, although H has been successfully)

In order to address this, a second target material was created using a 5mm $Ag_{70}Pd_{30}$ capsule packed with haplogranite (dry) starting mix (4% Na_2O + 7% K_2O + 18% Al_2O_3 + 70% SiO_2) and liquid D_2O. Haplogranite was chosen due to its lower melting point - creating a target that is a glass rather than microcrystalline is advantageous as, in theory, there is more likely to be a homogeneous distribution of deuterium and additionally it should be easier to polish. The specific composition was chosen as the mix had already been prepared for use in other work[31] and the melting point was known to be below 1000°C. Due to the larger capsule size, a tapered sample assembly to fit a 0.75inch piston cylinder bomb was used. The larger assembly uses a graphite-furnace housed in pyrex and talc, as for the smaller one, but the furnace is tapered to be thicker around the sample - see figure 4.39.

The assembly was placed into the piston cylinder stack - as previously described except that the hole in the centre of the bomb is 0.75inch) - and subject to 1050°C, 1GPa for 1hour before being quenched. The capsule was retrieved and cut open, and a fragment of the glass created was checked using SIMS to confirm it contained a relatively high proportion of detuerium. As can be seen in figure 4.38(b), the exposed surface of the glass displayed evidence of fracturing, and therefore the decision was taken not to try to polish the surface further and risk losing fragments (greater preserved surface area was deemed a higher priority than a greater degree of polish). The haplogranite glass recovered from the opposing side of the capsule was ground to a fine powder and cold-pressed into a pellet which was also sent to the Thin Film laboratory to serve as a back-up/alternative target.

---

[30] Around the level that would be expected from the normal concentration in air.

[31] By T. Stokes

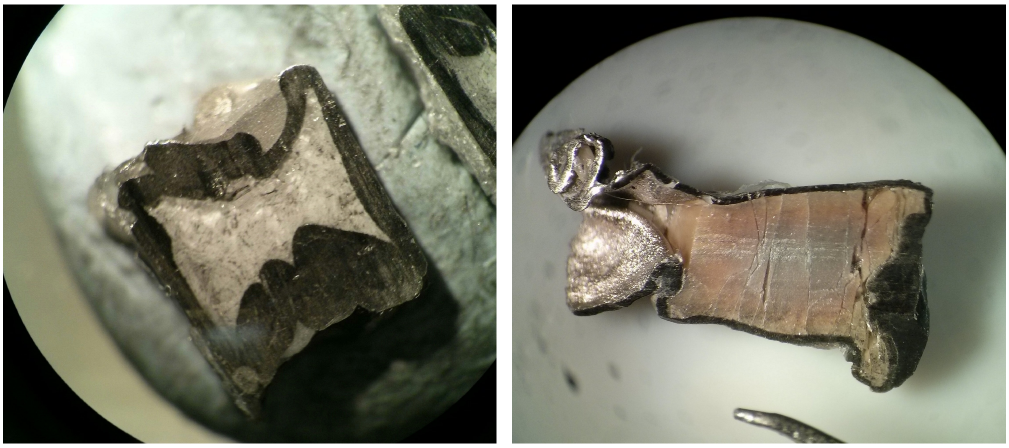

(a) ***(b)***

Figure 4.38: *(a) Cut capsule showing D-bearing microcrystalline forsterite created as the initial target for producing a thin film of deuterium on H-forsterite grains. SIMS analysis indicated that the thin film deposition using this as a target was unsuccessful. Field of view approximately 6mm. (b) Cut capsule showing D-bearing haplogranite glass created as a second attempt target for thin film deposition. Field of view approximately 12mm.*

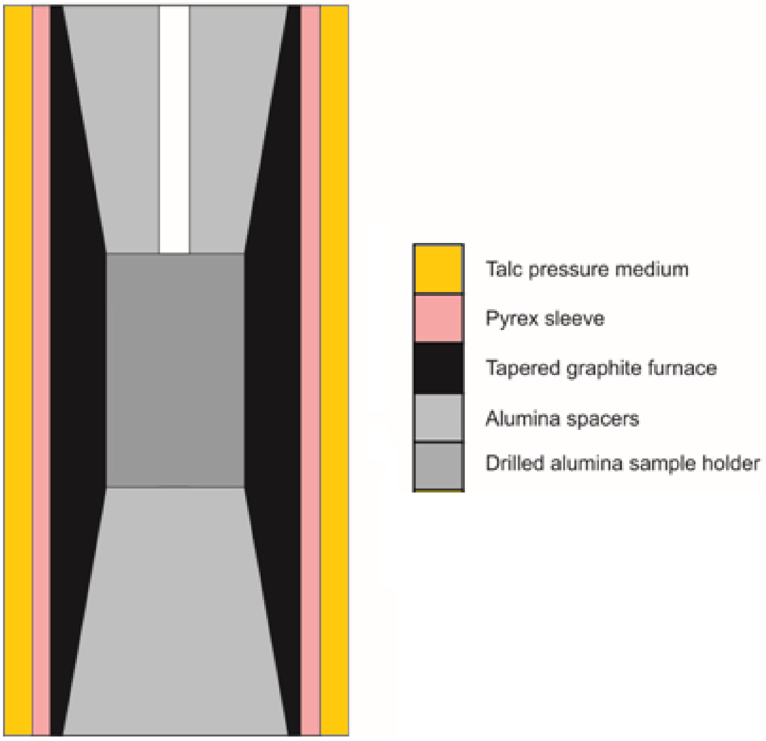

Figure 4.39: *The sample assembly used in 0.75inch bomb piston cylinder runs. The principle and materials are the same as for the smaller assembly, but the graphite furnace (and correspondingly the alumina spacers) are tapered as shown. Adapted from a diagram produced by G. Bromiley. Assembly is cylindrical with a diameter of 0.75inch.*

4.8 Summary

Hydrogen diffusion is complex and its measurement presents several challenges, even in a relatively simple material such as forsterite. Determining the diffusivity is a non-trivial task requiring the assiduous design of experimental and analytical procedures. Hydrogen diffusion is dependent on local point defect populations, which in turn are strongly controlled by chemical potentials, and the variability of defects even in samples synthesised under controlled conditions highlights the importance of using starting materials containing the relevant hydrogen defects to be studied. The temperature dependence of the diffusion rate changes as the mechanism responsible changes, and influences the extrapolation of data. If studies contain concentrations of defects that are out of equilibrium under the conditions of hydrogen diffusion, diffusion may be artificially influenced by complex crystal chemical changes. Knowledge of the relevant incorporation mechanisms and defects present in each study is therefore critical and, as a result, care should be taken with both the interpretation of results from previous hydrogen diffusion studies and the design of future ones. Additionally, the nature of the sample may influence hydrogen lattice diffusion, and the (faster) process of grain boundary diffusion may have a controlling role. Consequently an important aspect of the approach used in this study, compared to other previous studies, is that starting materials were synthesised to contain a hydrogen defect population fully equilibrated under the high pressure conditions being investigated.[32]

---

[32] While seemingly novel at the outset of this study, this method has since been independently adopted and advocated by other authors (i.e. Padrón-Navarta et al., 2014).

CHAPTER 5

Spinel

5.1 Introduction

The general formula AB_2X_4, where X can be O^{2-}, S^{2-} or Se^{2-}, describes a wide variety of minerals with a spinel-type structure. Amongst these are 24 described oxide spinels (in which $X = O^{2-}$), including spinel *sensu stricto* ($MgAl_2O_4$) - the common Mg-Al end member - and ringwoodite ($Si(Mg,Fe)_2O_4$) - the high-pressure isomeric polymorph of forsterite (predominant in the mantle transition zone).[1]

In contrast to other mantle NAMs, natural spinel (*sensu stricto*) is almost completely anhydrous. Hydrogen diffusion in natural spinel is therefore not well characterised (compared to olivine, pyroxene), as it does not contribute to the water content of the mantle and few studies have given it significant attention.[2] However, studies such as Bromiley et al. (2010) have shown that defect, or non-stoichiometric, spinel *is* capable of storing water in the same manner as other nominally anhydrous mantle minerals. The solubility of water in defect spinel is high, and the incorporation mechanisms are thought to be similar to ringwoodite, leading several authors (Bromiley et al., 2010; Hertweck and Ingrin, 2005) to consider the diffusion of hydrogen in non-stoichiometric spinel as a low-pressure analogue for ringwoodite in the transition zone. A study of D-H exchange in non-stoichiometric

---

[1] For a detailed review of all known spinel-type minerals, see (Biagioni and Pasero, 2014).

[2] A review of the main studies that have considered hydrogen diffusion in spinel is given in chapter 2.

spinel therefore provides a useful contribution to the literature on hydrogen diffusion in NAMs, as well as supplementing the data collected for olivine and supporting the method development as a test of the technique.

From this point on, to avoid confusion, the term ‘spinel’ will be used to refer to the experimental material ($Mg_{0.4}Al_{2.4}O_4$, technically defect spinel). The natural mineral spinel (*sensu stricto*), will be distinguished by the notation ‘natural spinel’, and ringwoodite will be referred to only by name. Any other compositions mentioned (as used in other studies) will be accompanied by the relevant chemical formula.

5.1.1 Experimental design

Synthetic crystals of spinel as used in this study are easily synthesised, with sizes of up to several centimetres. Because the spinel samples are larger in size than the H-forsterite samples, both long duration D-H exchange experiments (analysed by measuring the concentration of deuterium at set intervals across an exposed face) and short duration D-H exchange experiments (analysed via depth profiling, as for H-forsterite samples) were carried out, in order to provide a direct comparison between the data collection techniques. Previous work carried out by Bromiley et al. (2010) on the same starting material characterised the maximum water solubility (subject to IR calibrations).

In addition to D-H exchange experiments, a number of hydrogen and deuterium uptake experiments were also carried out. Rather than the exchange between hydrogen and deuterium, uptake experiments measure the amount of hydrogen/deuterium incorporated in to the spinel structure at different temperatures, providing additional data on the movement of hydrogen in defect spinel. Uptake experiments also serve as a means to compare the diffusion of hydrogen relative to deuterium, as runs were repeated using both hydrogen and deuterium at the same temperatures. Uptake experiments involve subjecting a dry spinel sample to defined pressure and temperature conditions alongside a source of hydrogen (or deuterium), allowing hydrogen (or deuterium) to diffuse in to the spinel structure. Diffusion profiles in to the spinel as a function of duration and temperature can be compared to those for exchange experiments, yielding additional data on the incorporation and diffusion of hydrogen/deuterium in non-stoichiometric spinel.

5.2 Experimental procedure

The experimental procedure used in this study to investigate the diffusion of hydrogen and/or deuterium in spinel is, for the most part, similar (if not the same) as described in chapter 4 for olivine, and will only be described in detail here where it differs. The major difference in approach is that, primarily due to time and resource constraints, the spinel was not specifically synthesised under mantle conditions for this study, and contains a low initial water concentration.

5.2.1 Starting material

The starting material used for spinel experiments was previously synthesised as a single large boule, using the Verneil method, for work carried out by Bromiley et al. (2010).[3] Following their experiments, the remaining piece of the boule (a circular slice approximately 2cm in diameter), was provided for use in this study. It has the composition $Mg_{0.4}Al_{2.4}O_4$ and initial FTIR measurements (and corresponding calibration), described by Bromiley et al., indicate a water concentration of 58 ppmw H_2O. However, recent recalculation of the water contents using the calibration of Libowitzky and Rossman (1997) suggests that the water contents given in Bromiley et al. (2010) may be overestimated by 20-30% (Bromiley et al., in prep - see appendix D). The sample was cut and polished by Mike Hall at the Sample Preparation Facility, School of Geosciences, University of Edinburgh to create 1mm cubes. Due to the cubic structure of spinel, no diffusion anisotropy is expected (and has not been previously observed) and orientation of the samples with respect to the crystallographic axes was therefore not considered. Each cube was polished on a single face using colloidal silica (SYTON polish method of Flynn and Powell (1979)).[4]

---

[3] Referred to as synthetic spinel 1 in their study.

[4] The SYTON polish method was used in place of a mechanical polishing technique to avoid damage to the crystal surface that might inhibit diffusion, see discussion in chapter 4, section 4.7.1.

5.2.2 Exchange experiments

Spinel hydration

As the initial spinel contains only a small quantity of water, samples to be used in D-H exchange experiments were first subject to a ‘wet’ anneal, in order to increase the initial hydrogen concentration (this was not necessary for uptake experiments). 3mm Pt capsules were prepared as for H-forsterite synthesis experiments (see 4.2.1) and either one or two spinel cubes were placed in to the capsule with the syton polished face/s facing towards the top of the capsule (to aid identification of orientation)[5] along with 3µl of de-ionised liquid water. Capsules were welded shut, weighed and checked for leaks (following the standard procedure outlined previously) but, in contrast to H-forsterite capsules, were not flattened after the final weld due to the increased the risk of damage to the spinel cubes.[6] Additionally, the resulting capsule asymmetry gives an indication of the orientation of the capsules and further eases the identification of the spinel orientation on retrieval. Initially (runs A1-A5), capsules were also packed with a buffer powder of the same composition as the spinel[7] but in these runs the recovered spinel cubes were substantially fractured and it was suggested that including the powder might have been a contributing factor (Chakraborty, personal communication).

Prepared capsules were placed into a talc-pyrex (graphite furnace) assembly and loaded in to the piston cylinder stack (see chapter 4, figure 3.1). In runs A1-A5, the assembly used was identical to that used for H-forsterite (shown in figure 4.2). However, as spinel cubes were fractured when recovered from these runs, an alternative assembly was used for runs A6-A11. In the modified assembly (shown in figure 5.1), the central spacer below the sample capsule is composed of fired salt (NaCl) rather than crushable alumina. The salt spacer in the modified assembly absorbs more of the compression when the sample is subject to high pressure, and consequently cushions the capsule, as well as helping to maintain hydrostatic conditions during decompression. Whereas the pieces for the standard assembly are all manufactured externally and ordered in bulk, the salt pieces for the modified assembly were specifically made by hand. A mixture of fine and medium ground salt was packed

---

[5] Although the crystallographic orientation is not important, the orientation of the polished face is, because diffusion potentially differs in this direction compared to the other, unpolished, faces.

[6] As they are larger in size; 1mm compared to the 100-200µm H-forsterite samples.

[7] Prepared from high purity oxide powders, in the same way as the starting mix for synthesis of H-forsterite.

into a steel ring mould and pressed (at approximately 1 ton), then retrieved from the mould and dried out in an oven at 100°C for an hour. The salt pieces were then baked in an enclosed air furnace at 650°C for 12-24 hours, in order to drive off any volatiles. Individual pieces were manually filed in order to ensure accurate final dimensions (12.5mm tall, 5mm diameter).

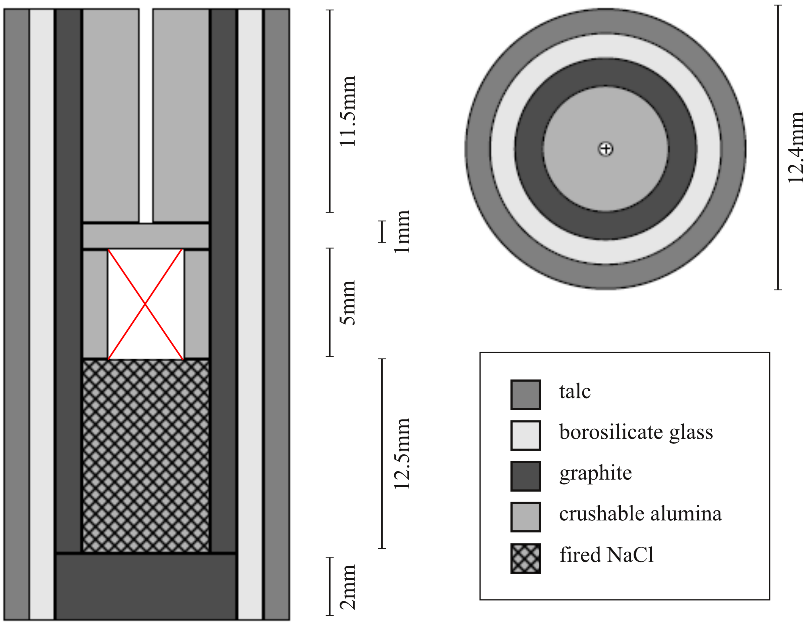

Figure 5.1: *Schematic cross-section (left) and top view (right) showing the modified 0.5" talc-pyrex piston cylinder assembly used in spinel hydration runs. Red cross indicates void for sample capsule.*

In order to minimise potential damage to the spinel samples, the sample pressure was increased to 1GPa over a minimum of 4 hours.[8] As with H-forsterite runs, temperature for spinel hydration runs (either 800°C or 900°C) was applied only after the target pressure had been reached, and was raised at a rate of approximately 50°C/min. Pressure and temperature were monitored and maintained for 24 hours, then temperature was reduced rapidly by shutting off power to the assembly, in order to quench the samples. Pressure was reduced slowly (at the same rate as it was increased, reduced to atmospheric pressure after 4-6 hours). Retrieved capsules were opened, and samples were checked optically for major cracks and/or any alteration, as well as to

---

[8] In initial experiments, pressure was increased faster but this resulted in fragmented samples unsuitable for further use.

ensure that the orientation of the polished face could be readily identified. In some (but not all) capsules, water was evident on piercing as an audible hiss and/or bubbles escaping - these runs are highlighted in table 5.1. In total, 11 hydration annealing experiments were run, resulting in five samples retrieved whole and suitable for use in subsequent D-H exchange runs. In addition, fragments of a further spinel cube that fractured during hydration (A5) were also polished and used in a supplementary D-H exchange run.

Table 5.1: *Experimental conditions for spinel hydration runs - all 24hr in duration.*

Run #	Assembly	P (GPa)	T (°C)	Notes
A1^{+}	alumina	-	-	PC failure
A2^{+}	alumina	2	800	spinel fractured - orientation lost
A3^{+}	alumina	2	800	sample lost during recovery
A4$^{+\dagger}$	alumina	2	800	evidence of reaction (with buffer?)
A5$^{+^{\dagger}}$	alumina	2	800	spinel highly fractured
A6	salt	1	800	sample lost
A7†	salt	1	800	
A8	salt	1	800	
A9	salt	1	800	
A10	salt	1	800	
A11	salt	1	900	

$^{+}$ *Denotes runs in which a buffer powder was included in the capsule (see text for discussion).*
† *Denotes runs in which evidence for liquid was observed on piercing the capsule.*

Short duration

Four short duration D-H exchange experiments were carried out following approximately the same method as for H-forsterite (outlined in 4.2.4). In two runs (E10 and E25), a single cube of hydrated spinel was placed into a 3mm Pt capsule (again with the syton polished face up) along with 1µl D_2O. In a further two runs (E11 and E12), fragments (100-200µm in size) of hydrated spinel recovered from run A2 were used in place of the whole cubes (having first been polished on one identifiable face). Filled capsules were welded shut, weighed and checked for leaks. As for the hydration runs, the top end of each capsule was not flattened and capsules were placed in a modified (salt) piston-cylinder assembly in the standard 0.5 inch bomb stack. Pressure was increased over 4-6 hours (again to minimise potential damage to the samples), and temperature was raised only once the target pressure had been achieved. Both temperature and pressure were maintained for the duration of the D-H exchange run. As with H-forsterite D-H exchange runs, each was 600s in length in order to provide a measurable diffusion profile over 1-2μm. Runs were then quenched and pressure was subsequently bled off over a further 4-6 hours. Once recovered from the assembly, each capsule was opened and the orientation of each sample was marked to aid identification when mounting for analysis. Details of all spinel D-H exchange runs are given in table 5.2.

Table 5.2: *Short duration spinel D-H exchange runs.*

Run #	Starting sample	P (GPa)	T (°C)	Duration	Notes
E10	A7	2	800	600s	
E11	A2	1	700	600s	
E12	A2	1	600	600s	fragmented
E25	A9	1	800	600s	spinel retrieved whole

Long duration

Three long duration D-H exchange runs were carried out for comparison following the same procedure as described above, but with the experimental duration varying from 3 days (at 1000°C) to 7 days (at 800°C) - see table 5.3. Analysis across the surface of each 1mm grain should, therefore, reveal a full diffusion profile, with concentration dropping off from either side to a minimum in the middle of the grain (as shown by the hypothetical profile A-B in figure 5.2). The grain orientation (relative to the syton polished face) was again recorded, as shown in figure 5.3.

Retrieved long duration D-H exchange samples were polished to expose the centre of each spinel cube, in order to measure diffusion by analysing a series of points across the surface (see figure 5.2). The polishing method is the same as described in section 4.2.3 for the preparation of H-forsterite grains, but samples are polished to 0.5mm thickness using grit paper (i.e. to expose the centre of the grain) before being polished with successively finer diamond solutions (6μm, 3μm, 1μm) to create a suitable face for SIMS analysis.

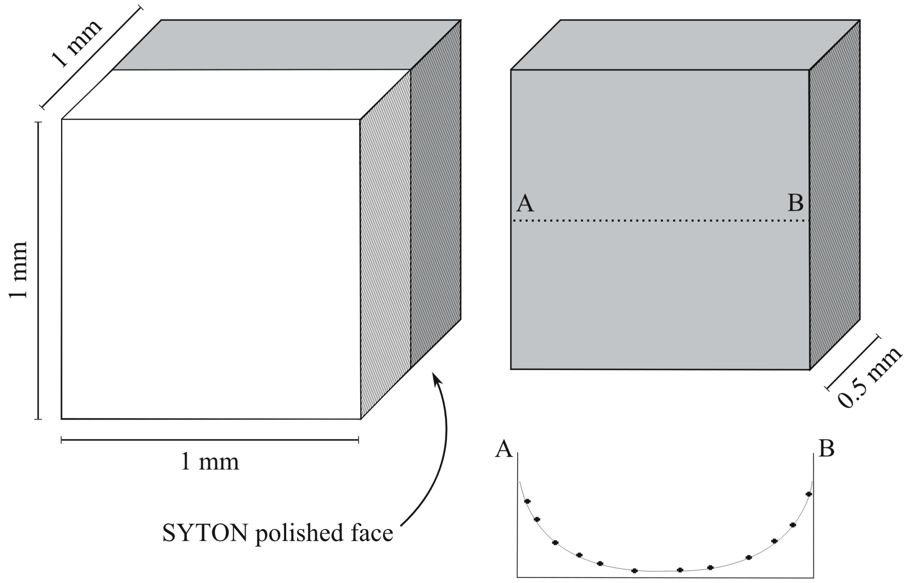

Figure 5.2: *1mm^3 cubes of spinel with one syton polished face (left) are used as the starting material. For both long duration D-H exchange runs and uptake runs, cubes are polished following experimental runs such that one half of the cube (white portion) is removed. Analysis is then carried out on the exposed central face of the resulting cuboid (right) to identify the diffusion profile A-B. As diffusion of H/D proceeds in to the spinel from both directions, an ideal profile should drop to a minimum in the middle (as shown). If the nature of the surface (due to polishing) influences diffusion, the profile A-B may be asymmetric.*

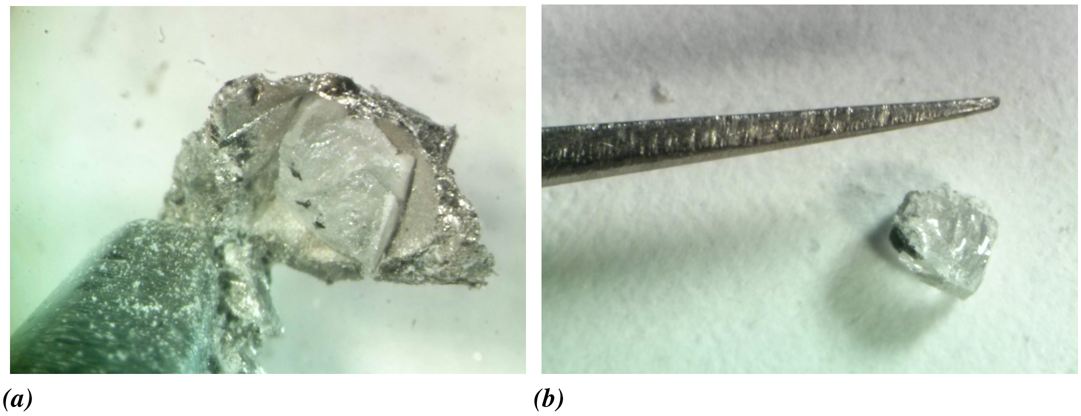
(a) ***(b)***

Figure 5.3: *(a) Reflected light image of an opened capsule containing an (almost) entire spinel cube (E14), (b) a recovered spinel cube (E10) with orientation marked. Both grains are approximately 1mm across.*

Table 5.3: *Long duration spinel D-H exchange runs.*

Run #	Hydration	P (GPa)	T (°C)	Duration (hrs)	Notes
E13	A8	2	800	168	
E14	A10	1	900	96	top corner fractured
E15	A11	1	1000	72	spinel recrystallised

5.2.3 Uptake experiments

In order to further investigate hydrogen diffusion in spinel, a set of experiments to measure the uptake of both hydrogen and deuterium in the same, non-stoichiometric $Mg_{0.4}Al_{2.4}O_4$ spinel were carried out. Deuterium is used in addition to hydrogen, primarily due to the relative ease of obtaining low backgrounds during SIMS analysis and therefore better quantification of data, but also in order to compare hydrogen and deuterium diffusion. The same original starting material as for spinel D-H exchange experiments was used (1mm cubes, with one syton polished face), but no initial hydration run was performed.

For each uptake run, a single spinel cube was loaded, syton polished face up, into a 3mm Pt capsule with 3µl of D_2O. As with previous spinel runs, the capsule was welded shut and checked for leaks, with the top end of each capsule left un-flattened. A total of nine uptake experiments were carried out at temperatures of 1000°C, 1200°C and 1400°C, with three separate runs of different durations at each temperature (see table 5.4). In all cases pressure was increased to 1GPa over a period of at least 4 hours and temperature was only applied once the target pressure had been reached. Pressure and temperature were monitored and maintained for the run duration and temperature was reduced rapidly to quench the samples. Pressure was then bled off over a further 4-6 hours. The orientation of each sample relative to the syton polished face was noted and marked as capsules were opened, and the spinel cubes were polished in the same manner as long duration D-H experiments, in order to expose the central face of the grain (figure 5.2).

Table 5.4: *Spinel deuterium uptake runs, all carried out at 1GPa.*

Run #	**T (°C)**	**Duration**	**Notes**
E16 / UP03†	1000	48hr	recrystallised - opaque white
E19 / UP02	1000	17hr	spinel highly fractured
E22 / UP04†	1,000	10hr	partially fragmented
E17 / UP06	1200	24hr	capsule slightly deformed - leak?
E20 / UP08	1200	12hr	
E23 / UP09	1200	6hr	some reaction/recrystallisation
E18 / UP01	1400	12hr	capsule compressed - leak?
E21 / UP05	1400	8hr	
E24 / UP07	1400	4hr	capsule split, spinel exposed

† *Denotes runs in which evidence for liquid was observed on piercing the capsule.*

5.3 Analysis methods

5.3.1 Sample Preparation

Spinel samples from long duration D-H experiments and uptake experiments were polished subsequent to piston cylinder runs in order to expose a central slice for analysis. All spinel samples were mounted in indium, with orientations carefully noted and marked on schematic drawings of the mounts. Figure 5.4 shows a sketch of mount M1 (two were used, M1 for uptake samples, M2 for D-H exchange samples) with grain orientations indicated (and some annotation from initial SIMS investigation. In conjunction with reflected light images,[9] mount maps like the one shown were used during analysis to aid the identification of samples and to determine appropriate measurement sites.

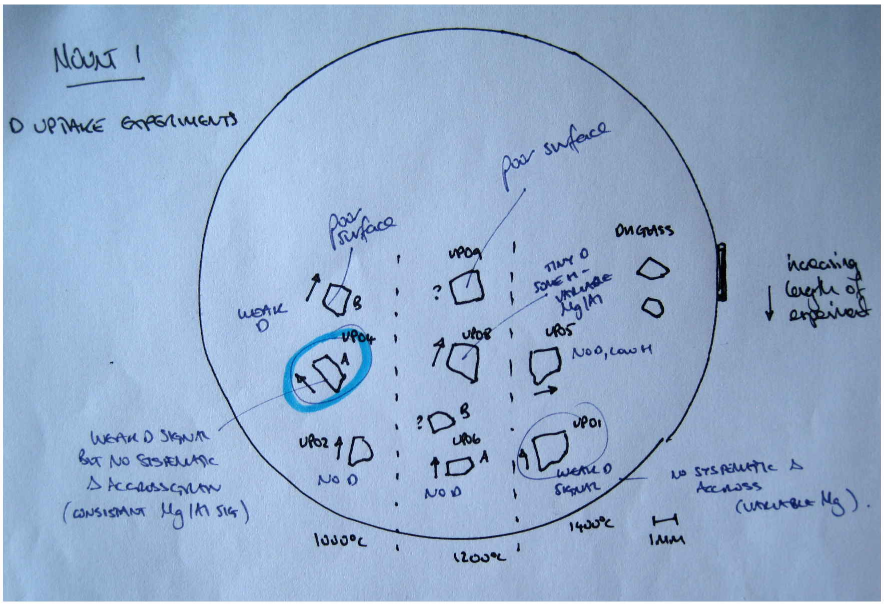

Figure 5.4: Schematic drawing of spinel SIMS mount M1, with direction of diffusion through SYTON polished face indicated by black arrows. Annotations are notes taken during SIMS analysis.

---

[9] Taken using a Leica DMLP reflected/transmitted light polarizing microscope.

5.3.2 SIMS

Three standards were used during SIMS analysis of the spinel samples; a lower water content spinel sample (from the same boule as the experimental starting material), a H-rich spinel (characterised by Bromiley et al., 2010), and a fragment of the DH glass created specifically as a SIMS standard for the work on H-forsterite (see 4.2.6). A spinel cuboid on which only the annealing step had been performed was also analysed, to quantify the starting hydrogen content for D-H exchange experiments. SIMS analysis was essentially the same for spinel samples as for H-forsterite - the aim being to identify hydrogen or deuterium concentration profiles with depth in to the samples. In short D-H exchange samples the depth profiling technique was used, as previously described and discussed in detail (sections 3.2.1 and 4.3.2). For long duration D-H exchange and uptake samples, the depth-concentration relationship was identified by measuring the concentration at spots across the (exposed, central) grain surface - as illustrated in figure 5.2.

5.3.3 SEM

The spinel samples analysed by SIMS were subsequently imaged using the SEM (SE imaging) in order to check for cracks or inclusions at the analysis sites. Additionally, SEM images were used to identify and map out the analysis spot trails for the longer profiles (long duration D-H exchange and uptake experiments). Images (such as shown in figure 5.5) were used to determine the spacing of the analysis spots, and hence quantify the diffusion profile distance. The depth of SIMS depth profile pits on a short D-H exchange samples were measured using WLI.

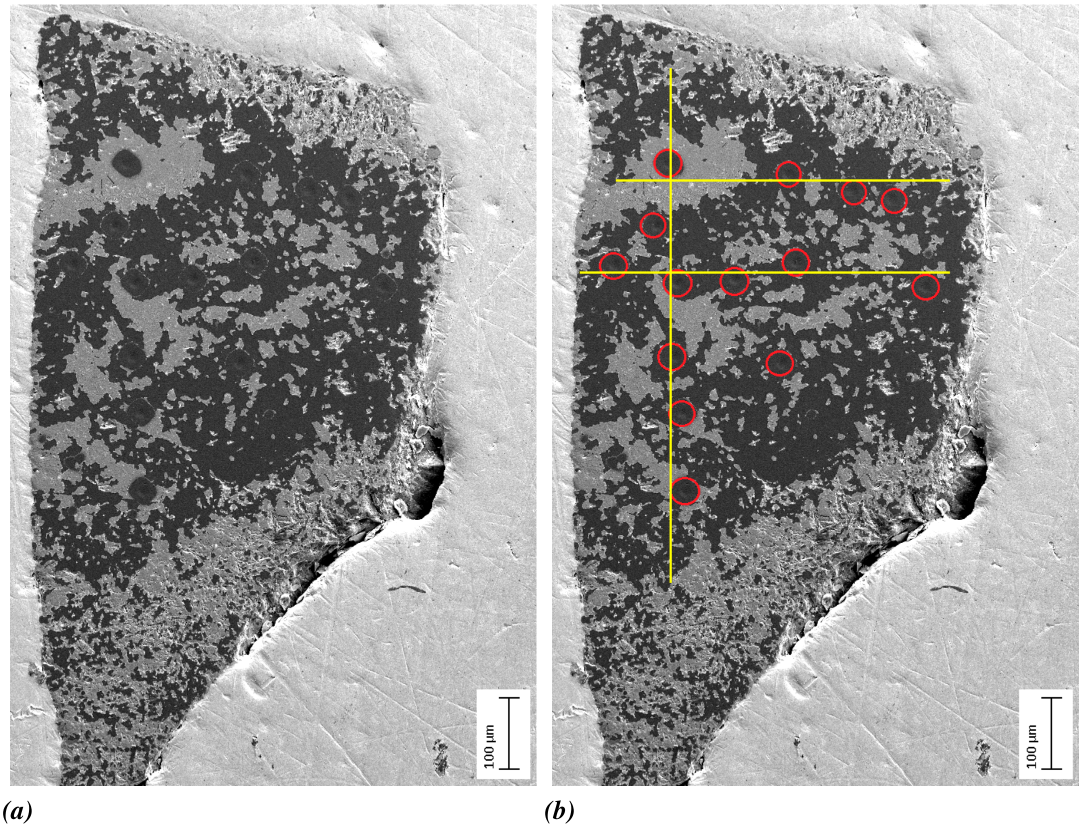

Figure 5.5: *(a) SEM image (SE) of spinel UP04_A; (b) analysis spots highlighted in red - yellow lines indicate transects taken across the grain to identify diffusion trends (note that points were chosen to avoid impurities and/or topography on the grain surface and are therefore not in straight lines).*

5.4 Additional H/D diffusion investigation

In addition to the D-H exchange and uptake runs described above, a secondary set of experiments designed to investigate hydrogen/deuterium diffusion profiles by FTIR were carried out. Following the lack of robust data obtained from initial D-H exchange and uptake runs (as will be discussed in section 5.6), the aim was to provide complimentary data and, additionally, to investigate potential mechanisms of hydrogen/deuterium loss during runs (contributing to low concentrations during SIMS analysis of previous samples). The approach and procedure was designed to be an extension of the previous uptake work (described above) and the experimental method is therefore based on the sample principles and follows largely the same steps. Due to time constraints, the majority of the experimental work was carried out by G. Bromiley and samples were then analysed by FTIR at The University of Bristol in April 2016 (alongside H-forsterite samples). An expansion of this work, as described below and discussed further in section 5.6, has been prepared for publication - a copy of the latest draft at the time of submission is included in appendix D.

5.4.1 Method

Similar to uptake experiments, this additional work was carried out as a series of annealing experiments, allowing either hydrogen or deuterium to diffuse in to the spinel structure under specified conditions. No prior hydration was carried out. The sample material (MgAl defect spinel as used for all other spinel runs) was prepared as 1mm x 1mm x 2mm cuboids, polished by hand to 1µm diamond. Capsules were prepared from 2mm Pt tube as previously described (final length approximately 5mm), loaded with a single spinel cuboid, and packed with a non-stoichiometric mix of Al_3O_3 and MgO (such that the powder was the same composition as the spinel). 10µl of either H_2O or D_2O was added and each capsule was then welded shut and checked for leaks. For each experimental run, a pair of capsules was prepared - one containing H_2O and one D_2O - in order to investigate the diffusion of both hydrogen and deuterium under identical conditions. A custom alumina sample holder was prepared to fit the 0.75inch bomb piston cylinder assembly, with two central voids to accommodate the two capsules in each run. Figure 5.6 illustrates the assembly for the 0.75 inch piston cylinder bomb, which differs from the 0.5 inch assembly by having a tapered graphite furnace, the design of which ensures that the thermal gradient within the capsule is minimal - less than 10°C under experimental conditions described (Bromiley, unpublished data). Pressure was increased slowly to 1GPa for all runs, and temperature was subsequently applied following the same procedure as for all other piston cylinder runs described. Experimental runs were deliberately performed at low temperatures (500°C - 800°C) in order to avoid recrystallisation. Details for each run are given in table 5.5.

After the specified duration, runs were quenched by shutting off power to the piston cyclinder stack, allowing temperature to drop rapidly (below 100°C within 30s). Recovered capsules were opened and D- and H-spinels were retrieved and identified.

Table 5.5: *Spinel hydrogen/deuterium diffusion runs and conditions.*

Run #	**T (°C)**	**Duration (hours)**	**Notes**
hysp1	400	97	H_2O - spinel completely recrystallised D_2O - spinel completely recrystallised
hysp5	500	97.5	
hysp3	600	75	
hysp6	700	47	
hysp4	800	41	sample slightly friable

All runs were carried out at 1GPa.

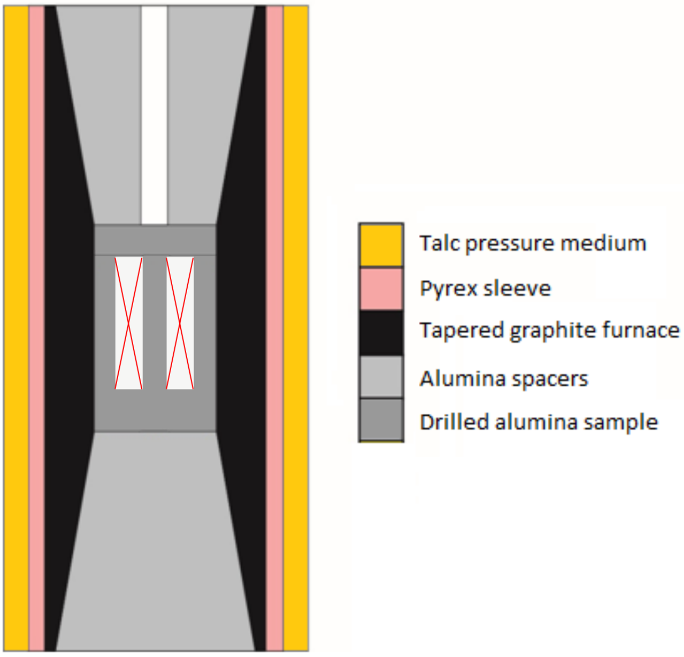

Figure 5.6: *The sample assembly used in 0.75inch bomb piston cylinder runs. The principle and materials are the same as for the smaller assembly, but the graphite furnace (and correspondingly the alumina spacers) are tapered as shown. The central piece is an alumina plug that is filed to create two voids (indicated with red x) in which the capsules sit. Adapted from a diagram produced by G. Bromiley. Assembly is cylindrical with a diameter of 0.75inch.*

5.4.2 Analysis

Samples from this additional set of samples were analysed by FTIR at The University of Bristol, and were not investigated by SIMS. As a result of the larger nature of the samples, it was possible to prepare double-polished wafers of known thickness - allowing a correction for thickness and subsequent calibration for concentration to be applied.

5.4.3 Sample preparation

Each spinel cuboid was sectioned using a 0.2mm diamond wire saw to produce a slice from the centre of the grain (as shown in figure 5.7). Each slice was mounted in crystalbond and polished on both sides (again using standard diamond polishing solutions) to produce double-polished wafers suitable for FTIR analysis. After polishing, samples were soaked in acetone and washed using distilled water to remove any residues.

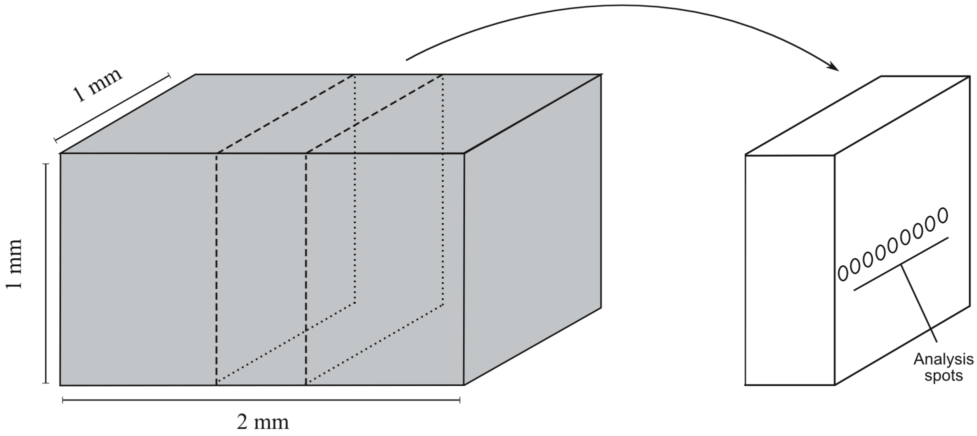

Figure 5.7: *Following experimental runs, a central slice is cut from each spinel cube (as illustrated) and polished for FTIR analysis.*

5.4.4 IR Spectroscopy

The main OH peaks identified in spinel samples are at 3,525cm^{-1} and 3,355cm^{-1}, consistent with previous work (i.e. Bromiley et al., 2010) that has suggested the dominant bands are a single absorption band at 3,343-3,352cm^{-1} and a doublet consisting of two bands at 3,505-3,517cm^{-1} and 3,557-3,566cm^{-1}.[10] OD peaks are evident at 2,615cm^{-1} and 2,490cm^{-1}, corresponding to a shift of the identified OH peaks by approximately 1.35 (as discussed in 4.5.4). These peaks are indicated in figure 5.8(a), which shows profiles taken along a transect from the edge to centre of grain hysp6 (as indicated by the red line in figure 5.8(b)). The deuterium peaks decrease in intensity with distance from the edge of the grain, defining a profile of deuterium diffusion in to the sample. Although spectra were collected at intervals of 20µm (as previously noted), only alternating profiles have been plotted in figure 5.8(a) for clarity and thus represent approximately 40µm intervals.[11]

The obtained FTIR spectra for samples hysp1, hysp3-6 were thickness corrected, and a linear background over the range 4,000cm^{-1} - 2,000cm^{-1} was subtracted. Fitting to determine OH/OD concentrations was then carried out using the Multipeak Fitting 2 toolbox within *IGOR Pro* software. Fitting was carried out by G. Bromiley, based on previous work and using a similar approach to that of Bromiley et al. (2010), with the exception of using the calibration of Libowitzky and Rossman (1997) (rather than Paterson (1982)) to determine OH contents. Further details of this fitting can also be found in Bromiley et al., in prep (appendix D).

---

[10] The doublet appears not to be resolvable into separate bands at the resolution of data available for this study.

[11] Deuterium therefore persists to a distance of around 100µm from the edge of hysp6.

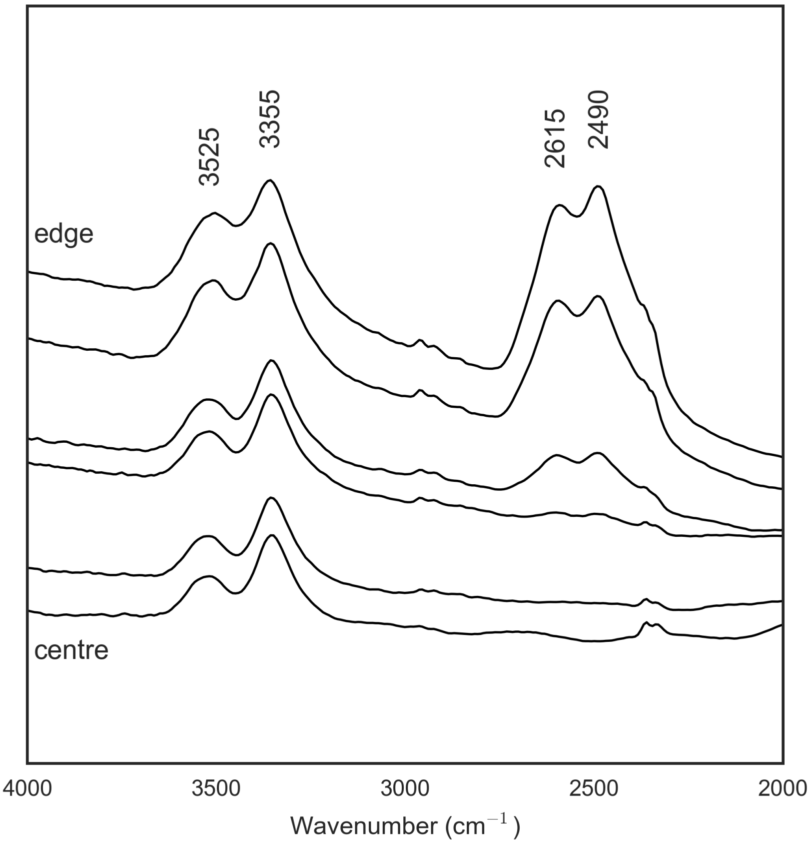

(a)

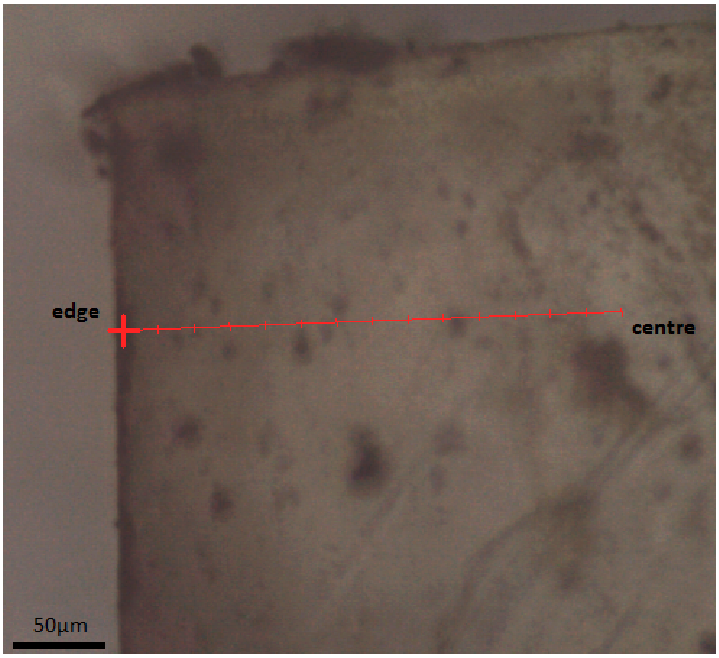

(b)

Figure 5.8: *A series of FTIR spectra (a) taken across spinel hysp6 from the edge to the centre (b), showing the decreasing intensity of the deuterium peaks (2,615cm^{-1}, 2,490cm^{-1}) with distance in to the crystal. Note that spectra shown are not background corrected, and have been offset vertically for clarity.*

5.5 Fitting data

The fitting of distance-concentration profiles for spinel data were carried out using a *Python* fitting script based on the one written for H-forsterite profiles (see section 4.4, appendix E). For D-H exchange and deuterium uptake experiments (E#, UP# - investigating diffusion of a species in to the crystal structure), the only adjustment to the script was the time parameter entered in Fick's law, as the spinel diffusion runs were longer (and varied) in duration.[12]

For the diffusion profiles in spinel samples hysp3-6, the *Python* fitting script was modified to fit data to the following iteration of Fick's law;[13]

$$C = C_0 - erf\frac{x}{2\sqrt{Dt}}\left(C_0 - C_i\right) \tag{5.1}$$

where C_i is the original H/D content (as previously, C (y data) is the concentration of the diffusing species at a given point in the crystal, d (x data) is the distance (m) of that point from the source (essentially distance from crystal edge), D is the diffusion coefficient (m^2/s), t is the duration of the D-H exchange experiment (s) and C_0 is the concentration of the diffusing species at the source-sink interface (crystal edge)).

---

[12] In fact, the *Python* script was edited to run as separate iterations for each spinel dataset, rather than to loop through data files in a specified folder as for H-forsterite.

[13] Note that for all experimental runs carried out in this study, one-dimensional diffusion is considered a valid model for the processes occurring.

5.6 Results

5.6.1 D-H exchange

In total, six D-H exchange samples were successfully recovered from runs and prepared for SIMS analysis; four from short duration runs (E10, E11, E12, E25 - mounted as recovered from piston cylinder capsules without further polishing), and two from long duration runs (E13, E14 - prepared as exposed and polished central slices of the grain).

Short D-H exchange runs

Samples E10, E12, E25 did not have good enough surfaces to obtain quality SIMS measurements. Subsequent SEM (SE) imaging indicated that, in all three grains, surface reaction and/or recrystallisation had taken place during the D-H exchange run. Figure 5.9 shows the surface of grain E10, demonstrating this.

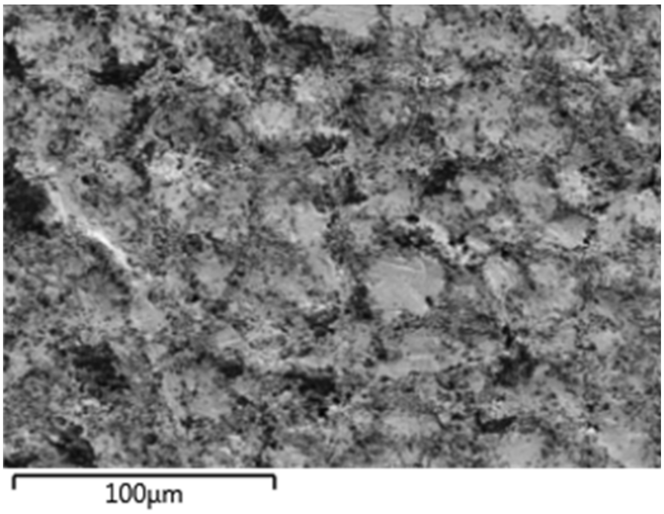

Figure 5.9: *SEM image of spinel grain E10, showing the poor quality surface.*

Deuterium was detected in spinel grain E11_A[14] at concentrations of approximately 10ppm, and therefore a full depth profile was taken - obliterating almost

---

[14] E11 split in to two fragments during retrieval from the experimental capsule and was therefore mounted as two separate grains. Fragment E11_B was not large enough to collect a SIMS depth profile for comparison.

the entire grain surface (figure 5.10). As with H-forsterite grains, WLI was used to measure the depth of the SIMS depth profile analysis pit in order to quantify the distance in the distance-concentration profile. However, the WLI measurement on E11_A did not yield high quality surface relief data (primarily due to difficulties in obtaining interference reflections from the original grain surface, as the depth profile left so little of the grain un-sputtered) and the distance is consequently only poorly constrained. The depth of the analysis pit is estimated to be 2 ± 0.5 µm,[15] leading to a diffusivity of $D = 1.29 \pm 0.25 \times 10^{-16} \mathrm{m}^2/\mathrm{s}$. The profile, and corresponding fit to Fick's law, is shown in figure 5.11.

Long D-H exchange runs

No deuterium was detected in either E13 or E14, and hydrogen concentrations were not above the analytical background signal. It is assumed that fluid was lost from the capsule during the experimental runs (therefore no source of deuterium) and hydrogen subsequently diffused out of the sample.

5.6.2 Uptake

Of the nine uptake experiments carried out, seven suitably whole, oriented spinel samples were recovered and prepared for analysis. During SIMS analysis, non-systematic changes in hydrogen and deuterium concentrations in higher temperature samples UP06, UP08, UP09 (1200°C) and UP01, UP05 (1400°C) were identified. The Mg:Al ratio for each analysis spot was measured, and was found to be variable across the grain in each case, indicating recrystallisation of the spinels during exchange runs. The extent of recrystallisation was subsequently confirmed by SEM (BSE) analysis, and can be clearly seen in figure 5.12. Data from these five experimental runs were therefore not considered further.

Of the two remaining uptake samples (UP02 and UP04), deuterium was only detected in UP04 (even then, only at ppm levels). The lack of deuterium in UP02 (and minimal concentration in UP04) may again be indicative of D_2O escape from the capsules during experimental runs - this is supported by low hydrogen contents in

---

[15] Significantly deeper than the SIMS depth profile pits in H-forsterite, due to differences in analytical set-up and variation in sputtering rates.

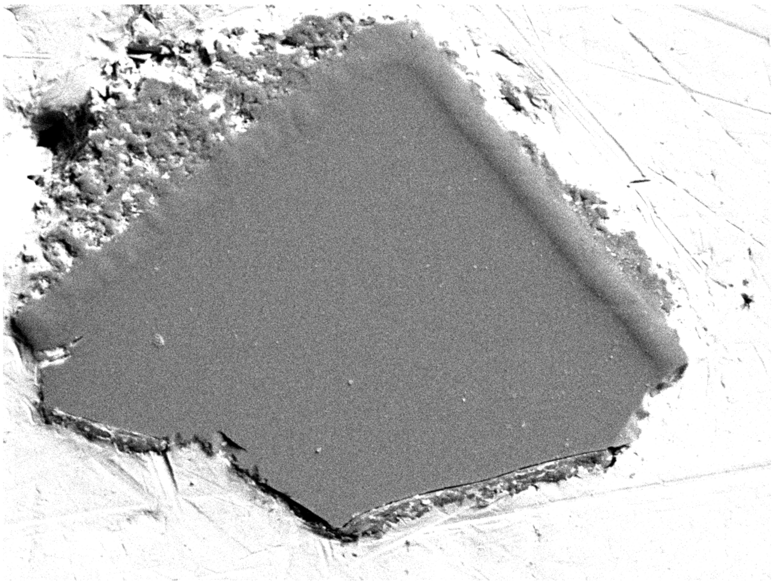

Figure 5.10: *SEM image of spinel grain E11_A, showing the extent to which the SIMS depth profile pit covers the grain surface. Field of view is approximately 300µm.*

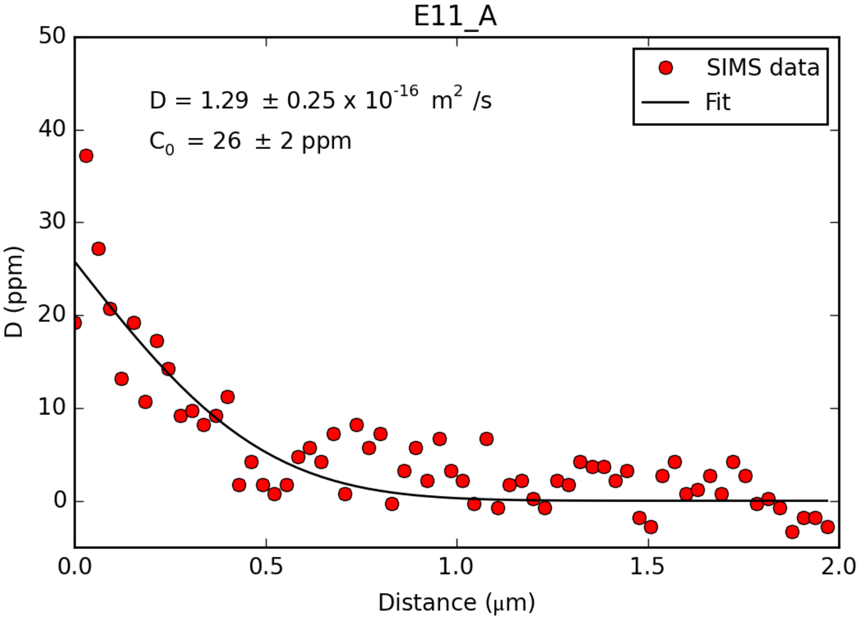

Figure 5.11: *Distance-concentration profile data, as identified by SIMS depth profile, for deuterium in spinel grain E11_A; D-H exchange run, 700°C, 1GPa, 600s.*

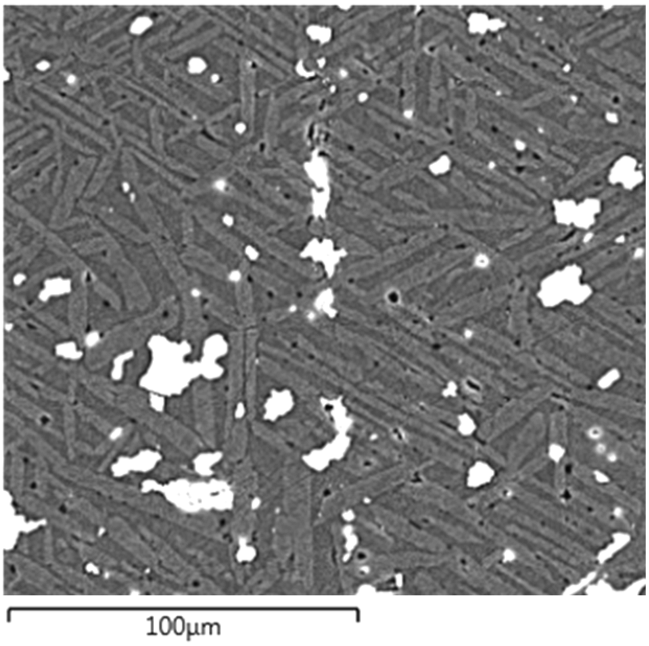

Figure 5.12: *SEM (BSE) image of a spinel grain from a high temperature uptake run (UP06_B - 1200°C) showing the separation of Mg and Al phases (distinguished as different shades in the image - light grey represents an Al-silicate, darker grey represents an Al-Mg-silicate phase) due to recrystallisation.*

the samples (UP02 - 11ppm, UP04_A - 25ppm), suggesting that although hydrogen diffused out, no deuterium was available to exchange (diffuse in).

Despite the low concentration (2-4ppm) of deuterium in UP04_A, a diffusion profile was identifiable,[16] and resulted in a credible fit to Fick's law, yielding a diffusivity of D = 7.49 ± 1.33 x 10^{-13} m^2/s, as shown in figure 5.13. This represents the diffusion of deuterium (considered to be equivalent to hydrogen[17]) in to the spinel sample.

Due to low (or zero) concentrations of hydrogen and/or deuterium, none of the D-H exchange or uptake spinel samples analysed by SIMS were included in further FTIR analysis.

---

[16] Largely due to the fact that deuterium background levels are so small as to be almost negligible during SIMS analysis.

[17] For a discussion on the equivalence of hydrogen and deuterium diffusion, see section 4.6.1.

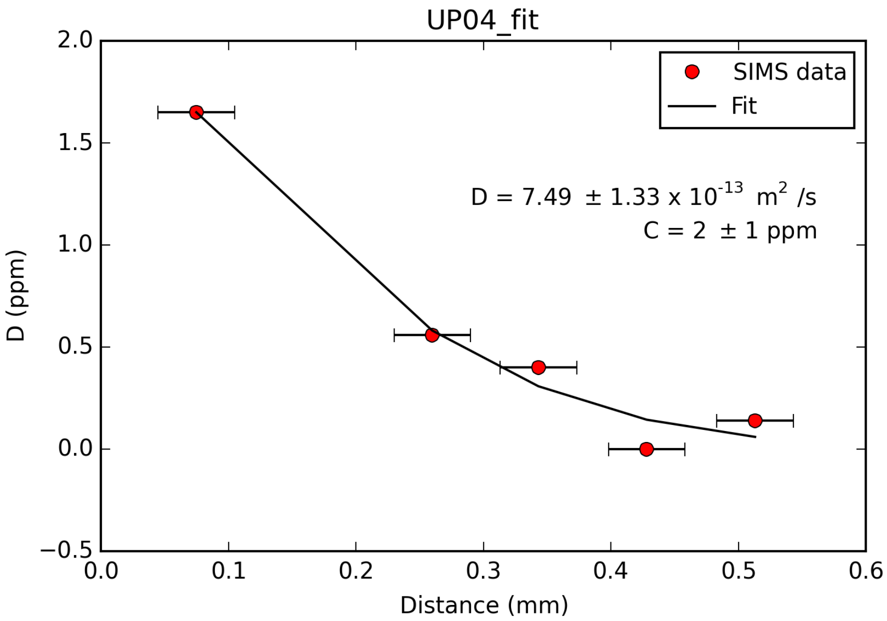

Figure 5.13: *Plotted concentration-distance data for spinel UP04_A (red circles), fit to Fick's law (black line). Values for the fit parameters D (m^2/s) and C (ppm) are given.*

5.6.3 Additional hydration/deuteration experiments

Calibration and fitting of IR spectra resulted in nine distance-concentration profiles across three spinel samples - hysp5 (two profiles: a,b), hysp3 (a,b,c), hysp6 (a,b,c) and hysp4 (a), from runs carried out at 500°C, 600°C, 700°C and 800 respectively. Figure 5.13 shows each profile (hysp3-6 as extracted from FTIR data), fit to equation 5.1.

Good visual fits to the data were found for the majority of the profiles, with the exception of hysp3_a, hysp4_a and hysp4_b. These data points were not considered further as they are thought to represent a more complex interaction between diffusion in and out of the samples that cannot be easily modelled (particularly the profiles for hysp4 - hysp3 may simply be too low concentrations). Table 5.6 lists the hydrogen diffusivities calculated for each profile, along with the corresponding C_i and C_0 values. There is good agreement between individual profiles taken on the same grain. Significant deuterium was only measured in sample hysp6 - the profiles extracted and fit for the diffusion of deuterium in to the grain are also given in table 5.6, and are shown in figure 5.14.

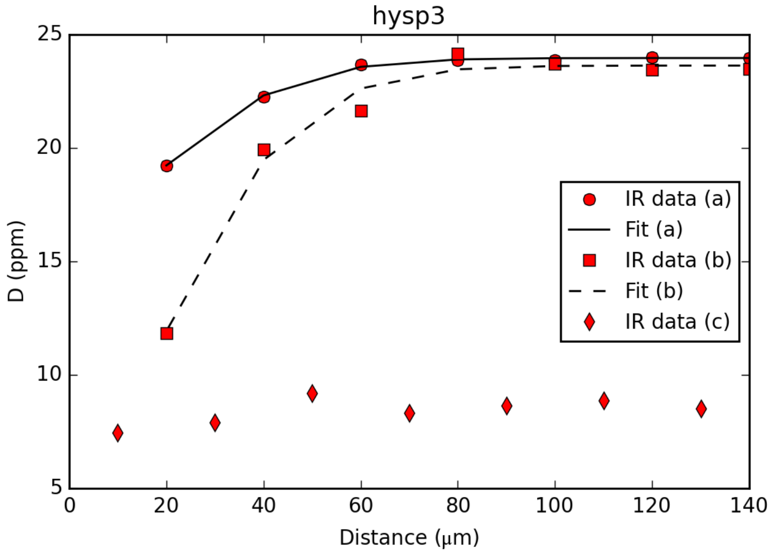

(a)

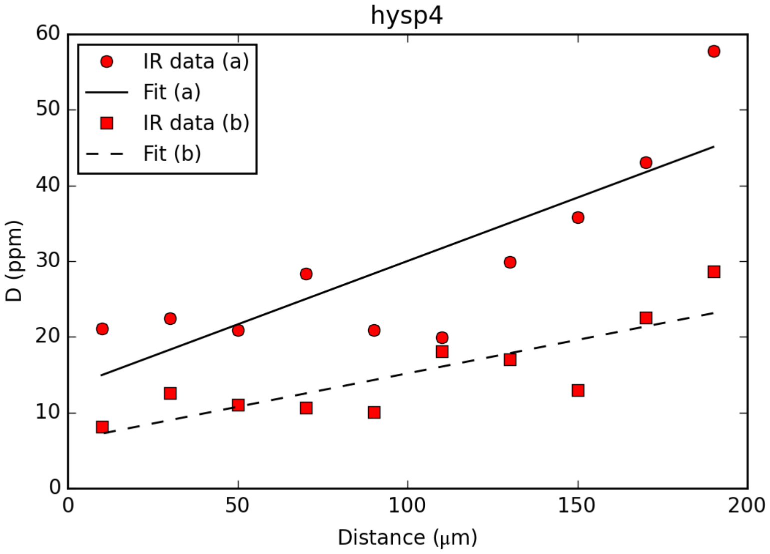

(b)

Figure 5.14: *Fitted distance-concentration profiles for (a) hysp3, (b) hysp4, (c) hysp5 and (d) hysp6, showing best fit to equation 5.1.*

(c)

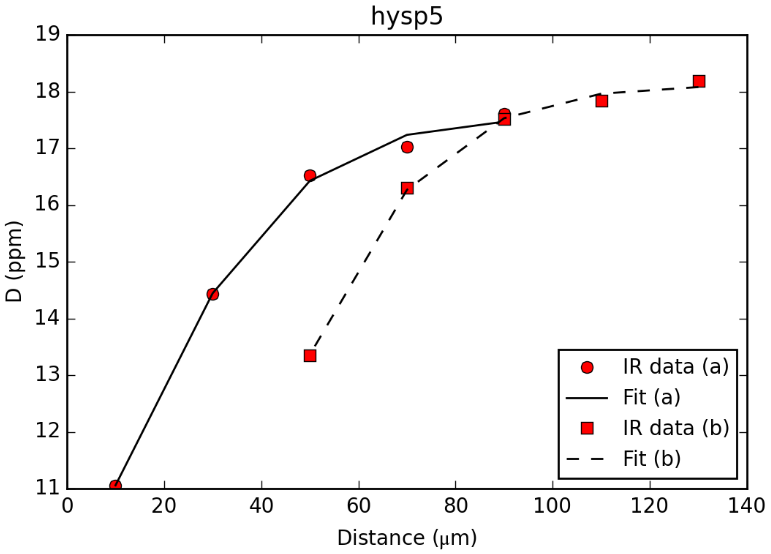
hysp5
D (ppm)
Distance (μm)
19
18
17
16
15
14
13
12
11
0
20
40
60
80
100
120
140
IR data (a)
Fit (a)
IR data (b)
Fit (b)

(d)

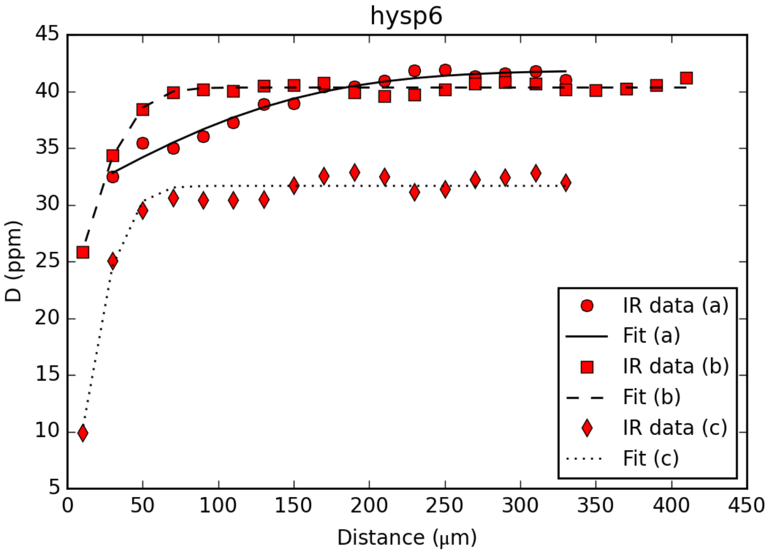
hysp6
D (ppm)
Distance (μm)
45
40
35
30
25
20
15
10
5
0
50
100
150
200
250
300
350
400
450
IR data (a)
Fit (a)
IR data (b)
Fit (b)
IR data (c)
Fit (c)

Table 5.6: *Diffusion values calculated from hysp distance-concentration profiles.*

Sample Number	**T (°C)**	C_0 **(ppm)**	C_i **(ppm)**	**D (m^2/s)**	**log D**
hysp_3a	600	14.4 ± 0.3	23.9 ± 0.0	1.59 ± 0.09 x10^{-15}	-14.79 ± 1.26
hysp_3b	600	0.2 ± 2.1	23.6 ± 0.2	1.63 ± 0.27 x10^{-15}	-14.78 ± 0.79
hysp_3c	600	-	-	-	-
hysp_5a	500	9.0 ± 0.3	17.5 ± 0.2	2.01 ± 0.28 x10^{-15}	-14.69 ± 0.85
hysp_5b	500	-3.7 ± 2.3	18.1 ± 0.1	3.05 ± 0.30 x10^{-15}	-14.51 ± 0.97
hysp_6a	700	30.6 ± 0.7	41.8 ± 0.3	2.80 ± 0.54 x10^{-14}	-13.55 ± 0.72
hysp_6b	700	20.6 ± 0.7	40.3 ± 0.1	1.61 ± 0.15 x10^{-15}	-14.79 ± 1.03
hysp_6c	700	0.1 ± 1.9	31.7 ± 0.2	1.13 ± 0.17 x10^{-15}	-14.94 ± 0.82
hysp_6a_D	700	4.21 ± 0.5		1.08 ± 0.21 x10^{-14}	-13.96 ± 0.71
hysp_6b_D	700	6.81 ± 0.6		2.26 ± 0.49 x10^{-15}	-14.64 ± 0.66

All runs were carried out at 1GPa.
Values for hysp_4 were discarded due to poor fits.

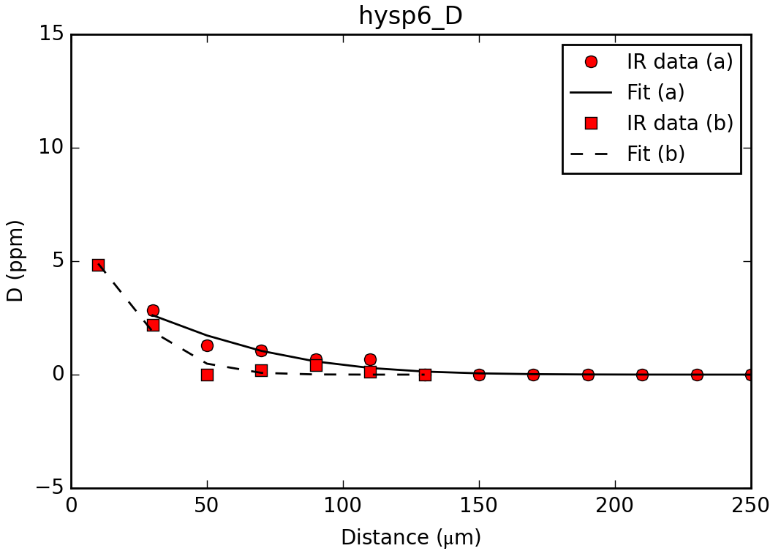

Figure 5.14: *Fitted distance-concentration profiles for deuterium diffusion in hysp6 (thought to occur via D-H exchange).*

5.6.4 Temperature dependence

Figure 5.15 shows the data points from this study for a) hydrogen loss/uptake and b) D-H exchange plotted on standard Arrhenius plots as lnD against 10^4/T. Both SIMS data and IR data are included, and deuterium and hydrogen values are considered without adjustment as the difference in values is negligible. The error bars on the SIMS D-H exchange points (E11_A) represent the minimum error on the depth of the analysis pit as measured by WLI. In reality, the error on this point is likely to be significantly greater as the profile could not be entirely constrained on the (small) grain surface - meaning that the data potentially includes some influence from the surface of the surrounding indium mount (and, additionally, the depth error is likely to be greater as there was none of the original grain surface left to serve as a reference point during WLI measurement). A best fit straight line through the hydrogen loss/uptake data (red line on figure 5.15a) yields the Arrhenius relationship;

$$D = 2 \pm 7 \times 10^{-10}\, e^{\,[-81 \pm 24 kJ.mol^{-1}/RT]} m^2/s \tag{5.2}$$

The activation energy, 81kJ.mol^{-1} is lower than that determined by Okuyama et al. (2009) for similar defect spinel (210kJ.mol^{-1})[18] but is within error of the value obtained by Sun et al. (2015) for D-H exchange in ringwoodite (101kJ.mol^{-1}). For comparison, Vogt et al. (2015) determined the activation energy for the exchange of Fe-Mg in synthetic Mg-spinel to be 213kJ.mol^{-1} (139kJ.mol^{-1} in Fe-bearing spinel).

5.6.5 Comparison of values

Figure 5.16 shows the values determined for hydrogen diffusion in defect spinel in comparison to previously published data. Values are shown for both D-H exchange and uptake experiments, analysed by both FTIR and SIMS, and compare well to diffusivities obtained by Fukatsu et al. (2002) and Okuyama et al. (2009) for defect spinel of similar composition. Values for hydrogen diffusion in ringwoodite (from D-H exchange experiments carried out by Sun et al. (2015)) and forsterite and olivine are also shown for comparison. Data for hydrogen self-diffusion (D-H exchange) in spinel appears to be similar to hydrogen uptake/loss, yielding diffusivity values within error - with the exception of the D-H exchange point analysed by SIMS (E11_A - which, as discussed, may have a significantly larger associated error). This may indicate that the diffusion of protons is the rate limiting step in spinel and, consequently, the self-diffusion of hydrogen is kinetically the same as coupled diffusion (as claimed by Okuyama et al. (2009) for Al-rich non-stoichiometric Mg spinel). Sun et al. (2015) suggest that this is also true in ringwoodite, with all H-related defects having comparable diffusivities. Alternatively, defect mobilities could appear to be similar because self-diffusion studies provide only a mean assessment of proton mobility - as suggested by Karato (2013) to be true in olivine. This would imply that, as in olivine, hydrogen diffusion in spinel and ringwoodite cannot be used to estimate electrical conductivity.

---

[18] The study of Fukatsu et al. (2002) shows a similar trend and therefore is expected to be similar, but data are not given in the paper.

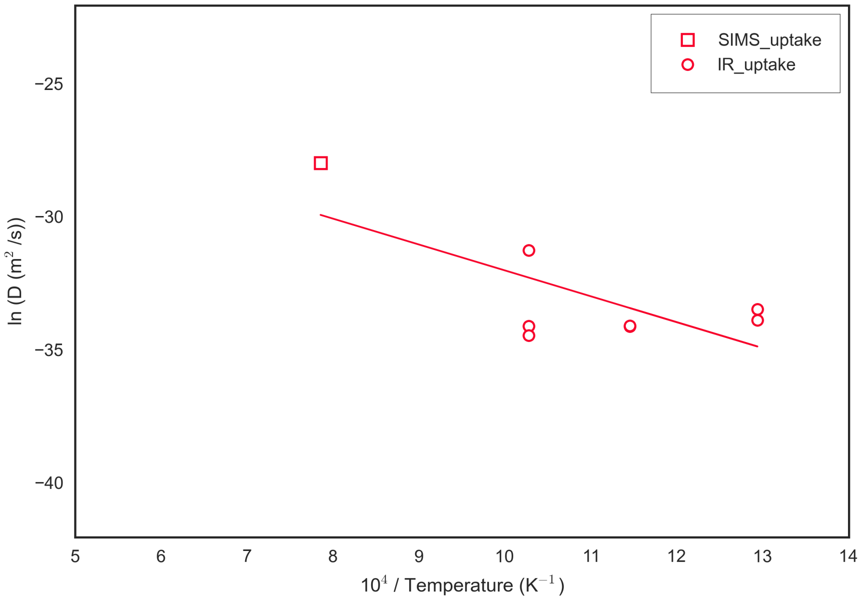

(a)

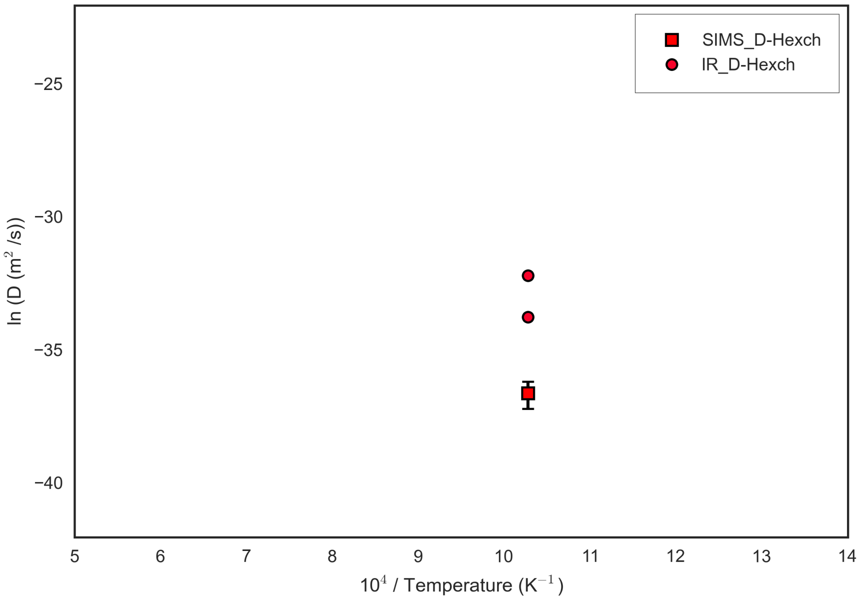

(b)

Figure 5.15: *Temperature dependence of hydrogen diffusion in spinel as identified from (a) hydrogen loss or gain in samples annealed in H_2O, (b) Deuterium gain in samples annealed in D_2O (D-H exchange).*

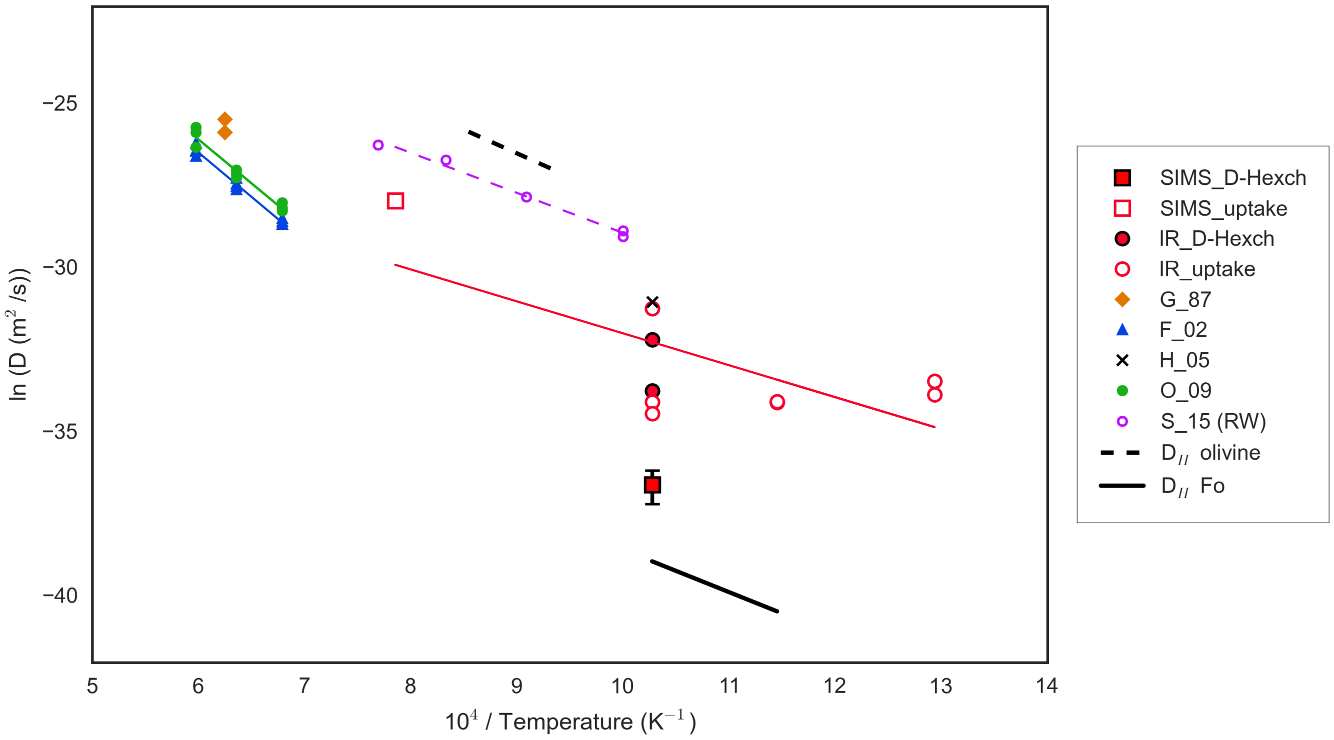

Figure 5.16: *Temperature dependence of hydrogen diffusion in spinel, by study. Values from this study (red open and filled squares) are shown in comparison to published data for spinel (G_87, F_02, H_05, O_09) and ringwoodite (S_15(RW)). Unless otherwise noted, all diffusion values were measured using IR techniques. Values for hydrogen self-diffusion in olivine (black dashed line - Du Frane and Tyburczy, 2012) and forsterite (black solid line - this study) are shown for comparison. References: G_87 - Gonzalez et al., 1987 (polycrystalline non-stoichiometric Mg-Al spinel with Mg:Al equal to 7:1), F_02 - Fukatsu et al., 2002 ($Mg_{1-x}Al_2O_{4-x}$ with x in the range 0-0.3), H_05 - Hertweck and Ingrin, 2005 (D-H exchange in Mg_2GeO_4 spinel), O_09 - Okuyama et al., 2009 ($Mg_{1-x}Al_2O_{4-z}$ with x in the range 0.06-0.34), S_15(RW) - Sun et al., 2015 (D-H exchange in Fe-bearing ringwoodite).*

5.6.6 Treatment of errors

As with olivine concentration profiles, error bars for depth-concentration points are not shown (see discussion in section 4.6.6). Errors in diffusivity and initial concentration values from best fits to Fick's law are given as one standard deviation from the least squares fitting solutions, as calculated by the curve fitting script used.[19] As the distance-concentration profile for spinel UP04_A was measured as SIMS analysis points along a line (see figure 5.5), the error in the distance measurement (x axis) is shown on figure 5.13 as the width of the analysis pit visible on the crystal surface.

---

[19] Using pcov values from scipy optimize curve_fit where the error on each parameter is calculated using np.sqrt(np.diag(pcov)).

5.7 Summary

Even considering the larger size of samples available, experimental work on spinel to determine the mobility of hydrogen under mantle conditions proved non-trivial. Initial D-H exchange experiments relied on recovering samples from high P/T twice - first to hydrate and then to exchange hydrogen for deuterium - which often resulted in fracturing, and many of the recovered samples did not contain deuterium when analysed, indicating the difficulty in maintaining a high-deuterium capsule environment. In addition, runs at high temperature recrystallised, preventing further analysis. Experimental runs at lower temperatures were more successful and were analysed by FTIR, indicating that there is no apparent switch in the relevant proportions of different OH defects as diffusion proceeds. In addition to this, data for hydrogen self-diffusion (D-H exchange) appears to be indistinguishable from coupled hydrogen diffusion - either implying that the diffusion of all defects is similar, or that self-diffusion only measures an average mobility (rather than true exclusive isotopic exchange) and is therefore not valid in considerations of electrical conductivity.

CHAPTER 6

Discussion

The aim of this study was to investigate the influence of water on the electrical conductivity of mantle minerals by determining hydrogen self-diffusion under relevant conditions. As has been demonstrated, the nature of hydrogen incorporation and, in turn, diffusion (even in the relatively simple case of Fe-free olivine) is not straightforward, and the relationship between hydrogen diffusion and the movement of protons during electrical conductivity is complex. Coupled with the reality that both performing and analysing experiments of this nature is non-trivial, the outcomes of the project are less wide-ranging than expected and focus primarily on the development and limitations of the approaches used.

6.1 Summary of results

6.1.1 Olivine

D-H exchange experiments were carried out at a range of temperatures on single crystals of forsterite, specifically synthesised to contain water under conditions relevant to those being investigated. The resulting deuterium diffusion profiles in the samples were identified using SIMS depth profiling, and fit to a suitable iteration of Fick's diffusion law (equation 2.4) in order to calculate diffusivity. Samples were also characterised by FTIR spectroscopy, exhibiting classic absorbance peaks in the OH region which were consistent with the peaks observed in the starting material (although some variation in the intensity and position of peaks between different synthesis runs was noted). Although ultimately only two data points were obtained, hydrogen diffusion results for forsterite from this study compare well to results from previous studies, falling within the general scatter of the data (figure 6.1). Fitting of the data to Fick's law[1] yields the Arrhenius relationship;

$$D_H = 5 \pm 4 \ \times 10^{-12} \ e^{\,[-105 \pm 7 kJ.mol^{-1}/RT]} \, m^2/s$$

Data suggest that the diffusivity of hydrogen in forsterite is slightly slower than previously determined, but has an activation energy (105kJ/mol) similar to values determined for hydrogen self-diffusion in other studies. The experimental technique used differs from other approaches by measuring short, near surface profiles of D-H exchange - theoretically measuring self-diffusion directly. The finding that self-diffusion is slower than hydrogen diffusion by other mechanisms is surprising (but also holds true for Fe-bearing olivine, according to the work of Du Frane and Tyburczy (2012)), since the uncoupled isotopic exchange of deuterium for hydrogen is expected to be the fastest occurring process. Hydrogen diffusion in forsterite is demonstrably slower than in Fe-bearing olivine (across all studies) but even when data for forsterite is considered in isolation, there is significant scatter in the results from different studies (figure 6.1). The likely explanation for this is the range in different defect mechanisms by which hydrogen is incorporated, and diffuses, through the crystal structure.

---

[1] A solution for one-dimensional diffusion from an infinite source - see section 2.1.

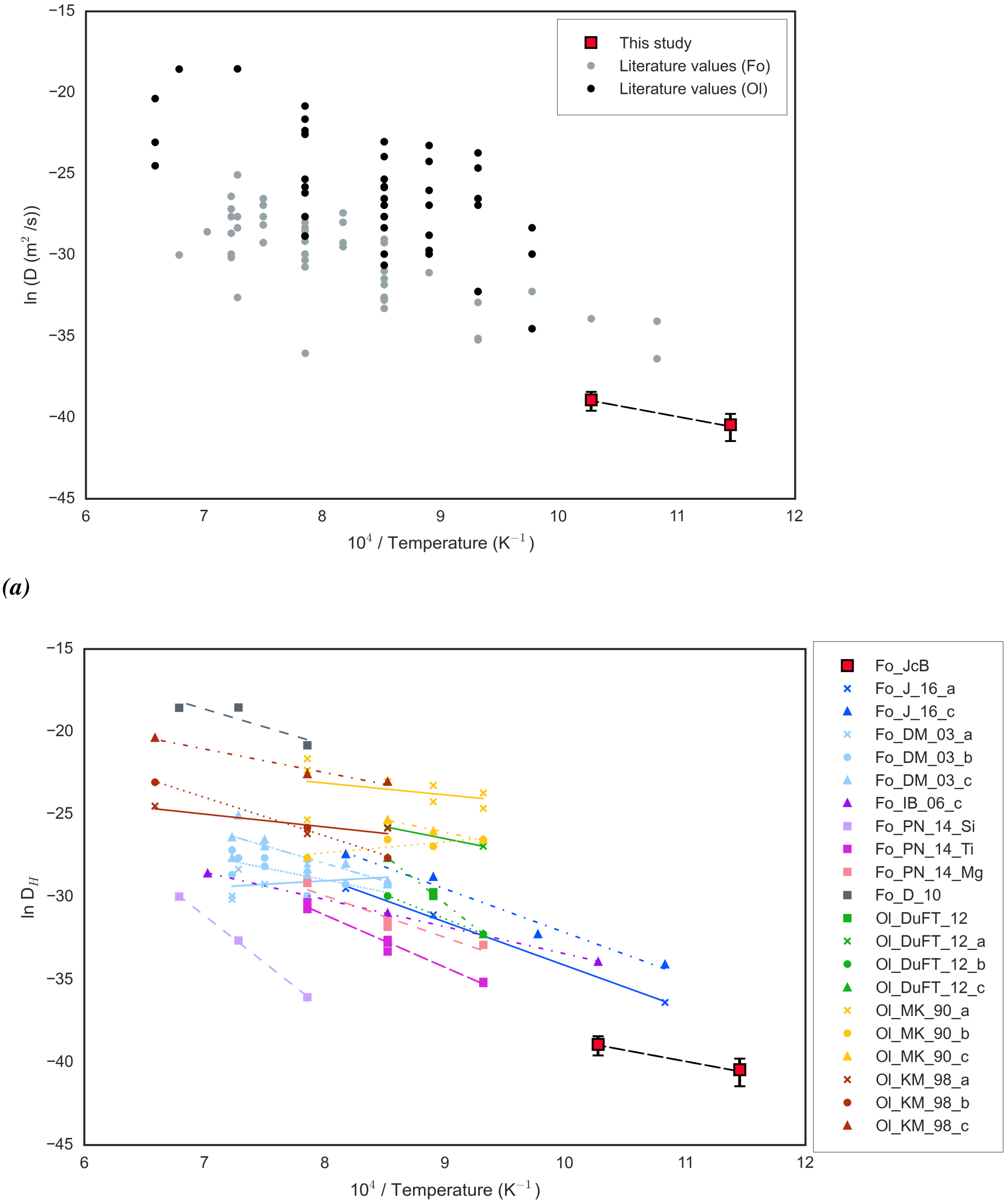

(a)

(b)

Figure 6.1: *Temperature dependence of hydrogen diffusion in olivine showing data from this study (red squares) in comparison to previous literature values showing (a) slower diffusion in forsterite than in Fe-bearing olivine and (b) trends for each study indicating activation energy. For full references see section 4.6.3.*

6.1.2 Spinel

Both D-H exchange and hydrogen uptake (annealing) experiments were performed on $Mg_{0.4}Al_{2.4}O_4$ defect spinel. Initial experiments encountered problems with cracking of samples under high pressure and recrystallisation at high temperature, with only two samples analysed by SIMS yielding diffusion data. A subsequent set of experiments at lower temperatures utilised a double-capsule design, allowing samples to be annealed in D_2O and H_2O under identical conditions. These samples were analysed by FTIR, and hydrogen diffusion profiles were identified, showing the diffusion of hydrogen both in and out of the samples. However, deuterium concentrations were very low, or absent, in the majority of (D_2O) samples - with a D-H exchange profile only identifiable in one case (hysp6).

Results for hydrogen diffusion in spinel are consistent with the findings of Fukatsu et al. (2002) and Bromiley et al. (2010) that mobility is charge-balanced by a counter flux of oxygen vacancies, yielding the Arrhenius relationship;

$$D_H = 2 \pm 7 \ \times 10^{-10} \ e^{\,[-81 \pm 24 kJ.mol^{-1}/RT]} \, m^2/s$$

for D (or H) uptake experiments. No temperature dependence was determined for D-H exchange experiments in spinel, as all well-constrained data points are at the same temperature. The spinel data are in reasonably good agreement with results by Fukatsu et al. (2002) and Okuyama et al. (2009) who carried out hydrogen uptake experiments on similar defect spinel (figure 6.2). Data from this study are also broadly comparable to hydrogen diffusion in ringwoodite, as determined by Sun et al. (2015). This favourable comparison supports the assertion by Bromiley et al. (2010) that defect spinel is a useful low-pressure analogue for hydrogen incorporation in ringwoodite.

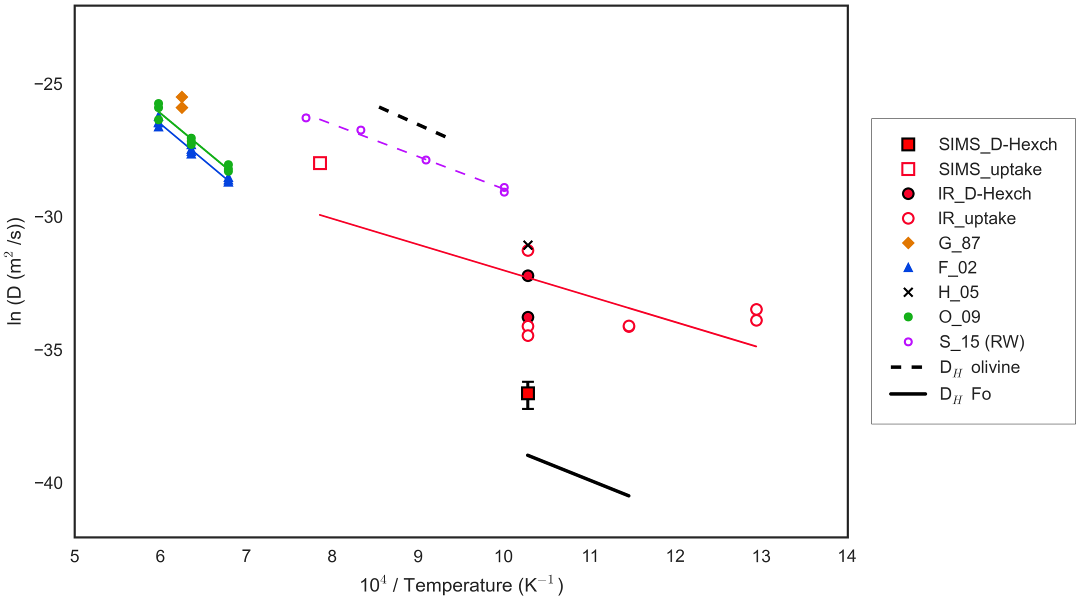

Figure 6.2: *Temperature dependence of hydrogen diffusion in spinel showing data from this study (red circles and squares) in comparison to previous literature values. Line of best fit to data from this study is for 'uptake' values only. For full references, see section 5.6.5.*

6.2 Implications

As introduced in chapters 1 and 2, H^+ has been proposed as the dominant charge-carrying species during electrical conduction and, consequently, increased water contents may be responsible for enhanced electrical conduction observed in the mantle. Electrical conductivity is therefore a potentially useful parameter for determining the distribution (and amount) of water in the Earth's mantle. The caveat is that the influence of hydrogen on the conductivity of mantle minerals - under relevant conditions - must be well-understood.

When this project was designed, it was based on theoretical and experimental work (such as Karato, 1990, Karato, 2006, Du Frane and Tyburczy, 2012) that suggested hydrogen self-diffusion[2] represented the free movement of protons (uncoupled to any other defects present) and was therefore directly comparable to the movement of H^+ as the charge-carrying species during electrical conduction. More recent work has suggested that the kinetics (and processes) involved in D-H exchange may be more complex than previously considered, and that the movement of charge-carrying protons during electrical conductivity may occur via an alternative pathway. The main proponent of this assertion is Karato (2013), who suggests that proton conductivities calculated from D_H do not provide an accurate assessment of σ_H. Instead, he argues that σ_H is dominated by the movement of highly mobile free protons, while diffusion experiments (even self-diffusion runs designed to measure isotopic exchange) measure the (coupled) mobility of complex species and therefore provide only a mean estimate of proton mobility. If this is true, data from D-H exchange experiments cannot be applied to a simple form of the Nernst-Einstein equation (equation 2.6) in order to calculate hydrogen-assisted electrical conductivity.

In forsterite, the diffusivities calculated from D-H exchange experiments are shown to be slower than data for other diffusion mechanisms. Slower self-diffusion is counter-intuitive, since the uncoupled substitution of hydrogen for deuterium should theoretically represent the fastest process, but this is also true for D-H exchange data obtained by Du Frane and Tyburczy (2012) for natural San Carlos olivine.[3] This appears to support Karato's argument that D-H exchange measurements do not represent the free movement of protons - instead being rate-controlled by the slowest

---

[2] As measured during D-H isotopic exchange experiments.

[3] When compared to other diffusion results for Fe-bearing olivine - see figure 4.33.

diffusing species.[4]

Given the expectation that the rate of diffusion differs depending on the species present, a change in the relative proportions of each defect/incorporation mechanism (as identified by IR spectroscopy) might be predicted. This is not observed in the IR data for either H-forsterite E6_A or E8_A when compared with the starting material (synthesis run S9, in both cases). However, it should be noted that a) the samples are of variable thickness[5] and therefore the data are not strictly quantifiable, and b) the D-H exchange experiments are short in duration therefore the change may be too small to identify.[6] Similarly, in spinel, over the temperature range studied, no change in the mechanism for hydrogen mobility is observed. Again this potentially indicates that D-H exchange experiments do not provide a true estimate of proton mobility, and has been suggested by Bromiley et al. (in prep - see appendix D), to indicate that protons are able to couple and uncouple to other defects during diffusion, with the implication that hydrogen mobility is equally slow for all mechanisms (in comparison to electrical conductivity which, according to (Karato, 2013), can selectively mobilise faster, free protons). Alternatively, it may be that, in spinel, all hydrogen-related defects have comparable diffusivities. This argument is favoured by Sun et al. (2015) for ringwoodite, based on their D-H exchange experiments which show no difference between self-diffusion and hydrogen diffusion. Additionally, their calculated σ_{total} (from σ_H) values correlate well to electrical conductivity data for ringwoodite in the transition zone. However, this correlation breaks down at higher water contents, and they use only a select study of electrical conductivity.[7] Their study also lacks any direct determination of the mobility of different hydrogen defects as profiles were identified by SIMS only.

6.2.1 Conductivity and water in the mantle

Despite this uncertainty surrounding the validity of applying diffusion studies to mantle electrical conductivity,[8] D_H data collected from this study was used to calculate σ_H

---

[4] Thought by Karato to be the substitution of two protons at the M1 site - [Mg] process.

[5] As they were not prepared as double-polished wafers for in-depth IR analysis.

[6] No strong deuterium signature is observed in samples indicating that there is minimal overall impact on the crystal/s.

[7] The scatter in values from electrical conductivity studies of mantle minerals is as great as the scatter in hydrogen diffusion data.

[8] And additionally because this work had already been planned and partly carried out before such discussions in the literature fully developed.

values for a range of mantle water contents.

Water content estimates in wt. % are translated into values of H^+ ions/m^3, then these values (along with determined D_H values for each relevant temperature) are applied to the Nernst-Einstien equation. Similar to the Arrhenius plots produced for diffusivity, the resulting σ_H values are plotted as log values against inverse temperature in order to give an indication of the temperature dependence (figure 6.3). Note that values are σ_H - representing the contribution of hydrogen to electrical conductivity, not total electrical conductivity for forsterite (σ_{tot}, as calculated by Du Frane and Tyburczy (2012)). The scatter of D_H values leads to a far greater spread in estimates for σ_H than the range of water contents possible for the mantle. This reiterates that electrical conductivty in mantle minerals cannot be accurately determined using this method, without a greater understanding of the mechanisms by which hydrogen is mobile during diffusion studies. There is also considerable scatter in values from direct measurements of hydrogen-assisted electrical conductivity in olivine, as is demonstrated by figure 6.4, taken from Jones (2016, figure 3A).

It is possible that, similar to diffusion measurements, this scatter indicates a difference in hydrogen mobility during electrical conductivity (i.e. in addition to the movement of free protons, coupled proton mobilities might also be important during conduction). Changes in mechanisms might influence mobility, and consequently the movement of protons during electrical conductivity could be influenced by parameters such as temperature, composition and water content. It is apparent, therefore, that the movement of hydrogen during electrical conductivity measurements, undertaken under relevant mantle conditions, also still requires further investigation be fully understood.

Resolving the mechanisms of hydrogen mobility in mantle minerals is key to determining how applicable existing (and future) diffusion data are to electrical conductivity. Currently, results cannot simply be applied to the Nernst-Einstein equation, and without further qualification, the data obtained from this study cannot be used to further investigate the distribution of water in the Earth's mantle.

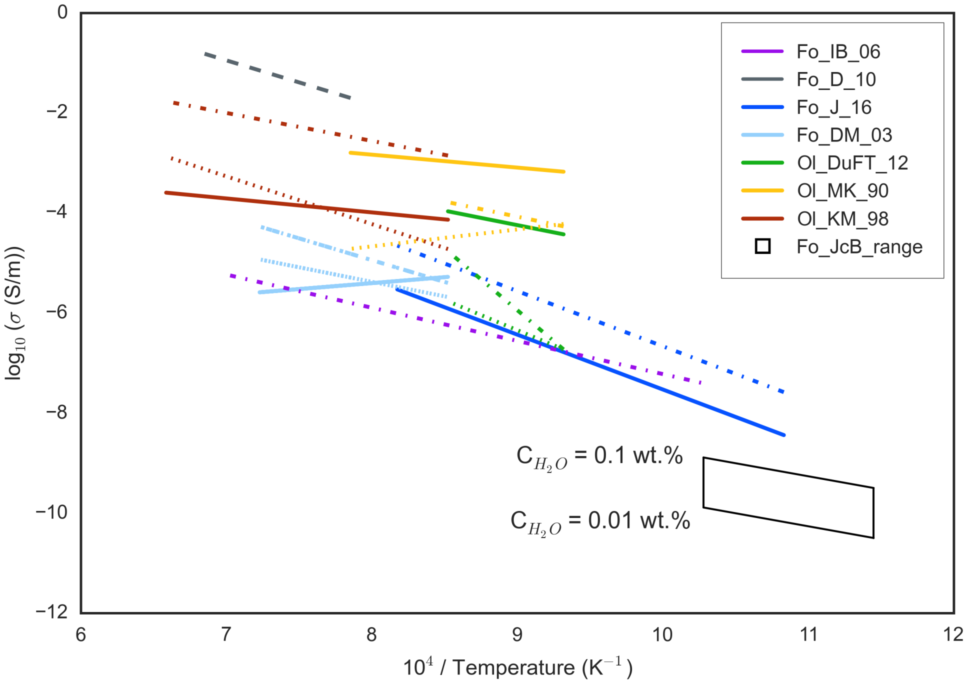

Figure 6.3: *Temperature dependence of hydrogen-assisted electrical conductivity (as calculated from equation 2.6). Values calculated using the forsterite diffusivities from this study (E6_A, E8_A - un-oriented) and a range of water contents from 0.01 - 0.1 wt. % are represented by the black box. For comparison, a selection of the published hydrogen diffusivity values have also been translated to* σ_H *values using equation 2.6 - references are as in previous plots. Un-oriented data is shown as dashed lines, [100] direction as solid lines, [010] as dotted lines, [001] as dot-dash lines.*

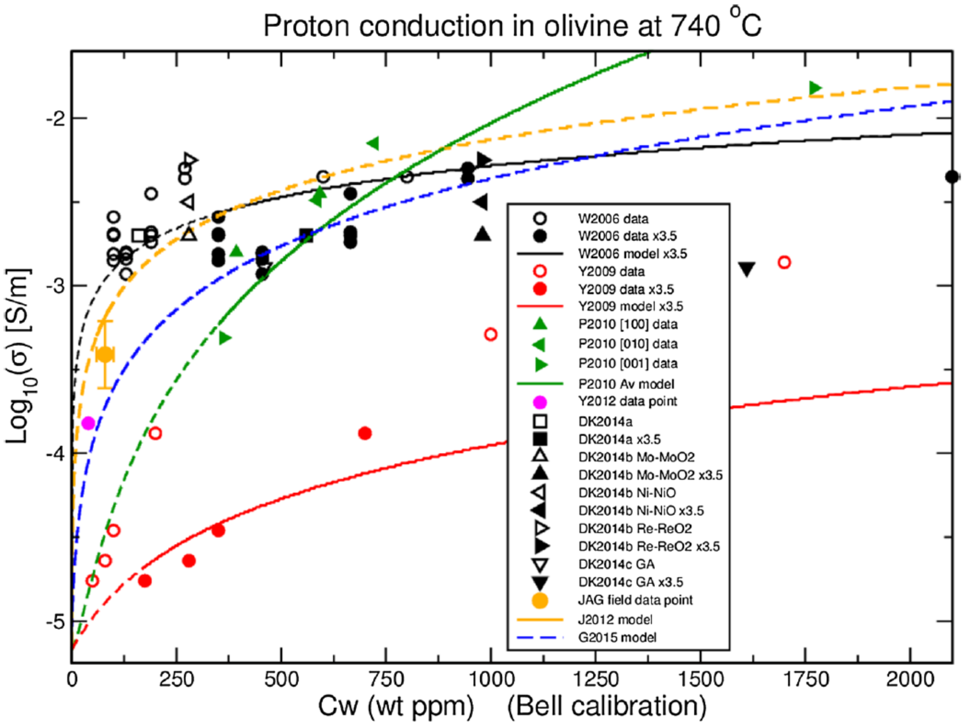

Figure 6.4: *Laboratory data for electrical conductivity at 740°C, with varying water content (0 - 2,000 wt ppm). For comparison, a field data point 100km below Jagersfontein kimberlite field (Western Kaapvaal Craton, South Africa) is shown (JAG - orange circle with error bars). Taken from Jones, 2016, figure 3A.*

6.3 Method development

One of the primary aims of this study was to design, and develop, a method to carry out D-H exchange experiments on samples specifically synthesised to contain water under mantle conditions - ensuring a relevant population of hydrogen-related defects. Crystals of H-forsterite were successfully synthesised and D-H exchange experiments were carried out, and analysed for a range of temperatures. However, as evidenced, there were several challenges to both the experimental and analytical approaches adopted - some of which were successfully overcome and some that remain to be addressed.

6.3.1 Experimental considerations

Maintaining deuterium during runs

One of the biggest challenges in carrying out the experimental work for this study was maintaining a deuterium-rich capsule environment during experimental runs. In the initial forsterite samples, no deuterium was detected, leading to the addition of a step during capsule preparation to check for leaks. Once this step was adopted, it became apparent that approximately 30% of capsules visually considered sealed contained contained leaks sufficient to allow D_2O to escape during experimental runs. Despite the addition of this check, deuterium contents were lower than expected in the majority of analysed samples.[9] Additionally, results demonstrated that even in runs where only D_2O was added to the capsule, hydrogen diffused in to the sample - indicating its unintended presence in the capsule environment. This was particularly evident in spinel samples (hydrogen profiles in the forsterite samples were hard to quantify, but appeared to show the same general trend), providing direct experimental evidence of the difficulty in maintaining a deuterium-rich environment. IR spectra in forsterite demonstrated the incorporation of boron, presumably originating from the piston-cylinder assembly[10] and it seems reasonable to assume that hydrogen may also diffuse in to the capsule from this source - although the presence of a thick cylinder of pyrex is designed to minimise this interaction. There may also be some exchange between deuterium and hydrogen in the surrounding environment during capsule filling

---

[9] In both forsterite and spinel, and both D-H exchange and uptake runs.

[10] Which contains borosilicate glass.

and sealing - particularly as a wet paper jacket was used, in some cases, to cool the capsule during the welding process. Sun et al. (2015) note a similar reduction in deuterium concentrations compared to hydrogen, citing ‘unavoidable’ contamination from H_2O in air before welding. It is worth noting that in the initial runs, the only capsule which exhibiting signs of water being present when pierced (UP04) contained the only sample in which deuterium was identified by SIMS. This further highlights the difficulty in maintaining D_2O in capsules during experimental runs, as all capsules were prepared following an identical procedure, and carefully checked for leaks.

As well as these mechanisms by which deuteirum may have been lost from the capsule environment, or hydrogen added, low concentrations of deuterium may also have stemmed from the limited volume of D_2O that was included in capsules. Approximately 10 wt.% D_2O was considered the limit in order to be able to successfully weld the capsule - above this the failure rate when capsules were tested was close to 90%. If the deposition of deuterium thin films on H-forsterite samples proves successful (see section 4.7.1 regarding on-going work with the lab in Bochum), this may represent a solution by providing a concentrated, deuterium-rich solid layer immediately adjacent to the sample surface. Additionally, if D-bearing forsterite can be more consistently synthesised, the coupled crystal method[11] employed by Sun et al. (2015) may also address this.

Consistent synthesis of starting materials

An important differentiation between the method used in this study and those previously carried out was the initial synthesis of samples under relevant conditions to ensure a relevant defect population. Although IR spectra indicated that the defect populations were consistent across grains from the same synthesis run, variability was noted between runs carried out under identical conditions - both with regard to total water content and the specific OH defects present. This indicates that synthesising a starting material with a homogeneous, relevant, defect population is less straightforward than initially thought, and may have contributed to the lack of diffusion profiles in some samples.[12] The lack of significant change in the OH defects present between the starting material and the post D-H exchange samples also emphasises the

---

[11] Whereby a single D-rich forsterite crystals is coupled to a H-rich forsterite crystal along a polished face, and D-H exchange between the two is identified.

[12] In which less water, or different OH defects, was initially present.

importance of the initial defect population. In addition, the synthesis method adopted did not produce crystals larger than 300μm (on average, grains were only 100-200μm), presenting a problem for SIMS analysis. A new method developed by Jollands et al. (2016) may resolve this issue, and should be investigated for any further studies.

The synthesis approach was not adopted for spinel in this study (primarily due to time constraints) but the considerations are equally valid for other mantle phases.

Temperature range

Using the piston-cylinder for D-H exchange experiments limited the temperature range that could be studied, primarily due to the time taken to reach the target temperature safely. In short (600s) D-H exchange runs, the time taken to reach temperatures above 800°C was considered too high a proportion of the run time.[13] For spinel samples, recrystallisation was also encountered at high temperatures, limiting the range studied. Temperature dependence for diffusion is an important parameter that differs with both crystallographic orientation (in olivine) and potentially the type of defect present. It is therefore important that data are collected over a large range of temperatures, particularly as different mechanisms may dominate at higher temperatures. In order to investigate higher temperature diffusion (in olivine), using the piston-cylinder, the experimental duration would have to be longer (to reduce the relative influence of diffusion at lower temperatures) - resulting in longer diffusion profiles that would potentially bring associated analytical challenges.[14]

6.3.2 Analytical considerations

Surface quality

The initial barrier to obtaining robust SIMS data was the lack of good quality analysis surfaces, since samples were not polished in preparation - to do so would remove the (shallow) diffusion profiles of interest. To some extent, this was rectified by polishing

---

[13] As hydrogen is highly mobile, even a short amount of time at lower temperatures could be enough to influence the diffusion profile - Sun et al. (2015) note the requirement (in high temperature experiments) to ensure a heating rate of 10K/s in order to avoid significant exchange at lower temperatures prior to the start of the run.

[14] Not least time, as even the shallow depth profiles analysed for this study took in excess of several hours to complete.

crystals prior to the D-H exchange step, but some samples were still too poor to analyse (particularly as their small nature makes the polished face difficult to identify). This lack of well-polished faces also contributed to the error in WLI measurements of depth, as the method relies on high surface reflectivity.

An additional consideration is the influence of the polish on surface interactions during diffusion - a comparison of diffusion in samples prepared using the STYTON polish method, compared to mechanical polishing, from runs under the same conditions would be useful to address this.

Depth profiling

The most significant contribution to the low number of diffusivity data points resulting from this study was the size constraint for SIMS depth profiling. Data obtained from SIMS analysis of forsterite samples clearly indicated that, when the primary beam drills down in one spot, material from high levels is dragged in to the analysis pit. This results in a smearing out of the diffusion profile, and an overestimated (faster) diffusion co-efficient. The solution is to create a large analysis pit and collect data only from the centre - but this requires sufficient sample area. In this study, the majority of forsterite grains were less than 200μm in size, approximately the lowermost limit for true depth profiling (with respect to the analytical set-up for this type of study).

An alternative is to focus solely on longer diffusion profiles measured by analysing spots across an exposed surface,[15] which is additionally relevant to the consideration of crystallographic orientation - it was not possible to measure crystal orientations using EBSD and therefore larger, pre-oriented blocks may prove more useful from this perspective. However, even if synthesis of larger, water-bearing, samples is possible, there are associated difficulties in recovering large crystals whole from high temperature/pressure (as noted for Cr-forsterite in this study, and in some samples by Du Frane and Tyburczy (2012)). This approach is therefore limited to lower pressure studies and was consequently not adopted for this study - the intention of the project was to investigate whether depth profiling can be used to determine hydrogen mobility in small samples as it is not straightforward to synthesise larger crystals of high pressure phases.

---

[15] Additionally solving the polishing issue as these are polished post-exchange.

6.4 Concluding remarks

The data obtained for both olivine (Fe-free forsterite) and spinel provides a useful contribution to the literature on hydrogen diffusion, but the non-trivial nature of both the experimental and analytical aspects mean that this method cannot be applied to other mantle phases without considered development and modification. Aside from the methodological developments and considerations, the main outcome of this study is therefore the caution that in order to fully address the topic, a range of approaches must be used that combine structural (e.g. IR) information on defect types with high resolution (e.g. SIMS) data. This must be coupled with in-depth mineral physics investigations such as by Karato (2013, 2014), in order to consider the true contributions to electrical conductivity. Both experimental and analytical procedures must be carried out meticulously to obtain robust data, and the importance of ensuring that the conditions (and hence defects) studied are directly relevant to mantle conditions must not be overlooked. Care must also be taken to address these considerations when interpreting and applying the results of previous studies.

Constraining the influence of hydrogen incorporated in NAMs on the electrical conductivity of the mantle is an ongoing investigation that is unlikely to be resolved until consensus of understanding can be reached regarding the mechanisms involved, and a consistent, relevant dataset for diffusivity values - based on structural information - can be agreed upon. As a result of the demonstration that SIMS depth profiling is not sufficiently robust unless the grain size is large enough for a full depth profile analysis, it remains difficult to easily and accurately measure hydrogen mobility in most mantle phases. Coupled with the inherent difficulties and inconsistencies in electrical conductivity studies, it is currently only possible to crudely estimate mantle water contents from geophysical data (such as MT). Furthermore, the influence of GBD must not be discounted in further studies, as it has been noted (e.g. Jones, 2016) to have significant influence on hydrogen mobility during electrical conductivity.

In conclusion, the diffusion of hydrogen in minerals under mantle conditions - likened by Chakraborty (2010) to ‘the random walk of drunken sailors’ - is clearly not a straightforward process, and requires further investigation to be truly understood, particularly in the context of its relevance to electrical conductivity.

6.5 Future directions

The outcomes of this study have highlighted the need to determine the true applicability of existing hydrogen mobility data to considerations of H^+ during measurements of electrical conductivity. This requires further in-depth study of the hydrogen species mobile - both during hydrogen diffusion experiments and during electrical conduction - and therefore requires a combination of approaches in order to obtain detailed structural information (e.g. IR measurements indicating the relative contributions of various species) alongside high resolution diffusion data (e.g. from SIMS). Detailed computational modelling of H^+ in olivine (and other phases) could also provide a useful tool for understanding the kinetics of hydrogen mobility, particularly in conjunction with theoretical considerations of diffusion/conductivity principles (such as those descirbed by Karato, 2013). The question of how truly D-H isotopic exchange experiments represent the self diffusion, and hence free mobility, of hydrogen is central to fully understanding the influence of hydrogen during electrical conduction and hence to any application of values to a calculation of the mantle water content. Thus the primary direction of any future work should be to address this using the combination of approaches outlined above.

Central to this project was the development of a method to investigate hydrogen diffusion under directly relevant mantle conditions, and this was achieved through the synthesis of hydrogen-bearing samples at high temperature and pressure conditions. Despite experimental challenges, the synthesis of such samples - suitable for further analysis - is possible and has been independently adopted and advocated by other authors (i.e. (Padrón-Navarta et al., 2014)). Future studies on hydrogen diffusion in such samples for all olivine compositions, as well as a range of mantle phases, [16] would yield a useful dataset. Although studies comparing the mobility of hydrogen species during diffusion experiments and measurements of electrical conductivity might mean this data was not applicable to electrical conductivity determinations, this dataset would be a important addition to diffusion literature and to the reconciliation of data from different studies.[17] Additionally the successful synthesis of D-Fo samples (and other deuterated phases) would allow for the further development of coupled diffusion studies (as carried out by Sun et al., 2015 for ringwoodite).

---

[16] Originally proposed within the scope of this project but not possible due to time and laboratory constraints, as discussed in previous chapters.

[17] Where data obtained may differ as a result of samples having non-relevant defect populations.

References

Asimow, D., C. Leo, J. Mosenfelder, and G. Rossman (2006). Quantitative polarized infrared analysis of trace OH in populations of randomly oriented mineral grains. *American Mineralogist* 91, pp. 278–284.

Balan, E., M. Blanchard, H. Yi, and J. Ingrin (2012). Theoretical study of OH-defects in pure enstatite. *Physics and Chemistry of Minerals* 40, pp. 41–50.

Bell, D. (1992). Water in mantle minerals. *Nature* 357, pp. 646–647.

Beran, A. and E. Libowitzky (2006). Water in Natural Mantle Minerals II: Olivine, Garnet and Accessory Minerals. *Reviews in Mineralogy & Geochemistry Vol. 62: Water in Nominally Anhydrous Minerals*. Ed. by H. Keppler and J. Smyth, pp. 169–191.

Bercovici, D. and S. Karato (2003). Whole-mantle convection and the transition-zone water filter. *Nature* 425, pp. 39–44.

Berry, A., J. Hermann, H. O'Neill, and G. Foran (2005). Fingerprinting the water site in mantle olivine. *Geology* 33, pp. 869–872.

Biagioni, C. and M. Pasero (2014). The systematics of the spinel-type minerals : An overview. *American Mineralogist* 99, pp. 1254–1264.

Bolfan-Casanova, N. (2005). Water in the Earth's mantle. *Mineralogical Magazine* 69, pp. 229–257.

Bolfan-Casanova, N., H. Keppler, and D. Rubie (2000). Water partitioning between nominally anhydrous minerals in the MgO–SiO2–H2O system up to 24 GPa: implications for the distribution of water in the Earth's mantle. *Earth and Planetary Science Letters* 182, pp. 209–221.

Bromiley, G., F. Nestola, S. Redfern, and M. Zhang (2010). Water incorporation in synthetic and natural MgAl2O4 spinel. *Geochimica et Cosmochimica Acta* 74, pp. 705–718.

Bucholz, C., G. Gaetani, M. Behn, and N. Shimizu (2013). Post-entrapment modification of volatiles and oxygen fugacity in olivine-hosted melt inclusions. *Earth and Planetary Science Letters* 374, pp. 145–155.

Carslaw, H. and J. Jaeger (1959). *Conduction of Heat in Solids*. 2nd. London: Oxford University Press.

Chakraborty, S. (2010). Diffusion coefficients in olivine, wadsleyite and ringwoodite. *Reviews in Mineralogy & Geochemistry Vol. 72: Diffusion in Minerals and Melts*. Ed. by Y. Zhang and D. Cherniak, pp. 603–639.

Constable, S. (2006). SEO3: A new model of olivine electrical conductivity. *Geophysical Journal International* 166, pp. 435–437.

Crank, J. (1975). *The Mathematics of Diffusion*. 2nd. London: Oxford University Press.

Dai, L. and S. Karato (2014). The effect of pressure on the electrical conductivity of olivine under the hydrogen-rich conditions. *Physics of the Earth and Planetary Interiors* 232, pp. 51–56.

Demouchy, S. (2010). Diffusion of hydrogen in olivine grain boundaries and implications for the survival of water-rich zones in the Earth's mantle. *Earth and Planetary Science Letters* 295, pp. 305–313.

Demouchy, S. and S. Mackwell (2003). Water diffusion in synthetic iron-free forsterite. *Physics and Chemistry of Minerals* 30, pp. 486–494.

— (2006). Mechanisms of hydrogen incorporation and diffusion in iron-bearing olivine. *Physics and Chemistry of Minerals* 33, pp. 347–355.

Dohmen, R., H. Becker, E. Meissner, T. Etzel, and S. Chakraborty (2002). Production of silicate thin films using pulsed laser deposition (PLD) and applications to studies in mineral kinetics. *European Journal of Mineralogy* 14, pp. 1155–1168.

Du Frane, W., J. Roberts, D. Toffelmier, and J. Tyburczy (2005). Anisotropy of electrical conductivity in dry olivine. *Geophysical Research Letters* 32.

Du Frane, W. and J. Tyburczy (2012). Deuterium-hydrogen exchange in olivine: Implications for point defects and electrical conductivity. *Geochemistry Geophysics Geosystems* 13.

Eaton, D., F. Darbyshire, R. Evans, H. Grütter, A. Jones, and X. Yuan (2009). The elusive lithosphere–asthenosphere boundary (LAB) beneath cratons. *Lithos* 109, pp. 1–22.

Farla, R., C. Peach, and S. Grotenhuis (2009). Electrical conductivity of synthetic iron-bearing olivine. *Physics and Chemistry of Minerals* 37, pp. 167–178.

Farver, J. (2010). Oxygen and hydrogen diffusion in minerals. *Reviews in Mineralogy & Geochemistry Vol. 72: Diffusion in Minerals and Melts*. Ed. by Y. Zhang and D. Cherniak, pp. 447–507.

Ferot, A. and N. Bolfan-Casanova (2012). Water storage capacity in olivine and pyroxene to 14 GPa: Implications for the water content of the Earth's upper mantle and nature of seismic discontinuities. *Earth and Planetary Science Letters* 350, pp. 218–230.

Ferriss, E., T. Plank, D. Walker, and M. Nettles (2015). The whole-block approach to measuring hydrogen diffusivity in nominally anhydrous minerals. *American Mineralogist* 100, pp. 837–851.

Flynn, G. and W. Powell (1979). *The Cutting and Polishing of Electro-optic Materials*. London: Adam Hilger.

Fukatsu, N., N. Kurita, H. Shiga, Y. Murai, and T. Ohashi (2002). Incorporation of hydrogen into magnesium aluminate spinel. *Solid State Ionics* 152-153, pp. 809–817.

Gardés, E., F. Gaillard, and P. Tarits (2014). Toward a unified hydrous olivine electrical conductivity law. *Geochemistry, Geophysics, Geosystems* 15, pp. 4984–5000.

Gonzalez, R., Y. Chen, J. Barhorst, and K. Tsang (1987). Protons and deuterons in stoichiometric and nonstoichiometric. *Journal of Material Research* 2, pp. 77–81.

Hae, R., E. Ohtani, T. Kubo, T. Koyama, and H. Utada (2006). Hydrogen diffusivity in wadsleyite and water distribution in the mantle transition zone. *Earth and Planetary Science Letters* 243, pp. 141–148.

Hertweck, B. and J. Ingrin (2005). Hydrogen incorporation in a ringwoodite analogue: Mg2GeO4 spinel. *Mineralogical Magazine* 69, pp. 337–344.

Huang, X., Y. Xu, and S. Karato (2005). Water content in the transition zone from electrical conductivity of wadsleyite and ringwoodite. *Nature* 434, pp. 746–749.

Hunter, J L (2009). Improving depth profile measurements of natural materials. *Mineralogical Association of Canada, Short Course 41*, pp. 133–145.

Ingrin, J. and M. Blanchard (2006). Diffusion of Hydrogen in Minerals. *Reviews in Mineralogy & Geochemistry Vol. 62: Water in Nominally Anhydrous Minerals Geochemistry*. Ed. by H. Keppler and J. Smyth, pp. 291–320.

Ingrin, J., I. Kovács, E. Deloule, E. Balan, M. Blanchard, S. Kohn, and J. Hermann (2014). Identification of hydrogen defects linked to boron substitution in synthetic forsterite and natural olivine. *American Mineralogist* 99, pp. 2138–2141.

Inoue, T., Y. Tanimoto, T. Irifune, T. Suzuki, H. Fukui, and O. Ohtaka (2004). Thermal expansion of wadsleyite, ringwoodite, hydrous wadsleyite and hydrous ringwoodite. *Physics of the Earth and Planetary Interiors* 143-144, pp. 279–290.

Jollands, M., J. Padrón-navarta, J. Hermann, and H. Neill (2016). Hydrogen diffusion in Ti-doped forsterite and the preservation of metastable point defects. *American Mineralogist* 101, pp. 1571–1583.

Jones, A. (2016). Proton conduction and hydrogen diffusion in olivine: an attempt to reconcile laboratory and field observations and implications for the role of grain boundary diffusion in enhancing conductivity. *Physics and Chemistry of Minerals* 43, pp. 237–265.

Jones, A., J. Fullea, R. Evans, and M. Muller (2012). Water in cratonic lithosphere: Calibrating laboratory-determined models of electrical conductivity of mantle minerals using geophysical and petrological observations. *Geochemistry Geophysics Geosystems* 13, pp. 1–27.

Karato, S. (1990). The role of hydrogen in the conductivity of the upper mantle. *Nature* 347, pp. 272–273.

— (2006). Influence of H-related defects on the electrical conductivity of mantle minerals: A critical review. In: *Earth's Deep Water Cycle*. Ed. by S. Jacobsen and S. van der Lee. Washington DC: American Geophysical Union, pp. 113–129.

— (2011). Water distribution across the mantle transition zone and its implications for global material circulation. *Earth and Planetary Science Letters* 301, pp. 413–423.

— (2013). Theory of isotope diffusion in a material with multiple species and its implications for hydrogen-enhanced electrical conductivity in olivine. *Physics of the Earth and Planetary Interiors* 219, pp. 49–54.

Khan, A. and T. Shankland (2012). A geophysical perspective on mantle water content and melting: Inverting electromagnetic sounding data using laboratory-based electrical conductivity profiles. *Earth and Planetary Science Letters* 317-318, pp. 27–43.

Kohlstedt, D. and S. Mackwell (1998). Diffusion of hydrogen and intrinsic point defects in olivine. *Zeitschrift für Physikalische Chemie* 207, pp. 147–162.

Kovacs, I., H. O'Neill, J. Hermann, and E. Hauri (2010). Site-specific infrared O-H absorption coefficients for water substitution into olivine. *American Mineralogist* 95, pp. 292–299.

Lemaire, C., R. Brooker, and S. Kohn (2004). The effect of silica activity on the incorporation mechanisms of water in synthetic forsterite : a polarised infrared spectroscopic study. *Contributions to Mineralogy and Petrology* 147, pp. 48–57.

Libowitzky, E. and A. Beran (2004). IR spectroscopic characterisation of hydrous species in minerals. In: *Spectroscopic Methods in Mineralogy, EMU Notes in Mineralogy Volume 6*, pp. 227–280.

Libowitzky, E. and G. Rossman (1997). An IR absorption calibration for water in minerals. *American Mineralogist* 82, pp. 1111–1115.

Mackwell, S. and D. Kohlstedt (1990). Diffusion of hydrogen in olivine: Implications for water in the mantle. *Journal of Geophysical Research* 95, pp. 5079–5088.

Martin, R. and G. Donnay (1972). Hydroxyl in the mantle. *American Mineralogist* 57, pp. 554–570.

Medin, A., R. Parker, and S. Constable (2007). Making sound inferences from geomagnetic sounding. *Physics of the Earth and Planetary Interiors* 160, pp. 51–59.

Okuyama, Y., N. Kurita, and N. Fukatsu (2009). Diffusion of proton in alumina-rich nonstoichiometric magnesium aluminate spinel. *Ionics* 15, pp. 43–48.

Padrón-Navarta, J., J. Hermann, and H. O'Neill (2014). Site-specific hydrogen diffusion rates in forsterite. *Earth and Planetary Science Letters* 392, pp. 100–112.

Paterson, M. (1982). The determination of hydroxyl by infrared absorption in quartz, silicate glasses and similar materials. *Bulletin de Minéralogie* 105, pp. 20–29.

Pearson, D., F. Brenker, F. Nestola, J. McNeill, L. Nasdala, M. Hutchison, S. Matveev, K. Mather, G. Silversmit, S Schmitz, B Vekemans, and L. Vincze (2014). Hydrous mantle transition zone indicated by ringwoodite included within diamond. *Nature* 507, pp. 221–224.

Poe, B., C. Romano, F. Nestola, and J. Smyth (2010). Electrical conductivity anisotropy of dry and hydrous olivine at 8GPa. *Physics of the Earth and Planetary Interiors* 181, pp. 103–111.

Regenauer-Lieb, K. and T. Kohl (2003). Water solubility and diffusivity in olivine: its role in planetary tectonics. *Mineralogical Magazine* 67, pp. 697–715.

Schock, R., G. Duba, and T. Shankland (1989). Electrical Conduction in Olivine. *Journal of Geophysical Research* 94, pp. 5829–5839.

Selway, K., J. Yi, and S. Karato (2014). Water content of the Tanzanian lithosphere from magnetotelluric data: Implications for cratonic growth and stability. *Earth and Planetary Science Letters* 388, pp. 175–186.

Smyth, J., D. Frost, F. Nestola, C. Holl, and G. Bromiley (2006). Olivine hydration in the deep upper mantle: Effects of temperature and silica activity. *Geophysical Research Letters* 33.

Sun, W., T. Yoshino, N. Sakamoto, and H. Yurimoto (2015). Hydrogen self-diffusivity in single crystal ringwoodite: Implications for water content and distribution in the mantle transition zone. *Geophysical Research Letters* 42, pp. 6582–6589.

Sykes, D., G. Rossman, D. Veblen, and E. Grew (1994). Enhanced H and F incorporation in borian olivine. *American Mineralogist* 79, pp. 904–908.

Thoraval, C. and S. Demouchy (2014). Numerical models of ionic diffusion in one and three dimensions: application to dehydration of mantle olivine. *Physics and Chemistry of Minerals* 41, pp. 709–723.

Vogt, K., R. Dohmen, and S. Chakraborty (2015). Fe-Mg diffusion in spinel: New experimental data and a point defect model. *American Mineralogist* 100, pp. 2112–2122.

Wang, D., M. Mookherjee, Y. Xu, and S. Karato (2006). The effect of water on the electrical conductivity of olivine. *Nature* 443, pp. 977–980.

Watson, E. and R. Dohmen (2010). Non-traditional and Emerging Methods for Characterizing Diffusion in Minerals and Mineral Aggregates. *Reviews in Mineralogy & Geochemistry Vol. 72: Diffusion in Minerals and Melts*. Ed. by Y. Zhang and D. Cherniak, pp. 61–105.

Yoshino, T., T. Matsuzaki, A. Shatskiy, and T. Katsura (2009). The effect of water on the electrical conductivity of olivine aggregates and its implications for the electrical structure of the upper mantle. *Earth and Planetary Science Letters* 288, pp. 291–300.

Yoshino, T., T. Matsuzaki, S. Yamashita, and T. Katsura (2006). Hydrous olivine unable to account for conductivity anomaly at the top of the asthenosphere. *Nature* 443, pp. 973–976.

Zhang, Y. (2010). Diffusion in minerals and melts: theoretical background. *Reviews in Mineralogy & Geochemistry Vol. 72: Diffusion in Minerals and Melts*. Ed. by Y. Zhang and D. Cherniak, pp. 5–59.

APPENDIX A

Python script to fit diffusion profiles to Fick's law

Fo_fit

February 10, 2016

Depth_profile

```
In []: import os
       import sys
       import numpy as np
       import matplotlib.pyplot as plt
       from scipy.special import erf
       from scipy.optimize import curve_fit

       wdir = 'M:\JcB\PhD\Experiments\Analysis\Python'
       os.chdir(wdir)

       os.getcwd()

       datadir = os.path.join( wdir, 'Depth_profile' ) #SUBFOLDER CONTAINING DATA FILES

       filepath = '/long/path/to/myfile.txt'
       os.path.basename(filepath)

       filelist = os.listdir(datadir)
       filelist

       datafiles = []
       sample_number = []
       for filename in filelist:
           if filename.endswith('.txt'):
               datafiles.append(filename)
               sample_number.append(filename[:-4])

       # function to open file and return data
       def get_data(filepath):
           dist, conc = np.loadtxt(filepath, unpack=True)
           return dist, conc

       # fitting function (Fick's Law - infinite source)
       def FI(dist, D, C):
           return (1-erf(dist/(2*((D*600)**0.5))))*C

       # function to fit data and create lists of D, C values
       D_values = []
       C_values = []
       def calculate_fit(dist, conc):
           D0 = 1e-15
           C0 = 500
```

```
    (D, C), pcov = curve_fit(FI, dist, conc, p0=[D0, C0])
    y = FI(dist, D, C)
    D_values.append(D)
    C_values.append(C)
    return y

# fitting function for FITTED data
def FI_fit(dist, D_fit, C_fit):
    return (1-erf(dist/(2*((D_fit*600)**0.5))))*C_fit

# function to fit data and create lists of FITTED D, C values
D_fit_values = []
C_fit_values = []
def calculate_fit_fit(dist, conc_fit):
    D0 = 1e-15
    C0 = 500
    (D_fit, C_fit), pcov = curve_fit(FI, dist, conc_fit, p0=[D0, C0])
    y = FI_fit(dist, D_fit, C_fit)
    D_fit_values.append(D_fit)
    C_fit_values.append(C_fit)
    return y

# function to open, fit and plot data
def plot_data(filepath):
    dist, conc = get_data(filepath)
    y = calculate_fit(dist, conc)
    plt.figure()
    plt.plot(dist, conc, ’ro’, label="SIMS data")
    plt.plot(dist, y, ’k-’, label="Fit")
    plt.ticklabel_format(style=’sci’, axis=’x’, scilimits=(0,0))
    plt.xlabel("Distance (m)")
    plt.ylabel("D (ppm)")
    D_values_list = [’D = ’ + ’%.2E’ % Dv for Dv in D_values]
    C_values_list = [’C = ’ + ’%.0f’ % Cv for Cv in C_values]
    plt.figtext(0.8, 0.75, ’’.join(D_values_list), ha=’right’)
    plt.figtext(0.8, 0.65, ’’.join(C_values_list), ha=’right’)
    filename = os.path.basename(filepath)
    plt.title(filename[:-4])
    figure_filename = filename.replace(’.txt’, ’.png’)
    savepath = os.path.join(datadir, figure_filename)
    plt.savefig(savepath, dpi=200)
    plt.close()
    return

# function to open, fix, fit and plot FITTED data
def plot_data_fix(filepath):
    dist, conc = get_data(filepath)
    av = np.average(conc[-10:-1])
    conc_fix =  [z - av for z in conc]
    y = calculate_fit_fit(dist, conc_fix)
    plt.figure()
    plt.plot(dist, conc_fix, ’ro’, label="SIMS data")
    plt.plot(dist, y, ’k-’, label="Fit")
    plt.ticklabel_format(style=’sci’, axis=’x’, scilimits=(0,0))
```

```
    plt.xlabel("Distance (m)")
    plt.ylabel("D (ppm)")
    D_fit_values_list = ['D = ' + '%.2E' % Dvfit for Dvfit in D_fit_values]
    C_fit_values_list = ['C = ' + '%.0f' % Cvfit for Cvfit in C_fit_values]
    plt.figtext(0.8, 0.75, ''.join(D_fit_values_list), ha='right')
    plt.figtext(0.8, 0.65, ''.join(C_fit_values_list), ha='right')
    filename = os.path.basename(filepath)
    newfilename = filename.replace('E', 'Fit_E')
    plt.title(newfilename[:-4])
    figure2_filename = newfilename.replace('.txt', '.png')
    savepath2 = os.path.join(datadir, figure2_filename)
    plt.savefig(savepath2, dpi=200)
    plt.close()
    return

# plot for all files
for datafile in datafiles:
    datafilepath = os.path.join(datadir, datafile)
    plot_data(datafilepath)
    plot_data_fix(datafilepath)
    D_values = []
    C_values = []
    D_fit_values = []
    C_fit_values = []

# rerun fitting to get list of values
for datafile in datafiles:
    datafilepath = os.path.join(datadir, datafile)
    dist, conc = get_data(datafilepath)
    calculate_fit(dist, conc)
    av = np.average(conc[-10:-1])
    conc_fix =  [z - av for z in conc]
    calculate_fit_fit(dist, conc_fix)

# insert headings into data lits
sample_number.insert(0, "Sample Number")
D_values.insert(0, "Diffusion Coefficient")
C_values.insert(0, "Initial Concentration")
D_fit_values.insert(0, "Diffusion Coefficient_fit")
C_fit_values.insert(0, "Initial Concentration_fit")

# create .txt file with list of data (and headings)
with open('Fit_data/Fitdata_Depth_profile.txt','w') as f:
    lis=[sample_number,D_values,C_values,D_fit_values,C_fit_values]
    for x in zip(*lis):
        f.write("{0}\t{1}\t{2}\t{3}\t{4}\n".format(*x))
```

HD_600s

```
In [7]: import os
        import sys
        import numpy as np
        import matplotlib.pyplot as plt
        from scipy.special import erf
```

```
from scipy.optimize import curve_fit

wdir = 'M:\JcB\PhD\Experiments\Analysis\Python'
os.chdir(wdir)
os.getcwd()
datadir = os.path.join( wdir, 'HD_600s_profiles' )
filepath = '/long/path/to/myfile.txt'
os.path.basename(filepath)
filelist = os.listdir(datadir)
filelist

datafiles = []
sample_number = []
for filename in filelist:
    if filename.endswith('.txt'):
        datafiles.append(filename)
        sample_number.append(filename[:-4])

def get_data(filepath):
    dist, conc = np.loadtxt(filepath, skiprows=1, unpack=True)
    return dist, conc

def FI(dist, D, C):
    return (1-erf(dist/(2*((D*600)**0.5))))*C

D_values = []
C_values = []
def calculate_fit(dist, conc):
    D0 = 1e-15
    C0 = 500
    (D, C), pcov = curve_fit(FI, dist, conc, p0=[D0, C0])
    y = FI(dist, D, C)
    D_values.append(D)
    C_values.append(C)
    return y

def FI_fit(dist, D_fit, C_fit):
    return (1-erf(dist/(2*((D_fit*600)**0.5))))*C_fit

D_fit_values = []
C_fit_values = []
def calculate_fit_fit(dist, conc_fit):
    D0 = 1e-15
    C0 = 500
    (D_fit, C_fit), pcov = curve_fit(FI, dist, conc_fit, p0=[D0, C0])
    y = FI_fit(dist, D_fit, C_fit)
    D_fit_values.append(D_fit)
    C_fit_values.append(C_fit)
    return y

def plot_data(filepath):
    dist, conc = get_data(filepath)
    y = calculate_fit(dist, conc)
    plt.figure()
```

```
    plt.plot(dist, conc, ’ro’, label="SIMS data")
    plt.plot(dist, y, ’k-’, label="Fit")
    plt.xlabel("Distance (m)")
    plt.ylabel("D (ppm)")
    plt.ticklabel_format(style=’sci’, axis=’x’, scilimits=(0,0))
    D_values_list = [’D = ’ + ’%.2E’ % Dv for Dv in D_values]
    C_values_list = [’C = ’ + ’%.0f’ % Cv for Cv in C_values]
    plt.figtext(0.8, 0.75, ’’.join(D_values_list), ha=’right’)
    plt.figtext(0.8, 0.65, ’’.join(C_values_list), ha=’right’)
    filename = os.path.basename(filepath)
    plt.title(filename[:-4])
    figure_filename = filename.replace(’.txt’, ’.png’)
    savepath = os.path.join(datadir, figure_filename)
    plt.savefig(savepath, dpi=200)
    plt.close()
    return

def plot_data_fix(filepath):
    dist, conc = get_data(filepath)
    av = np.average(conc[-10:-1])
    conc_fix =  [z - av for z in conc]
    y = calculate_fit_fit(dist, conc_fix)
    plt.figure()
    plt.plot(dist, conc_fix, ’ro’, label="SIMS data_fix")
    plt.plot(dist, y, ’k-’, label="Fit_fix")
    plt.xlabel("Distance (m)")
    plt.ylabel("D (ppm)")
    plt.ticklabel_format(style=’sci’, axis=’x’, scilimits=(0,0))
    D_fit_values_list = [’D = ’ + ’%.2E’ % Dvfit for Dvfit in D_fit_values]
    C_fit_values_list = [’C = ’ + ’%.0f’ % Cvfit for Cvfit in C_fit_values]
    plt.figtext(0.8, 0.75, ’’.join(D_fit_values_list), ha=’right’)
    plt.figtext(0.8, 0.65, ’’.join(C_fit_values_list), ha=’right’)
    filename = os.path.basename(filepath)
    newfilename = filename.replace(’E’, ’Fit_E’)
    plt.title(newfilename[:-4])
    figure2_filename = newfilename.replace(’.txt’, ’.png’)
    savepath2 = os.path.join(datadir, figure2_filename)
    plt.savefig(savepath2, dpi=200)
    plt.close()
    return

for datafile in datafiles:
    datafilepath = os.path.join(datadir, datafile)
    plot_data(datafilepath)
    plot_data_fix(datafilepath)
    D_values = []
    C_values = []
    D_fit_values = []
    C_fit_values = []

for datafile in datafiles:
    datafilepath = os.path.join(datadir, datafile)
    dist, conc = get_data(datafilepath)
    calculate_fit(dist, conc)
```

```
    av = np.average(conc[-10:-1])
    conc_fix =  [z - av for z in conc]
    calculate_fit_fit(dist, conc_fix)

sample_number.insert(0, "Sample Number")
D_values.insert(0, "Diffusion Coefficient")
C_values.insert(0, "Initial Concentration")
D_fit_values.insert(0, "Diffusion Coefficient_fit")
C_fit_values.insert(0, "Initial Concentration_fit")

with open('Fit_data/Fitdata_Fo_HD_600s.txt','w') as f:
    lis=[sample_number,D_values,C_values,D_fit_values,C_fit_values]
    for x in zip(*lis):
        f.write("{0}\t{1}\t{2}\t{3}\t{4}\n".format(*x))
```

HD_300s

```
In [5]: import os
        import sys
        import numpy as np
        import matplotlib.pyplot as plt
        from scipy.special import erf
        from scipy.optimize import curve_fit

        wdir = 'M:\JcB\PhD\Experiments\Analysis\Python'
        os.chdir(wdir)
        os.getcwd()
        datadir = os.path.join( wdir, 'HD_300s_profiles' )
        filepath = '/long/path/to/myfile.txt'
        os.path.basename(filepath)
        filelist = os.listdir(datadir)
        filelist

        datafiles = []
        sample_number = []
        for filename in filelist:
            if filename.endswith('.txt'):
                datafiles.append(filename)
                sample_number.append(filename[:-4])

        def FI(dist, D, C):
            return (1-erf(dist/(2*((D*300)**0.5))))*C

        def get_data(filepath):
            dist, conc = np.loadtxt(filepath, skiprows=1, unpack=True)
            return dist, conc

        D_values = []
        C_values = []
        def calculate_fit(dist, conc):
            D0 = 1e-15
            C0 = 500
            (D, C), pcov = curve_fit(FI, dist, conc, p0=[D0, C0])
            y = FI(dist, D, C)
```

```
    D_values.append(D)
    C_values.append(C)
    return y

def FI_fit(dist, D_fit, C_fit):
    return (1-erf(dist/(2*((D_fit*600)**0.5))))*C_fit

D_fit_values = []
C_fit_values = []
def calculate_fit_fit(dist, conc_fit):
    D0 = 1e-15
    C0 = 500
    (D_fit, C_fit), pcov = curve_fit(FI, dist, conc_fit, p0=[D0, C0])
    y = FI_fit(dist, D_fit, C_fit)
    D_fit_values.append(D_fit)
    C_fit_values.append(C_fit)
    return y

def plot_data(filepath):
    dist, conc = get_data(filepath)
    y = calculate_fit(dist, conc)
    plt.figure()
    plt.plot(dist, conc, 'ro', label="SIMS data")
    plt.plot(dist, y, 'k-', label="Fit")
    plt.xlabel("Distance (m)")
    plt.ylabel("D (ppm)")
    plt.ticklabel_format(style='sci', axis='x', scilimits=(0,0))
    D_values_list = ['D = ' + '%.2E' % Dv for Dv in D_values]
    C_values_list = ['C = ' + '%.0f' % Cv for Cv in C_values]
    plt.figtext(0.8, 0.75, ''.join(D_values_list), ha='right')
    plt.figtext(0.8, 0.65, ''.join(C_values_list), ha='right')
    filename = os.path.basename(filepath)
    plt.title(filename[:-4])
    figure_filename = filename.replace('.txt', '.png')
    savepath = os.path.join(datadir, figure_filename)
    plt.savefig(savepath, dpi=200)
    plt.close()
    return

def plot_data_fix(filepath):
    dist, conc = get_data(filepath)
    av = np.average(conc[-10:-1])
    conc_fix =  [z - av for z in conc]
    y = calculate_fit_fit(dist, conc_fix)
    plt.figure()
    plt.plot(dist, conc_fix, 'ro', label="SIMS data_fix")
    plt.plot(dist, y, 'k-', label="Fit_fix")
    #plt.legend()
    plt.xlabel("Distance (m)")
    plt.ylabel("D (ppm)")
    plt.ticklabel_format(style='sci', axis='x', scilimits=(0,0))
    D_fit_values_list = ['D = ' + '%.2E' % Dvfit for Dvfit in D_fit_values]
    C_fit_values_list = ['C = ' + '%.0f' % Cvfit for Cvfit in C_fit_values]
    plt.figtext(0.8, 0.75, ''.join(D_fit_values_list), ha='right')
```

```
     plt.figtext(0.8, 0.65, ’’.join(C_fit_values_list), ha=’right’)
     filename = os.path.basename(filepath)
     newfilename = filename.replace(’E’, ’Fit_E’)
     plt.title(newfilename[:-4])
     figure2_filename = newfilename.replace(’.txt’, ’.png’)
     savepath2 = os.path.join(datadir, figure2_filename)
     plt.savefig(savepath2, dpi=200)
     plt.close()
     return

 for datafile in datafiles:
     datafilepath = os.path.join(datadir, datafile)
     plot_data(datafilepath)
     plot_data_fix(datafilepath)
     D_values = []
     C_values = []
     D_fit_values = []
     C_fit_values = []

 for datafile in datafiles:
     datafilepath = os.path.join(datadir, datafile)
     dist, conc = get_data(datafilepath)
     calculate_fit(dist, conc)
     av = np.average(conc[-10:-1])
     conc_fix =  [z - av for z in conc]
     calculate_fit_fit(dist, conc_fix)

 sample_number.insert(0, "Sample Number")
 D_values.insert(0, "Diffusion Coefficient")
 C_values.insert(0, "Initial Concentration")
 D_fit_values.insert(0, "Diffusion Coefficient_fit")
 C_fit_values.insert(0, "Initial Concentration_fit")

 with open(’Fit_data/Fitdata_Fo_HD_300s.txt’,’w’) as f:
     lis=[sample_number,D_values,C_values,D_fit_values,C_fit_values]
     for x in zip(*lis):
         f.write("{0}\t{1}\t{2}\t{3}\t{4}\n".format(*x))
```

HSi_600s

```
In []: import os
       import sys
       import numpy as np
       import matplotlib.pyplot as plt
       from scipy.special import erf
       from scipy.optimize import curve_fit

       wdir = ’M:\JcB\PhD\Experiments\Analysis\Python’
       os.chdir(wdir)
       os.getcwd()
       datadir = os.path.join( wdir, ’HSi_600s_profiles’ )
       filepath = ’/long/path/to/myfile.txt’
       os.path.basename(filepath)
       filelist = os.listdir(datadir)
```

```
filelist

datafiles = []
sample_number = []
for filename in filelist:
    if filename.endswith('.txt'):
        datafiles.append(filename)
        sample_number.append(filename[:-4])

def FI(dist, D, C):
    return (1-erf(dist/(2*((D*600)**0.5))))*C

def get_data(filepath):
    dist, conc = np.loadtxt(filepath, skiprows=1, unpack=True)
    return dist, conc

D_values = []
C_values = []
def calculate_fit(dist, conc):
    D0 = 1e-15
    C0 = 500
    (D, C), pcov = curve_fit(FI, dist, conc, p0=[D0, C0])
    y = FI(dist, D, C)
    D_values.append(D)
    C_values.append(C)
    return y

def FI_fit(dist, D_fit, C_fit):
    return (1-erf(dist/(2*((D_fit*600)**0.5))))*C_fit

D_fit_values = []
C_fit_values = []
def calculate_fit_fit(dist, conc_fit):
    D0 = 1e-15
    C0 = 500
    (D_fit, C_fit), pcov = curve_fit(FI, dist, conc_fit, p0=[D0, C0])
    y = FI_fit(dist, D_fit, C_fit)
    D_fit_values.append(D_fit)
    C_fit_values.append(C_fit)
    return y

def plot_data(filepath):
    dist, conc = get_data(filepath)
    y = calculate_fit(dist, conc)
    plt.figure()
    plt.plot(dist, conc, 'ro', label="SIMS data")
    plt.plot(dist, y, 'k-', label="Fit")
    plt.xlabel("Distance (m)")
    plt.ylabel("D (ppm)")
    plt.ticklabel_format(style='sci', axis='x', scilimits=(0,0))
    D_values_list = ['D = ' + '%.2E' % Dv for Dv in D_values]
    C_values_list = ['C = ' + '%.0f' % Cv for Cv in C_values]
    plt.figtext(0.8, 0.75, ''.join(D_values_list), ha='right')
    plt.figtext(0.8, 0.65, ''.join(C_values_list), ha='right')
```

```
    filename = os.path.basename(filepath)
    plt.title(filename[:-4])
    figure_filename = filename.replace('.txt', '.png')
    savepath = os.path.join(datadir, figure_filename)
    plt.savefig(savepath, dpi=200)
    plt.close()
    return

def plot_data_fix(filepath):
    dist, conc = get_data(filepath)
    av = np.average(conc[-10:-1])
    conc_fix =  [z - av for z in conc]
    y = calculate_fit_fit(dist, conc_fix)
    plt.figure()
    plt.plot(dist, conc_fix, 'ro', label="SIMS data_fix")
    plt.plot(dist, y, 'k-', label="Fit_fix")
    plt.xlabel("Distance (m)")
    plt.ylabel("D (ppm)")
    plt.ticklabel_format(style='sci', axis='x', scilimits=(0,0))
    D_fit_values_list = ['D = ' + '%.2E' % Dvfit for Dvfit in D_fit_values]
    C_fit_values_list = ['C = ' + '%.0f' % Cvfit for Cvfit in C_fit_values]
    plt.figtext(0.8, 0.75, ''.join(D_fit_values_list), ha='right')
    plt.figtext(0.8, 0.65, ''.join(C_fit_values_list), ha='right')
    filename = os.path.basename(filepath)
    newfilename = filename.replace('E', 'Fit_E')
    plt.title(newfilename[:-4])
    figure2_filename = newfilename.replace('.txt', '.png')
    savepath2 = os.path.join(datadir, figure2_filename)
    plt.savefig(savepath2, dpi=200)
    plt.close()
    return

for datafile in datafiles:
    datafilepath = os.path.join(datadir, datafile)
    plot_data(datafilepath)
    plot_data_fix(datafilepath)
    D_values = []
    C_values = []
    D_fit_values = []
    C_fit_values = []

for datafile in datafiles:
    datafilepath = os.path.join(datadir, datafile)
    dist, conc = get_data(datafilepath)
    calculate_fit(dist, conc)
    av = np.average(conc[-10:-1])
    conc_fix =  [z - av for z in conc]
    calculate_fit_fit(dist, conc_fix)

sample_number.insert(0, "Sample Number")
D_values.insert(0, "Diffusion Coefficient")
C_values.insert(0, "Initial Concentration")
D_fit_values.insert(0, "Diffusion Coefficient_fit")
C_fit_values.insert(0, "Initial Concentration_fit")
```

```
        with open('Fit_data/Fitdata_Fo_HSi_600s.txt','w') as f:
            lis=[sample_number,D_values,C_values,D_fit_values,C_fit_values]
            for x in zip(*lis):
                f.write("{0}\t{1}\t{2}\t{3}\t{4}\n".format(*x))
```

HSi_300s

```
In [1]: import os
        import sys
        import numpy as np
        import matplotlib.pyplot as plt
        from scipy.special import erf
        from scipy.optimize import curve_fit

        wdir = 'M:\JcB\PhD\Experiments\Analysis\Python'
        os.chdir(wdir)
        os.getcwd()
        datadir = os.path.join( wdir, 'HSi_300s_profiles' )
        filepath = '/long/path/to/myfile.txt'
        os.path.basename(filepath)
        filelist = os.listdir(datadir)
        filelist

        datafiles = []
        sample_number = []
        for filename in filelist:
            if filename.endswith('.txt'):
                datafiles.append(filename)
                sample_number.append(filename[:-4])

        def FI(dist, D, C):
            return (1-erf(dist/(2*((D*300)**0.5))))*C

        def get_data(filepath):
            dist, conc = np.loadtxt(filepath, skiprows=1, unpack=True)
            return dist, conc

        D_values = []
        C_values = []
        def calculate_fit(dist, conc):
            D0 = 1e-15
            C0 = 500
            (D, C), pcov = curve_fit(FI, dist, conc, p0=[D0, C0])
            y = FI(dist, D, C)
            D_values.append(D)
            C_values.append(C)
            return y

        def FI_fit(dist, D_fit, C_fit):
            return (1-erf(dist/(2*((D_fit*600)**0.5))))*C_fit

        D_fit_values = []
        C_fit_values = []
```

```
def calculate_fit_fit(dist, conc_fit):
    D0 = 1e-15
    C0 = 500
    (D_fit, C_fit), pcov = curve_fit(FI, dist, conc_fit, p0=[D0, C0])
    y = FI_fit(dist, D_fit, C_fit)
    D_fit_values.append(D_fit)
    C_fit_values.append(C_fit)
    return y

def plot_data(filepath):
    dist, conc = get_data(filepath)
    y = calculate_fit(dist, conc)
    plt.figure()
    plt.plot(dist, conc, 'ro', label="SIMS data")
    plt.plot(dist, y, 'k-', label="Fit")
    plt.xlabel("Distance (m)")
    plt.ylabel("D (ppm)")
    plt.ticklabel_format(style='sci', axis='x', scilimits=(0,0))
    D_values_list = ['D = ' + '%.2E' % Dv for Dv in D_values]
    C_values_list = ['C = ' + '%.0f' % Cv for Cv in C_values]
    plt.figtext(0.8, 0.75, ''.join(D_values_list), ha='right')
    plt.figtext(0.8, 0.65, ''.join(C_values_list), ha='right')
    filename = os.path.basename(filepath)
    plt.title(filename[:-4])
    figure_filename = filename.replace('.txt', '.png')
    savepath = os.path.join(datadir, figure_filename)
    plt.savefig(savepath, dpi=200)
    plt.close()
    return

def plot_data_fix(filepath):
    dist, conc = get_data(filepath)
    av = np.average(conc[-10:-1])
    conc_fix =  [z - av for z in conc]
    y = calculate_fit_fit(dist, conc_fix)
    plt.figure()
    plt.plot(dist, conc_fix, 'ro', label="SIMS data_fix")
    plt.plot(dist, y, 'k-', label="Fit_fix")
    plt.xlabel("Distance (m)")
    plt.ylabel("D (ppm)")
    plt.ticklabel_format(style='sci', axis='x', scilimits=(0,0))
    D_fit_values_list = ['D = ' + '%.2E' % Dvfit for Dvfit in D_fit_values]
    C_fit_values_list = ['C = ' + '%.0f' % Cvfit for Cvfit in C_fit_values]
    plt.figtext(0.8, 0.75, ''.join(D_fit_values_list), ha='right')
    plt.figtext(0.8, 0.65, ''.join(C_fit_values_list), ha='right')
    filename = os.path.basename(filepath)
    newfilename = filename.replace('E', 'Fit_E')
    plt.title(newfilename[:-4])
    figure2_filename = newfilename.replace('.txt', '.png')
    savepath2 = os.path.join(datadir, figure2_filename)
    plt.savefig(savepath2, dpi=200)
    plt.close()
    return
```

```
        for datafile in datafiles:
            datafilepath = os.path.join(datadir, datafile)
            plot_data(datafilepath)
            plot_data_fix(datafilepath)
            D_values = []
            C_values = []
            D_fit_values = []
            C_fit_values = []

        for datafile in datafiles:
            datafilepath = os.path.join(datadir, datafile)
            dist, conc = get_data(datafilepath)
            calculate_fit(dist, conc)
            av = np.average(conc[-10:-1])
            conc_fix =  [z - av for z in conc]
            calculate_fit_fit(dist, conc_fix)

        sample_number.insert(0, "Sample Number")
        D_values.insert(0, "Diffusion Coefficient")
        C_values.insert(0, "Initial Concentration")
        D_fit_values.insert(0, "Diffusion Coefficient_fit")
        C_fit_values.insert(0, "Initial Concentration_fit")

        with open('Fit_data/Fitdata_Fo_HSi_300s.txt','w') as f:
            lis=[sample_number,D_values,C_values,D_fit_values,C_fit_values]
            for x in zip(*lis):
                f.write("{0}\t{1}\t{2}\t{3}\t{4}\n".format(*x))

In [9]: # creates a file containing all values calculated above
        import glob

        wdir = 'M:\JcB\PhD\Experiments\Analysis\Python\Fit_data'
        os.chdir(wdir)

        read_files = glob.glob("*.txt")
        open('Fitdata_Fo_ALL.txt', 'w').close()
        with open("Fitdata_Fo_ALL.txt", "wb") as outfile:
            for f in read_files:
                with open(f, "rb") as infile:
                    outfile.write(infile.read())
```

APPENDIX B

FTIR spectra for forsterite samples

Figure B.1: *FTIR spectra in the OH stretching region (3,700 - 3,100cm^{-1}) from samples following D-H exchange runs **a** - E5, **b** - E6, **c** - E7, **d** - E8, **e** - E9 & **e** - EF11. Note that the absorbance scale (y-axis) on **e** is not at the same scale as for the other plots.*

(a)

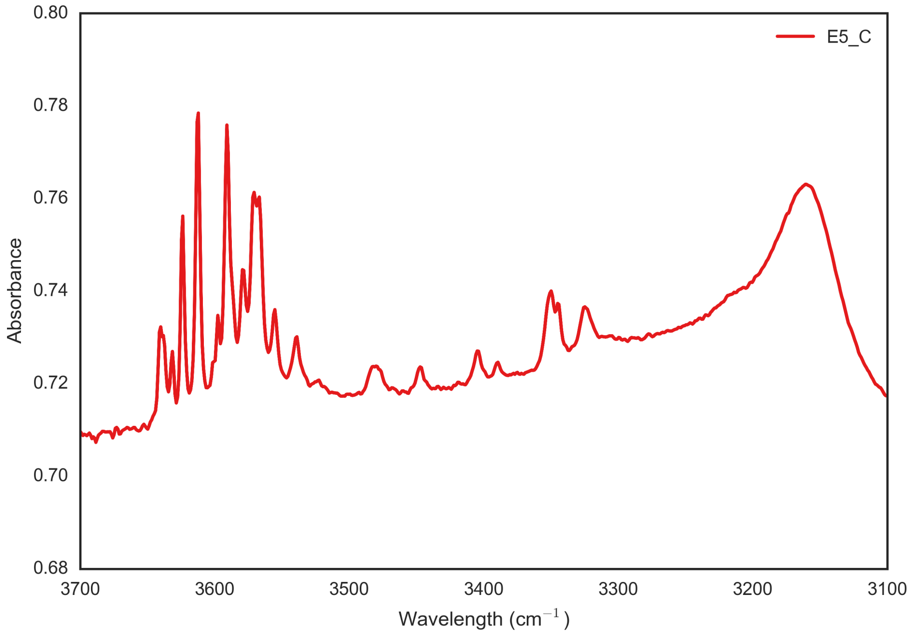

(b)

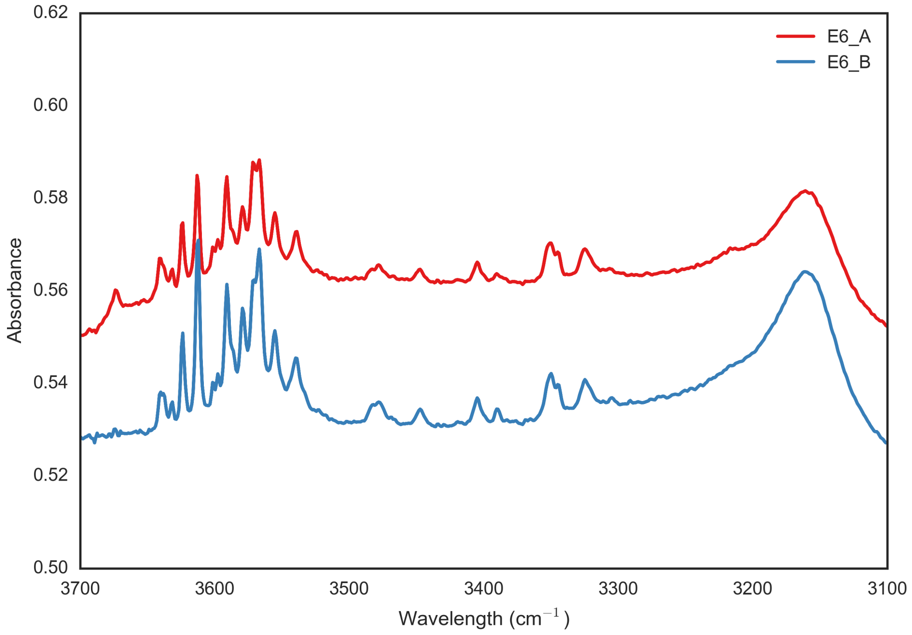

(c)

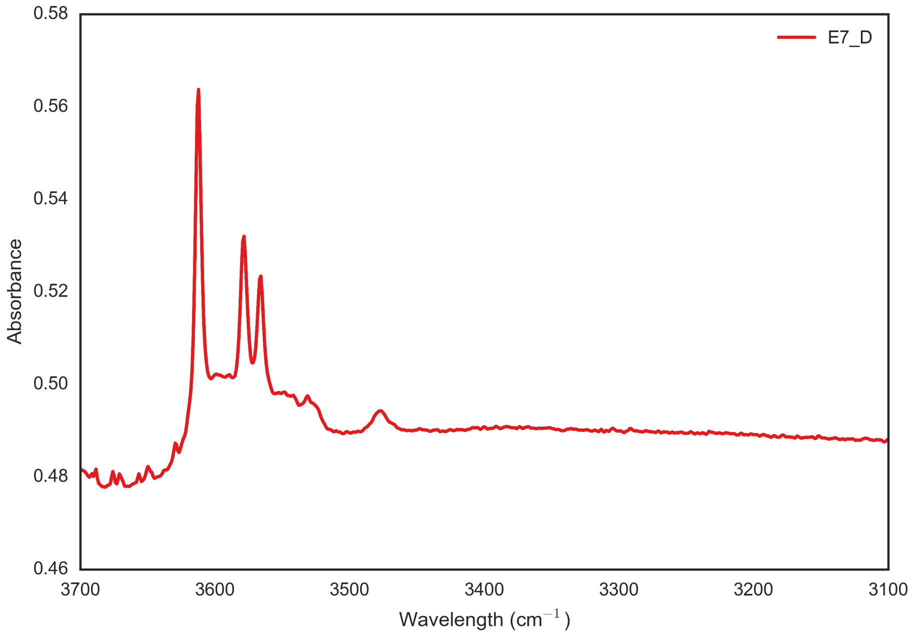
0.58
0.56
0.54
0.52
0.50
0.48
0.46
Absorbance
3700
3600
3500
3400
3300
3200
3100
Wavelength (cm^{-1})
E7_D

(d)

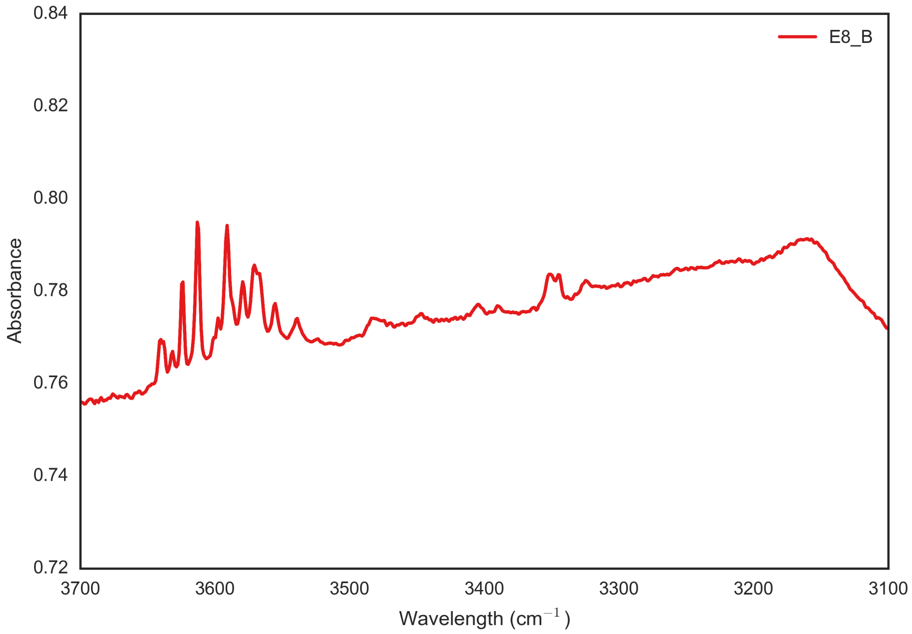
0.84
0.82
0.80
0.78
0.76
0.74
0.72
Absorbance
3700
3600
3500
3400
3300
3200
3100
Wavelength (cm^{-1})
E8_B

(e)

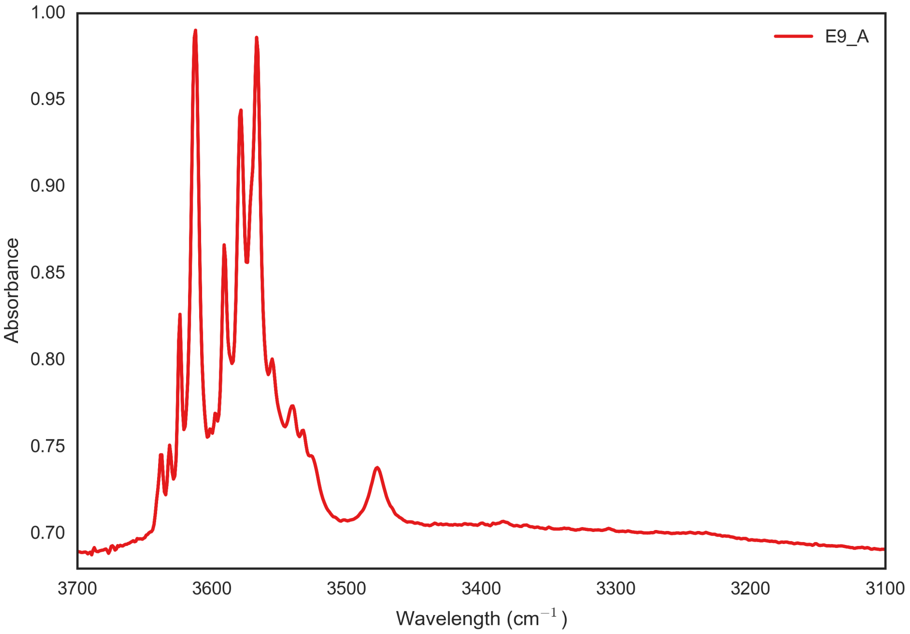

E9_A
Absorbance
1.00
0.95
0.90
0.85
0.80
0.75
0.70
3700
3600
3500
3400
3300
3200
3100
Wavelength (cm^{-1})

(f)

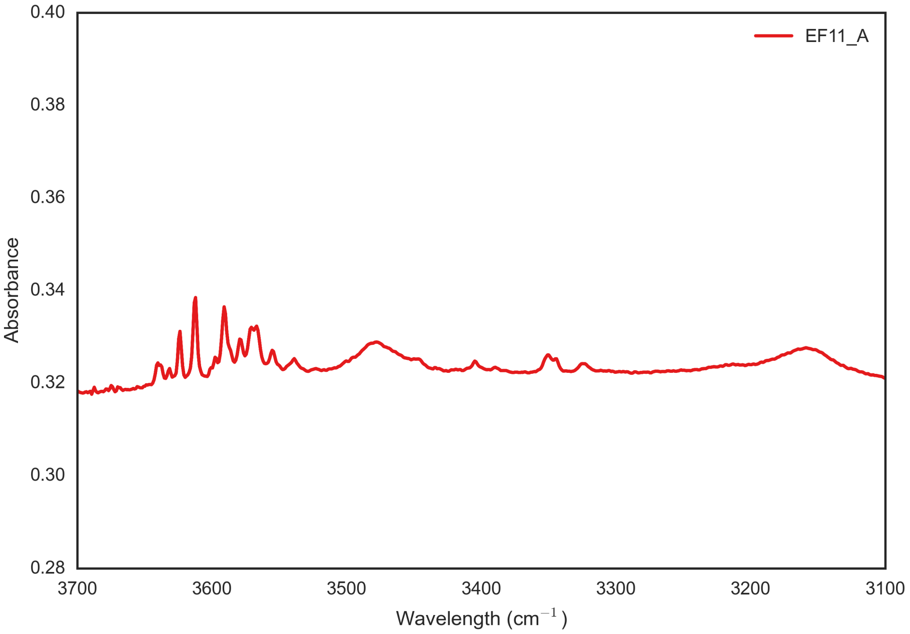

EF11_A
Absorbance
0.40
0.38
0.36
0.34
0.32
0.30
0.28
3700
3600
3500
3400
3300
3200
3100
Wavelength (cm^{-1})

APPENDIX C

Concentration-depth plots (with fit to Fick's law) for forsterite samples

Figure C.1: *Fitted concentration-depth profiles for forsterite samples. Errors on D, C values are given in table 4.8.*

(a)

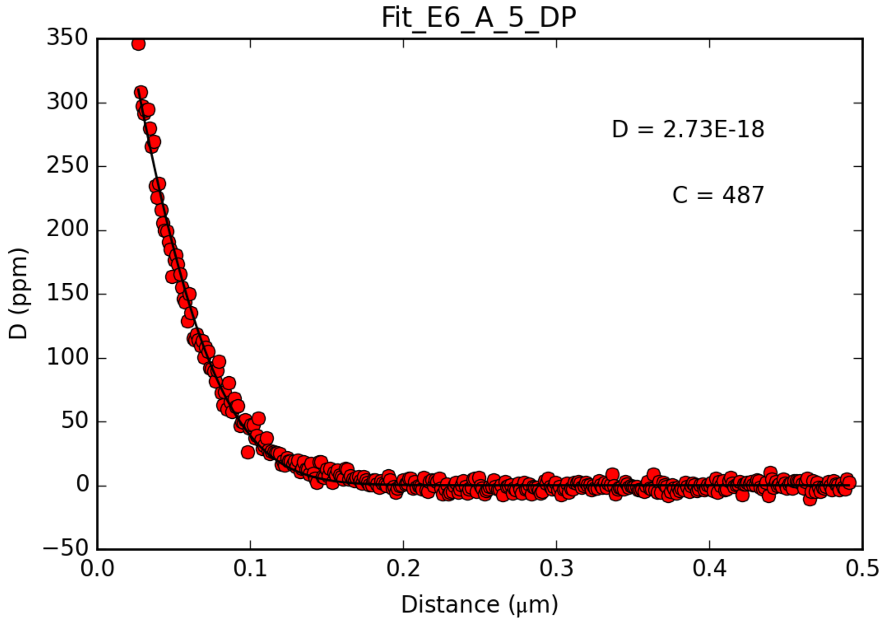

(b)

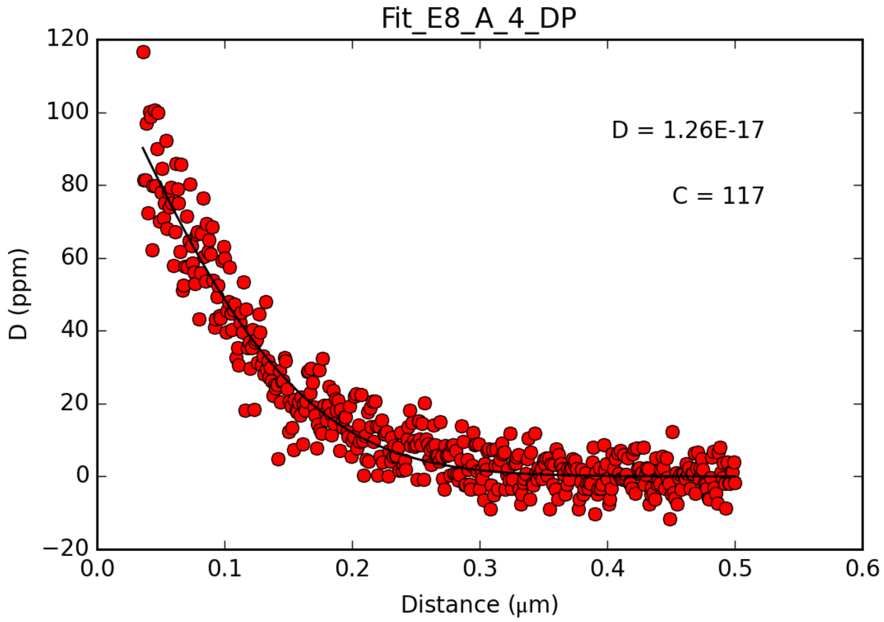

(c)

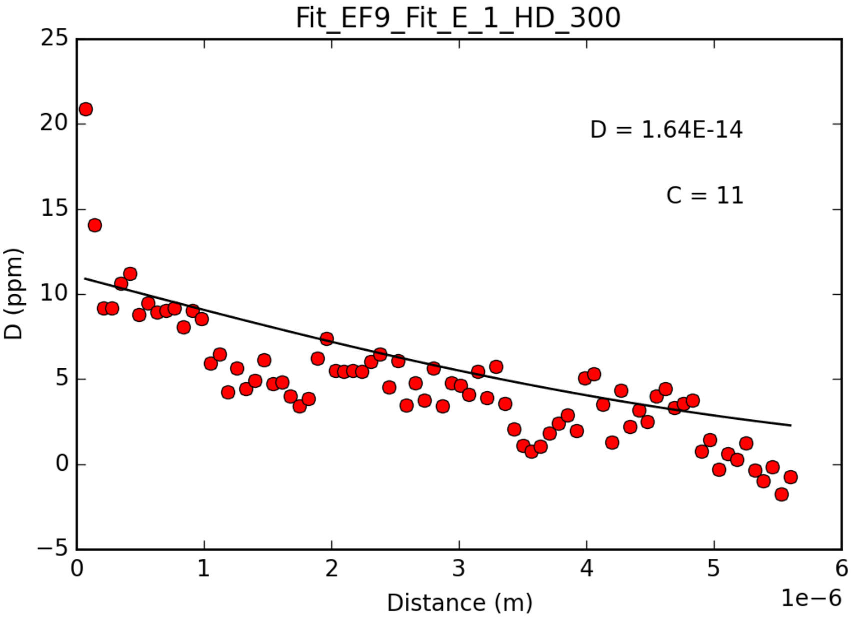
Fit_EF9_Fit_E_1_HD_300
D = 1.64E-14
C = 11
D (ppm)
Distance (m)
1e−6
25
20
15
10
5
0
−5
0
1
2
3
4
5
6

(d)

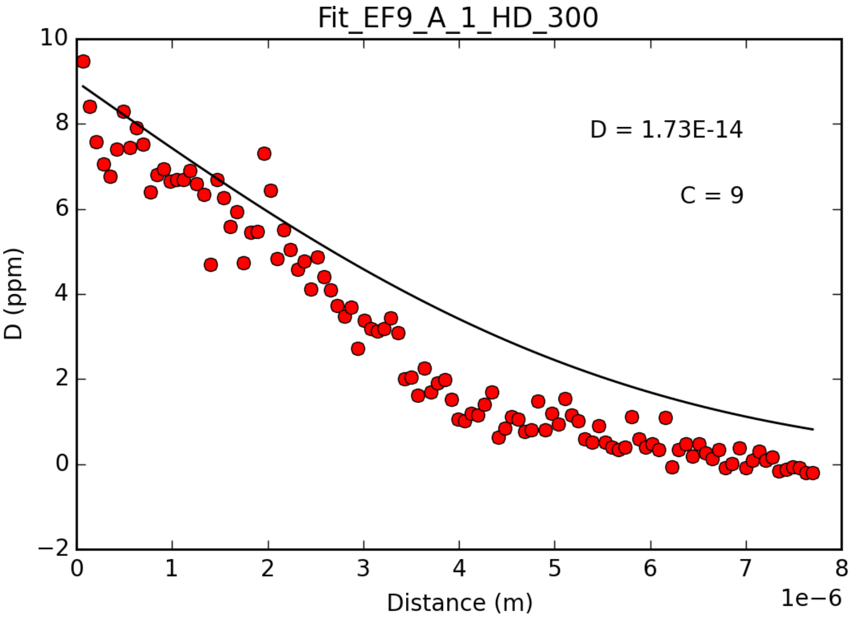
Fit_EF9_A_1_HD_300
D = 1.73E-14
C = 9
D (ppm)
Distance (m)
1e−6
10
8
6
4
2
0
−2
0
1
2
3
4
5
6
7
8

(e)

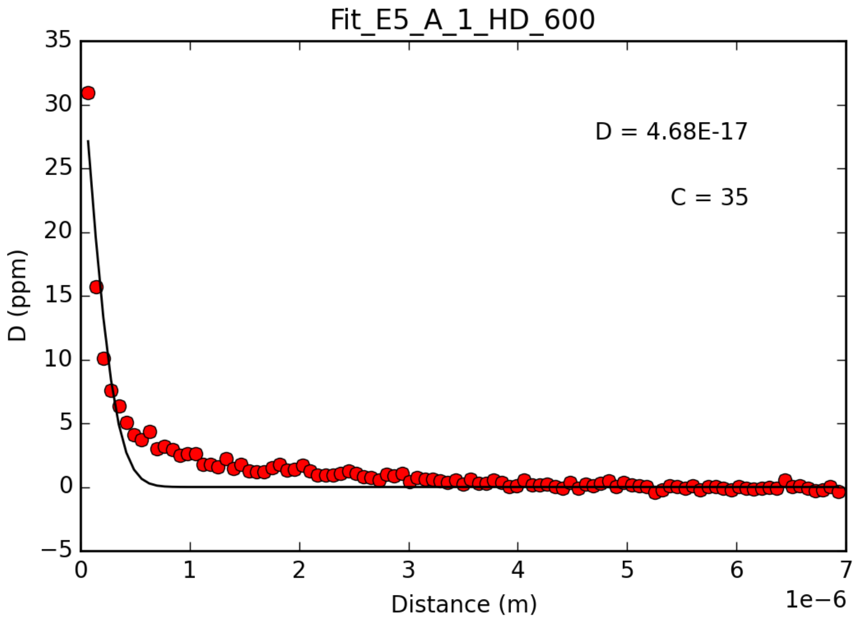
Fit_E5_A_1_HD_600
D = 4.68E-17
C = 35
D (ppm)
35
30
25
20
15
10
5
0
−5
0
1
2
3
4
5
6
7
Distance (m)
1e−6

(f)

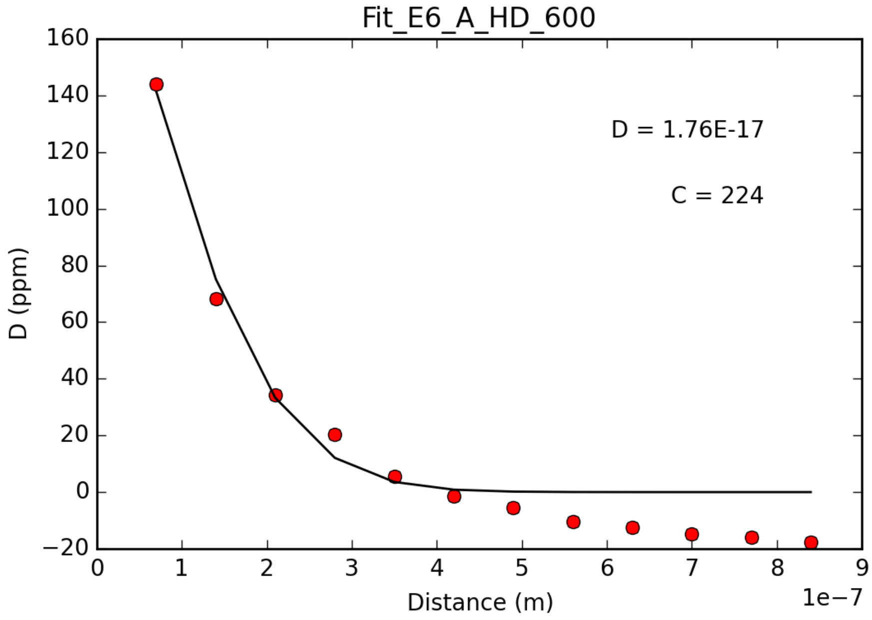
Fit_E6_A_HD_600
D = 1.76E-17
C = 224
D (ppm)
160
140
120
100
80
60
40
20
0
−20
0
1
2
3
4
5
6
7
8
9
Distance (m)
1e−7

(g)

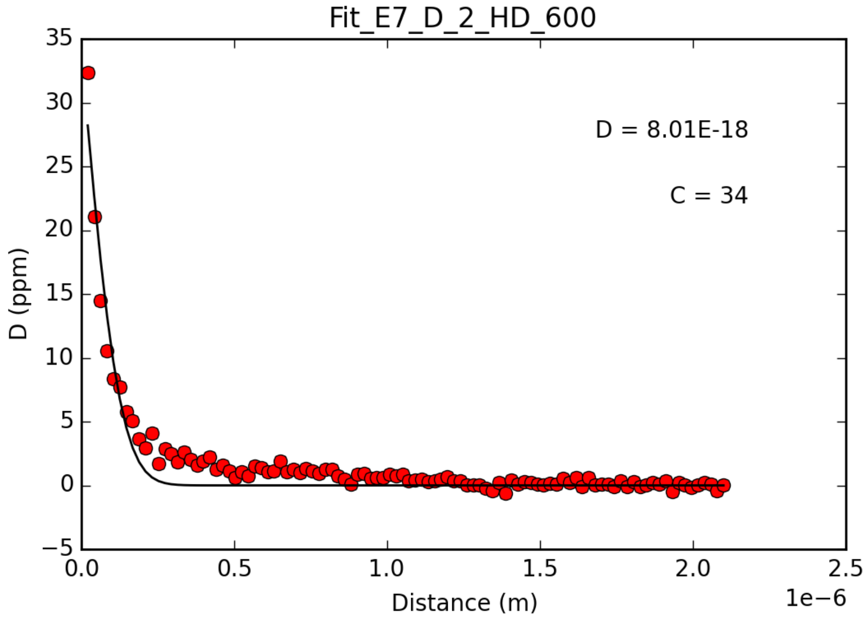
Fit_E7_D_2_HD_600
D = 8.01E-18
C = 34
D (ppm)
Distance (m)
1e−6
35
30
25
20
15
10
5
0
−5
0.0
0.5
1.0
1.5
2.0
2.5

(h)

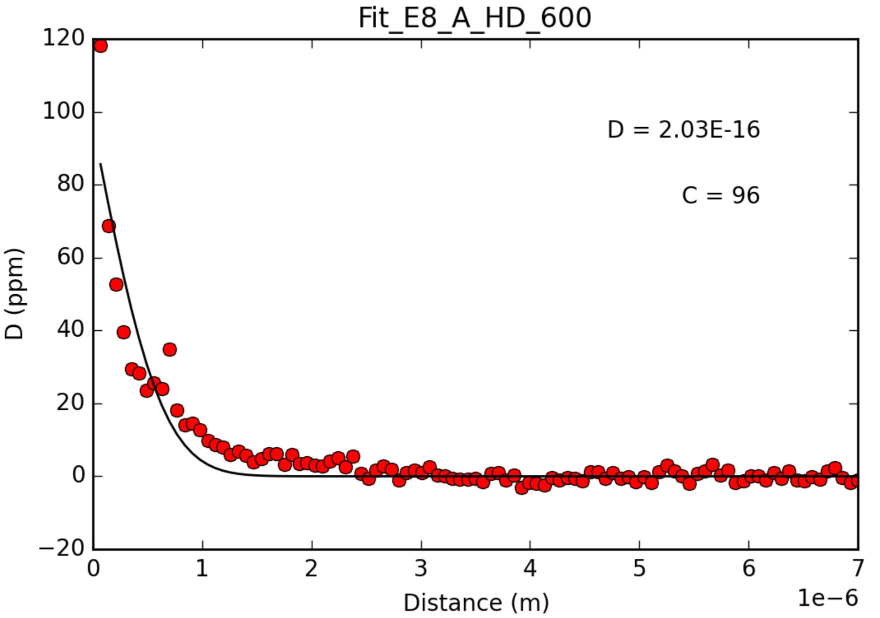
Fit_E8_A_HD_600
D = 2.03E-16
C = 96
D (ppm)
Distance (m)
1e−6
120
100
80
60
40
20
0
−20
0
1
2
3
4
5
6
7

(i)

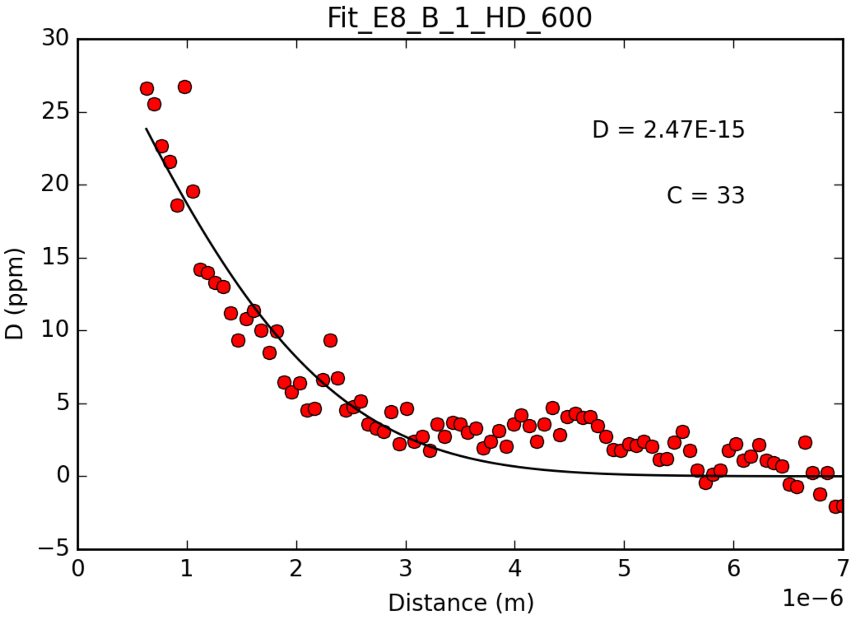
Fit_E8_B_1_HD_600
D = 2.47E-15
C = 33
D (ppm)
30
25
20
15
10
5
0
−5
0
1
2
3
4
5
6
7
Distance (m)
1e−6

(j)

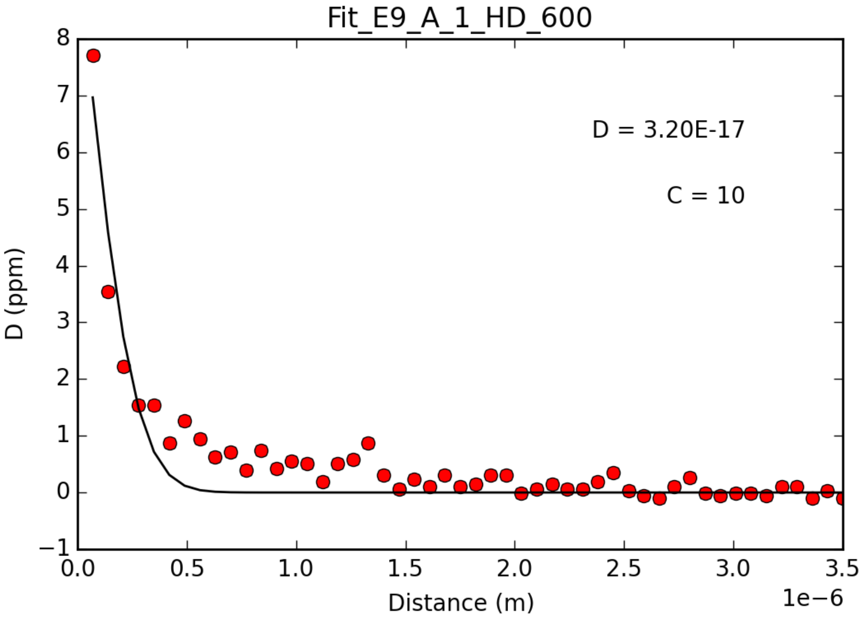
Fit_E9_A_1_HD_600
D = 3.20E-17
C = 10
D (ppm)
8
7
6
5
4
3
2
1
0
−1
0.0
0.5
1.0
1.5
2.0
2.5
3.0
3.5
Distance (m)
1e−6

(k)

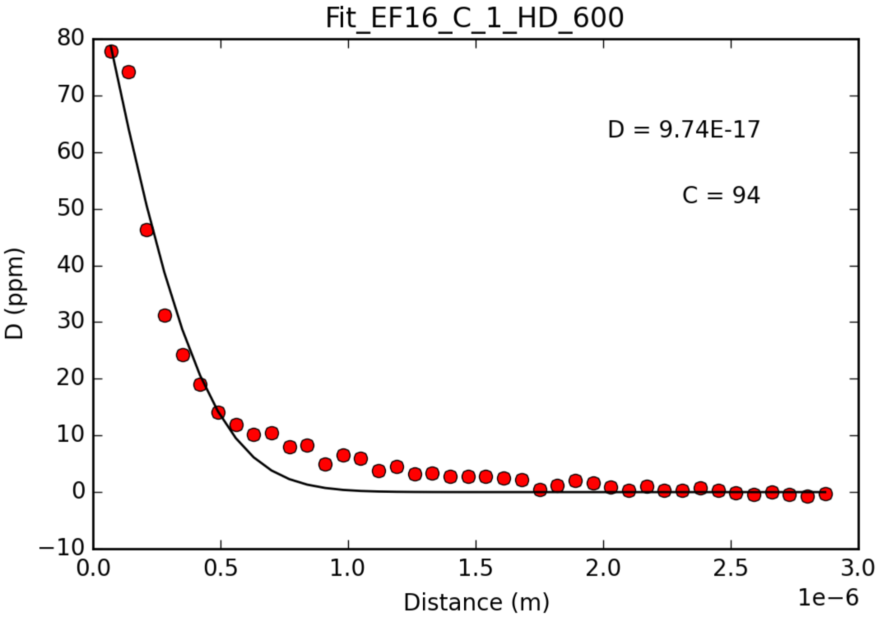
Fit_EF16_C_1_HD_600
D = 9.74E-17
C = 94
D (ppm)
80
70
60
50
40
30
20
10
0
−10
0.0
0.5
1.0
1.5
2.0
2.5
3.0
Distance (m)
1e−6

(l)

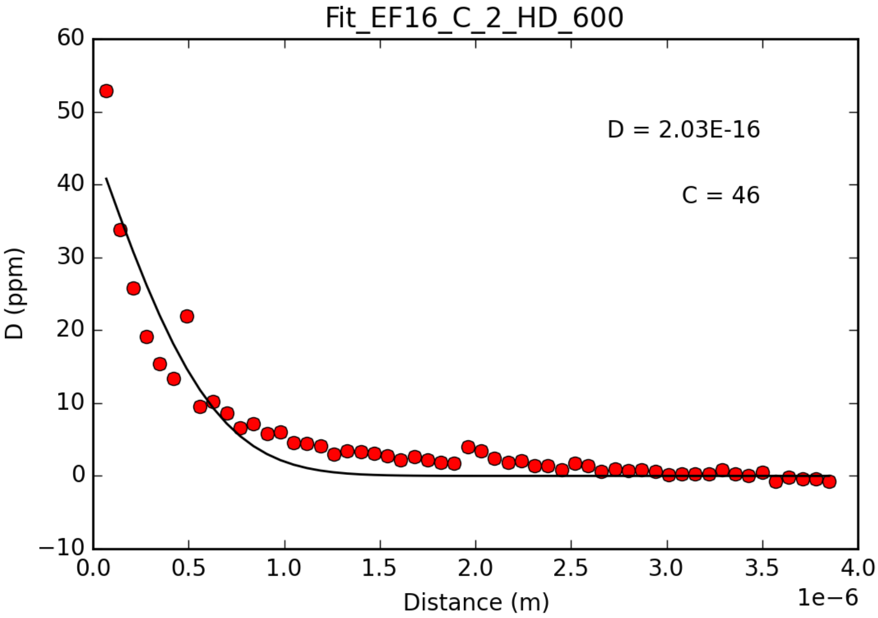
Fit_EF16_C_2_HD_600
D = 2.03E-16
C = 46
D (ppm)
60
50
40
30
20
10
0
−10
0.0
0.5
1.0
1.5
2.0
2.5
3.0
3.5
4.0
Distance (m)
1e−6

(m)

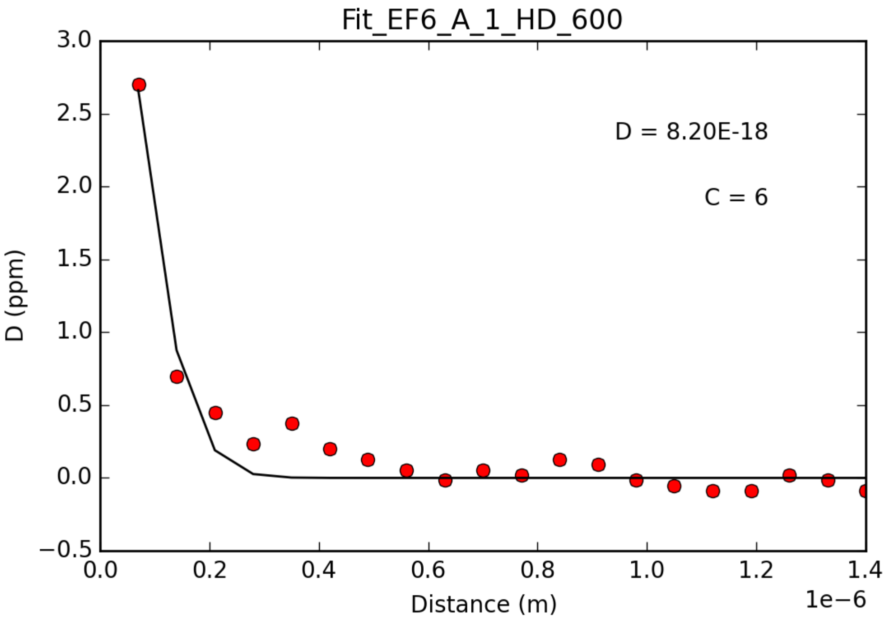
Fit_EF6_A_1_HD_600
D = 8.20E-18
C = 6
D (ppm)
3.0
2.5
2.0
1.5
1.0
0.5
0.0
−0.5
0.0
0.2
0.4
0.6
0.8
1.0
1.2
1.4
Distance (m)
1e−6

(n)

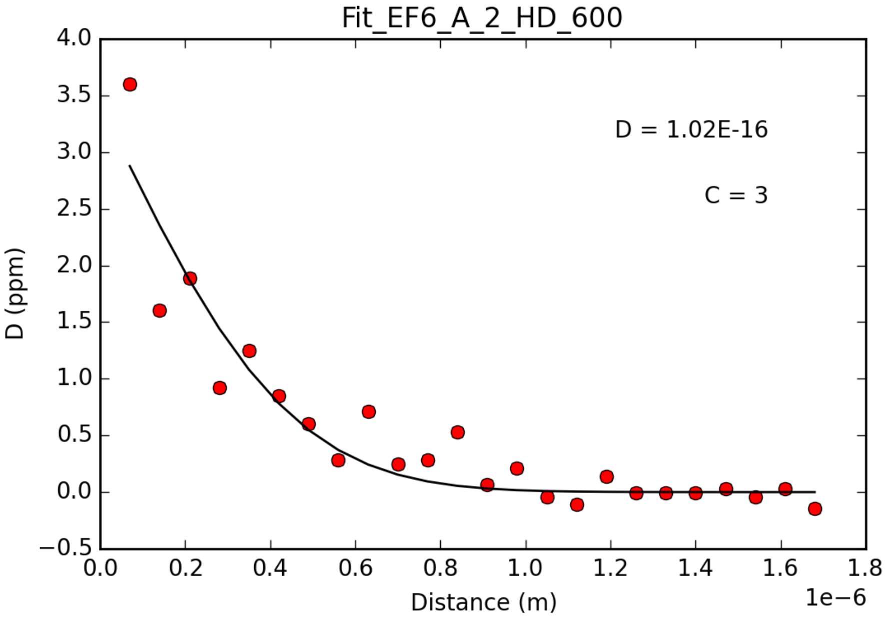
Fit_EF6_A_2_HD_600
D = 1.02E-16
C = 3
D (ppm)
4.0
3.5
3.0
2.5
2.0
1.5
1.0
0.5
0.0
−0.5
0.0
0.2
0.4
0.6
0.8
1.0
1.2
1.4
1.6
1.8
Distance (m)
1e−6

(o)

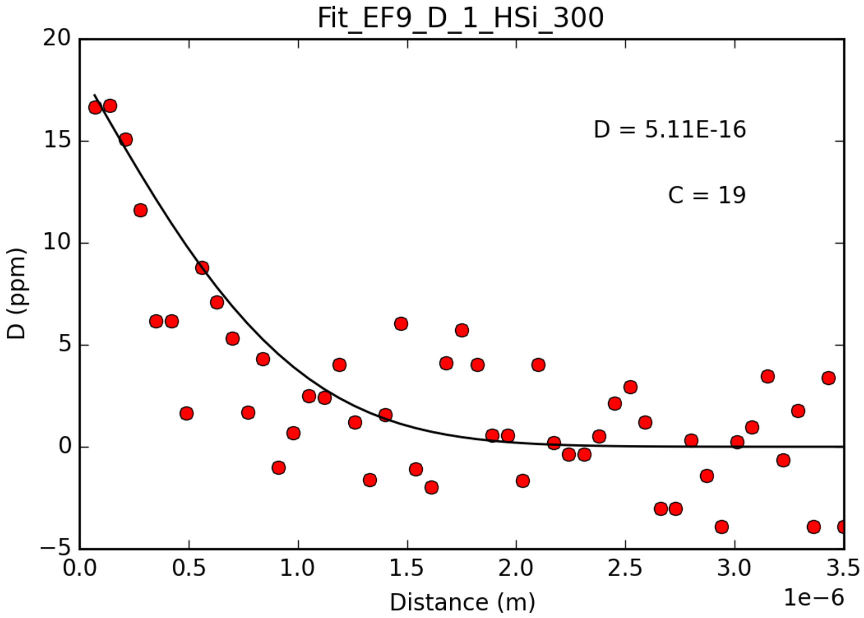
Fit_EF9_D_1_HSi_300
D = 5.11E-16
C = 19
D (ppm)
20
15
10
5
0
−5
0.0
0.5
1.0
1.5
2.0
2.5
3.0
3.5
Distance (m)
1e−6

(p)

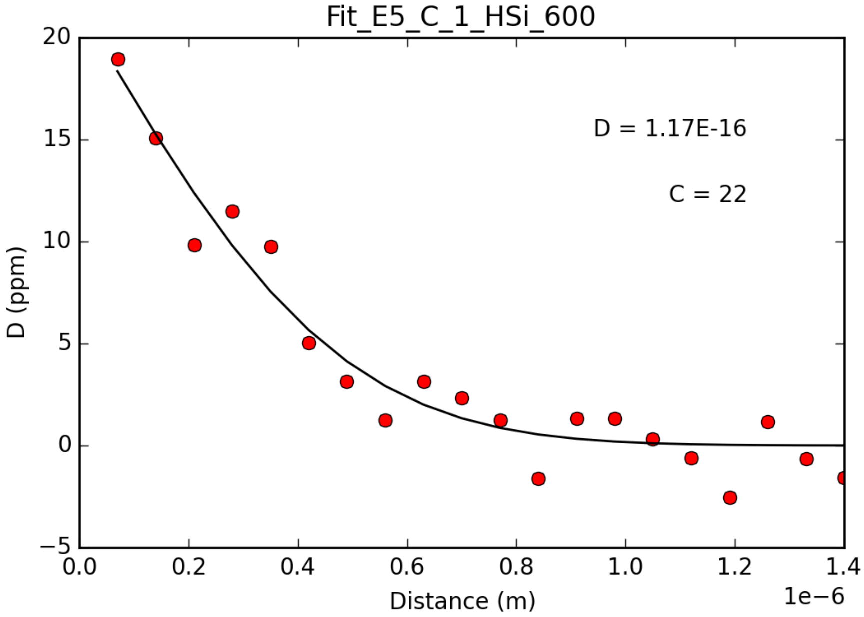
Fit_E5_C_1_HSi_600
D = 1.17E-16
C = 22
D (ppm)
20
15
10
5
0
−5
0.0
0.2
0.4
0.6
0.8
1.0
1.2
1.4
Distance (m)
1e−6

(q)

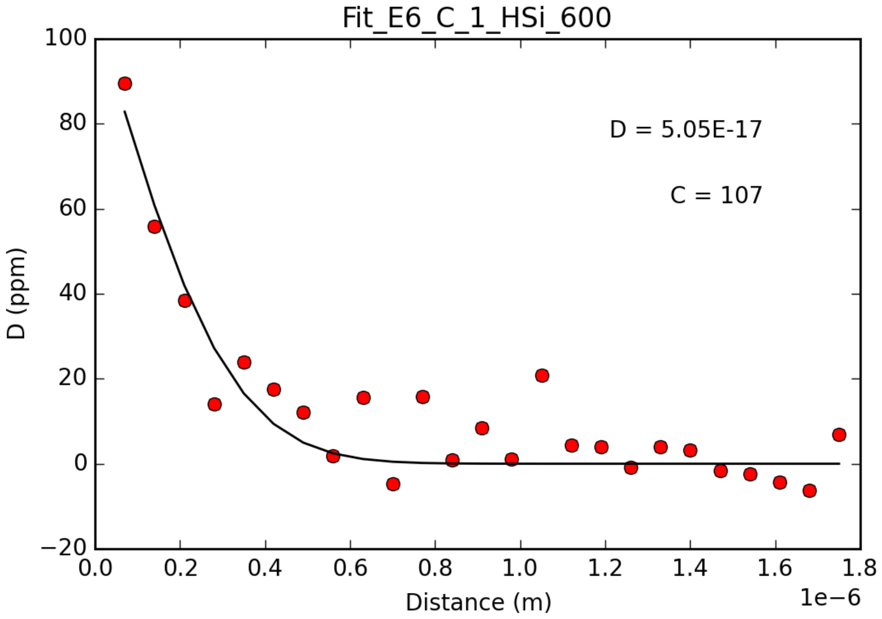
Fit_E6_C_1_HSi_600
D = 5.05E-17
C = 107
D (ppm)
100
80
60
40
20
0
−20
0.0
0.2
0.4
0.6
0.8
1.0
1.2
1.4
1.6
1.8
Distance (m)
1e−6

(r)

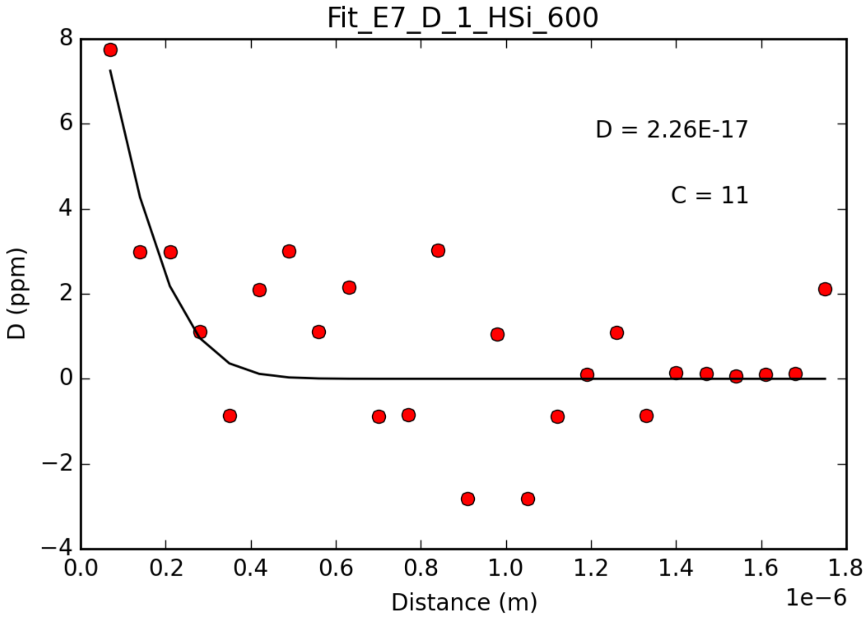
Fit_E7_D_1_HSi_600
D = 2.26E-17
C = 11
D (ppm)
8
6
4
2
0
−2
−4
0.0
0.2
0.4
0.6
0.8
1.0
1.2
1.4
1.6
1.8
Distance (m)
1e−6

(s)

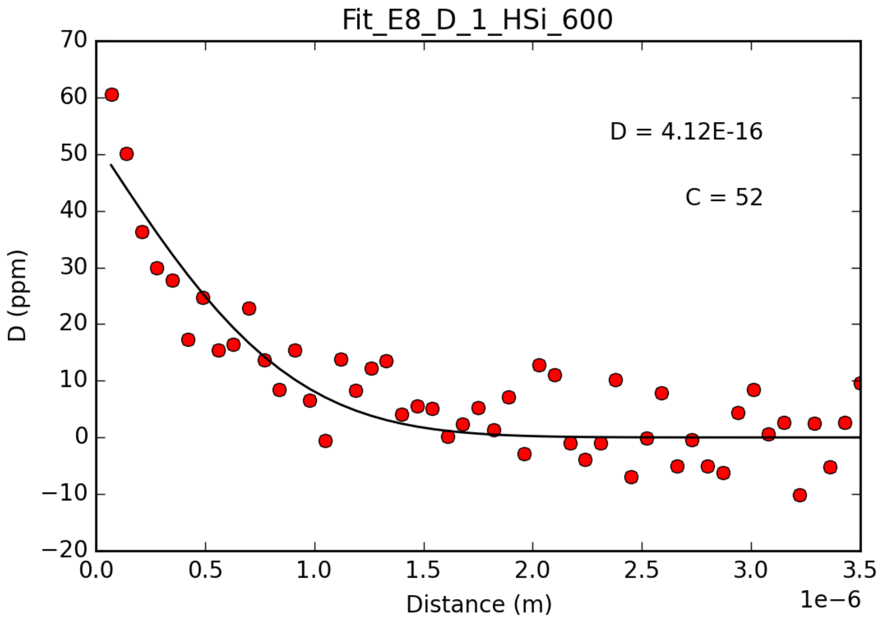
Fit_E8_D_1_HSi_600
D = 4.12E-16
C = 52
D (ppm)
70
60
50
40
30
20
10
0
−10
−20
0.0
0.5
1.0
1.5
2.0
2.5
3.0
3.5
Distance (m)
1e−6

(t)

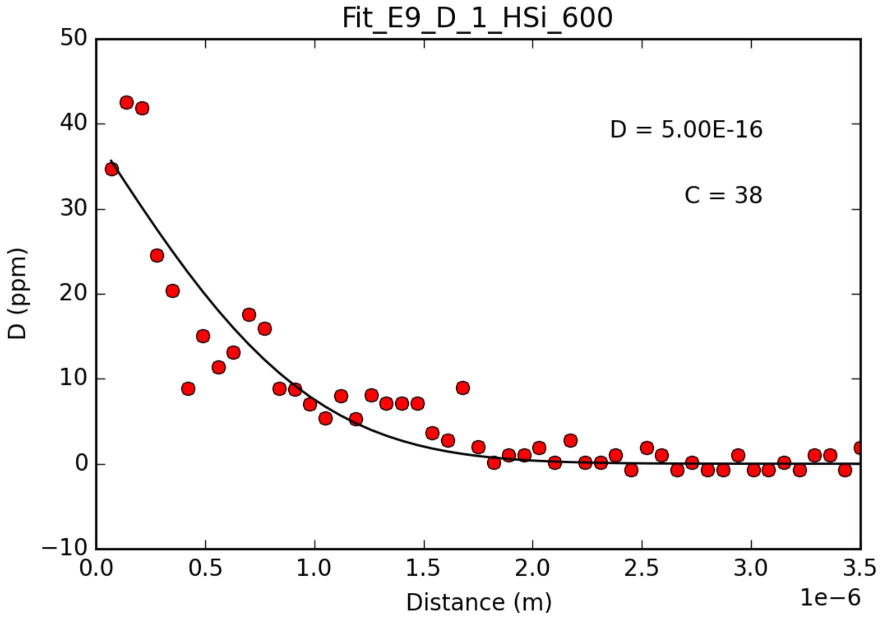
Fit_E9_D_1_HSi_600
D = 5.00E-16
C = 38
D (ppm)
50
40
30
20
10
0
−10
0.0
0.5
1.0
1.5
2.0
2.5
3.0
3.5
Distance (m)
1e−6

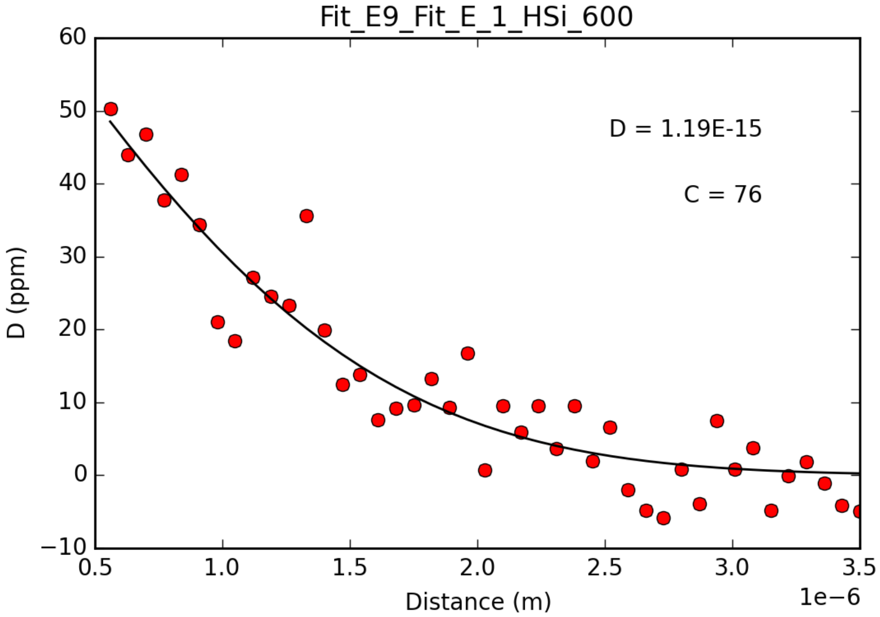
Fit_E9_Fit_E_1_HSi_600
D = 1.19E-15
C = 76
D (ppm)
60
50
40
30
20
10
0
−10
0.5
1.0
1.5
2.0
2.5
3.0
3.5
Distance (m)
1e−6

APPENDIX D

Spinel paper draft

Hydrogen and deuterium diffusion in non-stoichiometric (defect) spinel: implications for hydrogen mobility in Earth's mantle transition zone

Geoffrey D. Bromiley[1]*
Jennifer Brooke[1]
Simon Kohn[3]

[1]School of GeoSciences and Centre for Science at Extreme Conditions, University of Edinburgh, King's Buildings, Edinburgh, EH9 3FE, UK.
[2]Department of Earth Sciences, Will's Memorial Building, Bristol BS8 1RJ, UK.

***corresponding author: geoffrey.bromiley@ed.ac.uk**

Abstract

Non-stoichiometric (Al-rich) defect spinel provides a useful low-pressure analogue for investigating H (water) incorporation in nominally anhydrous minerals (NAMs) under mantle conditions. Here we perform a series of high-pressure/temperature annealing experiments to provide data on the diffusivities of H and D in defect spinel. All data can be fitted to the following Arrhenius law: Diffusivity (m^2/s) = $4\pm1\times10^{-12}$ exp(-54 ± 2 $kJ.mol^{-1}/RT$), where R is the gas constant and T temperature (K). Infrared (IR) spectra are consistent with protonation of both octahedral and tetrahedral O-O edges in defect spinel, with additional fine-structure in O-H absorption bands arising due to Mg-Al mixing and/or coupling of interstitial H with cation vacancies. H and D diffusion in defect spinel is most likely charge-balanced by flux of O site vacancies. Absence of changes in IR absorption across diffusion transects suggests that all H-related defects have similar mobilities, or that during diffusion, H can become coupled and uncoupled to other defects. This second possibility implies that

H diffusion and self-diffusion studies cannot be used to provide true insight into proton conduction in spinel group minerals and other NAMs. Defect spinel is isostructural with ringwoodite, and both phases have similar inferred H incorporation mechanisms. Results here also suggest that H and D diffusivities in defect spinel and ringwoodite also comparable, and results are used to discuss H mobility and proton conduction in ringwoodite within Earth's mantle transition zone.

Keywords: spinel, hydrogen, deuterium, diffusion, water, mantle, ringwoodite

1. Introduction.

The nominally anhydrous minerals (NAMs) which constitute the silicate mantles of Earth and the terrestrial planets can incorporate significant quantities of 'water' in the form of interstitial hydrogen defects (Bell and Rossman, 1992; Ingrin and Skogby, 2000). Interstitial H^+ is typically bound to relatively underbonded oxygen sites, forming spectroscopically active hydroxyl (OH^-) groups, often associated with other defects such as cation vacancies. Although the corresponding 'water' solubility in NAMs varies from a few tens to tens of thousands of ppm H_2O by weight (ppmw H_2O), this represents a highly efficient mechanism for storing considerable quantities of water in Earth's deep interior, comparable to the volume of water present in the hydrosphere (Bolfan-Casanova, 2005). The presence of interstitial H also has important influences on a range of mineral and bulk mantle properties, such as melting behaviour, electrical conductivity, seismic velocities, and rheology (e.g. Gaetani and Grove, 1998; Huang et al., 2005; Mackwell et al., 1985; Schmandt et al., 2014; Smyth et al., 2006).

Spinel sensu stricto, $MgAl_2O_4$, is volumetrically a minor phase in the upper part of the Earth's mantle where it is the main repository for Al to depths of 50-80 km, and can only incorporate trace amounts of 'water' (Lenaz et al., 2008). However, Bromiley et al.

(2010) demonstrated that synthetic, non-stoichiometric, Al-rich spinel (defect spinel) can incorporate significant quantities of 'water' in the form of interstitial H under high pressure/temperature (P-T) mantle conditions, and may provide a useful, low-pressure analogue for detailed investigations of H incorporation in NAMs. In particular, large gem-quality crystals of defect spinel can be readily synthesised, enabling detailed studies of H incorporation mechanisms and defect coupling using multiple techniques, which is challenging to perform on run products from high PT studies of mantle minerals. Defect spinel is isostructural with ringwoodite, $(Fe,Mg)_2SiO_4$, the main mineral stable in the lower part of Earth's transition zone, and a phase believed to incorporate significant volumes of 'water' in the deep Earth (Bolfan-Casanova et al., 2000; Kudoh et al., 2000; Pearson et al., 2014; Smyth et al., 2004). In addition to the insight which it provides on H incorporation in major mantle NAMs, defect spinel has several potential technological applications, most notably as a proton conductor and H sensor, and has been the subject of numerous investigations of electrochemical properties (e.g. Fukatsu et al., 2002; Gonzalez and Chen, 2002; Gonzalez et al., 1987).

Spinel sensu stricto and ringwoodite are both minerals within the spinel mineral class. Spinel class minerals have the general formula XY_2O_4, in which X and Y are divalent, trivalent or quadrivalent cations, and in which oxygen anions are arranged in a near cubic close-packed manner. X and Y cations occupy tetrahedral (T) and octahedral (M) interstices within the array of oxygens. In an ideal fully ordered spinel, 1/8 of the T sites and ½ of the M sites are occupied by X and Y cations respectively, although in practice, spinel group minerals are characterised by varying degrees of cation disorder and mixing of X and Y over both sites, especially at elevated temperature (Redfern et al., 1999). In fully ordered, stoichiometric spinel, $MgAl_2O_4$ ('ideal spinel'), Mg fully occupies T sites and Al fully occupies M sites. Bromiley et al. (2010) demonstrated that defect spinel contains a significant proportion of both Al-occupied T sites and vacant M sites, resulting in a structure with a H solubility several orders of magnitude higher than ideal spinel. However, although Bromiley et al. (2010) performed a series of high PT annealing experiments on defect spinel, problems with recrystallization prevented them from extracting key data on H diffusivity during annealing. Assessing H mobility in NAMs is essential in constraining the importance of H incorporation on mantle properties and processes with the deep Earth, and in providing additional insight into H incorporation mechanisms (e.g. Du Frane and Tyburczy, 2012; Karato, 2013; Mackwell and Kohlstedt, 1990; Watson and Baxter, 2007). H mobility in defect spinel has been investigated by Canova et al. (2012), Fukatsu et al. (2002) and Gonzalez et al. (1987), although these studies provide only limited insight into the relative mobility of different H defects. Futhermore, these studies were performed by annealing defect spinel in H-rich atmospheres at ambient pressure, and not at the high P-T conditions under which defect spinel can incorporate quantities of H comparable to other mantle NAMs. The purpose of this study is to conduct high PT experiments to determine both H and D mobility in defect spinel coupled with high-resolution spectroscopic examination of H incorporation mechanisms.

2. Methods

2.1 Starting material and high-pressure/temperature annealing.

The starting material for this study was a non-stoichiometric, ‘defect’ spinel from the same batch used in hydration experiments by Bromiley et al. (2010) (their sample ‘synthetic spinel 1’), synthesised at ambient pressure and high temperature using the Verneuil method. Pieces of this material were prepared as 1x1x2 mm polished blocks, cut using a diamond wire saw and polished gently using up to 1 micron diamond polishing solutions. Composition of the material, as determined by electron microprobe (details in section 2.2) is as follows: Mg: 6.62(5)%, Al: 47.43(14)%, O: 47.52(15), where values are averaged element weight percent, and values in parentheses are standard deviations on the last figure for averaged compositions. Single crystal X-ray data, presented in Bromiley et al. (2010), demonstrates that this synthetic spinel has excess Al_2O_3, resulting in T site contraction, and a significantly increased M site volume due to the present of a significant proportion of cation vacancies.

Prepared cuboids of the defect spinel were loaded into 2mm diameter Pt capsules, along with a high purity non-stoichiometric mix of Al_2O_3 and MgO (with the same composition as the spinel) and 10 wt% distilled H_2O or high-purity D_2O. Capsules were then welded shut and checked for leaks. For each high-pressure/temperature (HPT) annealing experiment, one H_2O and one D_2O bearing capsule were prepared. Both capsules were loaded side by side in an alumina sample holder, and then inserted into a 0.75” talc-pyrex-graphite piston-cylinder assembly, as described in (Bromiley et al., 2004) and shown in Figure 1. Piston-cylinder experiments were run using the ‘hot-piston out technique’, in which pressure was slowly ramped to 110% of the final run pressure (1 GPa in all experiments), and temperature then slowly ramped to the final run temperature whilst maintaining pressure. Pressure was then slowly released by bleeding off hydraulic fluid until the desired pressure was reached. Pressure and temperature were monitored and maintained throughout the duration of experiments. Temperatures were measured using a type R thermocouple, with the thermocouple junction placed within 0.5mm of the end of the Pt capules, separated by a thin alumina disc. Use of tapered graphite furnaces minimises thermal gradients across the capsules, which are <10°C under the run conditions used here (Bromiley, unpublished data). Experiments were quenched by switching off power to the heating circuit, resulting in rapid quenching (temperatures fall to below 100°C within 15s). Run conditions and results are listed in Table 1. After all experiments, both capsules were carefully recovered and examined, although recrystallisation of alumina around capsules prevented accurate weighing to check for the presence of water after the experiments. Recovered annealed samples were sectioned using a 0.2 mm diamond wire saw to produce a thin slice of spinel from the central portion of the cuboid, as shown in Figure 1. Slices were then polished to produce thin, double-polished plates using standard diamond polishing solutions. During preparation, spinel samples and slices were mounted and bonded using Crystalbond^{TM}. At each stage of preparation, and after the final stage of preparation of doubly-polished sections, all traces of Crystalbond^{TM} were removed by repeatedly soaking samples in high-purity acetone for up to 24 hours, before gently wiping with high-purity ethanol using lint-free tissue to remove any residues. After infrared analysis had been performed, polished sections were then remounted in epoxy and polished for electron microprobe analysis.

2.2 Sample analysis.

IR spectra were obtained along transects across prepared slices using a Thermo-Nicolet iN10MX infrared spectrometer and IR microscope at the Dept. Earth Sciences, University of Bristol. Samples were places on thin CaF_2 plates, and polarised spectra collected over the range 4000-450 cm^{-1}. Background spectra were obtained through the CaF_2 plate prior to each transect, and automatically subtracted from the sample spectra. For all samples, a 25x25 micron aperture was used and spectra obtained at 20 micron steps across sample slices, from edge to centre, with positioning automatically controlled by a motorised sample stage (see Figure 1b). Spectral resolution was set at either 4 or 8 cm^{-1}. Spectra were thickness and background corrected (using a linear background over the region 4000-2500 cm^{-1}) and fitted using IGOR Pro^{TM} software, using the Multipeak Fitting 2 toolbox.

Starting material and all annealed samples were subsequently prepared for compositional analysis by electron microprobe (EMP). A well characterised synthetic stoichiometric spinel standard (Spinel BLZ, University of Edinburgh) was used for analysing

Mg (Kα, LTAP, 20s count time), Al (Kα, TAP, 20s) and O (Kα, PC1, 20s) using a Cameca SX100 EMP with a finely focussed (approx. 1.5 μm diameter) beam running at 15 keV accelerating voltage and 10nA current.

3. O-H and O-D absorption in IR spectra.

Bromiley et al. (2010) noted that in contrast to previous studies, complexity in the O-H absorption region for defect spinel could be best fitted to at least 3 separate O-H stretching contributions, including an absorption band at 3343-3352 cm^{-1} and a doublet consisting of 2 distinct O-H bands at 3505-3517 cm^{-1} and 3557-3566 cm^{-1}. Similar, we noted that in the majority of spectra, it was clear that several contributions are needed to adequately fit IR spectra over the region due to both O-H and O-D stretching (4000-2000 cm^{-1}), and the 2 main contributions in the range of stretching frequencies corresponding to O-H absorption clearly exhibit some fine structure. As shown in Figure 2, although raw IR data appear to consist of 2 clear contributions, spectra cannot be adequately fitted to 2 single Gaussians, and residuals suggest the presence of additional contributions. The middle part of Figure 2 shows the result of fitting 3 contributions, as suggested by Bromiley et al. (2009). Although fit is improved, in particular relative to the doublet around 3500-3600 cm^{-1} residuals suggest that at least one additional contribution is required to fit the spectra, indicating that the absorption feature centred around 3300 cm^{-1} might also be a doublet. The upper part of figure 2 shows improvements when fitting data to 4 Gaussian contributions. However, no consistent method could be produced to adequately fit an additional contribution, especially in samples with lower bulk water contents, due to the extensive overlap between the 4 peaks, inherent problems with spectral deconvolution, and due to non-linear spectral backgrounds. This is apparent in Figure 2, in which a much broader 4th contribution always results from peak fitting. An approach of using several additional contributions to fit the typically non-linear spectral backgrounds was attempted, thereby increasing the overall quality of the fit. However, variations in the backgrounds between spectra across individual transects meant that this approach could not be used to obtain consistent, accurate, comparative data on trends in O-H absorption (i.e. in the area of individual H-O stretching contributions in absorption spectra). Therefore, we adopted an approach similar to that used by Bromiley et al. (2010), modelling the 2 O-H bands/regions separately using a combination of Gaussian and Lorentzian contributions to both. This consistent approach meant that relative error between spectral fitting in each line transect was minimised.

OH contents were determined from IR data using the calibration of Libowitzky and Rossman (1997) in which integrated area of O-H absorption bands is used to determine OH concentrations (in mol H_2O/l) in accordance with the Beer-Lambert law and a wavenumber-dependent generalised molar absorption coefficient for water. This provides a more accurate determination of ‘water’ contents of samples than the older calibration of Paterson (1982) used by Bromiley et al. (2010), due to the dependence of the Paterson calibration on absorption in hydrous glasses containing varied hydrous species. Recalculating water contents for the defect spinel starting material by Bromiley et al. (2010) using the Libowitzky calibration gives excellent agreement with the present study, as would be expected, and indicates that water contents given in Bromiley et al. (2010) might be overestimated by 20-30%. However, we also observed additional variations in the starting water contents of the defect spinel, from 10 to 40 parts per million H_2O by weight (ppmw); this variability was not noted by Bromiley et al. (2010) because they studied a small quantity of material prepared from a small volume of one single boule. In this study, spinel cuboids were prepared from different boules in the same sample batch. However, within each annealed sample slice, and within unannealed sample slices, no significant variation in volatile content was noted other than diffusion profiles arising from the annealing experiments.

4. Analysis of OH and OD diffusion data.

Experiments were designed to produce 1-d diffusion profiles for H and H-D exchange under experimental conditions. Cursory examination of IR line spectra is consistent with 1-d diffusion along the chosen transects, which are sufficient distance from other edges of samples to prevent any additional contributions to diffusion. As noted in Table 1, however, diffusion or H-D exchange did not occur as expected in a number of the experiments. Bromiley et al. (2010) demonstrated that under the experimental conditions chosen (1 GPa, elevated temperature) H affinity in defect spinel is expected to be significantly enhanced prior to the onset of recrystallisation, thereby promoting H diffusion into the spinel samples. In the case of samples annealed in D_2O we would also expect rapid H-D exchange between the sample and surrounding capsule environment to occur. In one sample annealed in D_2O, Hysp6, D diffusion into the spinel sample was noted, evident from the presence of 2 additional absorption features centred around 2484 cm^{-1} (OD band 1) and 2605 cm^{-1} (OD band 2), as shown in Figure 3. These are comparable to the OH absorption bands centred around 3350 cm^{-1} and the doublet at 3520 cm^{-1} in the same sample, suggesting that either H-D exchange or H-D exchange coupled with D diffusion into the sample has taken place during annealing. However, it is also apparent from the IR spectra in Figure 3 that substantial H diffusion into the same sample has also occurred. This is unexpected, as it suggests that the capsule, although loaded with high purity D_2O and sealed, also contained sufficient H to act as a source for substantial H diffusion into the sample. Most likely, this is due to H-D exchange during loading of the capsule, and then between the capsule and surrounding experimental charge during the actual annealing experiment; note that the sample assembly contains talc which may provide H which can then diffuse into the central sample volume, although the presence of a thick cylinder of pyrex glass is designed to minimise this interaction. Regardless of the use of a talc pressure medium, it is apparent that H-D exchange experiments in solid media devices are often difficult to perform due to similar issues with rapid H-D exchange between encapsulated samples and cell assemblies. This is the first case where we are aware of direct experimental evidence of the difficulties in maintaining a D-rich but H-poor sample environment in solid media experiments. Figure 3 also shows determined H_2O and D_2O concentrations across the annealed spinel sample. It is evident from the data that rates of H and diffusion into the sample are comparable. Either (1) this suggests that H and D diffusion into the spinel is the dominant process occurring during annealing, with only limited direct H-D exchange, or (2) the kinetics of H-D exchange and H diffusion are indistinguishable. This later possibility, if correct, would imply that H and D diffusion into the defect spinel is charge-balanced by flux of a faster diffusing species, such that H and D diffusivity determined in the present study is constrained by D and H diffusion kinetics alone. This point is discussed in detail below.

Given that H and D diffusion profiles are 1-d and the result of exchange of H and D between the capsule environment and sample, data on H and D diffusivity, D_{eff}, can be extracted by modelling diffusion profiles using a solution to Fick's 2nd law, assuming that the spinel and surrounding capsule act as a diffusion couple with a fixed interface (i.e. the position of the spinel crystal face, at x=0), that concentration of H_2O or D_2O vary only as a function of distance into the spinel, C(x,t) after annealing for time, t, that the H_2O or D_2O concentration in the 'sink' is fixed, and that the original H_2O or D_2O concentration in the spinel is C_s, such that:

$$C(x,t) = C_s - (C_s - C_O).erf\left[\frac{x}{2\sqrt{D_{eff}t}}\right]$$

This solution can be fitted to both scenarios encountered during annealing experiments performed here; namely: (1) H or D diffusion into the sample, where C_0 is the original H/D content in ppmw oxide, and H/D content increases due to progressive H/D diffusion from the sample edge, which has a fixed (high) concentration C_s; (2) H or D diffusion out of the sample, where C_0 is the original H/D content in ppmw oxide, and H or D loss occurs to the sample environment, with re-equilibration of H/D contents to a lower value, fixed at C_s at the sample edge. It is noteworthy that in all experiments performed here, recovered spinel cuboids showed no evidence of crystallisation or reaction with fluids or the oxide buffer used in the capsule. This is in contrast to Bromiley et al. (2010) who noted considerable spinel recrystallization. This can be attributed to (1) the lower temperatures used here for high pressure annealing, which presumably inhibit sample reaction, and (2) the fact that the oxide buffer used here is identical in composition to the spinel crystal, in contrast to Bromiley et al. (2010) who used a stoichiometric spinel oxide mix to buffer experiments. EMP analysis of samples also verified that no recrystallization or change in composition of crystals occurred during annealing experiments. Furthermore, EMP also did not reveal any gradients in Mg, Al or O towards the edge of samples, within the error of compositional analysis (standard deviations of 0.09% for Mg, 0.4% for Al, and 0.7% for O). Lack of reaction between the spinel and surrounding capsule material validates the solution to Fick's 2nd law used to determine diffusivities of H and D, which would otherwise be challenging to extract.

Using this solution, all diffusion profiles were fitted to extract H or D diffusivities. Diffusivities of H and D were determined independently for H-D exchange experiments. Due to the contrasting profiles noted in each sample, results of fitting for each sample are considered in turn.

Hysp3 (600°C)

In the sample annealed at 600°C in D_2O there is an obvious decrease in H_2O content towards the edge of the sample indicating H loss (figure 4a). However, there is no detectable D_2O in the sample. In contrast, the sample annealed in H_2O shows a corresponding increase in H_2O towards the edge of the sample (figure 4b). The most likely explanation for this is that the sample annealed in D_2O lost volatiles during initial heating of the experiment. As noted above, problems with recrystallization of the sample holder in piston-cylinder experiments meant that it was difficult to accurately test for the presence of volatiles in recovered samples.

Hysp4 (800°C)

Samples annealed at 800°C were friable and harder to prepare as polished slices for IR examination. The profile for the sample annealed in D_2O (Figure 4c) contrasts that from other samples. Some scatter is noted in the determined H_2O concentrations due to the fact that spectra contained a complex, irregular background due to interference fringes. However, in spite of this it is clear that H_2O concentrations up to approx. 100 microns into the spinel sample are uniform, and notably lower that the original H_2O content of the sample. This most likely indicates that H has been lost from the spinel due to diffusion, presumably again due to the fact that the capsule lost volatiles during heating, and that during annealing, the outer portions of the sample have re-equilibrated to a new, stable, lower H_2O content, which reflects the stability of the defect spinel at 1 GPa, 800°C under nominally anhydrous conditions. In order to fit this data, only the second part of the profile, with increasing H_2O contents, was fitted to the solution of Fick's 2^{nd} law given above. The sample annealed in H_2O again shows evidence for H diffusion into the sample during annealing (Figure 4d). The irregular background to spectra in this sample proved problematic, meaning that a number of spectra could not be adequately fitted; in these instances, data points are missing from the transect shown in Figure 4d.

Hysp5 (500°C)

In the sample annealed at 500°C in H_2O there is clear evidence for limited H loss from the sample (Figure 4e). The sample annealed in D_2O (Figure 4f) also shows evidence for H diffusion out of the sample, and there is again no evidence for D diffusion into the sample.

Hysp6 (700°C)

In the sample annealed at 700°C in H_2O there is again evidence for H loss, suggesting that the capsule also lost water during heating. However, profiles for the sample annealed in D_2O show clear evidence for both H diffusion into the sample (Figure 4h) and D diffusion into the sample (Figure 4i).

Figure 4 shows representative profiles from each sample. For some samples, several diffusion profiles along different transects were obtained. For other samples, only one transect was obtained due to the presence of cracks in the prepared sample, or where IR data revealed clear contamination. Where possible, multiple diffusion profiles from samples were fitted to determine multiple H or D diffusivities at each temperature. From the experiments performed here, it is clear that H gain, H loss and D gain has occurred in the different annealing experiments. Determined diffusivities are given in Table 2 and plotted in Figure 5.

5. H and D incorporation and diffusivity in defect spinel.

It is apparent that there is no significant difference in the diffusivities of H and D, within error of those values determined here, and that there is no significant difference in diffusivity of H determined in annealing experiments where H was lost (presumably due to capsule failure) vs those experiments which were 'successful' and where H diffused into the spinel. Errors presented in Table 2 are based on the fitting procedure used, and probably significantly underestimate true uncertainty in diffusivities determined here. A more significant source of error is likely to arise from how spectra are fitted (as discussed above), which can result in systematic and non-systematic errors in calculated H and D concentrations; sources of such error include non-uniform backgrounds to many of the spectra, thickness correction (thickness of samples was determined optically, and in a few samples, polishing resulted in non-uniform sample thickness which had to then be additionally corrected), and difficulties in accurately fitting spectra with multiple contributions (i.e. fine structure to all absorption bands) in a consistent manner. An additional source of error in determined diffusivities could also arise from the spectroscopic technique used. A fixed aperture was used to determine OH absorption as a function of distance, ensuring that spectra were recorded from 20x20 µm areas of the top surface of the prepared samples. However, the IR beam passing through the sample is slightly conical, implying that spectra are recorded through slightly cone-shaped volumes of the sliced samples. This could result in a slight overestimation of water contents in all spectra. This effect has not been corrected for in results presented here because the effect of this aberration cannot be readily assessed, and the effect may be somewhat reduced by the higher refractive index of the sample compared to air. However, to ensure that this did not result in discrepancies in determined water contents close to the edges of sample slices, spectra were not obtained immediately adjacent to sample edges, and where possible, samples were polished to similar thicknesses to minimise systematic error. Furthermore, determined diffusivities are compared for samples which exhibited both H loss and H gain during annealing, to assess systematic effects on calculated water content. As such, uncertainty in determined diffusivities can be more meaningfully assessed by examining consistencies in determined diffusivities during H/D loss and gain for the 4 temperatures used. From Figure 5, and with consideration to the fitting procedure used here, we would estimate uncertainties in H and D diffusivities at 800°C and 500°C to be approximately ±0.3 log units, and at 700°C and 600°C to be ±0.2 log units, with no observed difference in diffusivity during contrasting H loss or gain. Despite these uncertainties, a temperature dependence for both H and D diffusivity can be determined, and a straight line (i.e. Arrhenius law) is fitted to all data shown in Figure 5, of the form:

$$\text{Diffusivity } (m^2/s) = 4\pm1\text{x}10^{-12} \exp(-54\pm2 \text{ kJ.mol}^{-1}/RT)$$

There are 2 main O-H (and corresponding O-D) absorption features in IR spectra in all samples centred around 3345-3352 cm^{-1} and 3524-3530 cm^{-1}, assigned O-H bands 1 and 2, respectively, by Bromiley et al. (2010). Lenaz et al. (2008), in a study of water incorporation in natural and synthetic spinel, assigned these bands to protonation of unshared M O-O edges (^{VI}O-O_{unsh}) and T O-O edges (^{IV}O-O), with protonation coupled with T site vacancies (V_T). However, both Gonzalez et al. (1987) and Bromiley et al. (2010) noted additional fine structure in O-H absorption in defect spinel, and a splitting of OH band 2 into at least 2 Gaussian contributions. Fukatsu et al. (2002) suggested that O-H and corresponding O-D stretching frequencies in IR spectra were consistent with protonation of both octahedral and tetrahedral edges. On the basis of crystal structure refinements and correlation of O-H stretching frequencies with O-H….O bond distances, Bromiley et al. (2010) proposed two alternative assignments: (1) O-H band 1 due to protonation of ^{VI}O-O_{unsh} and splitting of O-H band 2 due to protonation ^{IV}O-O about both filled and vacant T sites; (2) band 1 due to protonation of a shared O-O M edge (^{VI}O-O_{sh}), band 2a due to protonation of a ^{VI}O-O_{unsh} and band 2b due to protonation of ^{IV}O-O. Corresponding O-D bands in spinel in the present study are centred around 2470-2480 cm^{-1} and 2603-2615 cm^{-}

^{1}, consistent with the previous observations of Gonzalez et al. (1987), and consistent with previous assignments of proton positions based on O-H…O bond distances. However, higher quality IR data in the present study indicate even greater fine structure in O-H and O-D absorption bands than previously noted, and spectra can be fitted to at least 4 Gaussian contributions. As noted by Bromiley et al. (2010), O-H stretching frequencies are not sufficiently different to allow accurate assignment of these different contributions to specific O-O edges in the spinel structure once the effects of defect coupling are taken into consideration, especially if O-H bands are not strictly collinear with O-O edges. Fine structure in O-H and O-D absorption bands indicates protonation of at least 2 of the 3 O-O edges in the spinel structure, with additional splitting most likely to occur due to coupling of interstitial H with cation vacancies and Mg-Al disorder (most notably due to protonation about $Mg_{Al}^{/}$ defect centres).

As previously suggested by Fukatsu et al. (2002) and Bromiley et al. (2010), H diffusion in defect spinel is most likely charge-balanced by counter-flux of oxygen vacancies ($V_{O}^{\cdot\cdot}$), due to the sluggish kinetics of cation diffusion. This is consistent with observed H diffusivity in the present study. Importantly, limited data on D diffusion suggest that there is no difference in diffusivity of H and D in defect spinel. This is consistent with absolute rate theory which predicts only a small difference between diffusivity of D and H due to similar mean thermal velocities, and provides validity to the assertion that H-D exchange experiments can be used to provide an assessment of H self-mobility in mantle minerals (e.g. Du Frane and Tyburczy, 2012; Sun et al., 2015). D diffusion coupled with $V_{O}^{\cdot\cdot}$ also explains why H and D diffusivities in Hysp6 are identical within error, even though D diffusion into this sample can occur via both D diffusion and D exchange for H.

Previous workers have indicated that H incorporation in defect spinel can be charge balanced by the Mg vacancies ($V_{Mg}^{//}$) and Al vacancies ($V_{Al}^{///}$). In particular, defect spinel contains high concentrations of M site vacancies, so additionally, protonation of vacancies would appear to be highly favourable due to the strong net negative charge associated with cation vacancies (i.e. coupled $H_i^{\cdot}$ - $V_{Al}^{///}$ defects involving single or multiple protons). However, in all IR spectra here, relative areas of all O-H contributions remain unchanged across diffusion profiles, during either H loss or H gain. Experiments were conducted at different temperatures, under which different degrees of Mg-Al ordering might be expected. Therefore, an absence of changes in relative O-H band area (and fine structure) in spectra implies that either Mg-Al ordering is supressed in defect spinel under these conditions (as suggested at higher temperatures in the study by Bromiley et al., 2010), or that Mg-Al ordering has no additional influence on defect coupling and protonation. Results could also imply that the mobilities of each H-related defect in the material are similar. Coupled interstitial H-cation vacancy defects would be expected to have a substantially reduced mobility compared to isolated interstitial H (free protons), so the lack of any noticeable changes in IR spectra across diffusion profiles suggests that either no defect coupling occurs, or that defect coupling provides no additional energetic barrier to hopping of interstitial H throughout the structure. This second possibility appears counter-intuitive, but could relate to the high concentration of cation vacancies within the sample which limits the stability of free protons. Fukatsu et al. (2002) noted that the concentration of H in defect spinel is proportional to the half power of partial pressure of water volume, which implies that H is incorporated as isolated OH defects, rather than clusters of OH about vacant sites. Initial consideration of results from this study would, therefore, be more consistent with a model of H incorporation in defect spinel where protonation of O-O edges, although charge balanced by metal vacancies, does not result in formation of stable defect complexes, at least at elevated temperature, with fine structure in O-H absorption due to NNN interactions arising due to partial Mg-Al disorder which does not vary with temperature.

Alternatively, lack of observed changes in fine structure of O-H absorption bands across diffusion profiles can be explained by considering temporal changes in defect coupling at elevated P-T. IR spectra provide insight into fine structure of O-H absorption bands due to defect coupling (i.e. NNN interactions) in quenched samples. In contrast, absolute determination of H_2O contents with distance may in fact provide only an assessment of bulk mobility of H during annealing. During high P-T annealing, it is clear that a significant proportion of interstitial H in defect spinel is mobile, and able to hop from interstitial site to interstitial site (both T and M O-O edges) throughout the structure, and that H mobility cannot be constrained by the mobility of other defects which give rise to fine structure in IR spectra. At any given distance, a certain proportion of interstitial H may be coupled with vacant cation sites, or, for example, with defects arising from Mg-Al ordering, such as octahedral sites containing Mg ($Mg_{Al}^{\cdot}$). These defects will be inherently less mobile during annealing, and for run conditions used here, can be considered relatively immobile compared to interstitial H. A considerably greater activation energy would be required to mobilise interstitial H coupled to such defects. However, during annealing, mobile interstitial H could become coupled, and then uncoupled from such defects during net diffusion through defect spinel; that is, at any given time, or at any given distance into the annealed defect spinel, only a proportion of the interstitial H is coupled to other defects. Direct evidence for such defect ‘uncoupling’ of interstitial H has been observed in long duration annealing experiments on H-bearing diopside. Bromiley et al. (2004) noted that changes in H solubility in diopside and fine structure of O-H absorption bands inferred from IR spectra could only be explained by diffusion of interstitial H away from substitutional defects and cation vacancies (i.e. defect centres) at elevated P-T. Therefore, it is possible that diffusivity measurements give only an average assessment of total H mobility through defect spinel, and that as interstitial H diffuses through the structure, it can become coupled and decoupled to other defects. This explanation essentially separates inferences on H incorporation mechanisms and defect coupling from consideration of the relative mobility of defects, and is preferred because it explains both the fine structure of IR bands and the observed lack of changes in IR spectra across profiles without requiring either unrealistically fast diffusion of slow moving species, or an absence of defect coupling, both of which are counter-intuitive.

Fukatsu et al. (2002) determined H diffusivity in defect spinel similar to that studied here in a series of H uptake/loss experiments at ambient pressure and high temperature. Results from their study are shown in Figure 6. Although conducted at substantially higher, their measured diffusivities are, within stated errors, consistent with data present here. Fukatsu et al. (2006) used a contrasting method to determine H diffusivity, in which platelets of defect spinel were annealed under controlled atmospheres at ambient pressures, and observed that during their high temperature annealing experiments rapid sample recrystallization occurred. Furthermore, they also determined H diffusion on the basis of total O-H absorption through thin plates of defect spinel in an H_2-rich atmosphere, which, coupled with sample recrystallization, could indicate some additional near-surface effect which additionally contributed to O-H uptake in their samples. For example, O-H absorption onto spinel (100) surfaces annealed in H_2 has been recently shown to differ considerably from O-H bulk incorporation (Canova et al., 2012), with O-H showing a high affinity for incorporation into alumina-rich (Mg-free) surface layers. Annealing of defect (non-stoichiometric) spinel at ambient pressure and the high temperatures used by Fukatsu et al. (2002) additionally promotes alumina precipitation, resulting in the penetration of reaction fronts into bulk crystals (Donlon et al., 1982). This precipitation reaction is not energetically favourable at high pressures due to the large lattice strain energy associated with alumina growth, and would be further supressed in the present study by the lower annealing temperatures used. The temperature dependence of H diffusivity determined by Fukatsu et al. (2002) differs considerably and in inconsistent with results from the present study. This could be due to an alternative mechanism for H mobility in their study. However, considering the sources of error in both studies, we instead suggest that absolutely diffusivities in these studies are, in fact comparable, and that a single Arrhenius law can be used to fit both data sets. This implies that H mobility in spinel is independent of pressure up to at least 1 GPa. Fukatsu et al. (2002) also demonstrated that bulk composition of defect spinel has no observable influence on H diffusivity, which further supports comparison of results between the two studies.

6. Implications for H mobility in ringwoodite, $(Fe,Mg)_2SiO_4$ and proton conduction in the transition zone.

On the basis of crystal chemistry and observed IR absorption, Bromiley et al. (2010) argued that defect spinel provides a useful, lower-pressure analogue for H incorporation in ringwoodite, $(Fe,Mg)_2SiO_4$. Ringwoodite is a high-pressure polymorph of olivine, and the main mineral phase stable in the lower part of the Earth's mantle transition zone. It is a 4-2 normal spinel, and as such, isostructural with $MgAl_2O_4$ spinel. Importantly, numerous studies have demonstrated that ringwoodite is one of the most H-rich nominally anhydrous minerals stable within the Earth, and can contain up to several weight % H_2O as $H_i^{\cdot}$ (e.g. Kohlstedt et al., 1996; Kudoh, 2001; Smyth et al., 2003). Pearson et al. (2014) also recently described a natural ringwoodite inclusion in a diamond originating from the transition zone containing approximately 2.5 wt%, demonstrating that ringwoodite not only has a high potential storage capacity for H, but can at least locally contain high concentrations of water in the deep Earth as interstitial H. Smyth et al. (2003) demonstrated that hydration of ringwoodite is strongly correlated with the number of Mg (M site vacancies) in a sample with close to full T site occupancy, and IR data indicate protonation of both tetrahedral and octahedral O-O edges (Kohlstedt et al., 1996; Kudoh, 2001; Smyth et al., 2004). Refinement of D positions in a deuterated Fe-bearing ringwoodite from powder neutron diffraction data (Purevjav et al., 2014) also provides direct evidence for protonation of both T and M edges. Therefore, recent studies of H incorporation in ringwoodite support the assertion that defect spinel provides a useful analogue material. However, in contrast to defect spinel, the high P-T conditions of ringwoodite stability mean that determining H diffusivity is experimentally challenging. To date the only published study of H diffusion in ringwoodite is that of Sun et al. (2015), who determined H self-diffusion by H-D exchange experiments using a (Fe-bearing) mineral couple under transition zone conditions. Determined H diffusivity data from the Sun et al. (2015) study are also shown in Figure 6, along with comparative data on H self-diffusion in olivine from Du Frane and Tyburczy (2012) and H diffusion in Fe-free olivine from Demouchy and Mackwell (2003).

H diffusivities in ringwoodite were determined by Sun et al. (2015) at comparable temperatures than those used in the present study. Figure 6 demonstrates that H mobility in ringwoodite is approximately 2 log units faster than in defect spinel, and has, possibly, a greater temperature dependence, indicating a higher activation energy for H mobility in the higher pressure structure (although given uncertainties in the diffusivity data, and the more limited temperature range studied in the Sun et al. (2015) study, temperature dependence could be more similar than shown in Figure 6). Sun et al. (2015) determined H self-diffusion in Fe-bearing ringwoodite by measuring H and D profiles by secondary ion mass spectrometry (SIMS), and as such, did not directly determine mobility of different H related defects. They further noted that proton conductivity, estimated from their H self-diffusion data, was consistent with direct electrical conductivity measurements in ringwoodite by Yoshino et al. (2008) for low bulk water contents, and from this inferred that the kinetics of free proton mobility (i.e. interstitial H) in ringwoodite were similar to those of coupled protons on vacant sites, considered to be the dominant mechanism for H incorporation. This is in contrast to diffusion, self-diffusion and conductivity studies in olivine (figure 6). Calculated proton conductivities in olivine have been argued by Karato

(2013) to provide an inaccurate assessment of electrical conductivity in H-bearing olivine because conductivity is dominated by the movement of highly mobile free protons at lower temperature, compared to mobility of more complex species such as coupled protons adjacent to cation vacancies $(2H)^{x}_{Me}$ which dominates in diffusion experiments.

Further consideration of the comparability of proton conduction and H self-mobility in spinel-group minerals such as ringwoodite requires consideration of the mobility of different H related defects. IR spectra for hydrous ringwoodite contain a dominant, broad O-H absorption feature at 3115 cm^{-1} which has been tentatively assigned to protonation of the T edge, and smaller bands at 3695 cm^{-1} and 2500 cm^{-1} which have been assigned to protonation of an M edge, and a mixed overtone or in plane X-OH bending mode, respectively (e.g. Bolfan-Casanova et al., 2000; Chamorro Perez et al., 2006; Smyth et al., 2003). Alternatively, the 3695 cm^{-1} band has been assigned to a hydrogarnet-type substitution mechanism of $4H_i^{\cdot}$ about a vacant (Si) T site (Blanchard et al., 2005) and the broad band at 3115 $cm^{=1}$ corresponds to protonation of M edges (Kudoh et al., 2000). As noted above, Purevjav et al. (2014) found evidence for protonation of both M and T edges in ringwoodite, and evidence for the presence of cation vacancies on both sites, which they inferred represented defect coupling of protons about vacant sites. Interestingly, both low temperature and high temperature *in-situ* IR studies have revealed that the large, dominant O-H band at 3115 cm^{-1} actually contains additional contributions (fine structure), suggesting that IR spectra are more complex than originally supposed (Panero et al., 2013; Yang et al., 2014). There is obvious comparison here with H incorporation in defect spinel, in which apart from the absence of a sharp O-H contribution which can be assigned to a hydrogarnet type OH defect centre, multiple O-H contributions are noted which imply protonation of at least 2 of the three distinct O-O edges, and some additional NNN interaction due to either to coupling of interstitial H with cation vacancies or splitting of O-H contributions due to cation mixing over the 2 sites. The key insight provided by studies of defect spinel are that (1) O-H contributions in IR spectra are considerably easier to deconvolute, due to sample size constraints in the study of high-pressure stable materials, and (2) that no changes are noted in IR spectra across defect spinel diffusion profiles, implying that either all defects have similar mobilities, which appears unlikely for H coupled with vacant cation sites, or that diffusion and self-diffusion studies provide a mean assessment of proton mobility. As argued above, it is possible that defect coupling inferred from room temperature IR spectra for defect spinel cannot be used to infer the relative stability of different H-related defects during diffusion, and that at elevated temperature, intersititial H is variably uncoupled from cation vacancies. Yang et al. (2014) noted systematic shifts in the main O-H contributions in ringwoodite IR spectra at elevated P-T, although the resolution in their data would not be sufficient to deconvolute individual contributions inferred from low T studies required to differentiate between mobile uncoupled H and coupled H. Comparison of defect spinel and ringwoodite could, therefore, infer that H diffusion studies of ringwoodite are not comparable to conductivity measurements. A lower concentration of cation vacancies in ringwoodite compared to defect spinel could explain the relative consistency between H self-diffusion and electrical conductivity in ringwoodite; however, as noted by Sun et al. (2015), their inferred proton conductivity is not in agreement with all lab studies of electrical conductivity.

If we accept the hypothesis that defect spinel provides an analogous system for considering H mobility in ringwoodite, then the following points can be considered. (1) In this study, we determine that H and D have comparable diffusivities, and that diffusion can only realistically be charge balanced by counter-flux of oxygen vacancies. Comparison with Sun et al. (2015) therefore suggests that, as would be expected, diffusivity of protons in defect spinel is the rate limiting step. This would further indicate that H self-diffusivity of H in both ringwoodite and defect spinel should be the same as H diffusion, regardless of the presence of Fe which would permit H diffusion coupled with polaron diffusion. (2) There is no observable change in the mechanism for H mobility in defect spinel or ringwoodite over the temperature range studied, in contrast to olivine. (3) The notable absence of any changes in IR spectra during H diffusion in defect spinel supports the assertion by Sun et al. (2015) that all H-related defects in ringwoodite (i.e. free protons vs coupled defects) have comparable diffusivities, but could alternatively indicate that in spinel structures, diffusion and self-diffusion studies provide a mean (and not true) estimate of proton mobility constrained by the extent of defect coupling. This would imply that H-D exchange experiments are not strictly comparable to proton conductivity experiments, in which only mobility of free protons is determined, comparable to studies of H mobility/conductivity in olivine, as argued by Karato (2013).

Acknowledgements

Work was supported by the National Environmental Research Council for NERC (PhD studentship NE/K500835/1) and by a grant to GDB by the School of GeoSciences, Edinburgh (EPS research institute). The authors acknowledge the assistance provided by Dr. Chris Hayward in EMP analysis.

Table 1: Run conditions and results for defect spinel experiments. 2 capsules were prepared for each experiment, one H_2O-bearing, the other D_2O-bearing. Pressure was 1 GPa for all annealing experiments.

Experiment	Temp (°C)	Time (h)	*Sample*	Notes
Hysp1	400	97	H_2O	Spinel completely recrystallized; hydrous phase formed
			D_2O	Spinel completely recrystallized; hydrous phase formed
Hysp5	500	97.5	H_2O	H loss from samples resulting in diffusion gradient
			D_2O	No O-D detected; H loss from samples resulting in diffusion gradient
Hysp3	600	75	H_2O	H diffusion into the sample resulting in diffusion gradient
			D_2O	No O-D detected; H loss from samples resulting in a diffusion gradient
Hysp6	700	47	H_2O	H loss from samples resulting in diffusion gradient
			D_2O	D and H diffusion into sample
Hysp4	800	41	H_2O	H diffusion into the sample resulting in diffusion gradient
			D_2O	No O-D detected; H loss from samples resulting in a diffusion gradient

Table 2: diffusivities for H and D in synthetic defect spinel at 1 GPa in both H diffusion and H-D exchange experiments. Numbers in parentheses are errors on the last s.f. in quoted diffusivities.

Sample	Type	Process	Log D	10000/T (K)
Hysp3	H diffusion	H gain	-14.84(6)	11.45
			-14.31(3)	
	H-D exchange	H loss	-14.91(2)	
			-14.89(8)	
Hysp4	H diffusion	H gain	-14.1(1)	9.32
			-13.8(8)	
	H-D exchange	H loss	-13.9(1)	
Hysp5	H diffusion	H loss	-14.6(1)	12.94
			-14.61(2)	
	H-D exchange	H loss	-15.19(3)	
Hysp6	H diffusion	H gain	-14.5(1)	10.28
			-14.2(2)	
	H-D exchange	H gain	-14.34(4)	
			-14.3(1)	
		D gain	-14.3(2)	
			-14.5(2)	

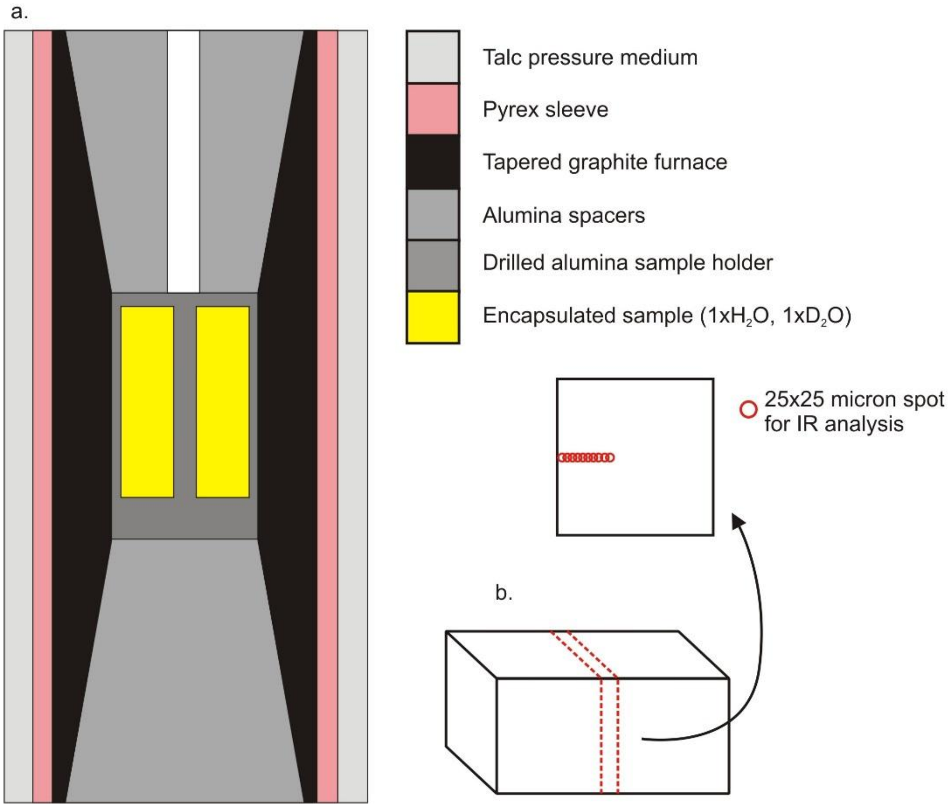

Figure 1. Experimental setup used for spinel diffusion experiments. a. 0.75” piston-cylinder assembly with tapered furnace used to reduce thermal gradients in sample volume. 2 capsules were loaded into both assembly, one saturated in H_2O, the other saturated in D_2O. b. Sketch showing spinel crystal (2x1x1mm) cuboids loaded into each capsule. Recovered cuboids were then cut as shown (dashed red line) using a diamond wire saw to produce a slice across the central region. Slices were polished doen to 1 micron using diamond pastes. IR spectra were then obtain from the edge of slices inwards to determine 1-d diffusion profiles, as shown.

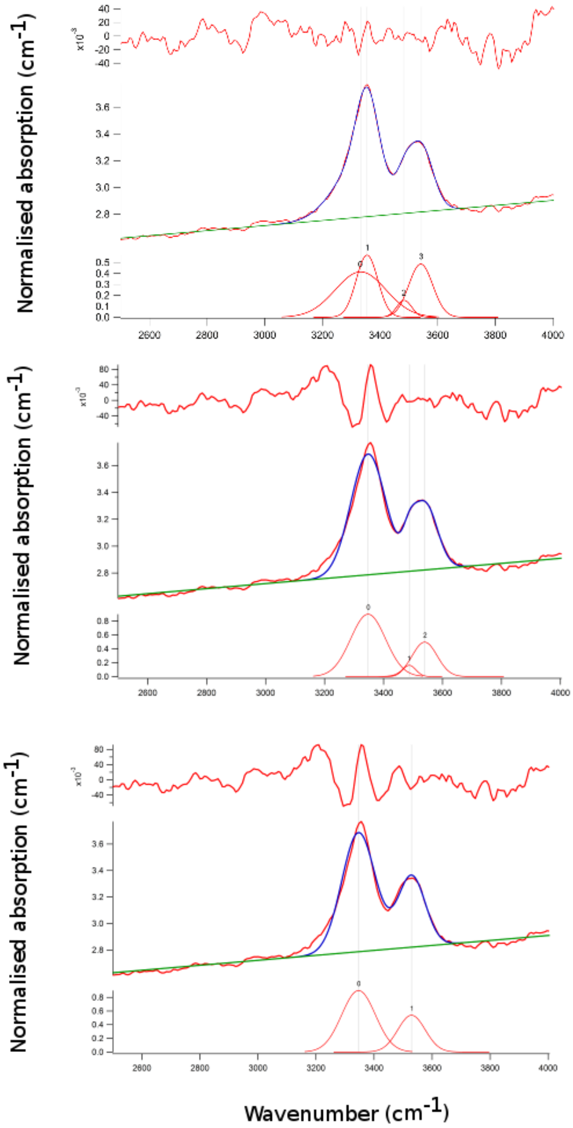

Figure 2. Examples of fitting defect spinel IR spectra using different numbers of contributions. Top: fitting Gaussians to 4 separate contributions results in a best fit to IR data and minimises residual. Middle: fitting Gaussians to 3 contributions, consistent with (Bromiley et al., 2010), results in a less satisfactory fit and indicates the presence of an additional peak in the residual. Bottom: fitting Gaussians to 2 contributions. Centre (red) line in each figure is the original IR data, fitted to a linear background (green) and to the various Gaussian peaks (lower part of each figure, line in red). Modelled spectra using

these contributions and backgrounds are shown in blue. Upper part of each figure shows residuals from fitting.

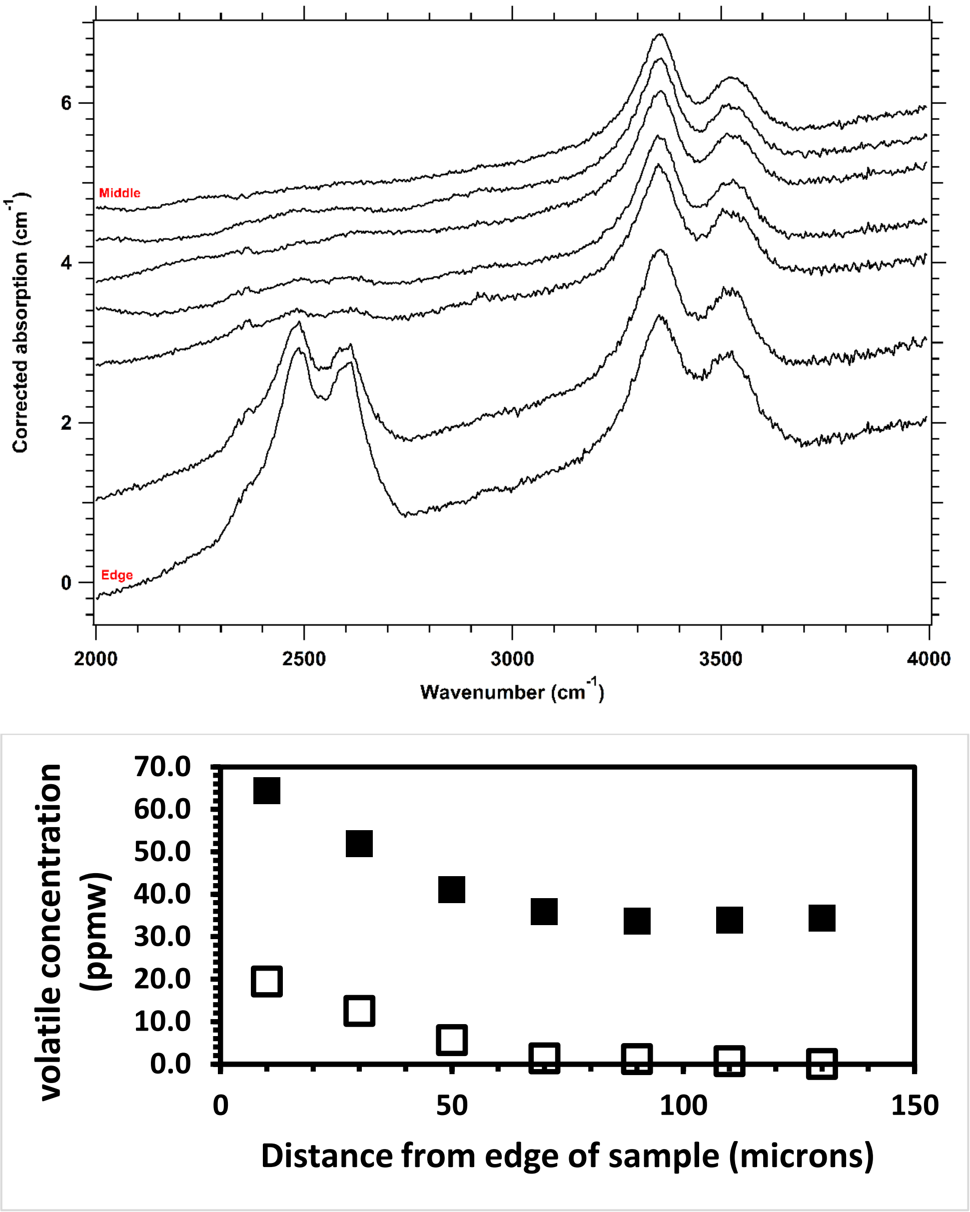

Figure 3. Top: Example of spectra from a line scan across Hysp6 6 (D_2O) showing the presence of O-H absorption bands over the region 3200-3700 cm^{-1}) and the presence of corresponding O-D bands over the region 2200-2800 cm^{-1}. Spectra have been thickness corrected but not background corrected, and are offset vertically for clarity, with the lowermost spectrum obtained from the edge of the annealed sample, and each overlying

spectrum obtained across a line transect towards the centre of the sample, perpendicular to the edge of the sample, at progressive 20 micron steps. Bottom: Calculated total OH and OD concentrations, in ppmw H_2O (filled squares) and D_2O (open squares) from IR spectra, showing diffusion gradient for both OH and OD, implying H and D diffusion into the spinel sample rather than simple O-D isotopic exchange.

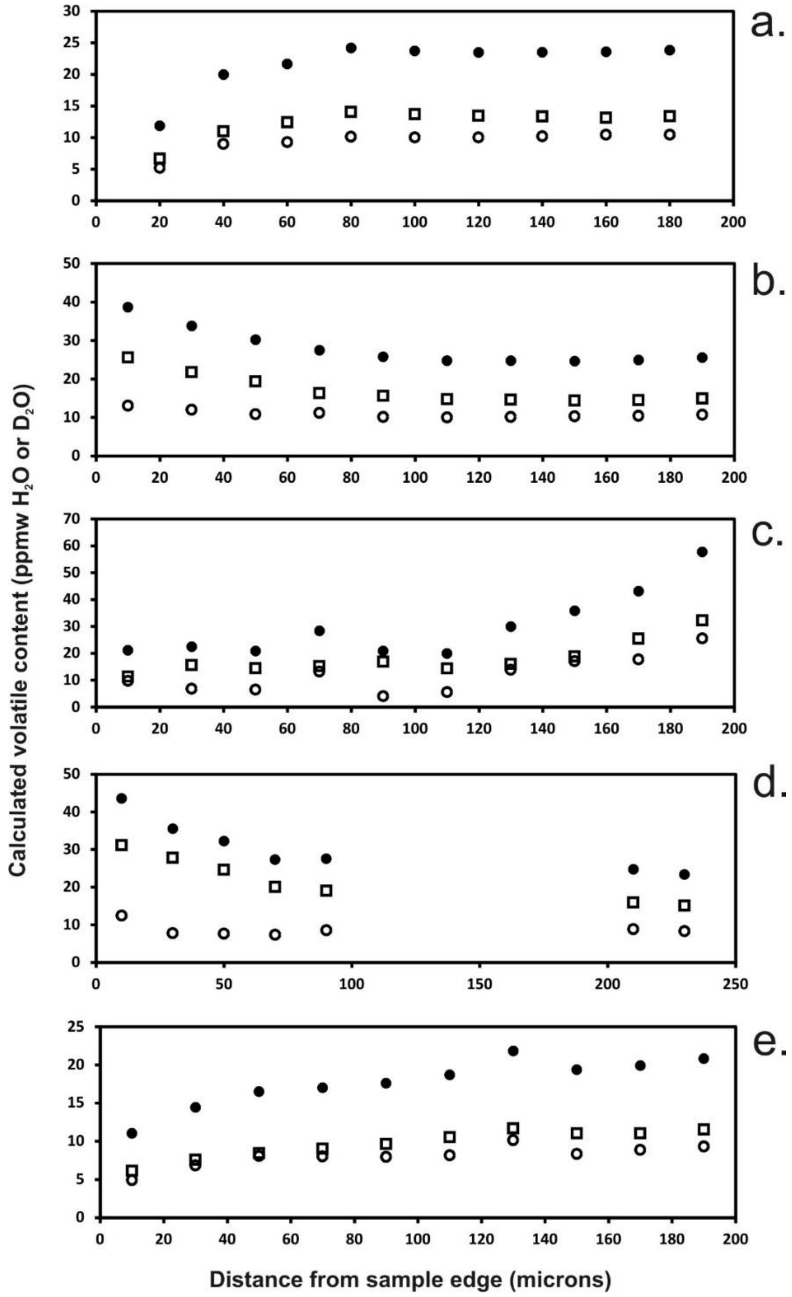

Figure 4. Diffusion profiles for H and D in annealed spinel, from edge to centre of samples. Filled circles show total volatile content, and open squares and circles volatile contents determined from bands 1 and 2, respectively. a. Hysp3 (600°C, D_2O) showing H loss and no O-D peaks; b. Hysp3 (600°C, H_2O) showing H gain; c. Hysp4 (800°C, D_2O) showing H loss and no O-D peaks, with potential re-equilibration of the edge of the sample to a lower H content; d. Hysp4 (600°C, H_2O) again showing H gain, with some data missing due to the

difficulty in accurately fitting spectra with complex, non-linear backgrounds due to interference fringes; e. Hysp5 (500°C, H_2O) showing H loss.

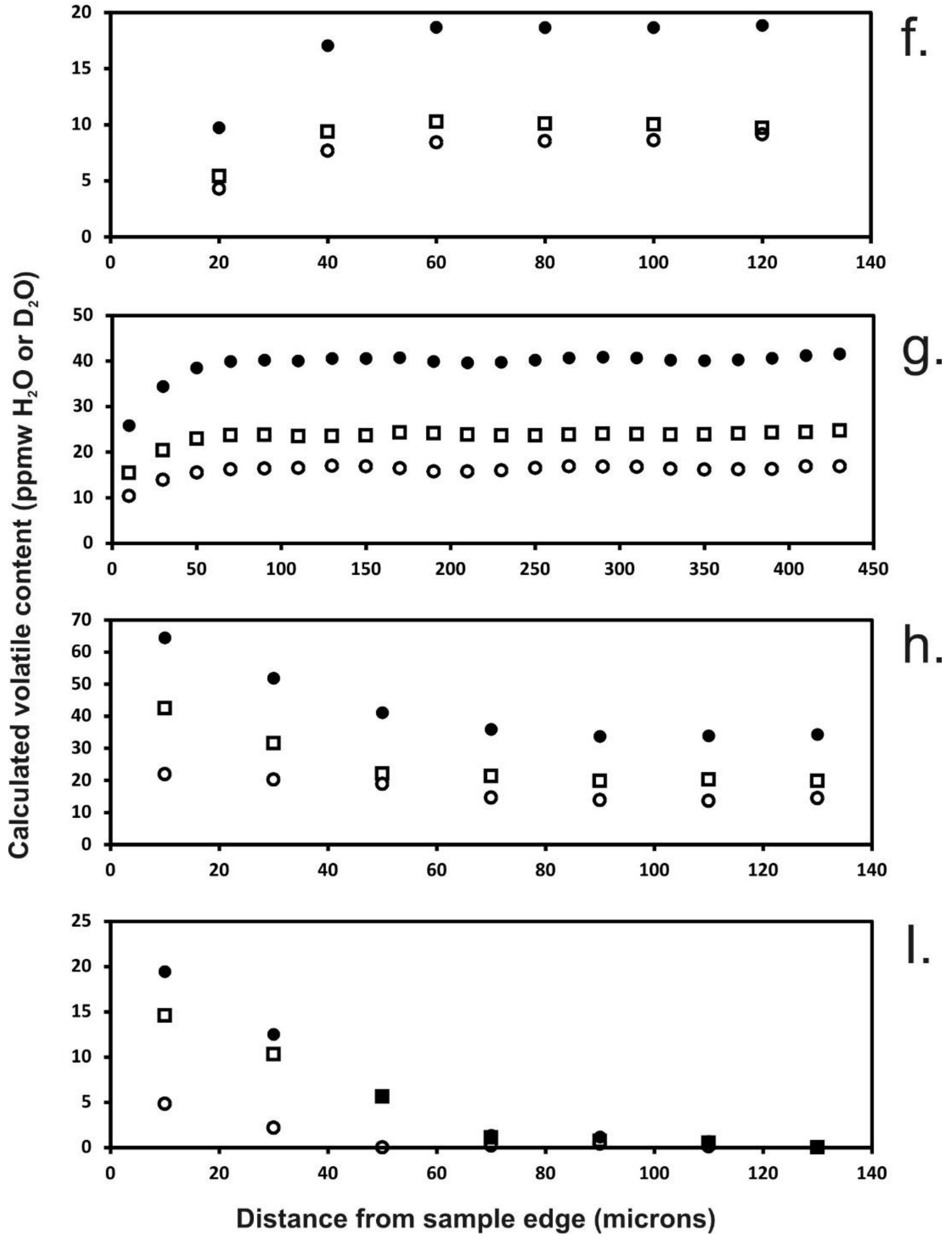

Figure 4 cont. f. Hysp5 (500°C, D_2O) showing H loss (no O-D detected); g. Hysp6 (700°C, H_2O) showing H loss; h. Hysp6 (700°C, D_2O) showing H gain; i. Hysp6 (700°C, D_2O) also showing D gain in the same sample.

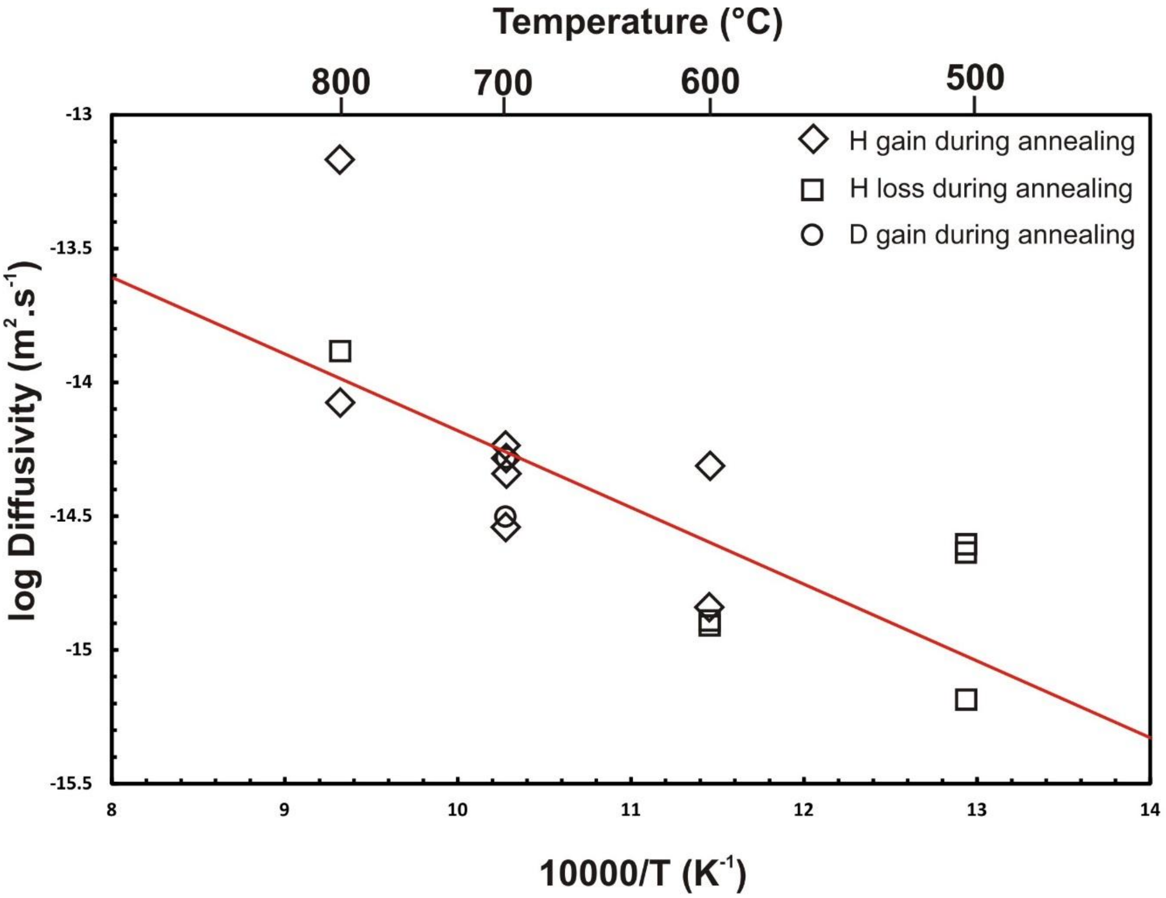

Figure 5. Arrhenius plot showing the temperature dependence of H and D diffusivity in defect spinel determined from IR analysis of annealed defect spinel. Multiple data points at each temperature, where present, show the results of fitting multiple diffusion transects in both samples. Error bars on determined diffusivities are smaller than plot size, although a more realistic error would be significantly larger, as a more significant source of error results from fitting IR data (see text for further discussion). Red line is fitted Arrhenius law to all data points.

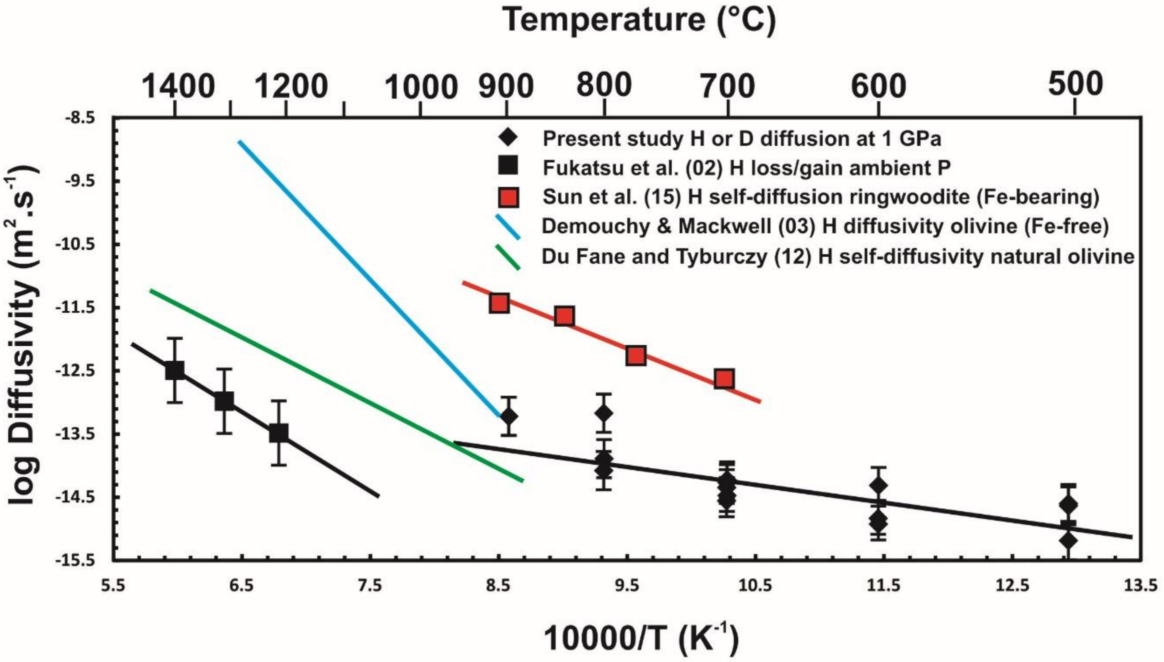

Figure 6. Arrhenius plot showing the temperature dependence of H and D diffusivity in defect spinel determined from the present study, based on H and D diffusion at 1 GPa, and the study by Fukatsu et al., (2002) who determine H loss/gain from spinel plates annealed at ambient pressure in different environments. Red data points are H self-diffusion in ringwoodite from Sun et al. (2015). Blue line shoes approximate temperature dependence of H diffusion in olivine from Demouchy and Mackwell (2003) and green line H self-diffusion in natural olivine Du Frane and Tyburczy (2012).

References

Bell, D., Rossman, G., 1992. Water in Earth's Mantle. The role of nominally anhydrous minerals. Science 255, 1391-1397.

Blanchard, M., Wright, K., Gale, J., 2005. A computer simulation study of OH defects in Mg2SiO4 and Mg2GeO4 spinels. Physics and Chemistry of Minerals 32, 585-593.

Bolfan-Casanova, N., 2005. Water in the Earth's mantle. Mineralogical Magazine 69, 229-257.

Bolfan-Casanova, N., Keppler, H., Rubie, D., 2000. Water partitioning between nominally anhydrous minerals in the MgO-SiO2-H2O system up to 24 GPa: implications for the distribution of water in the Earth's mantle. Earth and Planetary Science Letters 182, 209-221.

Bromiley, G., Keppler, H., McCammon, C., Bromiley, F., Jacobsen, S., 2004. Hydrogen solubility and speciation in natural, gem-quality Cr-diopside. Am. Miner. 89, 941-949.

Bromiley, G.D., Nestola, F., Redfern, S.A.T., Zhang, M., 2010. Water incorporation in synthetic and natural MgAl2O4 spinel. Geochimica Et Cosmochimica Acta 74, 705-718.

Canova, F.F., Foster, A.S., Rasmussen, M.K., Meinander, K., Besenbacher, F., Lauritsen, J.V., 2012. Non-contact atomic force microscopy study of hydroxyl groups on the spinel MgAl2O4(100) surface. Nanotechnology 23.

Chamorro Perez, E., Daniel, I., Chervin, J.-C., Dumas, P., Bass, J., Inuoe, T., 2006. Synchrotron IR study of hydrous ringwoodite (γ-Mg_2SiO_4) up to 30 GPa. Physics and Chemistry of Minerals 33, 502-510.

Demouchy, S., Mackwell, S., 2003. Water diffusion in synthetic iron-free forsterite. Physics and Chemistry of Minerals 30, 486-494.

Donlon, W.T., Mitchell, T.E., Heuer, A.H., 1982. PRECIPITATION IN NONSTOICHIOMETRIC SPINEL. Journal of Materials Science 17, 1389-1397.

Du Frane, W.L., Tyburczy, J.A., 2012. Deuterium-hydrogen exchange in olivine: Implications for point defects and electrical conductivity. Geochemistry Geophysics Geosystems 13.

Fukatsu, N., Kurita, N., Shiga, H., Murai, Y., Ohashi, T., 2002. Incorporation of hydrogen into magnesium aluminate spinel. Solid State Ionics 152-153, 809-817.

Gaetani, G., Grove, T., 1998. The influence of water on melting of mantle peridotite. Contributions to Mineralogy and Petrology 131, 323-346.

Gonzalez, R., Chen, Y., 2002. Transport of hydrogenic species in crystalline oxides: radiation and electric-field-enhanced diffusion. Journal of Physics: Condensed Matter 14, R1143-R1173.

Gonzalez, R., Chen, Y., Barhorst, J., Tsang, K., 1987. Protons and deuterons in stoichiometric and nonstoichiometric MgAl2O4. Journal of Materials Research 2, 77-81.

Huang, X., Xu, Y., Karato, S., 2005. Water content in the transition zone from electrical conductivity of wadsleyite and ringwoodite. Nature 434, 746-749.

Ingrin, J., Skogby, H., 2000. Hydrogen in nominally anhydrous upper-mantle minerals: concentration levels and implications. European Journal of Mineralogy 12, 543-570.

Karato, S.I., 2013. Theory of isotope diffusion in a material with multiple species and its implications for hydrogen-enhanced electrical conductivity in olivine. Physics of the Earth and Planetary Interiors 219, 49-54.

Kohlstedt, D., Keppler, H., Rubie, D., 1996. Solubility of water in the alpha, bet and gamma phases of (Mg,Fe)SiO4. Contibutions to mineralogy and petrology 123, 345-357.

Kudoh, Y., 2001. Structural relation of hydrous ringwoodite to hydrous wadsleyite. Physics and Chemistry of Minerals 28, 523-530.

Kudoh, Y., Kuribayashi, T., Mizohata, H., Ohtani, E., 2000. Structure and cation disorder of hydrous ringwoodite, γ-$Mg_{1.89}Si_{0.97}O_4$. Physics and Chemistry of Minerals 27.

Lenaz, D., Skogby, H., Nestola, F., Princivalle, F., 2008. OH incorporation in nearly pure $MgAl_2O_4$ natural and synthetic spinels. Geochimica et Cosmochmica Acta 72, 475-479.

Libowitzky, E., Rossman, G., 1997. An IR absorption calibration for water in minerals. Am. Miner. 82, 1111-1115.

Mackwell, S., Kohlstedt, D., 1990. Diffusion of hydrogen in olivine: Implications for water in the mantle. Journal of Geophysical Research 95, 5079-5088.

Mackwell, S., Kohlstedt, D., Paterson, M., 1985. The role of water in the deformation of olivine single crystals. Journal of Geophysical Research 90, 11319-11333.

Panero, W.R., Smyth, J.R., Pigott, J.S., Liu, Z.X., Frost, D.J., 2013. Hydrous ringwoodite to 5 K and 35 GPa: Multiple hydrogen bonding sites resolved with FTIR spectroscopy. Am. Miner. 98, 637-642.

Paterson, M., 1982. the determination of hydroxyl by infrared absorption in quartz, silicate glasses and similar materials. Bulletin of Mineralogy 105, 20-29.

Pearson, D.G., Brenker, F.E., Nestola, F., McNeill, J., Nasdala, L., Hutchison, M.T., Matveev, S., Mather, K., Silversmit, G., Schmitz, S., Vekemans, B., Vincze, L., 2014. Hydrous mantle transition zone indicated by ringwoodite included within diamond. Nature 507, 221-+.

Purevjav, N., Okuchi, T., Tomioka, N., Abe, J., Harjo, S., 2014. Hydrogen site analysis of hydrous ringwoodite in mantle transition zone by pulsed neutron diffraction. Geophysical Research Letters 41, 6718-6724.

Redfern, S., Harrison, R., O'Neill, H.S.C., Wood, D., 1999. Thermodynamics and kinetics of cation ordering in $MgAl_2O_4$ spinel up to 1600°C from in situ neutron diffraction. Am. Miner. 84, 299-310.

Schmandt, B., Jacobsen, S.D., Becker, T.W., Liu, Z.X., Dueker, K.G., 2014. Dehydration melting at the top of the lower mantle. Science 344, 1265-1268.

Smyth, J., Frost, D., Nestola, F., Holl, C., Bromiley, G., 2006. Olivine hydration in the deep upper mantle: Effects of temperature and silica activity. Geophysical Research Letters 33, L15301.

Smyth, J., Holl, C., Frost, D., Jacobsen, S., 2004. High pressure crystal chemistry of hydrous ringwoodite and water in the Earth's interior. Physics of the Earth and Planetary Interiors 143-144, 271-278.

Smyth, J., Holl, C., Frost, D., Jacobsen, S., Langenhorst, F., McCammon, C., 2003. Structural systematics of hydrous ringwoodite and water in Earth's interior. Am. Miner. 88, 1402-1407.

Sun, W., Yoshino, T., Sakamoto, N., Yurimoto, H., 2015. Hydrogen self-diffusivity in single crystal ringwoodite: Implications for water content and distribution in the mantle transition zone. Geophysical Research Letters 42, 6582-6589.

Watson, E.B., Baxter, E.F., 2007. Diffusion in solid-Earth systems. Earth and Planetary Science Letters 253, 307-327.

Yang, X.Z., Keppler, H., Dubrovinsky, L., Kurnosov, A., 2014. In-situ infrared spectra of hydroxyl in wadsleyite and ringwoodite at high pressure and high temperature. Am. Miner. 99, 724-729.

Yoshino, T., Manthilake, G., Matsuzaki, T., Katsura, T., 2008. Dry mantle transition zone inferred from the conductivity of wadsleyite and ringwoodite. Nature 451, 326-329.

APPENDIX E

Python script to fit diffusion profiles to Fick’s law

sp_fit

October 13, 2016

0.0.1 hysp3

In [3]:
```
import numpy as np
import matplotlib.pyplot as plt
from scipy.special import erf
from scipy.optimize import curve_fit

#define fitting function (Fick’s Law - infinite source)
def FI(dist, D, C, C2):
    return C - ((erf(dist/(2*((D*(60*60*75))**0.5))))*(C-C2))

#read data from file, ignoring header line
conc_3a, dist_3a = np.loadtxt('hysp3_a.txt', skiprows=1, unpack=True)
conc_3b, dist_3b = np.loadtxt('hysp3_b.txt', skiprows=1, unpack=True)
conc_3c, dist_3c = np.loadtxt('hysp3_c.txt', skiprows=1, unpack=True)

#initial estimates
D0 = 1e-10
C0 = 1
C20 = 1

#fit data - SciPy Levenberg-Marquart method (function, xdata, ydata, initial estimates)
(D_3a, C_3a, C2_3a), pcov = curve_fit(FI, dist_3a, conc_3a, p0=[D0, C0, C20])
(D_3b, C_3b, C2_3b), pcov = curve_fit(FI, dist_3b, conc_3b, p0=[D0, C0, C20])
#(D_3c, C_3c, C2_3c), pcov = curve_fit(FI, dist_3c, conc_3c, p0=[D0, C0, C20])

#create y data set using best fit values
y_3a = FI(dist_3a, D_3a, C_3a, C2_3a)
y_3b = FI(dist_3b, D_3b, C_3b, C2_3b)
#y_3c = FI(dist_3c, D_3c, C_3c)

#create plot
plt.plot(dist_3a*10**6, conc_3a, 'ro', label="IR data (a)")
plt.plot(dist_3a*10**6, y_3a, 'k-', label="Fit (a)")
plt.plot(dist_3b*10**6, conc_3b, 'rs', label="IR data (b)")
plt.plot(dist_3b*10**6, y_3b, 'k--', label="Fit (b)")
plt.plot(dist_3c*10**6, conc_3c, 'rd', label="IR data (c)")
axes = plt.gca()
axes.set_xlim([0,140])
axes.set_ylim([5,25])
plt.legend(prop={'size':10}, numpoints=1, loc='center right')
rcParams['mathtext.default']='regular'
plt.xlabel("Distance ($\mu$m)")
plt.ylabel("D (ppm)")
```

```
plt.title("hysp3")

plt.savefig(’hysp3.png’, dpi=200)
```

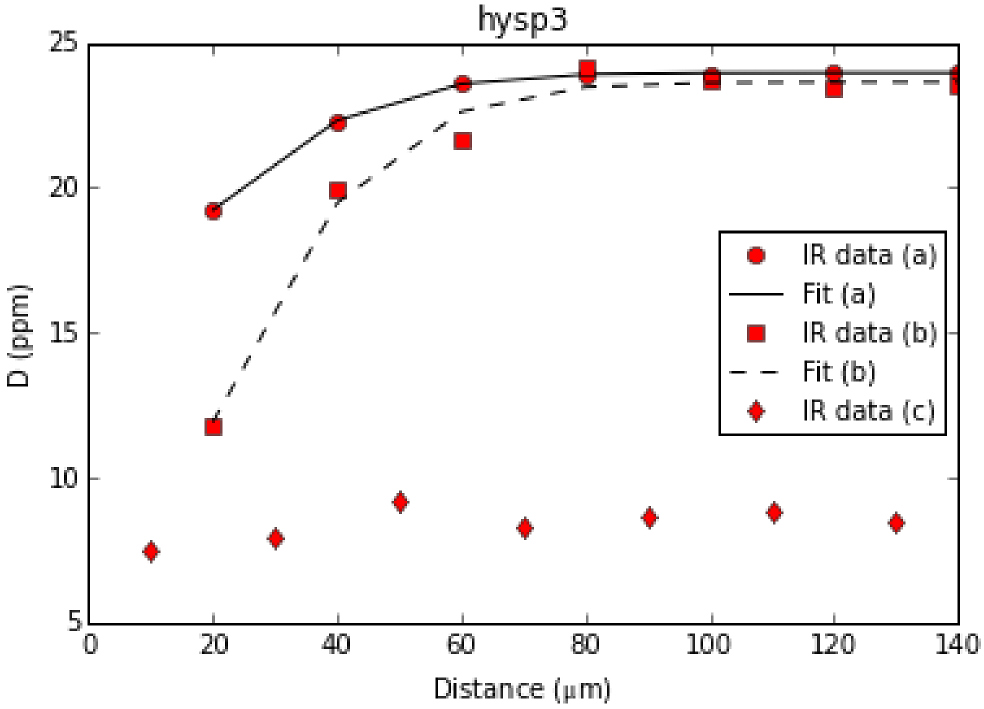

0.0.2 hysp4

In [4]:

```
import numpy as np
import matplotlib.pyplot as plt
from scipy.special import erf
from scipy.optimize import curve_fit

#define fitting function (Fick’s Law - infinite source)
def FI(dist, D, C, C2):
    return C - ((erf(dist/(2*((D*(60*60*75))**0.5))))*(C-C2))

#read data from file, ignoring header line
conc_4a, dist_4a = np.loadtxt(’hysp4_a.txt’, skiprows=1, unpack=True)
conc_4b, dist_4b = np.loadtxt(’hysp4_b.txt’, skiprows=1, unpack=True)

#initial estimates
D0 = 1e-10
C0 = 1
C20 = 1

#fit data - SciPy Levenberg-Marquart method (function, xdata, ydata, initial estimates)
(D_4a, C_4a, C2_4a), pcov = curve_fit(FI, dist_4a, conc_4a, p0=[D0, C0, C20])
(D_4b, C_4b, C2_4b), pcov = curve_fit(FI, dist_4b, conc_4b, p0=[D0, C0, C20])
```

```
#create y data set using best fit values
y_4a = FI(dist_4a, D_4a, C_4a, C2_4a)
y_4b = FI(dist_4b, D_4b, C_4b, C2_4b)

#create plot
plt.plot(dist_4a*10**6, conc_4a, 'ro', label="IR data (a)")
plt.plot(dist_4a*10**6, y_4a, 'k-', label="Fit (a)")
plt.plot(dist_4b*10**6, conc_4b, 'rs', label="IR data (b)")
plt.plot(dist_4b*10**6, y_4b, 'k--', label="Fit (b)")
axes = plt.gca()
plt.legend(prop={'size':10}, numpoints=1, loc='upper left')
rcParams['mathtext.default']='regular'
plt.xlabel("Distance ($\mu$m)")
plt.ylabel("D (ppm)")
plt.title("hysp4")

plt.savefig('hysp4.png', dpi=200)
```

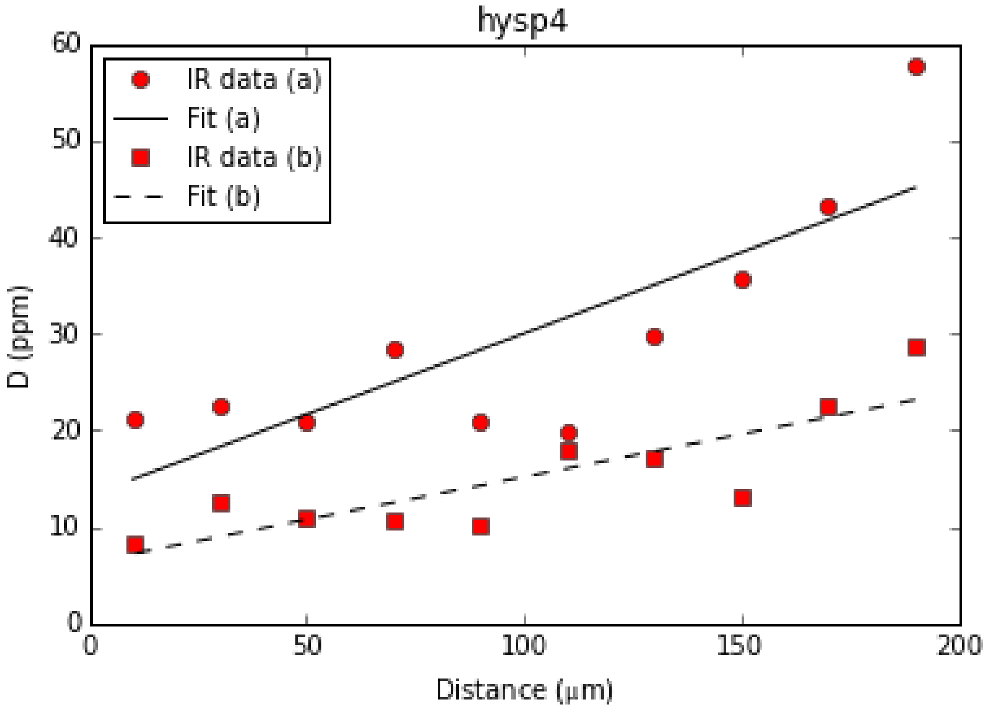

0.0.3 hysp5

```
In [5]: import numpy as np
        import matplotlib.pyplot as plt
        from scipy.special import erf
        from scipy.optimize import curve_fit

        #define fitting function (Fick's Law - infinite source)
```

```
def FI(dist, D, C, C2):
    return C - ((erf(dist/(2*((D*(60*60*75))**0.5))))*(C-C2))

#read data from file, ignoring header line
conc_5a, dist_5a = np.loadtxt('hysp5_a.txt', skiprows=1, unpack=True)
conc_5b, dist_5b = np.loadtxt('hysp5_b.txt', skiprows=1, unpack=True)

#initial estimates
D0 = 1e-10
C0 = 1
C20 = 1

#fit data - SciPy Levenberg-Marquart method (function, xdata, ydata, initial estimates)
(D_5a, C_5a, C2_5a), pcov = curve_fit(FI, dist_5a, conc_5a, p0=[D0, C0, C20])
(D_5b, C_5b, C2_5b), pcov = curve_fit(FI, dist_5b, conc_5b, p0=[D0, C0, C20])

#create y data set using best fit values
y_5a = FI(dist_5a, D_5a, C_5a, C2_5a)
y_5b = FI(dist_5b, D_5b, C_5b, C2_5b)

#create plot
plt.plot(dist_5a*10**6, conc_5a, 'ro', label="IR data (a)")
plt.plot(dist_5a*10**6, y_5a, 'k-', label="Fit (a)")
plt.plot(dist_5b*10**6, conc_5b, 'rs', label="IR data (b)")
plt.plot(dist_5b*10**6, y_5b, 'k--', label="Fit (b)")
axes = plt.gca()
plt.legend(prop={'size':10}, numpoints=1, loc='lower right')
rcParams['mathtext.default']='regular'
plt.xlabel("Distance ($\mu$m)")
plt.ylabel("D (ppm)")
plt.title("hysp5")

plt.savefig('hysp5.png', dpi=200)
```

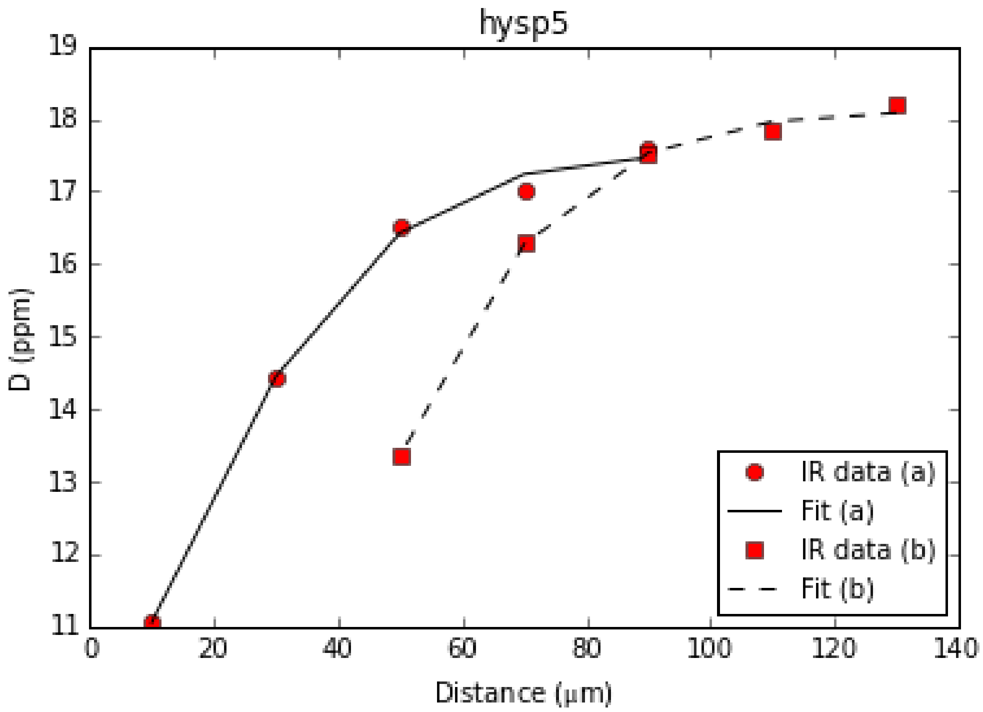

0.0.4 hysp6

```
In [2]: import numpy as np
        import matplotlib.pyplot as plt
        from scipy.special import erf
        from scipy.optimize import curve_fit

        #define fitting function (Fick's Law - infinite source)
        def FI(dist, D, C, C2):
            return C - ((erf(dist/(2*((D*(60*60*75))**0.5))))*(C-C2))

        #read data from file, ignoring header line
        conc_6a, dist_6a = np.loadtxt('hysp6_a.txt', skiprows=1, unpack=True)
        conc_6b, dist_6b = np.loadtxt('hysp6_b.txt', skiprows=1, unpack=True)
        conc_6c, dist_6c = np.loadtxt('hysp6_c.txt', skiprows=1, unpack=True)

        #initial estimates
        D0 = 1e-10
        C0 = 1
        C20 = 1

        #fit data - SciPy Levenberg-Marquart method (function, xdata, ydata, initial estimates)
        (D_6a, C_6a, C2_6a), pcov = curve_fit(FI, dist_6a, conc_6a, p0=[D0, C0, C20])
        (D_6b, C_6b, C2_6b), pcov = curve_fit(FI, dist_6b, conc_6b, p0=[D0, C0, C20])
        (D_6c, C_6c, C2_6c), pcov = curve_fit(FI, dist_6c, conc_6c, p0=[D0, C0, C20])

        #create y data set using best fit values
```

```
y_6a = FI(dist_6a, D_6a, C_6a, C2_6a)
y_6b = FI(dist_6b, D_6b, C_6b, C2_6b)
y_6c = FI(dist_6c, D_6c, C_6c, C2_6c)

#create plot
plt.plot(dist_6a*10**6, conc_6a, 'ro', label="IR data (a)")
plt.plot(dist_6a*10**6, y_6a, 'k-', label="Fit (a)")
plt.plot(dist_6b*10**6, conc_6b, 'rs', label="IR data (b)")
plt.plot(dist_6b*10**6, y_6b, 'k--', label="Fit (b)")
plt.plot(dist_6c*10**6, conc_6c, 'rd', label="IR data (c)")
plt.plot(dist_6c*10**6, y_6c, 'k:', label="Fit (c)")
axes = plt.gca()
plt.legend(prop={'size':10}, numpoints=1, loc='center right')
rcParams['mathtext.default']='regular'
plt.xlabel("Distance ($\mu$m)")
plt.ylabel("D (ppm)")
plt.title("hysp6")

plt.savefig('hysp6.png', dpi=200)
```

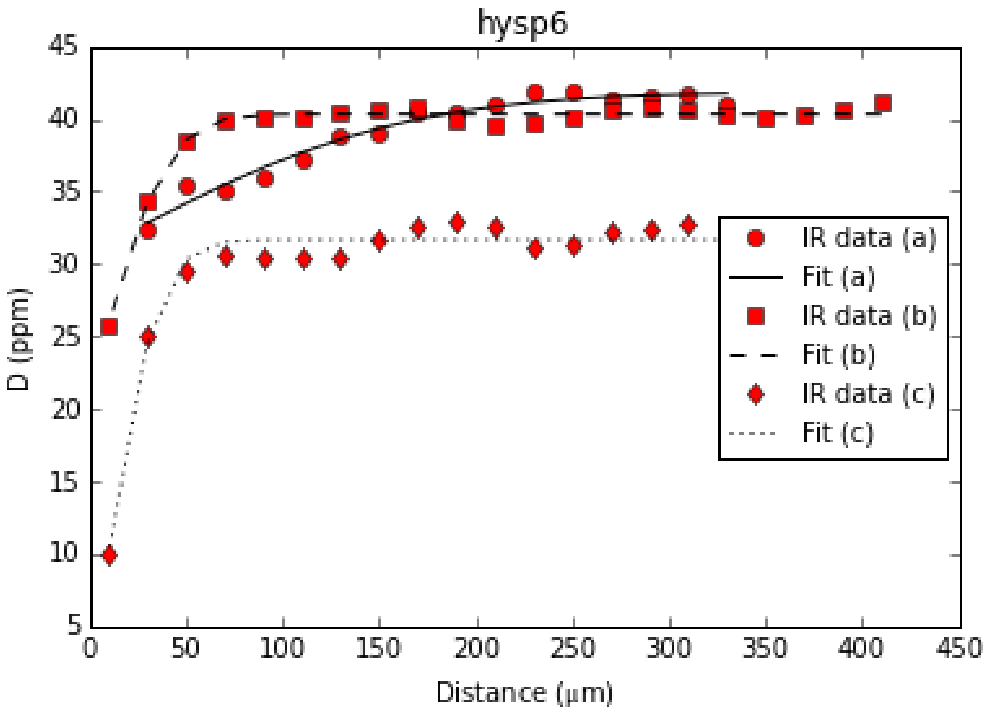

```
In [ ]:
```